DESY-Thesis 2009-031
TESLA-FEL 2009-08

Optical Synchronization of a Free-Electron Laser with Femtosecond Precision

Dissertation

zur Erlangung des Doktorgrades
des Fachbereichs Physik
der Universität Hamburg

vorgelegt von

Florian Löhl
aus Hamburg

Hamburg
2009

Gutachter der Dissertation	Prof. Dr. Jörg Roßbach Prof. Dr. F. Ömer Ilday (Bilkent University, Ankara)
Gutachter der Disputation	Prof. Dr. Jörg Roßbach PD Dr. Bernhard Schmidt
Datum der Disputation	27. März 2009
Vorsitzender des Prüfungsausschusses	Dr. Klaus Petermann
Vorsitzender des Promotionsausschusses	Prof. Dr. R. Klanner
Dekan der Fakultät für Mathematik, Informatik und Naturwissenschaften	Prof. Dr. Heinrich H. Graener

Abstract

High-gain free-electron lasers (FELs) are capable of generating sub-10 fs long light pulses. In order to take full advantage of these extremely short light pulses in time-resolved experiments, synchronization with a so far unprecedented timing accuracy is required.

Within this thesis, an optical synchronization system providing sub-10 fs stability has been developed and was implemented at the ultra-violet and soft X-ray free-electron laser FLASH at DESY, Hamburg. The system uses a mode-locked laser as a timing reference. The laser pulses are distributed via length stabilized optical fiber-links to the remote locations. A key feature of the system is a bunch arrival-time monitor detecting the electron bunch arrival-time with an unrivaled resolution of 6 fs.

A feedback system based on the arrival-time monitor was established, improving the arrival-time fluctuations from 200 fs in the unstabilized case to 25 fs with active feedback. In order to achieve the high peak current of several thousand amperes required for the FEL process, the electron bunches are longitudinally compressed in two magnetic chicanes. A second feedback system was developed stabilizing the bunch compression process based on measurements of diffraction radiation. The combination of both feedback systems improves the stability of the FEL radiation significantly.

Zusammenfassung

High-gain Freie-Elektronen-Laser (FEL) ermöglichen die Erzeugung von Lichtpulsen mit Pulsdauern von unter 10 fs. Um in zeitaufgelösten Experimenten den vollen Nutzen aus diesen extrem kurzen Lichtpulsen ziehen zu können, ist eine bisher unerreichte Synchronisationsgenauigkeit erforderlich.

Im Rahmen dieser Arbeit wurde ein optisches Synchronisationssystem entwickelt, welches eine Stabilität von besser als 10 fs gewährt. Dieses System wurde am Freie-Elektronen-Laser FLASH bei DESY, der im ultraviolett und weichen Röntgenbereich arbeitet, implementiert. Das System nutzt einen modengekoppelten Kurzpulslaser als Zeitreferenz. Die Laserpulse werden in längenstabilisierten Glasfaserleitungen zu den Subsystemen im Beschleuniger übertragen. Ein Hauptbestandteil des Systems ist ein Elektronenpuls-Ankunftszeitmonitor, der eine bislang unerreichte Auflösung von 6 fs bietet.

Basierend auf dem Ankunftszeitmonitor wurde ein Rückkoppelsystem entwickelt, welches die Ankunftszeitschwankungen der Elektronenpulse von 200 fs im unstabilisierten Fall auf 25 fs mit aktiver Rückkopplung verbessert. Um den für den FEL Prozess benötigten Spitzenstrom von einigen tausend Ampere zu erreichen, werden die Elektronenpakete in zwei magnetischen Schikanen longitudinal komprimiert. Um den Kompressionsprozess zu stabilisieren, wurde ein zweites Rückkoppelsystem entwickelt, welches die Emission von elektronenstrahlinduzierter Diffraktionsstrahlung

stabilisiert. Die Kombination aus beiden Rückkoppelsystemen führt zu einer wesentlichen Verbesserung der Stabilität der FEL Pulsenergie.

Contents

1 Introduction **1**
- 1.1 Principle of a free-electron laser . . . 3
  - 1.1.1 Undulator radiation . . . 3
  - 1.1.2 FEL process . . . 4
  - 1.1.3 FEL operation modes . . . 7

2 The free-electron laser FLASH **10**
- 2.1 Electron source . . . 10
- 2.2 Time structure . . . 12
- 2.3 Bunch compressors . . . 13
- 2.4 Undulators . . . 13

3 Diagnostic techniques **16**
- 3.1 Transverse electron beam diagnostics . . . 16
- 3.2 Longitudinal electron beam diagnostics . . . 17
  - 3.2.1 Transverse deflecting cavity . . . 17
  - 3.2.2 Electro-optical beam profile measurements . . . 18
  - 3.2.3 Coherent radiation diagnostics . . . 20

4 Timing of the electron beam **29**
- 4.1 Influence of the electron gun . . . 29
- 4.2 Influence of the first accelerating section . . . 33
- 4.3 Influence of the accelerating section upstream of BC2 . . . 39
- 4.4 Reduction of timing variations from the electron gun by bunch compression . . . 42
- 4.5 Impact of collective effects on the bunch arrival-time . . . 43
- 4.6 Phase space linearization with a third-harmonic cavity . . . 44

5 Synchronization schemes **52**
- 5.1 Timing sensitive devices in the accelerator . . . 52
- 5.2 Conventional RF based synchronization scheme . . . 52
- 5.3 Optical synchronization scheme . . . 53
- 5.4 Required long-term frequency stability of the MLO . . . 55

6 Master Laser Oscillator **58**

6.1 Requirements . . . 58
6.2 Setup . . . 59
6.3 Operation principle . . . 60
6.4 Measurement of the timing stability . . . 62
6.5 Locking of the MLO to an RF source . . . 64
6.6 Measurement of the relative intensity noise . . . 66
6.7 Measurement of the optical spectrum under different operation conditions . . . 66
6.8 Measurement of the pulse duration under different operation conditions 72

7 Fiber-link stabilization 75
7.1 Setup . . . 75
7.1.1 Laser pulse broadening in the fiber-link . . . 77
7.2 Balanced optical cross-correlator . . . 79
7.3 Measurement results of the fiber-link stability . . . 81
7.4 Fiber-links installed at FLASH . . . 84
7.5 Influence of erbium-doped fiber amplifiers on the timing stability of optical pulse trains . . . 87
7.6 Drift-free RF based timing detector . . . 92

8 Bunch arrival-time monitor 96
8.1 Principle of the arrival-time monitor . . . 96
8.2 Arrival-time measurements with a ring-type beam pick-up . . . 98
8.2.1 Determination of the resolution of the BAM prototype . . . 100
8.2.2 Orbit dependence of the beam pick-up signal . . . 103
8.2.3 Arrival-time measurements of the electron bunches . . . 104
8.2.4 Reduction of the orbit dependence of the beam pick-up . . . 106
8.3 The BAM system for FLASH . . . 107
8.3.1 Button-type beam pick-up . . . 109
8.3.2 Orbit dependence of the pick-up signal . . . 110
8.3.3 Charge dependence of the pick-up signal . . . 110
8.3.4 Fast charge measurement with a BAM . . . 115
8.4 Bunch arrival-time measurements at FLASH . . . 115
8.4.1 Comparison of arrival-time measurements with a BAM and with electro-optic spectral decoding . . . 118
8.5 Measurement of the BAM resolution and the stability of the optical synchronization system. . . . 120

9 Injector timing characterization and correction 127
9.1 Measurement of the relative timing between gun and photo-cathode laser . . . 127
9.2 Photo-cathode laser response measurement . . . 129
9.3 Correction of the photo-cathode laser timing across the electron macro-pulse . . . 131

10 Longitudinal feedback system **133**
10.1 Bunch arrival-time feedback 133
10.2 Beam compression feedback 137
10.3 Effect of the feedback systems on the FEL radiation stability 139

11 Conclusions and outlook **143**

A Abbreviations **145**

B Transfer matrix formalism **147**

C Transfer matrices of important beam line elements **151**

D Propagation of light pulses in optical fibers **153**
D.1 Fiber losses 153
D.2 Dispersion 153
D.3 Dispersive pulse broadening 154
D.4 Self-phase modulation 155
D.5 Nonlinear Schroedinger Equation and split step technique 156

E Images and drawings of selected experimental set-ups **158**

List of Tables

6.1 Fiber lengths of the 216.7 MHz soliton laser. 60
6.2 Properties of the 216.7 MHz fiber laser beam for different pump power settings and wave-plate settings. 70
6.3 Autocorrelation and pulse widths for different settings of the 216.7 MHz fiber laser. 70

8.1 Summary of correlation measurements between two BAMs. 121

A.1 Abbreviations used inside the text. 145
A.2 Abbreviations used inside the text (continued). 146

List of Figures

1.1 Comparison of the peak brilliance of different synchrotron radiation sources and existing and planned free-electron lasers. 2
1.2 Relation between electron oscillation and light wave for sustained energy transfer from the electron to the light wave. 6
1.3 Dependence of the gain length at FLASH on the transverse emittance calculated with a 1D and a 3D FEL model. 7

2.1 Schematic layout of FLASH. 11
2.2 Schematic setup of the photo-cathode laser. 12
2.3 Schematic of the RF electron gun. 12
2.4 Time structure of the electron bunches at FLASH. 13
2.5 Schematic of the first bunch compressor BC1 and illustration of the bunch compression principle. 14

3.1 Schematic setup to measure the longitudinal charge distribution with a transverse deflecting cavity. 17

3.2 Different schemes to measure the longitudinal charge distribution of an electron bunch by electro-optic methods. 19
3.3 Transition radiation for normal and oblique incidence. 21
3.4 Spectral energy density of transition radiation emitted by a single electron. 22
3.5 Spectral energy density of diffraction radiation emitted by a single electron. 23
3.6 Form factor for different Gaussian shaped bunches of different lengths. 26
3.7 Intensity increase by coherent effects for different bunch lengths. . . . 26

4.1 Simulated longitudinal phase space distributions at the entrance of ACC1 for different gun phases. 30
4.2 Peak current and rms bunch length at the entrance of ACC1 as functions of the gun phase. 31
4.3 Relative bunch arrival-time at the entrance of BC1 for different gun phases. 31
4.4 Influence of timing changes of the laser, the gun, and ACC1 on the electron bunch arrival-time at the entrance of BC1. 32
4.5 Longitudinal phase space distributions after BC1 and BC2 and corresponding current profiles for different phases in ACC1. 36
4.6 Example of a current distribution of the electron bunch. 37
4.7 Different beam parameters after BC1 for various ACC1 phases. 38
4.8 Influence of ACC1 amplitude changes on the bunch arrival-time downstream of BC2. 39
4.9 Influence of ACC1 phase changes on the bunch arrival-time downstream of BC2. 40
4.10 Influence of ACC23 amplitude changes on the bunch arrival-time downstream of BC2. 40
4.11 Influence of ACC23 phase changes on the bunch arrival-time downstream of BC2. 41
4.12 Modification of bunch arrival-time variations from the electron gun after the first bunch compressor as a function of the ACC1 phase. . . 42
4.13 Modification of bunch arrival-time variations from the electron gun after both bunch compressors as a function of the ACC1 and ACC23 phases. 43
4.14 Effect of longitudinal space charge on the longitudinal phase space distribution and the bunch timing. 45
4.15 Effect of longitudinal space charge on the current profiles and the bunch timing. 46
4.16 Resulting sum signal from ACC1 and the third harmonic cavity. . . . 48
4.17 Example phase space distributions and corresponding current profiles after BC1 with linearization of the ACC1 accelerating field with a third-harmonic cavity. 49

4.18 Sensitivity of the peak current and the bunch arrival-time after BC1 on changes of the phases and amplitudes of ACC1 and the third harmonic cavity. 50

5.1 General concept of the optical synchronization system. 53
5.2 Illustration of the effect of MLO frequency changes on the fiber-link lengths. 56

6.1 Schematic setup of the 216.7 MHz soliton fiber laser. 60
6.2 Nonlinear and dispersive phase shifts for a Gaussian- and sech^2-shaped laser pulse in an optical fiber. 61
6.3 Schematic setup to measure the laser timing stability. 62
6.4 Comparison of the timing stability of a 200 MHz soliton fiber laser and a 40.8 MHz stretched pulse fiber laser. 63
6.5 Schematic setup to lock the MLO to an RF source. 65
6.6 Schematic setup to measure the laser amplitude noise. 66
6.7 Relative intensity noise of the 216.7 MHz soliton fiber laser. 67
6.8 Optical spectra of the 216.7 MHz soliton laser for different pump power settings. 68
6.9 Pulse shapes calculated from the optical spectra of the 216.7 MHz fiber laser operated at different pump power settings. 69
6.10 Optical spectra of the 216.7 MHz fiber laser for a constant pump power but different wave-plate settings. 71
6.11 Pulse shapes calculated from the optical spectra of the 216.7 MHz fiber laser operated at a constant pump power but different wave-plate settings. 72
6.12 Interferometric autocorrelation of the 216.7 MHz soliton fiber laser with different fits to the autocorrelation envelope. 73
6.13 Interferometric autocorrelation of the 216.7 MHz fiber laser operated at different pump power settings. 74
6.14 Interferometric autocorrelation of the 216.7 MHz fiber laser operated at a constant pump power but different wave-plate settings. 74

7.1 Schematic setup of the fiber-link stabilization. 76
7.2 Operation principle of the balanced optical cross-correlator. 79
7.3 Measured signal strength of the two cross-correlator detectors for different temporal offsets of the two laser pulses at the crystal entrance. . 81
7.4 Measured spectral timing jitter density of a 300 m long stabilized fiber-link. 82
7.5 Measured short- and long-term stability of a 400 m long stabilized fiber-link. 83
7.6 Required timing correction of two fiber-links installed at FLASH over a period of two months. 85

7.7 Short-term oscillation of the required link-timing correction of two fiber-links installed at FLASH. 86
7.8 Short-term oscillation of the FEL pulse energy. 86
7.9 Experimental setup to characterize the influence of an EDFA on the timing stability of an optical pulse train. 87
7.10 Timing jitter added to the optical pulse train by the EDFA measured in the frequency range from 500 Hz to 4.5 MHz. 88
7.11 Autocorrelation traces of the amplified laser pulses for different optical input powers and different pump powers of the EDFA. 89
7.12 Autocorrelation traces of the amplified laser pulses for different optical input powers and different pump powers of the EDFA (continued). . . 90
7.13 Timing jitter spectral density of the amplified laser pulses for different EDFA pump power settings. 91
7.14 Schematic setup of the RF based timing detector. 93
7.15 Superposition of two optical pulse trains and corresponding power spectral density of the photo-detector signal. 94
7.16 Difference signal between the power levels of the 22^{nd} and 23^{rd} harmonics of the laser repetition rate as a function of the temporal offset Δt. 94
7.17 Long-term stability of the RF based timing detector. 95

8.1 Schematic setup to measure the arrival-time of the beam pick-up signal. 97
8.2 Operation principle of the bunch arrival-time monitor. 97
8.3 Technical drawing and 3D model of the ring-type beam pick-up used for the bunch arrival-time measurements. 99
8.4 Measured laser amplitude at different sample positions along the beam pick-up signal. 99
8.5 Analysis steps to determine the energy of the modulated laser pulses. . 101
8.6 Arrival-time measurement of the pick-up signal. 102
8.7 Dependence of the arrival-times of the zero-crossings from the two signals of the ring-type beam pick-up on the horizontal beam position. 103
8.8 Electron bunch arrival-time for different settings of the ACC1 field amplitude. 104
8.9 Comparison of the averaged arrival-time at the end of the accelerator and the energy variation along the bunch train downstream of ACC1. 105
8.10 Change of the BAM calibration constant with the horizontal beam position. 106
8.11 Signal shape of the ring-type beam pick-up for different horizontal beam positions. 107
8.12 Schematic layout of the bunch arrival-time monitors for FLASH. . . . 108
8.13 Technical drawing and 3D model of the button-type beam pick-up used for the bunch arrival-time measurements. 109
8.14 Signal shape of the button-type beam pick-up for different horizontal beam positions. 110

8.15 Scan of laser pulses over the signal of the button-type beam pick-up. . 111
8.16 Arrival-time of the zero-crossing of the button-type beam pick-up signal as a function of the beam orbit. 112
8.17 Dependence of the BAM calibration constant on the beam orbit. . . . 112
8.18 Dependence of the arrival-time of the pick-up signal's zero-crossing on the bunch charge. 113
8.19 Variation of the longitudinal charge distribution for different bunch charges. 113
8.20 Dependence of the BAM calibration constant on the bunch charge. . . 114
8.21 Correlation between the normalized amplitude of two laser pulses which sample the ringing of the beam pick-up signal and the bunch charge measured with a toroid. 115
8.22 Bunch arrival-time distribution along the bunch train for ten consecutive trains. 116
8.23 Correlation between the arrival-times of two adjacent bunches in the bunch train. The BAM resolutions estimated from the correlation widths of 1000 consecutive shots are 17.5 fs (left) and 15.6 fs (right). . 117
8.24 Dependence of the uncorrelated arrival-time jitter between two adjacent bunches along the bunch train. 117
8.25 Determination of the bunch arrival-time from the electro-optic spectral decoding signal. 118
8.26 Bunch arrival-time measured by a BAM and an electro-optic spectral decoding setup. 119
8.27 Relative jitter between the arrival-times measured by a BAM and by an electro-optic spectral decoding setup. 119
8.28 Locations of the two bunch arrival-time monitors used for the resolution measurement. 120
8.29 Correlation of the arrival-times measured with two BAMs which are separated by 60 m. 121
8.30 Arrival-time measured by two BAMs over a duration of about 9 minutes together with the difference signal of both measurements. 122
8.31 Arrival-time measured by two BAMs over a duration of about 1.5 hours together with the difference signal of both measurements. 123
8.32 Arrival-time measured by two BAMs over a duration of about 4.5 hours together with the difference signal of both measurements. 124
8.33 Arrival-time measured by two BAMs over more than 7 hours together with the difference signal of both measurements. 125

9.1 Charge emitted by the electron source for different phases of the RF gun. 128
9.2 Response measurement of the photo cathode laser to a time step. . . . 130
9.3 Correction of the timing between photo cathode laser and gun RF by adding a timing slope of about 6.4 ps over the 800 μs of the bunch train to the laser timing. 131

10.1 Schematic principle of the bunch arrival-time and compression feedback. 133
10.2 Bunch arrival-time stability of the electron beam without the arrival-time feedback. . . . 134
10.3 Bunch arrival-time stability of the electron beam with the arrival-time feedback active. . . . 135
10.4 Best bunch arrival stability achieved with the feedback. . . . 136
10.5 Generation of well defined arrival-time patterns along the electron bunch train using the bunch arrival-time feedback. . . . 137
10.6 Effect of the bunch compression feedback. . . . 138
10.7 Distribution of the FEL radiation pulse energy along the bunch train with and without active bunch compression and arrival-time feedbacks. 140
10.8 Average FEL radiation pulse energy with and without active compression and arrival-time feedbacks. . . . 141
10.9 Effect of the bunch compression and arrival-time feedback on the stability of the FEL pulse energy along the bunch train. . . . 141

B.1 Accelerator coordinate system. . . . 148

E.1 Prototypes of the master laser oscillator and two fiber-link stabilization units used at FLASH. . . . 158
E.2 Engineered version of the fiber-link stabilization front-end. . . . 159
E.3 Engineered version of the master laser oscillator. . . . 160
E.4 Technical drawing and image of the optical front-end used for the bunch arrival-time measurements. . . . 161
E.5 BAM readout and regulation electronics. . . . 162

1 Introduction

High intensity X-ray beams are needed in multiple disciplines of science ranging from physics, chemistry, and biology to material sciences and medical diagnostics. Due to their short wavelengths, they provide atomic spatial resolution, and their long penetration depth and strong interaction with core electrons allows for the study of the structure and properties of single atoms, large macro-molecules and biological systems.

A figure of merit for characterizing a light source is the *peak brilliance*. For transversely coherent radiation sources, it is defined as

$$\text{brilliance} = \frac{4\Phi}{\lambda^2}\,, \tag{1.1}$$

where λ is the radiation wavelength and Φ the spectral flux given as

$$\Phi = \frac{N_{\text{ph}}}{\sigma_t \sigma_\omega}\,, \tag{1.2}$$

with N_{ph} being the number of photons within the spectral width σ_ω of typically 0.1% and the duration of the light pulse σ_t.

Over the last decades, advances in accelerator and laser-based X-ray sources have increased the achievable peak brightness by many orders of magnitude. Amongst the most powerful X-ray sources are third generation electron storage rings with a very small beam emittance and undulator magnets to produce the radiation pulses. A limitation of a storage ring based light source is the long pulse duration, set by the equilibrium electron bunch length which is typically on the order of 10 ps to 100 ps (FWHM) [Wie03a, Wie03b].

Special slicing techniques can overcome this limitation by manipulating a fraction of the electron bunch with an ultra-short laser pulse and by spatially separating the manipulated electrons from the main bunch [ZZ96, SCC$^+$00]. A major disadvantage of this technique, however, is the small number of photons contained in the femtosecond long slices.

High-gain free-electron lasers (FELs) are a promising candidate for the generation of ultra-short, high power X-ray pulses. Such light pulses combine atomic spatial resolution with a temporal resolution in the femtosecond range. Figure 1.1 gives an overview of the peak brilliance achieved at different synchrotron light sources and free-electron lasers. The tremendous advantage of an FEL is evident.

The combination of the large number of photons per pulse and the short pulse duration in the femtosecond range opens up entirely new experimental opportunities to study the dynamics of electronic and magnetic processes on a single shot basis. A

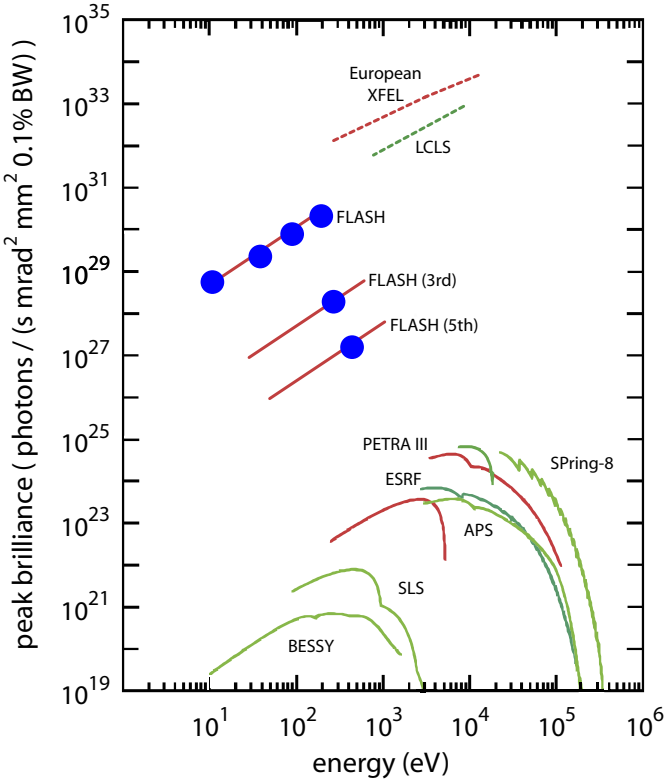

Figure 1.1: Comparison of the peak brilliance of different synchrotron radiation sources and existing and planned (dashed line) free-electron lasers (adapted from [SDR08]).

popular technique to investigate the dynamics of fast processes is the pump-probe scheme. In this scheme, the system is excited by a 'pump' light pulse, in many applications from a visible or infrared short-pulse laser, and the excited state of the system is probed by the FEL pulse. By varying the temporal offset between the two pulses, the development of the excitation and its decay can be measured.

Since both light pulses are generated by independent sources, the timing of both light pulses fluctuates independently and it is a challenge to precisely synchronize both light sources. Any uncertainty of the temporal offset between the two light pulses degrades the experiment's temporal resolution. In order to achieve a high resolution, either very precise arrival-time measurements for both light pulses are needed or both sources must have a very small temporal jitter. To fully exploit the experimental opportunities offered by FEL pulses, the timing of the two light pulses has to be established with an accuracy that is better than the FEL pulse duration. Since the FEL pulses can have durations well below 10 fs [AAA+07], an as yet unreached synchronization accuracy is required.

Within this thesis, optical techniques to synchronize a free-electron laser with femtosecond precision have been developed. The work was carried out at the free-electron laser in Hamburg, FLASH, at DESY.

A mode-locked, erbium-doped fiber laser is used as a timing reference. The laser pulses are distributed within the facility via dispersion compensated optical fibers.

Balanced optical cross-correlators are used to measure length changes of the optical fibers with femtosecond resolution. These length changes are compensated with piezo-electric actuators. Various end-stations are foreseen at the end of the fiber-links to synchronize different components in the accelerator driving the FEL. One of them is an electro-optic bunch arrival-time monitor which measures the arrival-times of the electron bunches with sub-10 femtosecond resolution. A feedback system, which uses this precise arrival-time measurement, has been established to improve the timing stability of the FEL to 25 fs (rms).

1.1 Principle of a free-electron laser

In the following, a brief introduction of the physical principles of an FEL is given. It is based on the descriptions in [SSY99, SDR08, Wie03b, Jac98], where more details can be found.

1.1.1 Undulator radiation

Electrons, which are deflected inside the magnetic field of a dipole magnet, emit synchrotron radiation with a broad, continuous frequency spectrum ranging from zero to beyond the critical frequency ω_c

$$\omega_c = \frac{3c\gamma_{\mathrm{rel}}^3}{2R}. \tag{1.3}$$

Here, c is the speed of light, $\gamma_{\mathrm{rel}} = E/m_{\mathrm{e}}c^2$ the Lorentz factor, E the electron energy, m_{e} the electron rest mass, and R the bending radius.

By using periodic magnetic structures consisting of many short dipole magnets of alternating polarity, so-called *undulator* magnets, the electrons emit nearly monochromatic radiation. Compared to a single bending magnet of same length, the same radiation energy is emitted, but the photon beam is much better collimated and the spectral width of the radiation can be strongly reduced.

An undulator magnet is characterized by the undulator parameter K, defined as

$$K = \frac{eB_{\mathrm{u}}\lambda_{\mathrm{u}}}{2\pi m_{\mathrm{e}}c}, \tag{1.4}$$

with the undulator period λ_{u} and the peak magnetic field in the undulator B_{u}.

Inside an undulator magnet, the electrons move on a sinusoidal trajectory. The undulator parameter K characterizes the oscillation strength of the electrons and the maximum deflection angle with respect to the undulator axes is given by

$$\Theta_{\mathrm{max}} \approx \frac{K}{\gamma_{\mathrm{rel}}}. \tag{1.5}$$

Since most of the radiation emitted by a relativistic electron is concentrated in a narrow cone with an opening angle of $1/\gamma_{\mathrm{rel}}$, this defines a limit for the undulator

parameter K, such that there is spatial overlap of the radiation fields emitted from various sections of the electron trajectory. This results in

$$\Theta_{\max} \lesssim \frac{1}{\gamma_{\mathrm{rel}}} \quad \Rightarrow \quad K \lesssim 1. \tag{1.6}$$

If the undulator parameter is very large, $K \gg 1$, the radiation fields emitted along the magnetic structure have no spatial overlap and quasi-continuous *wiggler radiation* will be emitted. In this discussion, we will not consider this case.

For an undulator parameter $K \lesssim 1$ many radiation fields originating from various sections of the electron trajectory are superimposed resulting in a narrow spectral width of the emitted radiation. The fundamental wavelength λ_{ph} of undulator radiation in forward direction is given by

$$\lambda_{\mathrm{ph}} = \frac{\lambda_{\mathrm{u}}}{2\gamma_{\mathrm{rel}}^2}\left(1 + \frac{K^2}{2}\right). \tag{1.7}$$

As one can see from Eq. 1.7, the wavelength of the undulator radiation can be varied by changing the electron energy or the undulator parameter K. The latter possibility exists in electro-magnetic undulators and in permanent-magnet undulators with a variable gap.

The spectral width of the radiation depends on the number of undulator periods N_{u} and the full width at half maximum (FWHM) is

$$\Delta\omega \approx \frac{\omega_{\mathrm{ph}}}{N_{\mathrm{u}}}, \tag{1.8}$$

where $\omega_{\mathrm{ph}} = 2\pi c/\lambda_{\mathrm{ph}}$ is the central frequency of the emitted radiation. If the undulator radiation is generated by a bunch of electrons, the line width is increased due to electron beam energy spread and betatron oscillations.

The radiation from a planar undulator is linearly polarized with the electric field vector in the plane of the sinusoidal electron trajectory.

1.1.2 FEL process

Undulator radiation by a single electron is generated by coherent superposition of the radiation fields generated in the single undulator periods. Compared to the radiation of a bending magnet, this increases the spectral brightness by a factor of N_{u}^2. The intensities of different electrons, however, are added incoherently. The radiation field emitted by an electron with the longitudinal position z_0 is canceled by the radiation field emitted by an electron with the longitudinal position $z_0 + \lambda_{\mathrm{ph}}/2$. Let us consider an electron bunch with randomly distributed electrons traveling along the undulator. Due to the point-like nature of the electron, the spectral distribution of the current density $J(\omega)$ of such a bunch is frequency independent and its magnitude scales with the square root of the number of electrons N

$$J(\omega) = \sqrt{\frac{e^2 N}{\pi A_{\mathrm{b}}^2 \sigma_t}}, \tag{1.9}$$

where A_b is the cross sectional area of the electron bunch and σ_t the bunch duration [SDR08]. The electron bunch has, therefore, a density modulation with a white frequency spectrum, referred to as *shot noise*. This implies that the field amplitude emitted by N electrons is $\sqrt{N}$ time larger than the one from a single electron, yielding an N times higher intensity. This also means that an electron bunch can radiate only because of the statistical fluctuations of the charge density.

In a high-gain FEL, the phase relations between the electrons are no longer randomly distributed. By a mechanism called *microbunching*, a state is generated in which many of the electrons emit their radiation in phase. The consequence is an increase of the electric and magnetic fields which is now directly proportional the number of coherently emitting electrons N_c, leading to an intensity increase by the factor of N_c^2. Taking into account that in a typical FEL N_c can be on the order of 10^4 to 10^6 or even larger, this results in a tremendous increase of the radiation intensity.

An FEL can be considered as an amplifier in which an incident light wave gains energy from the electron beam. Let us assume a light wave

$$E_x(z,t) = E_0 \cos(k_\mathrm{ph} z - \omega_\mathrm{ph} t + \psi_0) \quad \text{with} \quad k_\mathrm{ph} = \frac{\omega_\mathrm{ph}}{c} = \frac{2\pi}{\lambda_\mathrm{ph}} \tag{1.10}$$

of wavelength λ_ph which co-propagates with the electron beam along the undulator. The energy transfer from a single electron to the light wave is given by the time derivative of the electron energy $W = \gamma_\mathrm{rel} m_\mathrm{e} c^2$

$$\frac{\mathrm{d}W}{\mathrm{d}t} = -e v_x(t) E_x(t). \tag{1.11}$$

The electron speed along the undulator is slower than that of the light wave due to its motion on the sinusoidal trajectory at a speed slower than c. The average speed in z-direction is given by [SDR08]

$$\bar{v}_z = \frac{c(1-(2+K^2))}{4\gamma_\mathrm{rel}^2}\,. \tag{1.12}$$

Equation 1.11 states that without the slippage, there would be no energy transfer from the electron to the light wave, since every half period of the electron oscillation, energy is alternately transferred from the electron to the light wave and vice versa. If the slippage between electron and light wave is adjusted in a way that per half period of the electron motion the light wave has a phase advance of π, sustained energy transfer from the electron to the light wave can be achieved (see Fig. 1.2). This is the case when the light wavelength fulfills the resonance condition of Eq. 1.7.

The energy transfer described above is only possible for electron bunches which are short compared to the light wavelength. In long bunches, part of the electrons transfer energy to the light wave while another part withdraws energy from it and the net energy gain of the light wave is zero, if the light wavelength is chosen according to Eq. 1.7. It can be shown, however, that when a light wavelength slightly larger

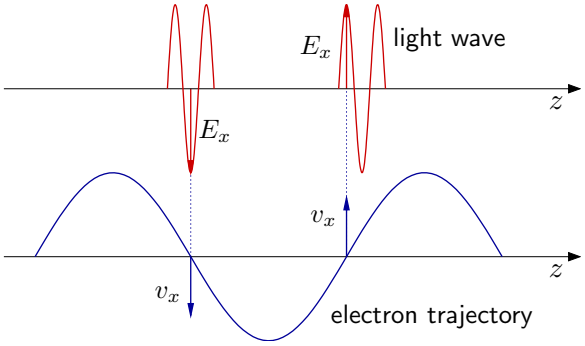

Figure 1.2: Relation between electron oscillation and light wave for sustained energy transfer from the electron to the light wave.

than the resonant wavelength (Eq. 1.7) is chosen, a net energy transfer to the light wave can still be achieved. This is used in *low gain* FELs, in which the undulator is centered in an optical cavity. Many electron bunches, which are typically recycled by using a storage ring, are used to drive the amplification process. During every path through the undulator, the intensity of the light wave is increased by a few percent. Such kind of FELs operate typically in the infrared and optical range.

At shorter wavelength in the ultraviolet or X-ray range, no suitable mirrors are available to build an optical cavity with low losses and, therefore, the light amplification must be achieved during a single pass through a very long undulator (*high gain* FEL). The process with which this is possible is called *microbunching*. Since some of the electrons in the bunch gain and others lose energy, the trajectories of these electrons within the undulator are different. This leads to a shorter path of the electrons with higher energy and a longer one for those with lower energy. The consequence is the generation of an electron density modulation with the light period. The short electron slices of larger charge density are referred to as *microbunches*. These electron slices emit their radiation in phase which yields to a quadratic enhancement of the emitted intensity.

The formation of the microbunches is accelerated with the increase of the light wave intensity yielding an exponential growth of the light power P along the undulator:

$$P(z) \propto \exp\left(\frac{z}{L_\mathrm{G}}\right) \qquad \text{for} \quad z \gtrsim 2L_\mathrm{G}. \tag{1.13}$$

The growth rate is characterized by the gain length L_G which in the one-dimensional FEL theory is proportional to

$$L_\mathrm{G} \propto \left(\frac{\sigma_\perp^2}{I_0}\right)^{\frac{1}{3}}. \tag{1.14}$$

The quantity $\sigma_\perp$ denotes the transverse rms beam size and I_0 is the peak current. Equation 1.14 shows that a high peak current and a small transverse beam size are

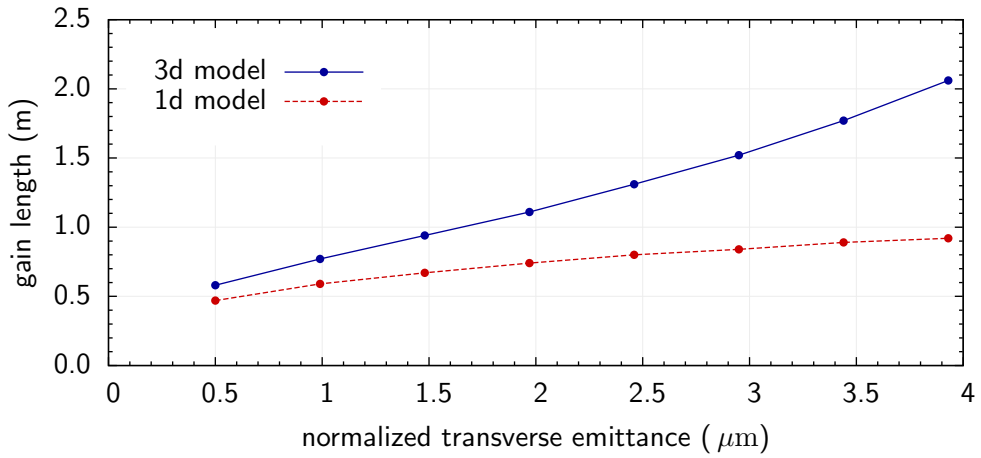

Figure 1.3: Dependence of the gain length at FLASH on the transverse emittance calculated with a 1D and a 3D FEL model [Sch08].

needed to obtain a short gain length. Peak currents of several thousand amperes are needed to keep the gain length sufficiently short.

A three-dimensional calculation shows that in addition to the high charge density, the transverse emittance and the bunch energy spread must be sufficiently small in order to achieve a short gain length. Betatron oscillations of the electrons lead to a reduction and a spread of the longitudinal velocities. This causes different phase shifts with respect to the light wave and, therefore, a reduced FEL gain. Figure 1.3 shows the influence of the transverse emittance on the gain length, calculated for a 1 GeV electron beam at FLASH with a peak current of 2500 A.

1.1.3 FEL operation modes

Conventional lasers can be classified into laser-oscillators and laser-amplifiers. A similar classification can be made for FELs. Low gain FELs with an optical resonator for the emitted light can be considered as a laser-oscillator. In a certain way, a high gain FEL in which the spontaneous undulator radiation generated in the first part of the undulator is amplified, can also be regarded as a laser oscillator, since the origin of the radiation - as in a quantum laser oscillator - is spontaneous emission. This mode of operation is called *self amplified spontaneous emission* (SASE). Another mode of operation is to superpose an external light field at the entrance of the undulator. This light fields is then amplified along the undulator. Such a *seeded* FEL can therefore be considered as a laser amplifier.

Using spontaneous undulator radiation to initiate the FEL process has the advantage that the resonance condition of the FEL is automatically fulfilled and it is available at all wavelengths, also in the X-ray range. A major disadvantage is that the frequency spectrum of the undulator radiation underlies strong statistical fluctuations. These fluctuations are present, even if we neglect the shot noise on the charge distribution, since the emission points along the undulator vary from shot-to-shot.

At the beginning of the undulator, therefore, many different radiation modes exist which are amplified. As the different radiation modes are generated at different positions along the undulator, their entire propagation length is different and, therefore, their amplification and interaction with the electron beam. If the electron bunch is short enough, this can lead to a single dominant mode with very large shot-to-shot fluctuations in wavelength and intensity.

An important parameter of an FEL is the so called *cooperation length* or *coherence length* l_c, which in the one-dimensional FEL theory is given by [SDR08]

$$l_\mathrm{c} \approx \frac{c\lambda_\mathrm{ph}}{6\sqrt{2\pi}\rho_\mathrm{FEL}\sqrt{\frac{L_\mathrm{G}}{z}}}. \tag{1.15}$$

In this equation, ρ_FEL is the dimensionless FEL parameter which is defined as

$$\rho_\mathrm{FEL} = \frac{1}{4\pi\sqrt{3}}\frac{\lambda_\mathrm{u}}{L_\mathrm{G}}. \tag{1.16}$$

A correlation between the radiation fields exists only within this cooperation length. In the saturation regime, an electron bunch which is shorter than l_c generates a photon pulse consisting of only a single longitudinal mode. In longer bunches of length σ_b, however, an average number of $m = \sigma_\mathrm{b}/l_\mathrm{c}$ different longitudinal modes exists, each of them fluctuating from shot-to-shot. With increasing number of modes, the temporal profile gets more and more structured. This can result in a temporal sequence of many light pulses of different wavelengths and amplitudes (see e.g. [BSP+94]). When using these FEL pulses for time resolved experiments, the time resolution will be limited by the length of the electron bunch.

There is another mode of operation in which the statistical fluctuations can be removed. Instead of using the spontaneous undulator radiation as a seed of the FEL, a well defined light field fulfilling the undulator resonance condition can be superimposed with the electron bunch. In this way, the spectral and temporal profile of the seed pulse defines the output pulse amplified along the undulator. The first experimental demonstration of this principle at wavelengths down to 160 nm was done at the SPring-8 Compact SASE Source test accelerator [LHG+08]. Many facilities aim to use this scheme at even shorter wavelengths [KAB+08, B+07, G+05, V+07].

High-gain FELs typically operate in the ultraviolet and X-ray regimes and it can be problematic to generate adequate seeding light pulses. In the ultraviolet and soft X-ray ranges one way of producing suitable light pulses is the generation of high harmonics of a powerful infrared laser in a gas target [FLL+88]. By using *high harmonic generation* (HHG), wavelengths down to around 1 nm were generated [SSJ+05]. However, the required pulse energies on the nano-Joule level were achieved only at wavelengths larger than around 10 nm. Aside from the pulse energy requirement, it is a challenge to maintain spatial overlap between the electron beam and the seed pulse over at least three gain lengths, a process which requires a well collimated laser beam.

A big advantage of this seeding technique is that the temporal and spectral properties of the driving infrared laser can be controlled very precisely, resulting in stable seed light pulses. A remaining challenge of seeding an FEL by an external laser source is the synchronization between the external laser and the electron beam. Any fluctuation of the relative arrival-times leads to changes in the FEL output power.

In the hard X-ray regime, no suitable laser based light sources are yet available. That is the reason that the first X-ray FELs [A$^+$02a, Shi06, ABC$^+$07] will be based on the SASE principle.

2 The free-electron laser FLASH

The free-electron laser in Hamburg, FLASH, is an FEL user facility at DESY (Hamburg) [AAA+07]. It is an upgrade [The02] of the TESLA Test Facility (TTF) linac[1], which was operated until November 2002 to perform various tests related to the TESLA[2] Linear Collider Project [B+01] and to perform a proof-of-principle of a SASE FEL at wavelength ranging from 120 nm to 80 nm [AAA+00, A+02b, A+02c]. With an upgraded photo injector, an increased electron beam energy of up to 1 GeV and a longer undulator, wavelengths down to 6.5 nm are achieved.

FLASH consists of an electron gun, six accelerator modules (ACC1 to ACC6) each including eight superconducting 9-cell niobium cavities with a resonance frequency of 1.3 GHz, two magnetic chicane bunch compressors (BC1 and BC2[3]), and an undulator section composed of six 4.5 m long undulator segments. The total length of the linac is about 250 m. A schematic layout is shown in Fig. 2.1.

The commissioning of the FLASH facility started in the beginning of 2004. First lasing with a wavelength of 32 nm was achieved in January 2005 [A+06]. Saturation at a wavelength of 13.5 nm was measured in August 2006 [AAA+07]. After an energy upgrade in Summer 2007, lasing at a wavelength of 6.5 nm was achieved in October 2007 [HFS08].

2.1 Electron source

In a high-gain FEL, the electron beam quality requirements are very demanding. As we have seen above, a high charge density is required in order to minimize the gain length L_G and, therefore, the undulator length. An electron bunch with a peak current of several thousand amperes and a normalized transverse emittance of a few micrometers is required at the undulators. The generation of such a low emittance electron beam is very challenging and at FLASH, this is done by using a photo-injector. It is driven by an actively mode-locked Nd:YLF laser system operating at a wavelength of 1047 nm. The Cs_2Te-cathode requires a photon energy of around 3.5 eV to extract electrons and to achieve this, the laser pulses are frequency-doubled two times yielding a final wavelength of 262 nm. This frequency doubling is done in 5 mm long LBO[4] and BBO[5] crystals. The frequency converted light is guided

[1] linear accelerator
[2] TeV Energy Superconducting Linear Accelerator
[3] To be compatible with the TTF1 nomenclature, the DESY internal names, which are sometimes also used in the literature, are BC2 and BC3.
[4] Lithium Triborate (LiB_3O_5)
[5] Beta Barium Borate (β-BaB_2O_4)

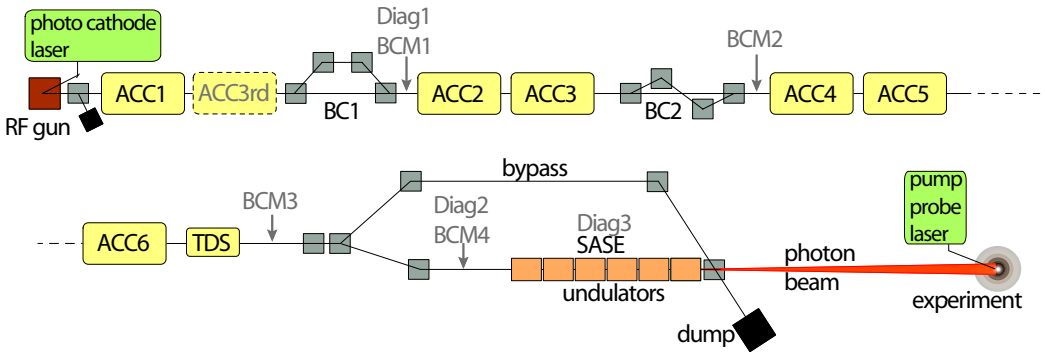

Figure 2.1: Schematic layout of FLASH. The electron source is an RF photo-injector. The electrons are accelerated in six modules (ACC1 to ACC6) up to an energy of 1 GeV. The bunches are longitudinally compressed in two bunch compressors BC1 and BC2. The total length is about 250 m. TDS: transverse deflecting structure, BCM: bunch compression monitor, Diag: diagnostic section for transverse beam properties.

onto the cathode. An iris is installed in the laser beam line and used to generate a transversely flat profile as well as to reduce the effect of the source's pointing jitter. A schematic of the laser system is depicted in Fig 2.2.

The quantum efficiency of the cathode material is up to 10% for a fresh cathode, depending on the vacuum conditions. As the cathode ages, the efficiency drops gradually to around 0.5%, at which point the cathode has to be replaced. The life time of a cathode is several months.

Since there is a high interest in synchronizing the photo-cathode laser, it is important to note that the oscillator does not deliver the required pulse energy. Four amplification stages increase the laser pulse energy from 300 nJ at the exit of the oscillator up to 300 μJ before entering the nonlinear crystals. These amplifications stages may introduce additional timing jitter.

The longitudinal profile of the laser pulses is Gaussian with an rms width of about 4.4 ps. Simulations have shown [FFG+01, ABH+06] that the transverse emittance of the electron beam is better for a 20 ps long, flat-top laser pulse with rise and fall times of 2 ps. Such a longitudinally shaped laser beam is currently evaluated at the photo injector test facility DESY, Zeuthen site.

The laser profile must also be transversely flat, since the space charge forces for a cylindrical beam with a constant charge density increase linearly from the center to the tails and can be compensated with a magnetic lens.

Figure 2.3 shows a schematic of the electron gun. The electron beam generated at the cathode is accelerated in a normal conducting $1\frac{1}{2}$ cell 1.3 GHz cavity. With a solenoid (main solenoid) the beam is focused to counteract repulsive space charge forces and to minimize emittance growth. A second solenoid, called a bucking coil, is used to cancel the magnetic field on the cathode surface, where the electrons emitted

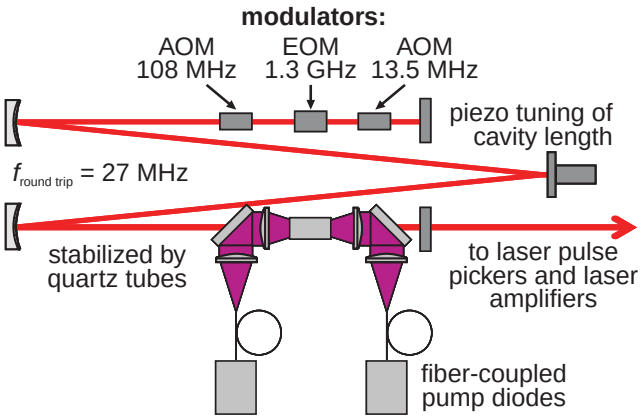

Figure 2.2: Schematic setup of the photo-cathode laser.

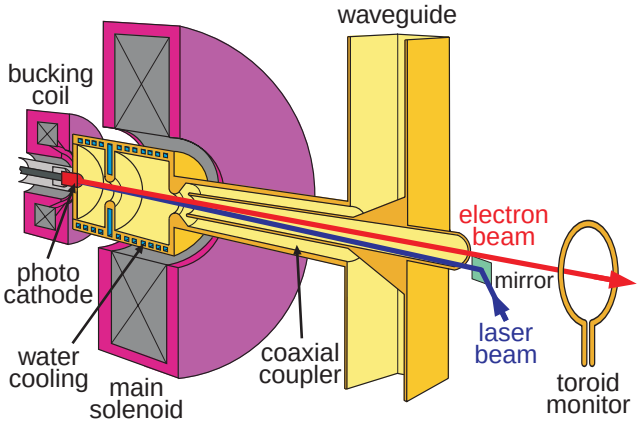

Figure 2.3: Schematic of the RF electron gun.

by the photo effect have a very low energy. A non-vanishing magnetic field at this position would lead to an emittance increase.

The beam energy after the gun is around 5 MeV. At these energies, space charge effects are still very strong so the first acceleration module is installed as close as possible after the gun, increasing the beam energy to about 130 MeV.

2.2 Time structure

The accelerating cavities in the linac are operated at a frequency of 1.3 GHz and they are made from superconducting niobium and operated at a temperature of 2 K. The accelerating gradients are between 12 and 25 $\frac{\text{MV}}{\text{m}}$. The resistive losses in the cavity walls are very small in superconducting cavities. This results in a very high quality factor of above $2 \cdot 10^{10}$ for an unloaded cavity [A+00], which is about 5 to 6 orders of magnitude higher than that of normal conducting cavities. Due to the small

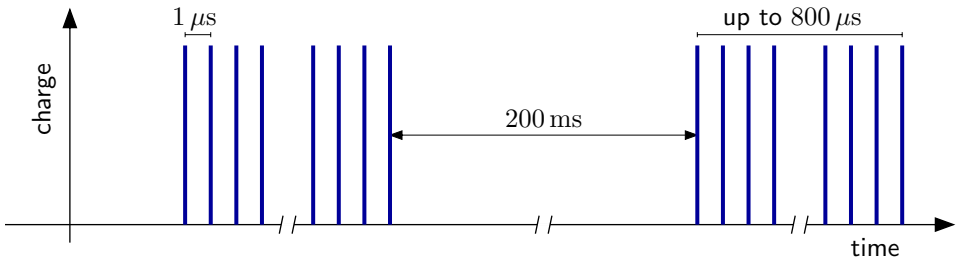

Figure 2.4: Time structure of the electron bunches at FLASH. Each macro-pulse contains up to 800 bunches. The bunch spacing within the macro-pulse is 1 μs. Larger bunch spacings are possible as well. The repetition rate of the macro-pulses is 5 Hz.

losses, the accelerating fields in the cavities can be sustained over long durations. At FLASH, the RF pulse duration over which electron bunches can be accelerated is up to 800 μs. Within this time, up to 800 bunches are accelerated, each separated by 1 μs. This sequence of electron bunches is called macro-pulse or pulse-train. The repetition rate of these pulse trains is 5 Hz; a 10 Hz operation is planned in the future.

2.3 Bunch compressors

The electron bunches produced inside the gun are rather long. With the Gaussian longitudinal shape, as it is currently produced, the rms length is around 1.7 mm. The peak current is on the order of 40 A, which is far below the requirement for the FEL process. Due to space charge forces, it is not possible to generate the required current density in the gun. This problem necessitates the introduction of bunch compressors, which shorten the electron bunches at higher beam energies where the repulsive Coulomb forces are largely compensated by attractive magnetic forces.

The bunch compressors are realized as magnetic chicanes: electrons of different energies have different path lengths through the chicane. By accelerating the electron bunch off of the crest of the sinusoidal RF field, an energy gradient along the bunch is generated. The electrons in the bunch-head then have a slightly lower energy than the ones in the tail and the bunch is longitudinally compressed (see the schematic in Fig. 2.5). The bunch compression is done at two locations in the accelerator: at a beam energy of 130 MeV and again at around 460 MeV. A more detailed discussion of the bunch compression process is given in chapter 4.

2.4 Undulators

The undulator section used to generate the FEL radiation consists of six 4.5 m long undulator segments. The permanent magnets in the undulator segments create a nearly sinusoidal magnetic field with a periodic length of 27.3 mm and a peak mag-

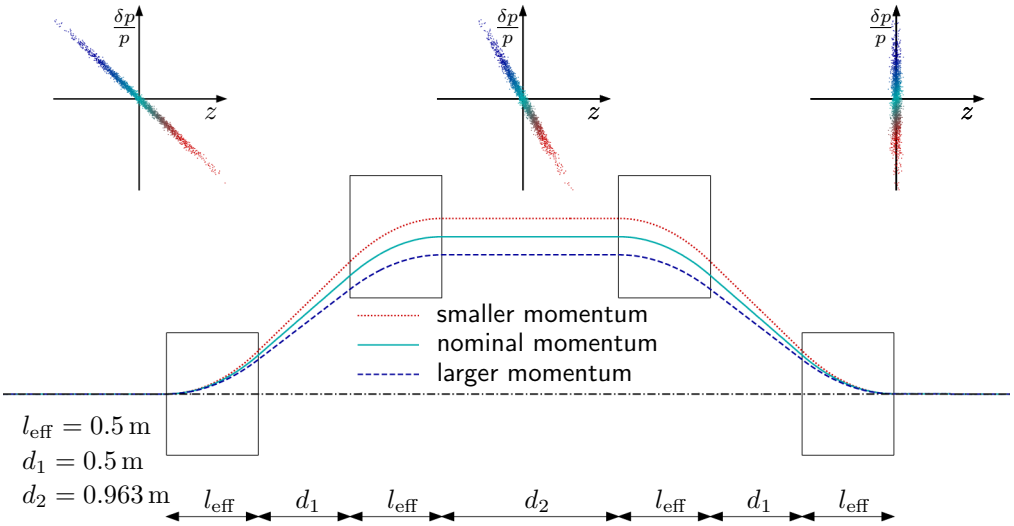

Figure 2.5: Schematic of the first bunch compressor BC1 and illustration of the bunch compression principle. The bunch compressor shears the longitudinal phase space distribution allowing for the compression of a bunch with a longitudinal energy chirp.

netic field of $B_{\mathrm{u}} = 0.46\,\mathrm{T}$. Quadrupole doublets are installed between the undulator segments in order to focus the electron beam. Beam position monitors and wire scanners are also installed between the undulator segments. Both monitors can be used to measure the electron beam trajectory through the undulator. It is important to precisely control this trajectory because it must be almost perfectly aligned with the photon trajectory in order for the interaction between the electron beam and the photon pulse to take place. A correction of the electron beam orbit can be made with steering magnets which are installed between the undulator segments or by transversely moving the single quadrupole magnets. The wire scanners enable monitoring of the transverse beam profile within the undulator with only minor disturbances to the beam operation.

The undulators have a fixed magnetic gap of 12 mm so the resonant radiation wavelength (see Eq. 1.7) can only be tuned by adjusting the electron energy. The wavelength change procedure requires, in addition to changes of the beam energy, adjustments of the beam optics and of the trajectory through the undulator. In order to have an easier and faster method for wavelength changes, most future FELs, like LCLS, the European XFEL, and a potential second beam line at FLASH will use undulators in which the field strength on the electron beam axis can be tuned. Furthermore, in very long undulators, such as those to be used at LCLS and the European XFEL, the electron beam loses so much energy by spontaneous emission along the undulator that the undulator parameter has to be varied in order to fulfill the resonance condition along the entire undulator length.

After the main undulator, another undulator is installed; it has a large period of 40 cm and only 9 full magnetic periods [G$^+$07]. This undulator is designed with the purpose of generating infrared pulses with wavelengths between 50 μm and a few hundred micrometers. Generated by the same electron pulses which generated the FEL light in the first undulator, these infrared pulses are precisely synchronized to the FEL pulses. The two light pulses are separated and guided to the experimental hall where pump-probe experiments are planned.

The infrared pulse is generated by spontaneous emission and all electrons in the bunch contribute. The FEL pulse, however, is only generated by the leading spike which has a sufficiently high current. We will see in chapter 4 that there are mechanisms which change the timing of the lasing beam fraction with respect to the bunch centroid. This also changes the timing between the infrared pulses and the FEL pulses. In chapter 4, the influence of the different machine parameters on the two timings will be discussed.

3 Diagnostic techniques

Since the quality of the electron beam driving the FEL needs to be exceptionally good in all six dimensions of phase space, many diagnostic tools are required to characterize the electron beam. This chapter gives a short overview of important diagnostic techniques with an emphasis on the characterization of the longitudinal beam properties.

3.1 Transverse electron beam diagnostics

Three diagnostic sections (see Fig 2.1) are dedicated to measure the transverse properties of the electron bunches.

In the first section, which is located downstream of the first bunch compressor, four optical transition radiation (OTR) screens and four wire scanners are installed inside a three cell FODO lattice[1] to measure the transverse phase space distribution and the emittance [LSC+06]. The results are used to manipulate the phase space distribution with the upstream quadrupole magnets so that it matches the design optics of the machine. Five quadrupole magnets, a doublet and a triplet upstream of BC1, generate a waist in the beta functions near the last dipole magnet of the bunch compressor. The reason for this is that inside the dipole magnets, coherent synchrotron radiation (CSR) is generated at wavelengths exceeding the bunch length. The CSR generated upstream can catch up with the electron bunch downstream and its interaction with the electrons leads to an emittance increase. The most CSR is generated in the last dipole of BC1 and a waist at this position leads to a large angular spread of the CSR, thereby reducing the interaction between the CSR and the electron bunch. Downstream of the bunch compressor, five additional quadrupole magnets are installed in order to match the phase space distribution to the FODO lattice and the accelerator.

A FODO lattice with OTR screens, similar to the one in the first diagnostic section, is installed in the diagnostic section upstream of the undulators. In this section, a final phase space matching can be done with another five quadrupole magnets upstream of the FODO lattice.

[1] A FODO lattice is a periodic sequence of a focusing quadrupole magnet, a drift section, a defocusing quadrupole magnet and a second drift section.

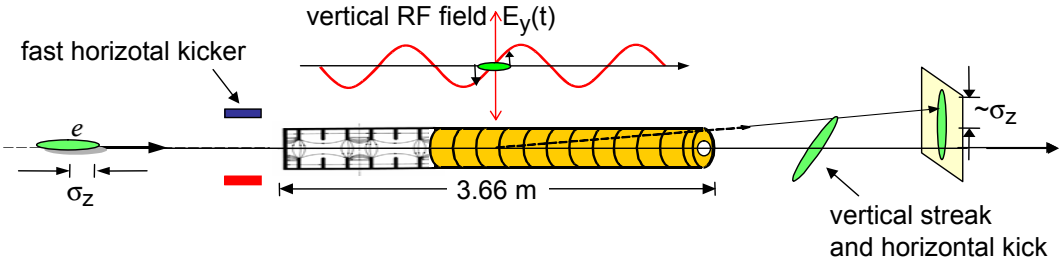

Figure 3.1: Schematic setup to measure the longitudinal charge distribution with a transverse deflecting cavity.

3.2 Longitudinal electron beam diagnostics

The longitudinal properties of the electron bunches are not easily accessible because the length- and time-scales of interest are on the micrometer or femtosecond scale, respectively. Since the longitudinal properties are of such an importance for the FEL operation, many different measurement devices are implemented. The charge distribution along the electron bunch is of special importance. In the following, the most important devices to measure the longitudinal charge distribution and the arrival-time of the electron bunches are briefly introduced. This will be helpful because some comparison measurements between these devices and the arrival-time monitor developed within this thesis will be shown later.

3.2.1 Transverse deflecting cavity

Of instruments that directly measure the longitudinal charge distribution in the time domain, the transverse deflecting traveling wave structure (TDS) has the highest resolution. The principle is depicted in Fig. 3.1. A traveling wave structure is excited with a mode that possesses a transverse deflecting field. The phase of the accelerating voltage is adjusted so that the center of the electron bunch passes the TDS at the zero-crossing of the accelerating wave. In this way, the head and tail of the bunch are accelerated in opposite directions, transverse to the axis of the beam pipe. After several meters of propagation, this leads to transverse displacements of individual longitudinal beam slices. The transverse beam distribution on an OTR screen is then a direct image of the longitudinal beam profile where the transverse beam size of an unstreaked bunch limits the longitudinal resolution. The best performance is achieved for a large beta function in the streaking plane at the position of the TDS and a phase advance of 90° to the OTR screen. With optimized beam optics, a resolution of better than 30 fs is reached.

The transverse deflecting structure offers more than the longitudinal charge distribution measurement. By measuring the streaked distribution for at least three different transfer matrices, which can be achieved by using either different screens or different quadrupole settings, the transverse phase space distribution for different slices of the electron beam can be determined for the direction perpendicular to the

streak direction [Röh08]. Since the FEL process requires not only a high peak current but also a small transverse emittance, this measurement is of special interest. Only a small fraction of electrons within the bunch fulfills both of these criteria and with the transverse deflecting cavity, a tool is available with which the properties of this slice of the bunch can be characterized and optimized.

Another application of the transverse deflecting cavity is the measurement of the electron bunch arrival-time with respect to the streaking RF field. This can be either done by analyzing the beam position with a beam position monitor (BPM), or by analyzing the beam position on the OTR image. The latter option offers the possibility to measure not only the beam centroid but also the timing change of any longitudinal beam fraction of interest, like, for example, the positions with the highest current and lowest emittance. The resolution of these kinds of measurements is mainly limited by the synchronization quality of the streaking field to the machine timing reference. Currently, this is on the order of 400 fs for a time scale of minutes.

An intrinsic disadvantage of the transverse deflecting structure is the fact that the bunches, which are analyzed, are severely perturbed by the measurement and cannot be used for the FEL operation anymore. In order to monitor the longitudinal bunch parameters under normal operation conditions, non-interceptive diagnostics are needed.

The TDS is, due to its complexity, the high operational costs and the fact that it is an interceptive diagnostics not suited as a permanent diagnostics. However, the TDS can perform special control measurements. In this thesis, a bunch arrival-time monitor (BAM) was developed and the TDS was used to analyze the dependence of the BAM on several machine parameters.

3.2.2 Electro-optical beam profile measurements

Driven by the demand of measuring the longitudinal charge density distribution and the arrival-time in a non-destructive way, different kinds of electro-optical detections schemes were developed. They use the Pockels effect inside of certain crystals to imprint the Coulomb field of an electron bunch onto a laser pulse.

So far, three different schemes have been demonstrated. In the first scheme, depicted in Fig. 3.2a), an ultra-short laser pulse is chirped so that a few-picoseconds-long pulse is created in which the different longitudinal positions contain different light wavelengths. This chirped pulse is sent through the electro-optic crystal installed inside the beam pipe a few millimeters away from the electron beam. The arrival-time of the laser pulse is adjusted such that it coincides with the electron bunch. The Coulomb field, whose strength is proportional to the electron bunch charge density, leads to a change of the birefringence in the EO crystal. This birefringence change causes a polarization change and the different Coulomb field amplitudes along the bunch lead to different polarization changes along the laser pulse. By measuring the spectrum of the laser pulse after a polarizer, the longitudinal charge distribution of the electron bunches can be observed. This scheme is referred to as *spectral decoding* and was first demonstrated in [WMG+02].

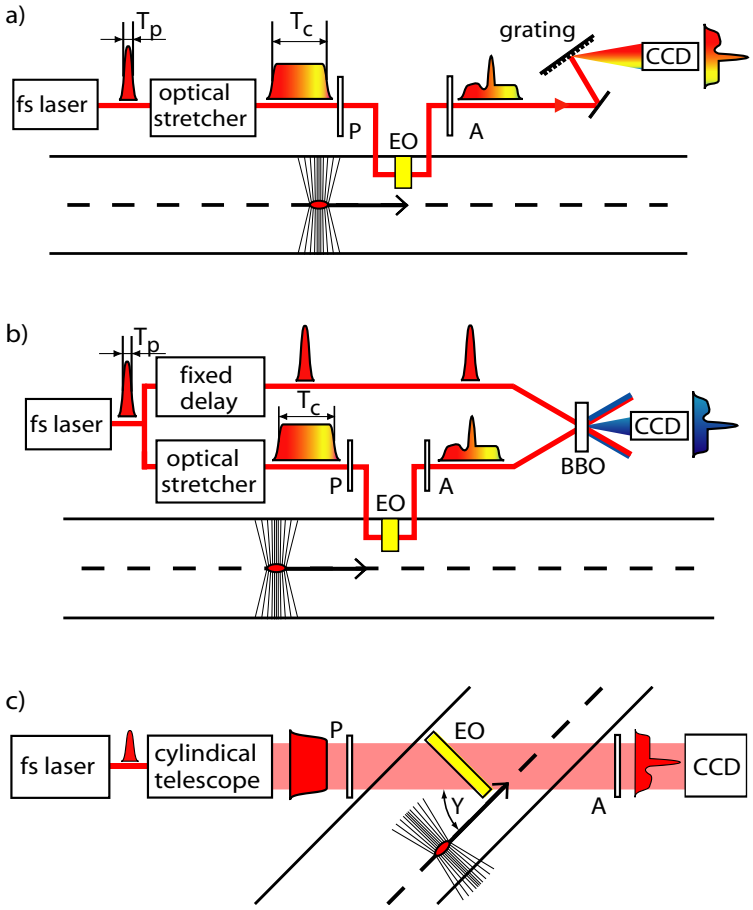

Figure 3.2: Different schemes to measure the longitudinal charge distribution of an electron bunch by electro-optic methods. Top: spectral decoding. Center: temporal decoding. Bottom: spatial decoding (adapted from [Ste07]).

The temporal resolution of the above scheme is limited to around 100 fs rms due to the fact that after the polarizer the temporal profile of the laser pulse is changed and the laser pulse is intensity modulated. This intensity modulation is equivalent to spectral sidebands which are superimposed on the signal of interest. Since the amplitude and shape of these sidebands depends on the longitudinal shape of the electron bunch, a deconvolution is not possible. This resolution limitation can be overcome by applying a single-shot cross-correlation method, in which the temporal intensity profile of the laser pulse is mapped into a spatial intensity profile using non-collinear second harmonic generation [BJM$^+$04] (see Fig. 3.2b). This scheme provides a resolution of around 50 fs rms and is referred to as *temporal decoding*.

In a third scheme, an ultra-short laser pulse passes the electro-optic crystal at an angle with respect to the electron trajectory. In this way, different transverse positions of the laser pulse see different electron bunch timings. With a line array detector or a camera, the laser amplitude can be measured after a polarizer. The temporal profile of the electron bunch is then mapped onto the spatial profile of the laser pulse. This scheme was demonstrated in [Cav05]. It is depicted in Fig. 3.2c) and referred to as *spatial decoding*. The best demonstrated resolution is about 75 fs rms [Azi09].

It should be noted that the resolution of all three detection schemes is limited by the velocity mismatch between the THz-field from the electron bunch and the laser pulse. This limitation can be reduced by using very thin crystals at the expense of signal strength. The strongest limitation, which is intrinsic to the crystal type, is due to phonon resonances excited by the THz-field.

At FLASH, all three methods were implemented. If one is only interested in the bunch arrival-time and not in the precise temporal profile, all three methods are suited to measure the bunch arrival-time with precisions which are currently limited only by the accuracy of the laser synchronization, which is around 50 fs to 100 fs.

3.2.3 Coherent radiation diagnostics

Instead of measuring the longitudinal properties of the electron bunches in time domain as is done with the methods described above, another approach is to deduce longitudinal bunch parameters from the properties of electro-magnetic radiation generated by the electron beam. Three different processes to generate the radiation are discussed.

Radiation processes

Whenever a charged particle crosses a boundary between two media with different dielectric properties, *transition radiation* is emitted. This was first predicted by Ginzburg and Frank in 1945 [GF45]. The transition radiation is emitted in the forward and backward direction with respect to the incoming beam (see Fig. 3.3).

Assuming an infinitely large, perfectly reflecting metallic surface, the spectral and spatial angular distribution of the backward-emitted energy in the far-field can be

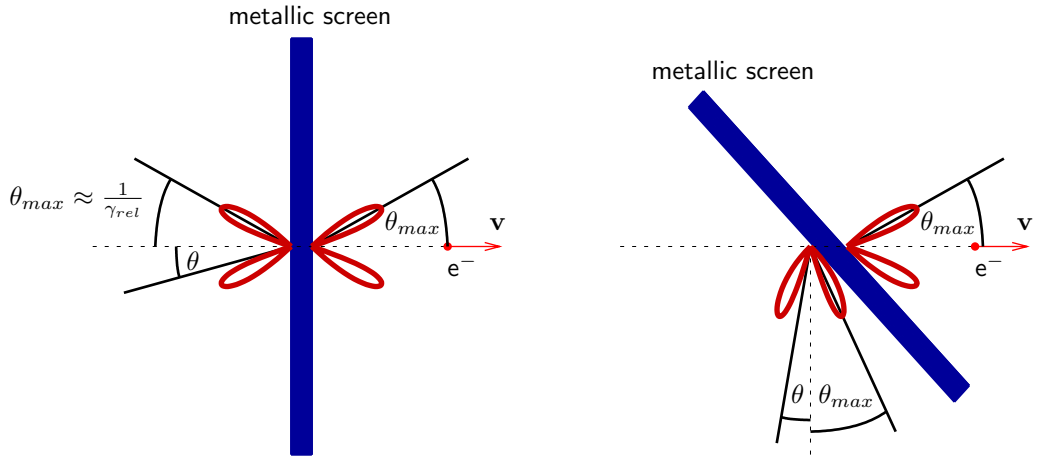

Figure 3.3: Schematic of transition radiation transmitted in forward and backward direction for normal incidence (left) and incidence under an angle of 45° (right).

described by the Ginzburg-Frank equation

$$\frac{\mathrm{d}^2 U_{\mathrm{GF}}}{\mathrm{d}\omega \mathrm{d}\Omega} = \frac{e^2}{4\pi^3 \epsilon_0 c} \cdot \frac{\beta_{\mathrm{rel}}^2 \sin^2\theta}{(1-\beta_{\mathrm{rel}}^2 \cos^2\theta)^2}. \tag{3.1}$$

A finite size of the metallic screen influences the spectral distribution of the transition radiation. As soon as the effective source size $\gamma_{\mathrm{rel}} \cdot \lambda$ exceeds the screen size, the emitted spectral energy decreases significantly. For a circular screen of radius r, the emitted energy can be calculated from the generalized Ginzburg-Frank formula [CSS05]

$$\frac{\mathrm{d}^2 U_{\mathrm{TR}}}{\mathrm{d}\omega \mathrm{d}\Omega} = \frac{\mathrm{d}^2 U_{\mathrm{GF}}}{\mathrm{d}\omega \mathrm{d}\Omega} \cdot [1 - T(\theta, \omega, r)]^2 \tag{3.2}$$

with

$$\begin{aligned} T(\theta,\omega,r) = & \frac{\omega r}{c\beta_{\mathrm{rel}}\gamma_{\mathrm{rel}}} J_0\left(\frac{\omega r \sin\theta}{c}\right) K_1\left(\frac{\omega r}{c\beta_{\mathrm{rel}}\gamma_{\mathrm{rel}}}\right) \\ & + \frac{\omega r}{c\beta_{\mathrm{rel}}^2\gamma_{\mathrm{rel}}^2 \sin\theta} J_1\left(\frac{\omega r \sin\theta}{c}\right) K_0\left(\frac{\omega r}{c\beta_{\mathrm{rel}}\gamma_{\mathrm{rel}}}\right). \end{aligned} \tag{3.3}$$

Here, J_i and K_i are the Bessel functions and modified Bessel functions, respectively.

The overall radiation power emitted in a certain solid angle can be obtained by numerically integrating Eq. 3.2. Figure 3.4 shows the spectral energy density emitted in a solid angle of 100 mrad for different electron momenta, each for a screen with $r = 20$ mm and for an infinitely extended screen. One can see that in the latter case, the distribution is flat and that the finite screen size only affects the long-wavelength

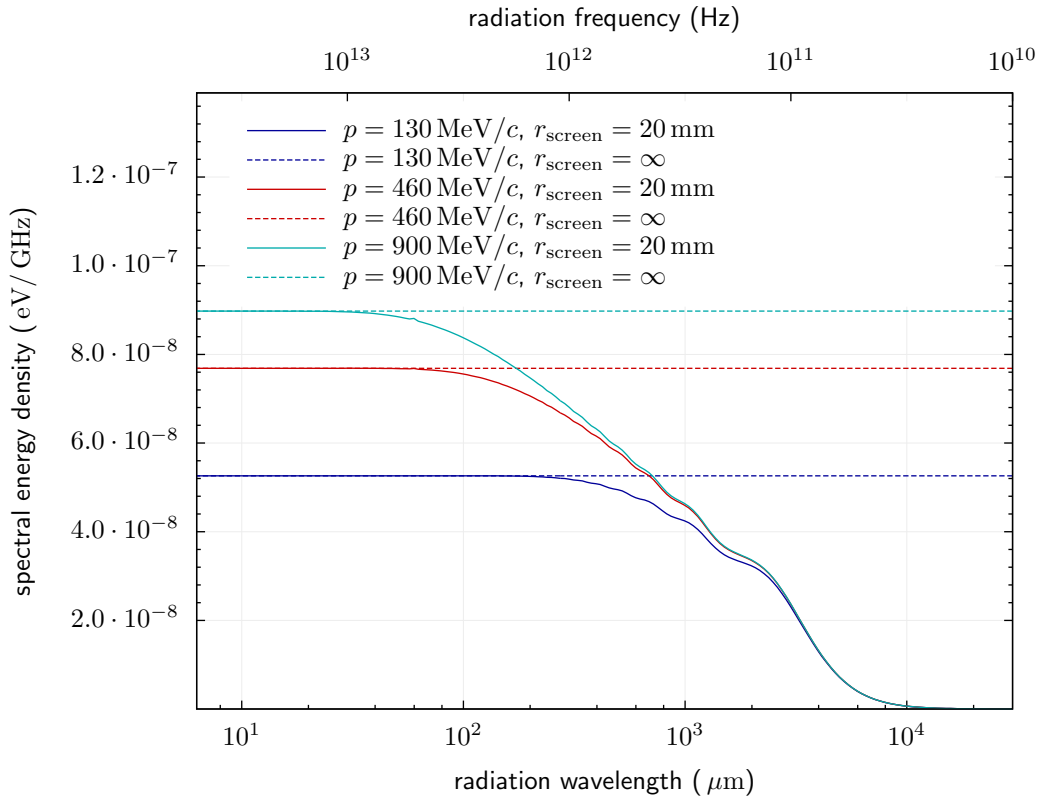

Figure 3.4: Spectral energy density of transition radiation emitted by a single electron integrated over a solid angle of 100 mrad for two different screen configurations: an infinitely large screen and a screen with a radius of 20 mm.

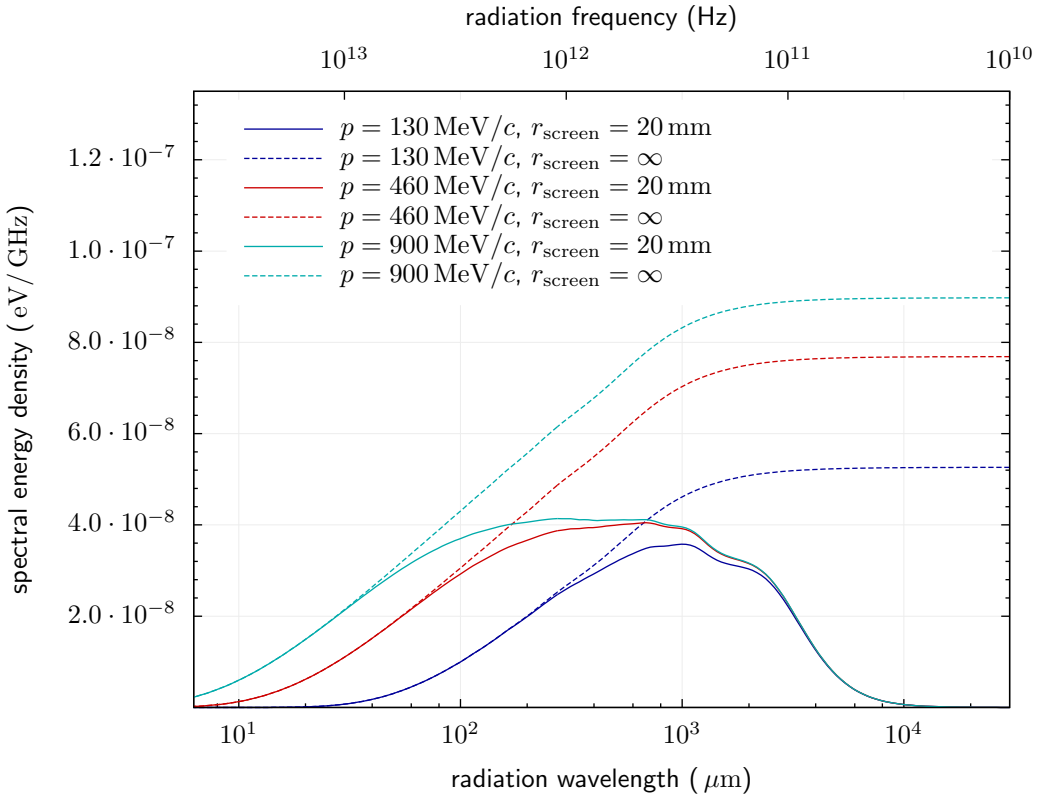

Figure 3.5: Spectral energy density of diffraction radiation emitted by a single electron integrated over a solid angle of 100 mrad for two different screen configurations: an infinitely large screen and a screen with a radius of 20 mm. Both screens have a hole of 2 mm radius, through which the electron beam is guided.

range. The ultimate limit for the emitted radiation is the plasma frequency of the metal, which is deep in the ultraviolet for most metals.

The flat frequency spectrum of transition radiation makes it ideal for beam diagnostic purposes, since frequencies from the optical range to the millimeter range are obtained. A major drawback, however, is that the metallic screen, even if it is a very thin foil, deteriorates the quality of the electron beam due to scattering processes. Therefore, transition radiation is not well suited as an on-line diagnostics.

A way to prevent the scattering is to use a screen with a small hole through which the electron beam is guided. Although the beam quality can still be reduced by wake-fields from the small aperture, this effect is tolerably small for a sufficiently large hole. Since the electric field has an extension on the order of $\gamma_{\mathrm{rel}} \cdot \lambda$, electromagnetic radiation is generated when the electron beam passes through the hole. This radiation is called *diffraction radiation* and the spectral and spatial angular distribution of the backward-emitted energy is given by [CSS05]

$$\frac{\mathrm{d}^2 U_{\mathrm{DR}}}{\mathrm{d}\omega \mathrm{d}\Omega} = \frac{\mathrm{d}^2 U_{\mathrm{GF}}}{\mathrm{d}\omega \mathrm{d}\Omega} \cdot \left[T(\theta, \omega, r_{\mathrm{hole}}) - T(\theta, \omega, r) \right]^2 . \tag{3.4}$$

The spectral energy density emitted in a solid angle of 100 mrad was again evaluated by numerical integration for different electron momenta (see Fig. 3.5). As before, the results for a screen with $r = 20\,\mathrm{mm}$ and an infinitely extended screen are shown. In all cases a hole of radius $r_{\mathrm{hole}} = 2\,\mathrm{mm}$ is assumed.

As expected, the dependence on the screen size is the same as for transition radiation. Additionally, the low wavelength components are missing for diffraction radiation. When the beam energy gets smaller, the wavelength at which a significant amount of intensity is available increases. For an electron momentum of $460\,\mathrm{MeV}/c$ as after the second bunch compressor, most of the intensity is emitted in a wavelength range between $100\,\mu\mathrm{m}$ and a few millimeters.

A third radiative process is synchrotron radiation in a bending or undulator magnet. This is an interesting alternative to diffraction radiation, since it permits parasitic measurements as well. Within this work no synchrotron radiation diagnostics was used, so it will not be discussed. Detailed information about synchrotron radiation diagnostics at FLASH can be found in [Beh08].

Coherent radiation

The radiation characteristics discussed above is valid for a single electron. When we consider a bunch consisting of many electrons, the radiation intensity scales with the number of electrons as long as the electrons radiate with random phases. This is the case for an electron bunch which is long compared to the radiation wavelength and which has no substructure at the radiation wavelength. The intensity, $I_N = NI_1^2$, is then proportional to the number of electrons. The optical part of this incoherent light from a transition radiator is used at many locations at FLASH to measure the transverse beam profiles.

When the electron bunch dimensions or bunch sub-structures are on the order of the radiation wavelength, the radiation phases of the single electrons are no longer randomly distributed. If we consider N electrons whose distances are small compared to the wavelength, then these electrons emit their radiation coherently, the overall electrical field amplitude is $E_N = NE_1$, resulting in an intensity of the emitted radiation which scales with the square of the number of particles:

$$I_N = N^2 E_1^2 = N^2 I_1. \tag{3.5}$$

For an arbitrary electron distribution and radiation wavelength, the situation is more complicated and the radiation can be only partly coherent. In the following we will introduce the bunch *form factor*, with which the intensity at an arbitrary radiation wavelength can be calculated from a known electron distribution. We will follow the introduction in [LS97].

Let us consider an electron charge distribution $\rho(\boldsymbol{r})$ whose radiation is observed with a detector in the far field. Due to the different positions within the bunch, the radiation fields of the single electrons are superimposed at the detector with a

different phase, resulting in the total field

$$\boldsymbol{E}_N(\omega) = \sum_{j=1}^{N} \boldsymbol{E}_j(\omega) \cdot e^{i\frac{\omega}{c}\boldsymbol{n}\cdot\boldsymbol{r}_j}, \tag{3.6}$$

where $\boldsymbol{n}$ is a unit vector from the center of the electron bunch to the detector and $\boldsymbol{r}_j$ is a position vector of the j^{th} electron. The total intensity $I_N(\omega)$ at the detector is then given by

$$\begin{aligned} I_N(\omega) &= I_1(\omega) \sum_{j=1}^{N} \left| e^{i\frac{\omega}{c}\boldsymbol{n}\cdot\boldsymbol{r}_j} \right|^2 \\ &= I_1(\omega) \sum_{j=1}^{N} e^{i\frac{\omega}{c}\boldsymbol{n}\cdot\boldsymbol{r}_j} \sum_{k=1}^{N} e^{-i\frac{\omega}{c}\boldsymbol{n}\cdot\boldsymbol{r}_k}. \end{aligned} \tag{3.7}$$

As the double sum yields unity for each term with $j = k$ it may be expressed as

$$I_N(\omega) = I_1(\omega) \left(N + \sum_{j\neq k}^{N} e^{i\frac{\omega}{c}\boldsymbol{n}\cdot(\boldsymbol{r}_k - \boldsymbol{r}_j)} \right). \tag{3.8}$$

When we now introduce the continuous charge distribution $\rho(\boldsymbol{r})$, we get

$$I_N(\omega) = I_1(\omega) \left(N + N(N-1) \iint \mathrm{d}^3 r \, \mathrm{d}^3 r' \, \frac{\rho(\boldsymbol{r})\rho(\boldsymbol{r'})}{Q^2} e^{i\frac{\omega}{c}\boldsymbol{n}\cdot(\boldsymbol{r}-\boldsymbol{r'})} \right), \tag{3.9}$$

where

$$Q = \int \rho(\boldsymbol{r}) \mathrm{d}^3 r \tag{3.10}$$

is the total charge.

We can now define the bunch form factor $F(\omega)$ as the three dimensional Fourier transform of the charge density distribution

$$F(\omega) = \frac{1}{Q} \int \mathrm{d}^3 r \, \rho(\boldsymbol{r}) e^{i\frac{\omega}{c}\boldsymbol{n}\cdot\boldsymbol{r}}, \tag{3.11}$$

with which we can express the radiation intensity $I_N(\omega)$ as

$$I_N(\omega) = I_1(\omega) \left(N + N(N-1) \left| F(\omega) \right|^2 \right). \tag{3.12}$$

Since transition radiation as well as diffraction radiation is emitted in a very small opening angle, it is often sufficient to consider only the longitudinal charge distribution $\rho(z)$. The longitudinal form factor can then be evaluated as the one-dimensional integral

$$F(\omega) = \frac{1}{Q} \int \mathrm{d}z \, \rho(z) e^{-i\frac{\omega}{c}z}. \tag{3.13}$$

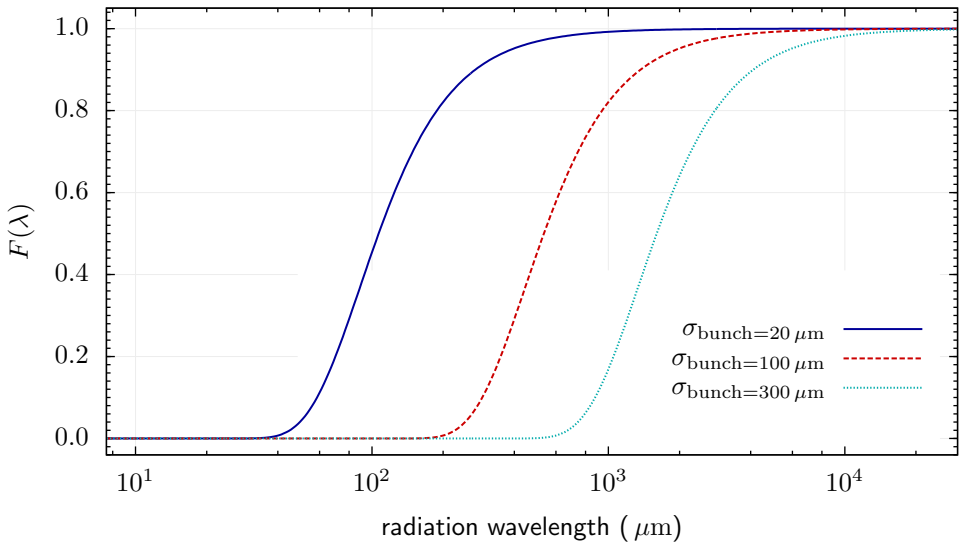

Figure 3.6: Form factor for different Gaussian shaped bunches of different lengths.

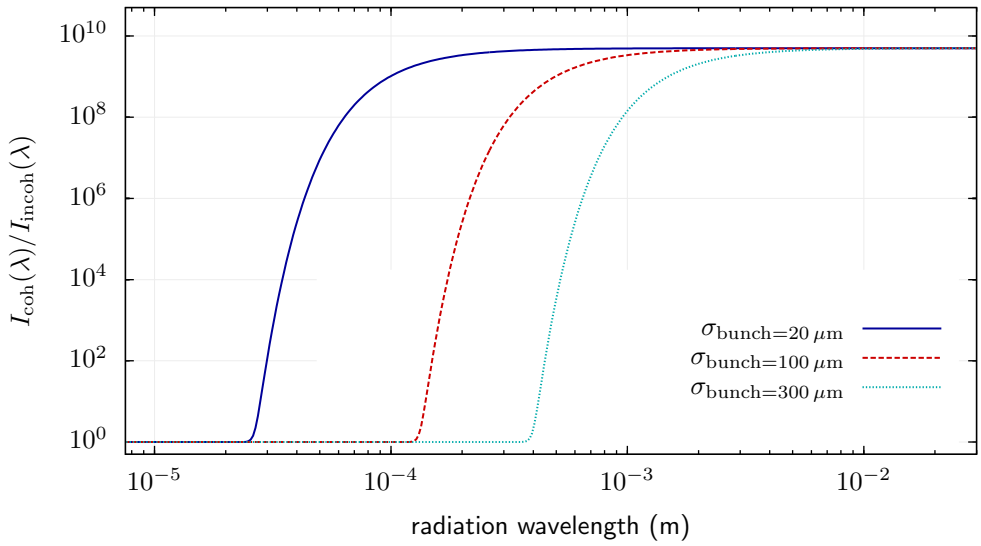

Figure 3.7: Intensity increase by coherent effects for different bunch lengths. A Gaussian bunch shape is assumed and a charge of 0.8 nC.

Figure 3.6 shows the form factor for a Gaussian longitudinal charge distribution of different lengths. At large radiation wavelengths, it converges to unity, which means that the emission of the radiation becomes completely coherent. At radiation wavelengths much smaller than the rms length of the charge distribution, the form factor vanishes and the radiation is incoherent.

To illustrate the intensity enhancement by coherent radiation, in Fig. 3.7 the intensity ratio

$$\frac{I_{\mathrm{coh}}(\omega)}{I_{\mathrm{incoh}}(\omega)} = \frac{I_N(\omega)}{I_1(\omega)} \approx 1 + N\,|F(\omega)|^2 \tag{3.14}$$

is plotted for different Gaussian bunches with a charge of 0.8 nC.

Longitudinal diagnostic with coherent radiation

There are two different schemes applied at FLASH which use coherent radiation as a tool for longitudinal beam diagnostics. The first one is the measurement of the integrated radiation intensity over a large wavelength range with a single detector. When the bunches become shorter, the integral increases, since the non-vanishing part of the bunch form factor shifts towards shorter wavelength. This is a convenient way to monitor the stability of the bunch compression process and to suppress fluctuations by means of a feedback. In order to have a non-intercepting measurement, one uses diffraction radiation.

A second, more sophisticated way to analyze the coherent radiation is to measure the spectral distribution of the emitted THz-radiation with a spectrometer [DH08, Wes08]. This allows resolving characteristic bunch-lengths and even substructures within the bunch. Since the phase information of the radiation is not available, a unique reconstruction of the temporal bunch shape is not possible, even when phase retrieval techniques like the Kramers-Kronig analysis (see [LS97]) are applied. Therefore, for a complete understanding, a complementary measurement in the time domain is needed.

The coherent radiation is mainly emitted at infrared wavelengths, ranging from a few micrometers up to the millimeter range. Due to their very broad spectral range, thermal detectors are the most suitable type of detectors. Examples of such detectors are bolometers and pyroelectric elements. In order to cope with bunch-to-bunch fluctuations, single shot measurements are needed, which at FLASH requires response times of less than 1 μs. This is too fast for bolometers, but can be reached with pyroelectric elements. Detailed information about the applied pyro-detectors can found in [Sch05a].

The transport of the radiation from the source to the detector is of special importance. Vacuum windows tend to absorb the short wavelength part of the spectrum. Frequently, fused silica windows are installed. They have a good transmission in the infrared only for wavelengths larger than about 80 μm. At a special THz beam line [CSS05], a diamond window is used, whose spectral response is very flat for wavelengths larger than 7 μm and below 5 μm. The transport of long-wavelength radiation is mainly limited by diffraction and a large aperture is needed. Another lim-

itation arises due to absorption in humid air and for precise spectral measurements, an evacuated transport line, as used in [CSS05], is an ideal choice. The standard bunch compression monitors, which integrate over the spectrum, have short sections of normal air between the beam pipe vacuum window and the detector.

4 Timing of the electron beam

The main sources for timing fluctuations of the electron bunches are the electron source and the amplitudes and phases of the accelerating cavities upstream of the two bunch compressor chicanes.

4.1 Influence of the electron gun

The timing in the electron gun is mainly determined by the timing of the photo-cathode laser and the phase in the RF cavity. Since the electrons are not yet relativistic, the dynamics in this section are strongly influenced by space charge forces. Different electron velocities lead to further changes of the longitudinal bunch profile.

The effect of photo-cathode laser timing changes and the influence of gun phase changes are investigated using numerical simulations. The simulations are performed using the space charge tracking code ASTRA [Flo08]. A laser pulse with a Gaussian longitudinal shape is assumed. The laser pulse duration is 5.66 ps rms, according to the bunch length measurements in [Sch05b]. A typical bunch charge of 0.8 nC is used. In order to have enough statistics and sufficiently small noise levels on the current profiles, 10^5 macro-particles are used in each simulation[1].

Figure 4.1 shows the simulated longitudinal phase space distribution at the entrance of ACC1 together with the corresponding current profile for different gun phases, where $\varphi_{\mathrm{gun}} = 0$ is defined as the phase at which the electrons receive the largest energy gain. One can see that the bunches get shorter with decreasing gun phases and the energy gradient along the bunch, which will be called *energy chirp* in the following, gets smaller. Due to this dependence of the energy chirp on the gun phase, the bunch compression is affected by a change of the gun phase. Although the energy chirp needed for the bunch compression is mainly imprinted onto the bunch by accelerating it off-crest in ACC1, a large change of the gun phase requires a different ACC1 phase setting in order to get a similar compression factor.

In Fig. 4.2 the rms bunch length and the peak current are shown as functions of the gun phase. The peak current ranges between 40 A and 50 A and the bunch length varies from 1.6 mm to 2.0 mm.

The relative timing between the RF field in the gun and the arrival-time of the injector laser pulses is not only crucial for the longitudinal phase space distribution, but also for the electron bunch arrival-time in front of BC1. Figure 4.3 shows the

[1] A typical FLASH bunch (~ 0.8 nC) consists of about $5 \cdot 10^9$ electrons. Tracking of all particles would be much too time consuming and, therefore, a reduced number of macro-particles with an increased charge is tracked.

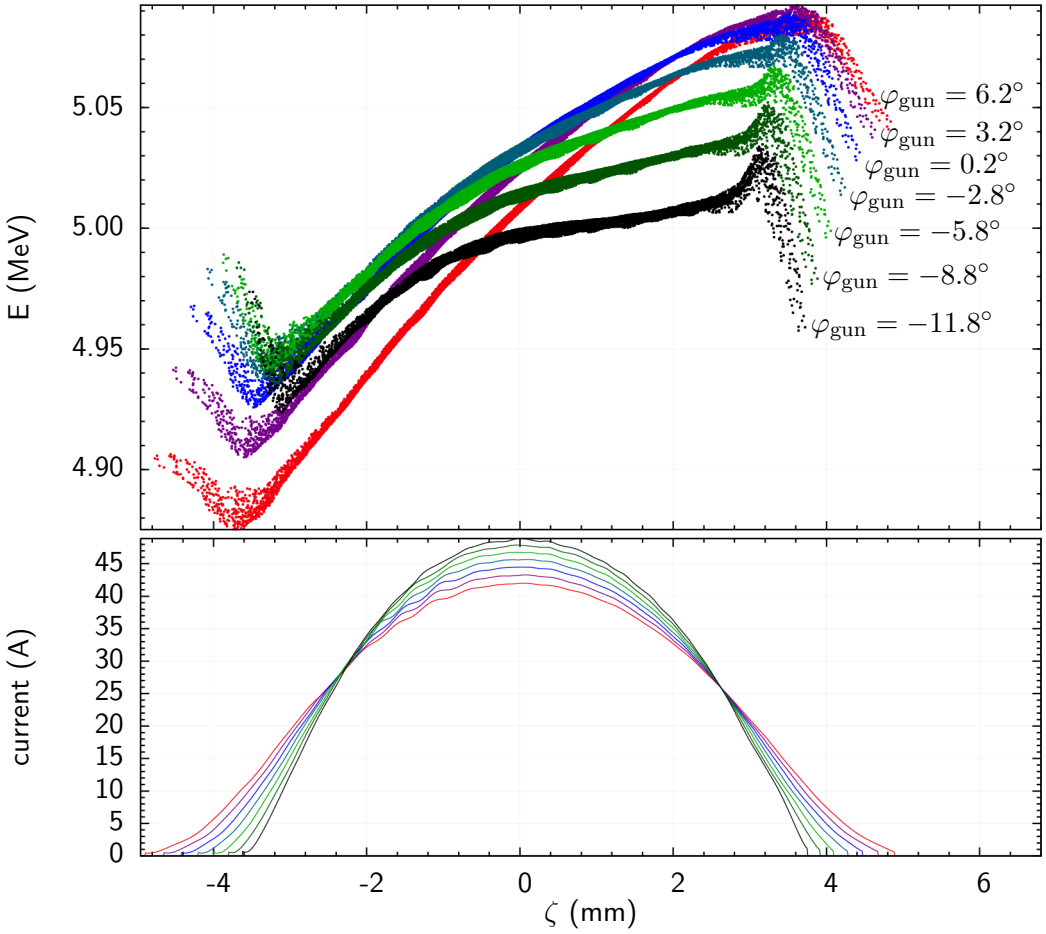

Figure 4.1: Simulated longitudinal phase space distributions at the entrance of ACC1. The different colors denote different gun phases. The nominal operation point is around $\varphi_{\mathrm{gun}} = -8°$.

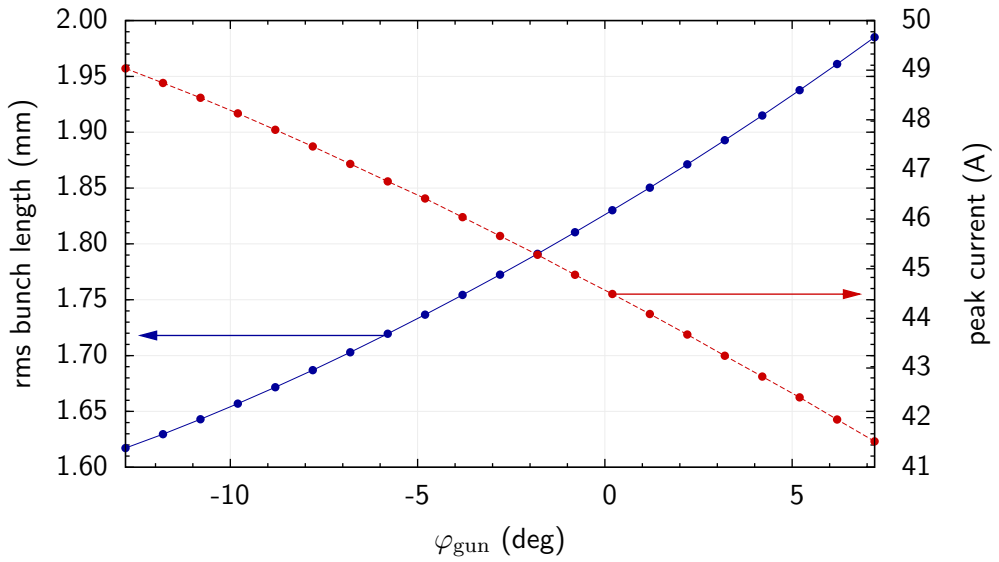

Figure 4.2: Peak current and rms bunch length at the entrance of ACC1 as functions of the gun phase.

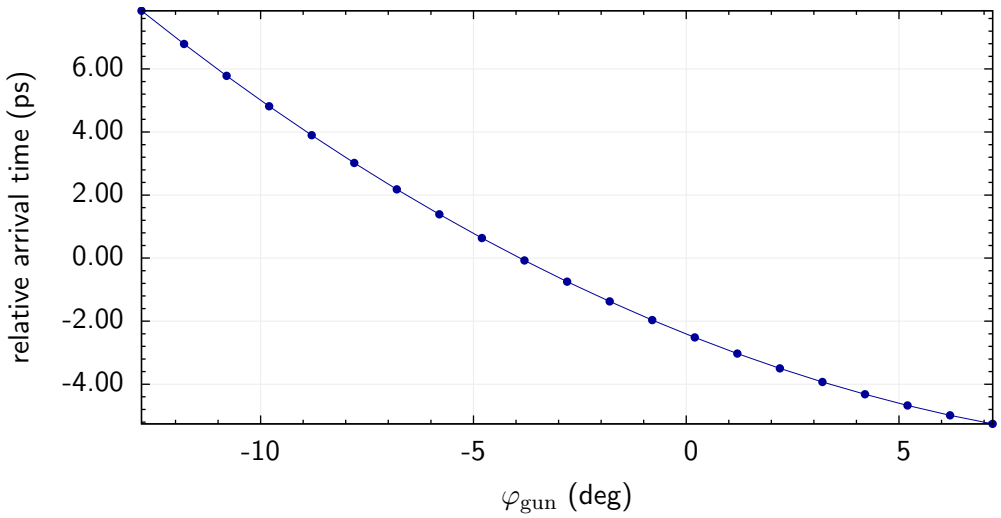

Figure 4.3: Relative bunch arrival-time at the entrance of BC1 for different gun phases.

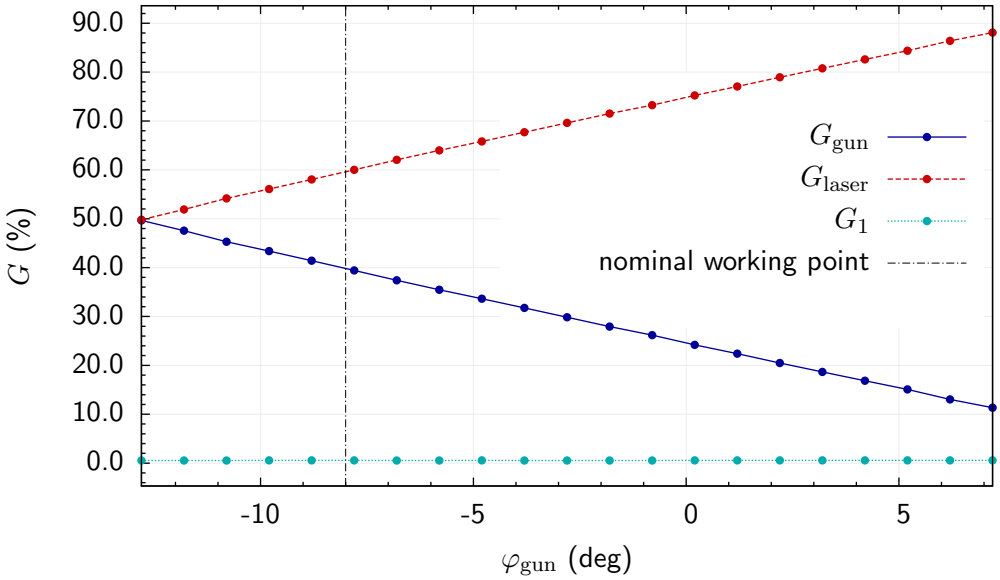

Figure 4.4: Influence of timing changes of the laser, the gun, and ACC1 on the electron bunch arrival-time at the entrance of BC1. A value of $G_i = 50\%$ means that 50% of a timing change of the device i is transferred to the electron beam.

change of the bunch arrival-time at the entrance of BC1 for different gun phases. The phase of ACC1 was adjusted for each gun phase setting to accelerate the bunch on the crest of the RF field.

The influence of different parameters on the bunch arrival-time must be known for the machine operation. To estimate the influence of the gun phase, the ACC1 phase, and the laser arrival-time on the electron bunch timing, the three timings were shifted by a small amount (1 ps or 0.5 deg).

The timing change of the electron beam Δt_{beam} is given by

$$\Delta t_{\mathrm{beam}} = G_{\mathrm{laser}} \cdot \Delta t_{\mathrm{laser}} + G_{\mathrm{gun}} \cdot \Delta t_{\mathrm{gun}} + G_1 \cdot \Delta t_1 \,, \tag{4.1}$$

where the factors G_i represent the fractional part of the timing change from the laser, the gun, and ACC1, which is transferred to the beam and Δt_{gun} as well as Δt_1 are given by

$$\Delta t_{\mathrm{gun}} = \frac{\Delta \varphi_{gun}}{\omega_{\mathrm{RF}}} \qquad \text{and} \qquad \Delta \mathrm{t}_1 = \frac{\Delta \varphi_1}{\omega_{\mathrm{RF}}} \,. \tag{4.2}$$

Due to the fact that a similar timing change of all three devices corresponds to a timing shift of the entire machine, the sum of all G_i has to be unity:

$$G_{\mathrm{laser}} + G_{\mathrm{gun}} + G_1 = 1 \,. \tag{4.3}$$

The results of these simulations are shown in Fig. 4.4. As expected, the influence of the ACC1 phase is almost negligible. The curve shown in the figure is for on-crest acceleration in ACC1, giving a $G_1 = 0.6\%$. The weight factor G_1 increases,

when ACC1 is operated off-crest, but even at an off-crest phase of 10° this only corresponds to $G_1 = 1.4\%$. Timing changes of the laser and the gun RF field have a different influence on the electron bunch timing for different gun phases. At the nominal working point of $\varphi_{\text{gun}} = -8°$, about $G_{\text{gun}} = 40\%$ of gun timing changes and $G_{\text{laser}} = 60\%$ of the laser timing changes are transferred onto the electron beam timing.

4.2 Influence of the first accelerating section

The bunch compression process inside the magnetic chicanes is controlled by imprinting an energy chirp onto the electron bunch. The bending radius r in a dipole depends on the electron momentum p and the magnetic dipole field B

$$\frac{1}{r} = e \cdot \frac{B}{p} \tag{4.4}$$

and, therefore, the trajectory length through the bunch compressor is different for electrons of different momentum. For a rectangular dipole magnet in which the electron enters or exits perpendicularly to one of the magnet faces, the arc-length of the electron trajectory is given by

$$l_{\text{arc}} = r \cdot \alpha, \tag{4.5}$$

where α is the bending angle introduced by the magnet. The relation between the effective dipole length l_{eff}, the bending angle, and radius is given by

$$l_{\text{eff}} = r \cdot \sin\alpha. \tag{4.6}$$

Using these equations, the path length l_{BC1} through the first bunch compressor chicane (see Fig. 2.5) can be expressed by

$$\begin{aligned} l_{\text{BC1}}(p) &= 4r\alpha + 2 \cdot \frac{d_1}{\cos\alpha} + d_2 \\ &= \frac{4p \arcsin\left(\frac{l_{\text{eff}} eB}{p}\right)}{eB} + \frac{2d_1}{\sqrt{1 - \frac{e^2B^2l_{\text{eff}}^2}{p^2}}} + d_2. \end{aligned} \tag{4.7}$$

When we now consider an electron bunch consisting of many electrons of different momenta and different longitudinal positions, we can calculate the change of the longitudinal beam position of the single electrons using Eq. 4.7.

The path length of an electron with an energy deviation of $\delta = \Delta p/p$ with respect to a reference particle can be expressed by expanding 4.7 in a Taylor series about the reference momentum p:

$$\begin{aligned} l_{\text{BC1}}\left(p(1+\delta)\right) &= l_{\text{BC1}}(p) + p\frac{\partial l_{\text{BC1}}(p)}{\partial p} \cdot \delta + \frac{1}{2}p^2\frac{\partial^2 l_{\text{BC1}}(p)}{\partial p^2} \cdot \delta^2 \\ &\quad + \frac{1}{6}p^3\frac{\partial^3 l_{\text{BC1}}(p)}{\partial p^3} \cdot \delta^3 + \cdots \\ &= l_{\text{BC1}}(p) + R_{56} \cdot \delta + T_{566} \cdot \delta^2 + U_{5666} \cdot \delta^3 + \cdots . \end{aligned} \tag{4.8}$$

With the coefficients R_{56}, T_{566}, and U_{5666}, the longitudinal position change with respect to the reference particle can be calculated. These coefficients are given for BC1 by the expressions

$$R_{56} = -\frac{4l_{\text{eff}}}{\sqrt{1-\frac{e^2B^2l_{\text{eff}}^2}{p^2}}} - \frac{2e^2B^2d_1l_{\text{eff}}^2}{p^2\left(1-\frac{e^2B^2l_{\text{eff}}^2}{p^2}\right)^{\frac{3}{2}}} + \frac{4p\arcsin\left(\frac{eBl_{\text{eff}}}{p}\right)}{eB} \tag{4.9}$$

$$T_{566} = \frac{e^2B^2l_{\text{eff}}^2\left(-2e^2B^2l_{\text{eff}}^3+(3d_1+2l_{\text{eff}})\,p^2\right)}{\left(-e^2B^2l_{\text{eff}}^2+p^2\right)^2\sqrt{1-\frac{e^2B^2l_{\text{eff}}^2}{p^2}}} \tag{4.10}$$

$$U_{5666} = -\frac{1}{3}\frac{e^2B^2l_{\text{eff}}^2\left(2e^4B^4l_{\text{eff}}^5+e^2B^2l_{\text{eff}}^2p^2\left(3d_1-10l_{\text{eff}}\right)+4p^4\left(3d_1+2l_{\text{eff}}\right)\right)}{\left(-e^2B^2l_{\text{eff}}^2+p^2\right)^3\sqrt{1-\frac{e^2B^2l_{\text{eff}}^2}{p^2}}}\,. \tag{4.11}$$

The higher order terms proportional to T_{566} and U_{5666} can be neglected in situations, where very short bunches and small energy changes are considered. Quite often in literature, the relation $T_{566} = -3/2R_{56}$ is used. It is important to note that this relation is only valid for $\alpha \ll 1$. In the first bunch compressor at FLASH, the nominal bending angle is 18.0355° and this approximation is not valid anymore[2].

From R_{56} one can predict without simulations that the electron arrival-time changes by approximately $\Delta t = 0.01 \cdot R_{56}/c \approx 6\,\text{ps}$ per percent beam energy variation.

Let us consider an electron bunch with a uniform longitudinal energy distribution upstream of ACC1. In the acceleration module ACC1, a systematic energy variation along the bunch, an energy chirp, can be generated by accelerating the electron bunch not on the crest of the sinusoidal accelerating field but several degrees off-crest. The electrons at different longitudinal positions within the bunch then see different accelerating fields due to their different arrival-times. This effect is of course also present when the bunches are accelerated on-crest, but the effect is much less pronounced due to the smaller slope of the sinusoidal field near the crest. The energy chirp has to be applied in a way that the leading electrons gain less energy than the trailing ones.

The curvature of the sinusoidal field implies that the energy chirp has a nonlinear component. Consequently, different longitudinal bunch sections experience different compressions. This leads to a current profile with a narrow leading spike, followed by a long tail. Since for the FEL operation a high peak current is required, only the electrons in this spike can contribute to the FEL process. The nonlinear component of the energy chirp is stronger for a larger ratio of bunch length and RF wavelength.

To evaluate the dependence of the electron beam arrival-time on the settings of the accelerating phases and amplitudes, a simple tracking code was developed which calculates the path length through the bunch compressors according to Eq. 4.7 and a similar relation for the second bunch compressor. Since this code only considers the

[2] For the nominal bending angle, $R_{56} \approx -181.4\,\text{mm}$, $T_{566} \approx -1.63 \cdot R_{56}$, and $U_{5666} \approx 2.42 \cdot R_{56}$.

longitudinal motion and neglects space charge, the simulations are much faster than with ASTRA, allowing to analyze a large set of different compression parameters.

The initial phase space distribution at the entrance of the first accelerating module is calculated with the space charge tracking code ASTRA, assuming the nominal gun phase $\varphi_{\text{gun}} = -8°$. To limit statistical fluctuations, $2 \cdot 10^5$ particles are used in this simulation. The longitudinal displacement ζ of an electron with respect to a reference particle is used to determine the accelerating phase seen by this electron. When the reference particle is accelerated on-crest, the final energy after ACC1 is 130 MeV. The field strength of the dipole magnets from the first bunch compressor is chosen such that the bending angle for the 130 MeV reference particle is 18.0355°, which is the nominal bending angle in the bunch compressor. The accelerating gradients in ACC23 are set so that the final energy is 460 MeV for on-crest acceleration. The fields of the BC2 dipoles are set to achieve the nominal bending angle of 3.8°.

Figure 4.5 shows the longitudinal phase space and the corresponding current profile resulting from the tracking calculation after the first and second bunch compressor for different phases of ACC1. It is interesting to note that even for on-crest acceleration the longitudinal bunch shape is asymmetric after the compressors. One can clearly see the curvature on the energy distribution. The bunch compressors shear this distribution and with φ_1 and φ_{23}, the longitudinal positions of the initial electron distribution which is moved into the spike region can be chosen. Figure 4.6 shows the longitudinal current profile. There is some noise on the data, because the number of particles used in the simulation is too small. Since one of our interests is the arrival-time of the current spike, a filter algorithm based on wavelets is applied [BCF+02]. A spline is fitted to the filtered signal allowing interpolating in between the bins. The maximum of this interpolated signal is defined as the spike of the current density (see Fig 4.6).

By varying the phases of the accelerating cavities upstream of the bunch compressors, their influence on the arrival-time is determined. During this scan, the amplitude of the accelerating fields are kept constant. Although this means that only the on-crest settings correspond to the nominal bending angles, this has the advantage that the influence of phase fluctuations can be directly determined by calculating the numerical partial derivatives. In order to determine the influence of the accelerating field amplitudes, two additional tracking runs were made for every phase setting, in which either the amplitude of ACC1 or the one of ACC23 was increased by 1%. This allows for the calculation of the derivatives for every phase setting. For a small number of settings, it was verified that the resulting error from this asymmetric numerical derivative calculation is small by additionally tracking the particles for a 1% decreased amplitude in ACC1 or ACC23 in order to be able to calculate the numerical derivative in a symmetric way.

Figure 4.7 shows the dependence of different beam parameters after the first bunch compressor on the ACC1 phase. As soon as the spike in the current distribution develops, starting at an ACC1 phase of around $-5°$, the FWHM decreases much faster than the root mean square (rms) value. At the same time, the peak current after BC1 increases significantly compared to the current upstream the bunch compres-

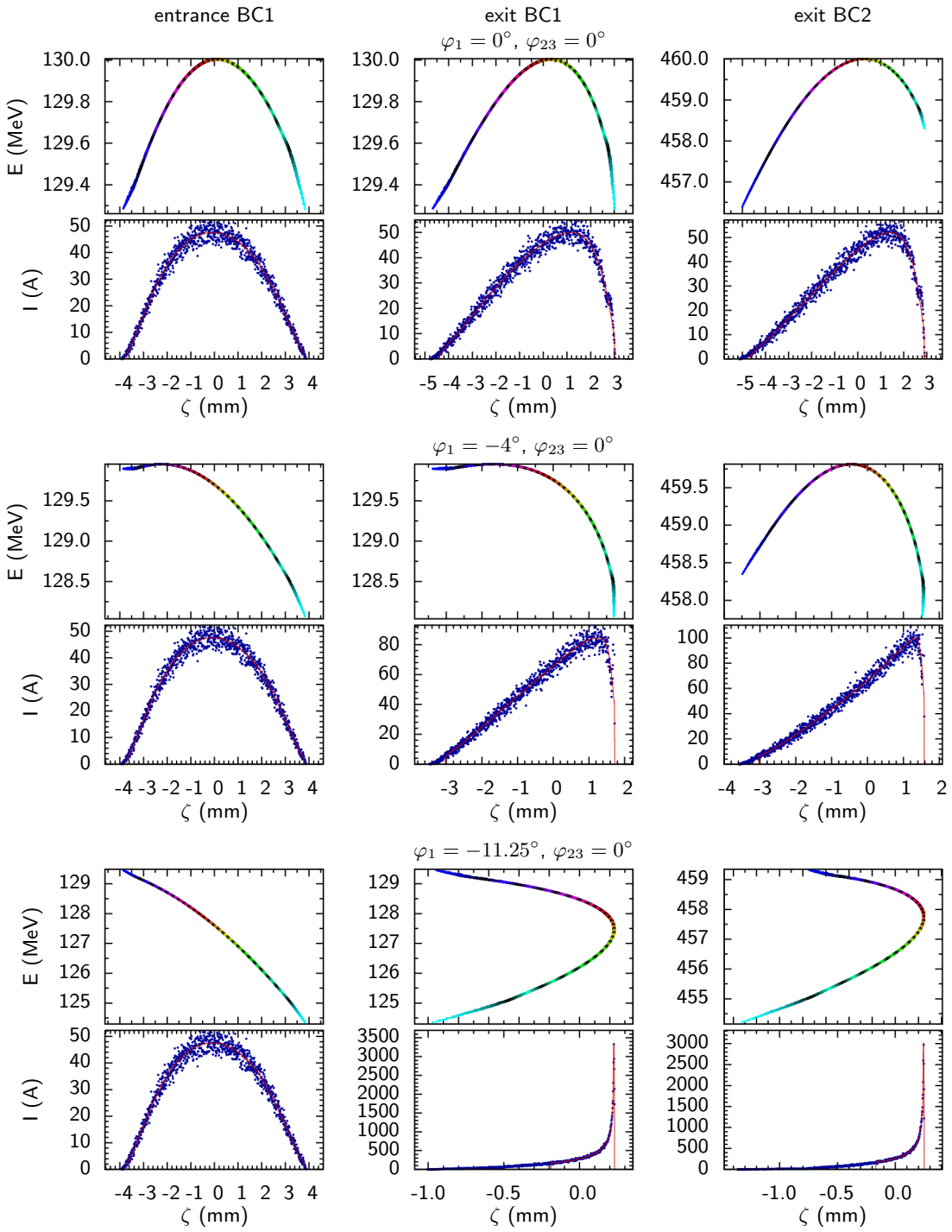

Figure 4.5: Longitudinal phase space distributions after BC1 and BC2 and corresponding current profiles for different phases in ACC1.

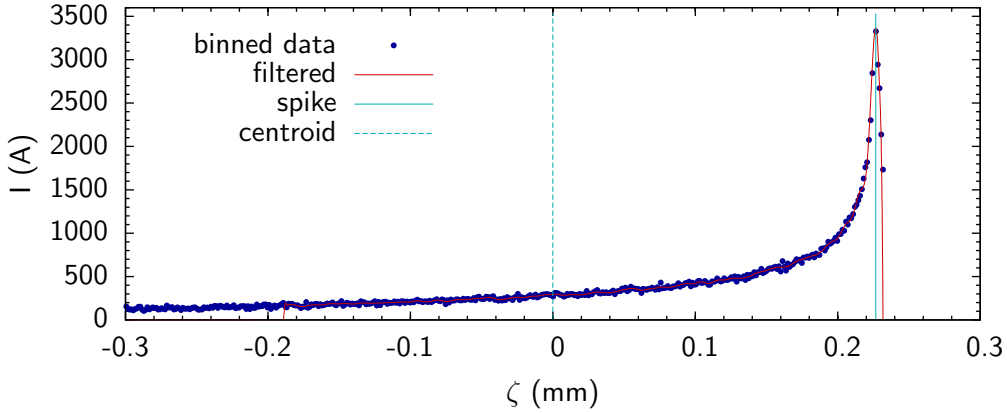

Figure 4.6: Example of a current distribution (blue). A wavelet based filter is applied to remove noise. From the filtered signal (red), the timing of the spike is determined.

sor. Over a large range of ACC1 phases, the FWHM of the current profiles is nearly constant. The reason is that due to the shearing of the phase space distribution the longitudinal position within the bunch is changed at which the compression is maximum. The pronounced maximum of the peak current is caused by the highest electron density in the central part of the Gaussian-shaped initial bunch distribution.

It is very interesting to see that the spike of the current profile reacts in a different way to phase and amplitude changes than the centroid. Over a large range of about $-6°$ to $-16°$, an ACC1 phase change shifts the time position of the spike by

$$\Delta t_{\mathrm{spike}} = \frac{\Delta\varphi_1}{\omega_{\mathrm{RF}}} = 2.14 \frac{\mathrm{ps}}{\mathrm{deg}} \,. \tag{4.12}$$

The reason for this behavior was explained already: The phase change shifts the optimum compression to a different longitudinal section of the bunch. In contrast to this, the arrival-time of the centroid is determined by the sinusoidal shape of the accelerating field. There is only one ACC1 phase at which the dependence for the centroid and the spike is identical, namely when the phase space distribution is symmetric after the compression (see bottom plot of Fig. 4.5).

The dependence of the bunch arrival-time on the ACC1 amplitude shows the same difference between the centroid and the spike, although it is much less pronounced. The consequence of an amplitude change is a smaller or larger energy chirp. Due to the different energy, the value of R_{56} in the chicane is changed. These two effects lead to a change of the compression along the bunch. Also here, the behavior of the centroid and the spike is similar for a symmetric phase space distribution as shown in Fig. 4.5.

As expected from the value of R_{56}, an ACC1 amplitude change of 1% corresponds to about 6 ps of beam arrival-time change. This large sensitivity has the consequence that the main contribution to the FLASH electron beam timing jitter is due to beam energy fluctuations upstream of the first bunch compressor.

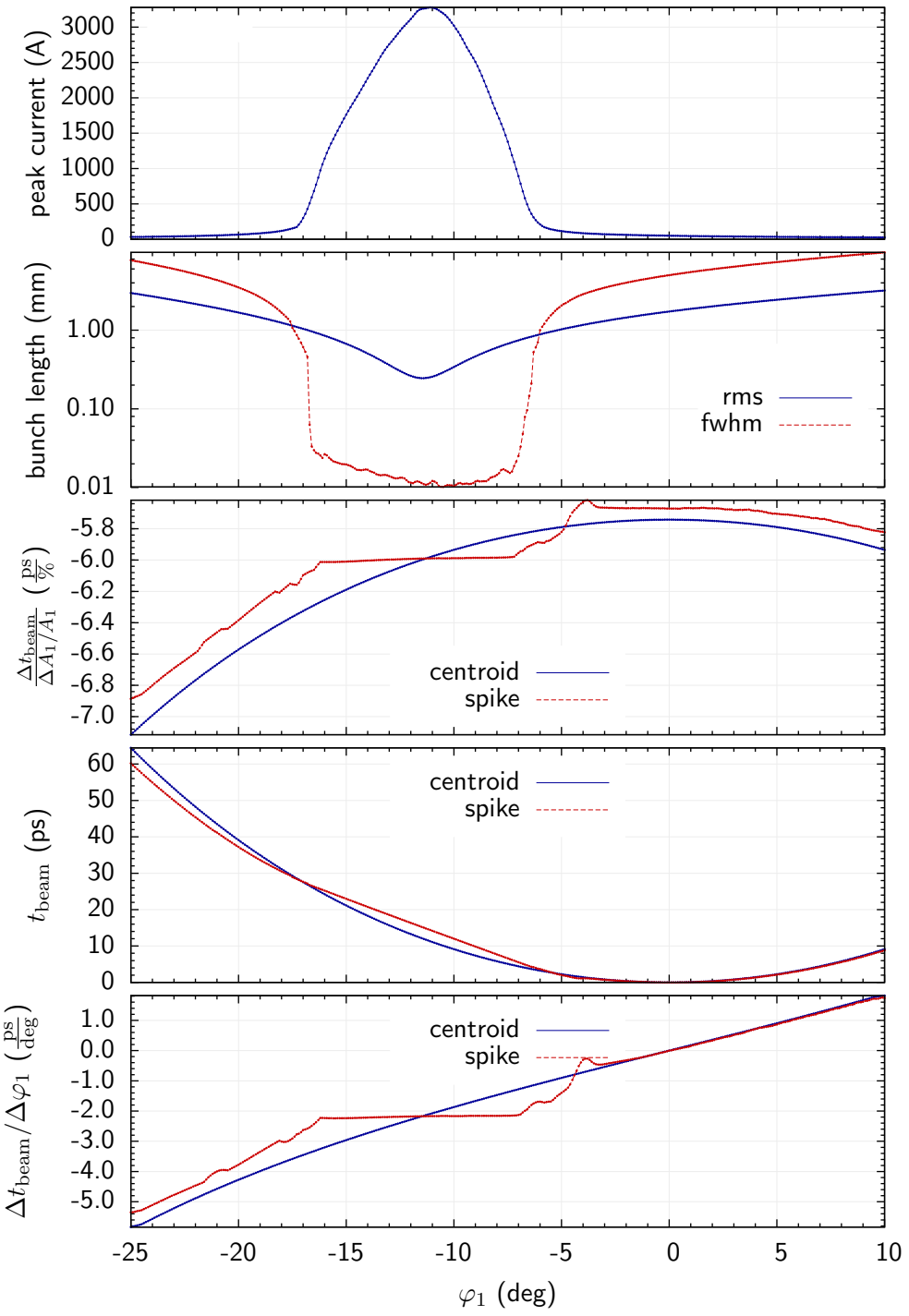

Figure 4.7: Different beam parameters after BC1 for various ACC1 phases. A bunch of 0.8 nC charge simulated with ASTRA is assumed at the entrance of ACC1. From this location on, collective effects are not considered in this simulation.

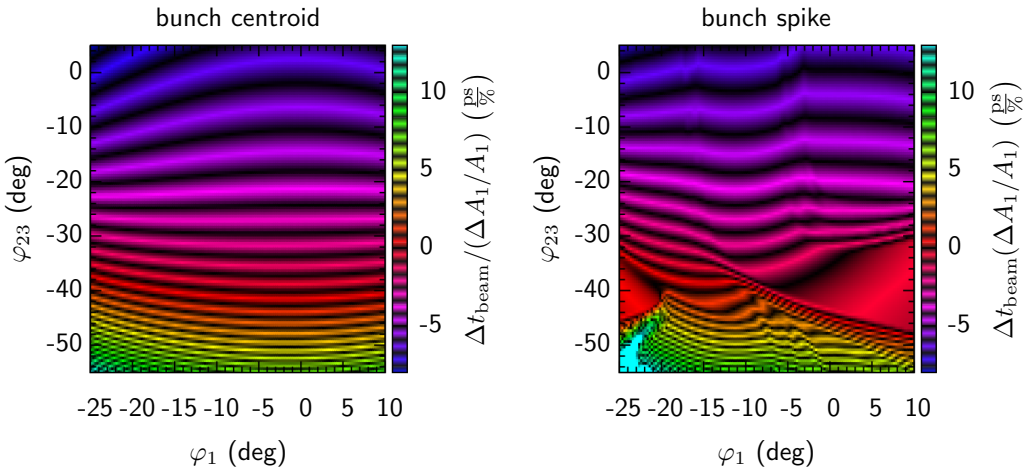

Figure 4.8: Influence of ACC1 amplitude changes on the bunch arrival-time downstream of BC2. The abscissa and the ordinate show the phase settings of ACC1 and ACC23. The color code of the contour plot represents the dependence of the bunch arrival-time after BC2 on ACC1 amplitude variations.

4.3 Influence of the accelerating section upstream of BC2

The influence of the phases and amplitudes of the accelerating sections upstream of the first and second bunch compressor on the timing stability after the final compression is depicted in figures 4.8 – 4.11.

Figure 4.8 shows the influence of the ACC1 field amplitude A_1 on the bunch arrival-time. The dependence of the arrival-time on the ACC1 field amplitude is about the same as it was after the first bunch compressor, when the accelerating section ACC23 is operated near the on-crest phase setting ($\varphi_{23} = 0°$). When ACC23 is operated off-crest, an additional energy chirp is imprinted onto the bunch leading to a different compression factor. In Fig. 4.8 one can see that the compression is increased towards negative ACC23 phases and the influence of A_1 fluctuations gets weaker. At an ACC23 phase of $\varphi_{23} \approx -35°$, ACC1 amplitude variations do not influence the arrival-time anymore and when φ_{23} is further decreased, ACC1 amplitude changes affect the arrival-time in the opposite direction. The behavior for the centroid and for the spike is very similar.

The arrival-time dependence on the ACC1 phase is very similar after the first and second bunch compressor. As before, the centroid and the current spike show a different behavior and the relationship between the arrival-time of the spike and φ_1 is again almost linear for $-16° < \varphi_1 < -6°$. Changes of the ACC23 phase have only a minor impact on this behavior and only at very negative off-crest phases the

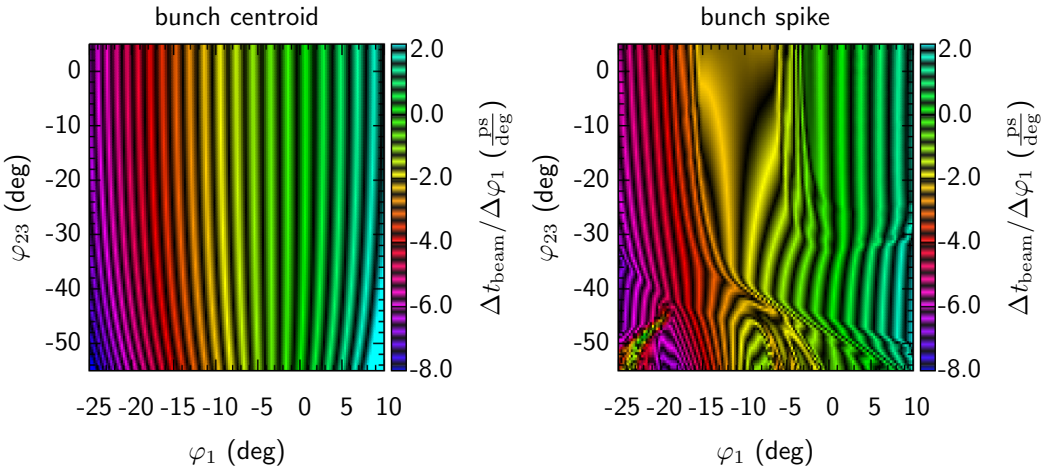

Figure 4.9: Influence of ACC1 phase changes on the bunch arrival-time downstream of BC2. The abscissa and the ordinate show the phase settings of ACC1 and ACC23. The color code of the contour plot represents the dependence of the bunch arrival-time after BC2 on ACC1 phase variations.

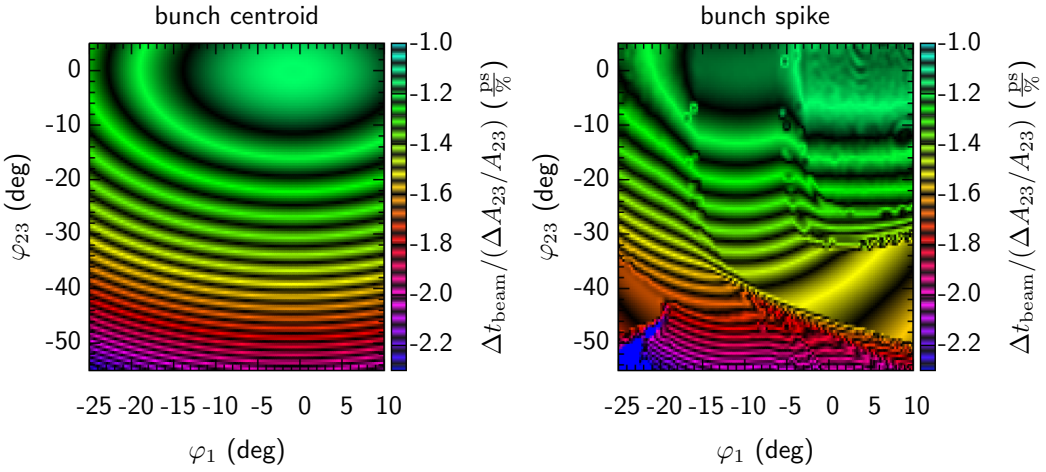

Figure 4.10: Influence of ACC23 amplitude changes on the bunch arrival-time downstream of BC2. The abscissa and the ordinate show the phase settings of ACC1 and ACC23. The color code of the contour plot represents the dependence of the bunch arrival-time after BC2 on ACC23 amplitude variations.

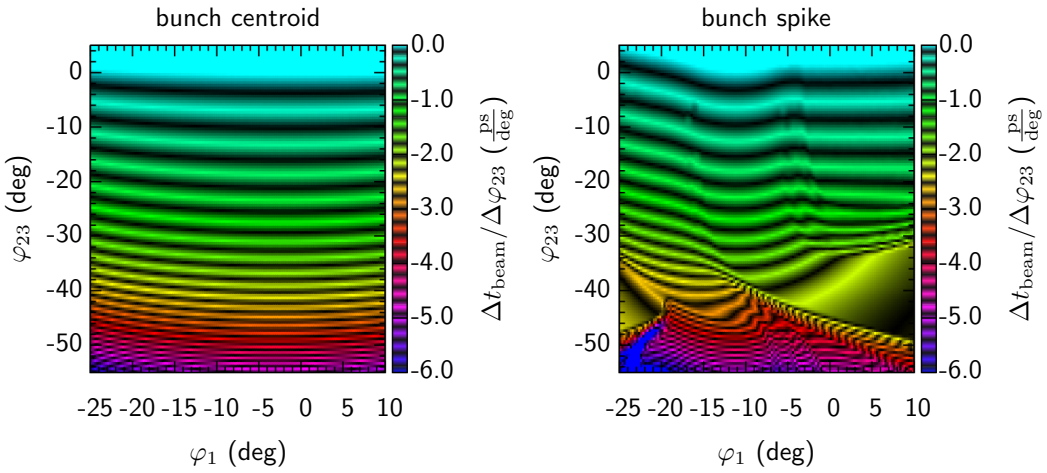

Figure 4.11: Influence of ACC23 phase changes on the bunch arrival-time downstream of BC2. The abscissa and the ordinate show the phase settings of ACC1 and ACC23. The color code of the contour plot represents the dependence of the bunch arrival-time after BC2 on ACC23 phase variations.

current spike shows a different dependence. It should be noted that most of the time, the energy chirp is generated only with ACC1 while ACC23 is operated on-crest.

Figure 4.10 depicts the influence of ACC23 amplitude variations on the bunch arrival-time. As one can see, $\Delta t/(\Delta A_{23}/A_{23}) \approx 1.2\,\mathrm{ps}/\%$ for small ACC23 phases. This is almost six times smaller than the corresponding value for the ACC1 amplitude. The reason is that the R_{56} matrix element of the second bunch compressor is only $-48.7\,\mathrm{mm}$ compared to the $R_{56} \approx -180\,\mathrm{mm}$ in BC1. This reduces the energy dependence by a factor of almost four. Furthermore, the electrons already have an energy of 130 MeV when they enter ACC23. This further reduces the impact of ACC23 amplitude variations. When ACC23 is operated far off-crest, the dependence increases due to the fact that the dipole field is kept constant in the simulation. The smaller energy gain in ACC23 leads to an increased matrix element R_{56}. The behavior of the bunch centroid and the current spike is very similar.

Figure 4.11 shows the dependence of the bunch arrival-time on ACC23 phase variations. Again, the impact is much smaller than for ACC1, which is due to the smaller value of R_{56} and an energy of 130 MeV at the entrance of ACC23. The arrival-time depends on the ACC23 phase in the same way as we have seen it for the ACC1 phase. Over a large range of ACC23 phases, centered around $\varphi_{23} = -40°$, there is an almost linear relationship. During normal FEL operation, the ACC23 phase is close to zero and, therefore, phase changes of ACC23 have only a minor influence on the bunch arrival-time.

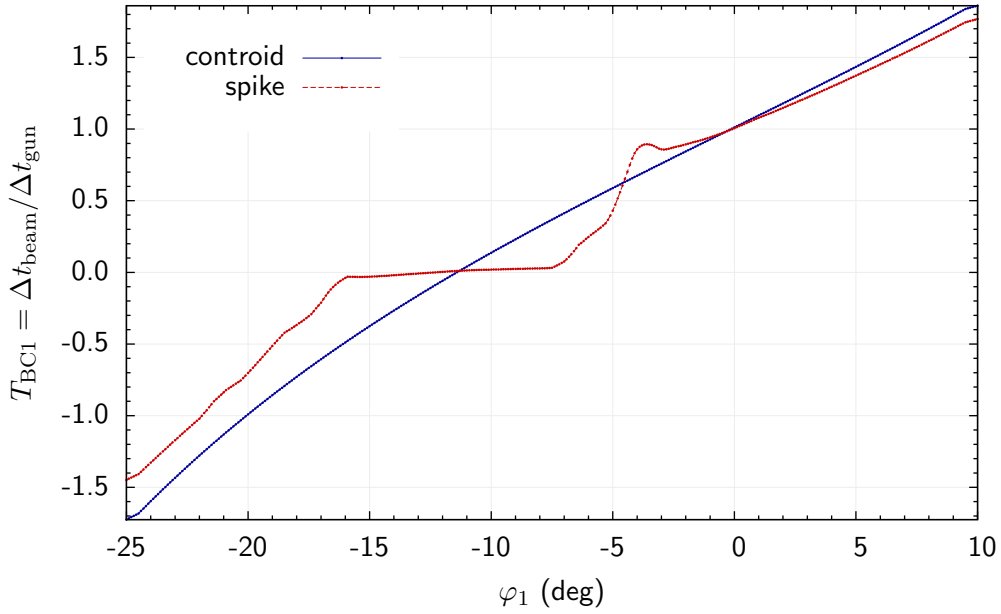

Figure 4.12: Modification of bunch arrival-time variations from the electron gun after the first bunch compressor as a function of the ACC1 phase.

4.4 Reduction of timing variations from the electron gun by bunch compression

Electron beam timing variations, which are generated in the electron gun due to photo-cathode laser timing fluctuations or phase changes in the RF gun, can be partly compressed in the two bunch compressors. Timing changes of either the gun or the photo-cathode laser do not only affect the bunch arrival-time upstream of the bunch compressors, but, as we have seen earlier, also the longitudinal energy distribution. To consider this inside the simulation, additional tracking simulations were performed with initial phase space distributions in which the gun phase was either increased or decreased by 1°. From the differences in the arrival-times compared to the tracking calculations of the reference ASTRA phase space, it can be deduced how electron beam timing variations generated in the RF gun are modified by the bunch compressors.

Figure 4.12 shows the time transformation factor T_{BC1}

$$T_{\mathrm{BC1}} = \frac{\Delta t_{\mathrm{beam}}}{\Delta t_{\mathrm{gun}}}, \tag{4.13}$$

where Δt_{beam} is the bunch arrival-time change downstream of BC1 caused by the arrival-time variation Δt_{gun} from the electron gun. When the ACC1 phase is adjusted such that the bunch is compressed, the arrival-time variations from the gun get smaller after BC1. The remaining arrival-time variation of the beam centroid

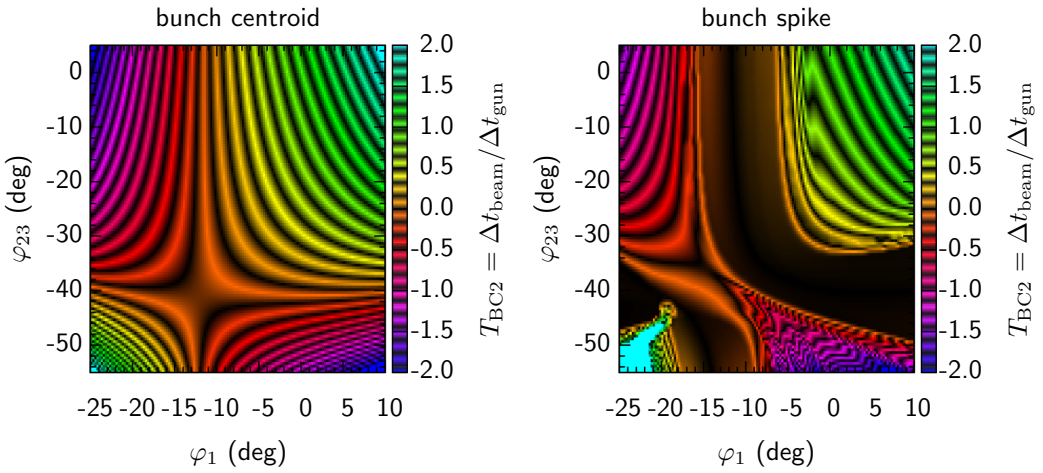

Figure 4.13: Modification of bunch arrival-time variations from the electron gun after both bunch compressors as a function of the ACC1 and ACC23 phases. The abscissa and the ordinate show the phase settings of ACC1 and ACC23. The color code of the contour plot represents the time transformation factor $T_{\mathrm{BC2}} = \Delta t_{\mathrm{beam}}/\Delta t_{\mathrm{gun}}$.

decreases almost linearly with decreasing ACC1 phase until the maximum compression is reached. From then on, the timing variation after BC1 has the opposite sign compared to the timing change from the electron source. The absolute value of the remaining timing change after BC1 increases again.

The current spike shows again a completely different behavior. As soon as the spike develops, timing changes from the gun are strongly reduced. In the ACC1 phase range from $-16^\circ < \varphi_1 < -7^\circ$, less than 5% of the injector arrival-time change is visible downstream of BC1, since in this phase range the electrons in the spike are almost ideally compressed.

Figure 4.13 shows the remaining beam arrival-time variation from the gun after the second bunch compressor. Over a large range of ACC23 phases (up to around -30°), the situation is very similar to the one after the first compressor. At $\varphi_{23} \approx -40^\circ$, the gun timing variation is almost completely compressed, independently of the ACC1 phase. The reason for this is that the compression in the second compressor is maximum for this ACC23 phase.

4.5 Impact of collective effects on the bunch arrival-time

Up to now, only external electric and magnetic fields have been considered. This simplification is justified as long as the bunch charge density is sufficiently low. The

current in the bunch spike, however, is on the order of several thousand amperes after final compression and longitudinal space charge forces cause a significant distortion of the beam even at higher energies.

The effect of space charge forces on the longitudinal phase space distribution was simulated by tracking calculations using ASTRA. For simplicity, space charge forces were neglected within the bunch compressors but since their length is short compared to the length of the accelerator, this causes only a small error. The settings of the machine are the same as in the previous calculations. After final acceleration, the energy is around 900 MeV. The phases of ACC23 and ACC456 are chosen to be on-crest for a particle which is accelerated on-crest in ACC1.

Figure 4.14 shows the simulated longitudinal phase space distributions at the entrance of the energy collimator for different settings of the ACC1 phase. The corresponding current profiles are depicted in Fig. 4.15. For comparison, the simulation results obtained by neglecting space charge forces downstream of BC1 are also shown. At bunch positions with a small current, the effect of the space charge forces is negligible. For $\varphi_1 < -7°$, the charge density in the current spike increases significantly and a fraction of the electrons in the spike gains energy from the space charge field while other electrons lose energy. This results in two tails in the leading part of the phase space distribution. In the current profiles, these tails appear as additional spikes. The first one with a very low current is ahead of the main spike and contains the electrons which gained energy from the space charge field. The second one trails the main spike and corresponds to the electrons which have lost part of their energy. Since the two tails remove electrons from the main spike, the predicted peak current is significantly reduced in comparison to the simulations in which space charge forces are neglected.

Although the bunch spike acquires a substructure, resulting in increased length and reduced peak current, its timing is only very slightly affected compared to the simulations without space charge forces.

A second collective effect, which can have a severe influence on the electron beam, is coherent synchrotron radiation (CSR) in the bunch compressors. Since the radiating electrons lose energy to the light wave, their trajectories within the bunch compressors change, resulting in a change of their longitudinal positions. Furthermore, the emitted radiation takes shorter paths through the magnetic chicane and can interact with the electron bunch at a downstream position. The energy change due to this interaction will again be transformed into a change of longitudinal position by dispersion. The current profile of the bunch spike can be severely affected by CSR. Detailed simulations can be found in [Röh08, Beu07]. Also these simulations show that the timing of the current spike is only slightly influenced.

4.6 Phase space linearization with a third-harmonic cavity

In order to generate a larger fraction of the beam with a sufficiently high current to contribute to the FEL process, it is planned to install a superconducting cavity

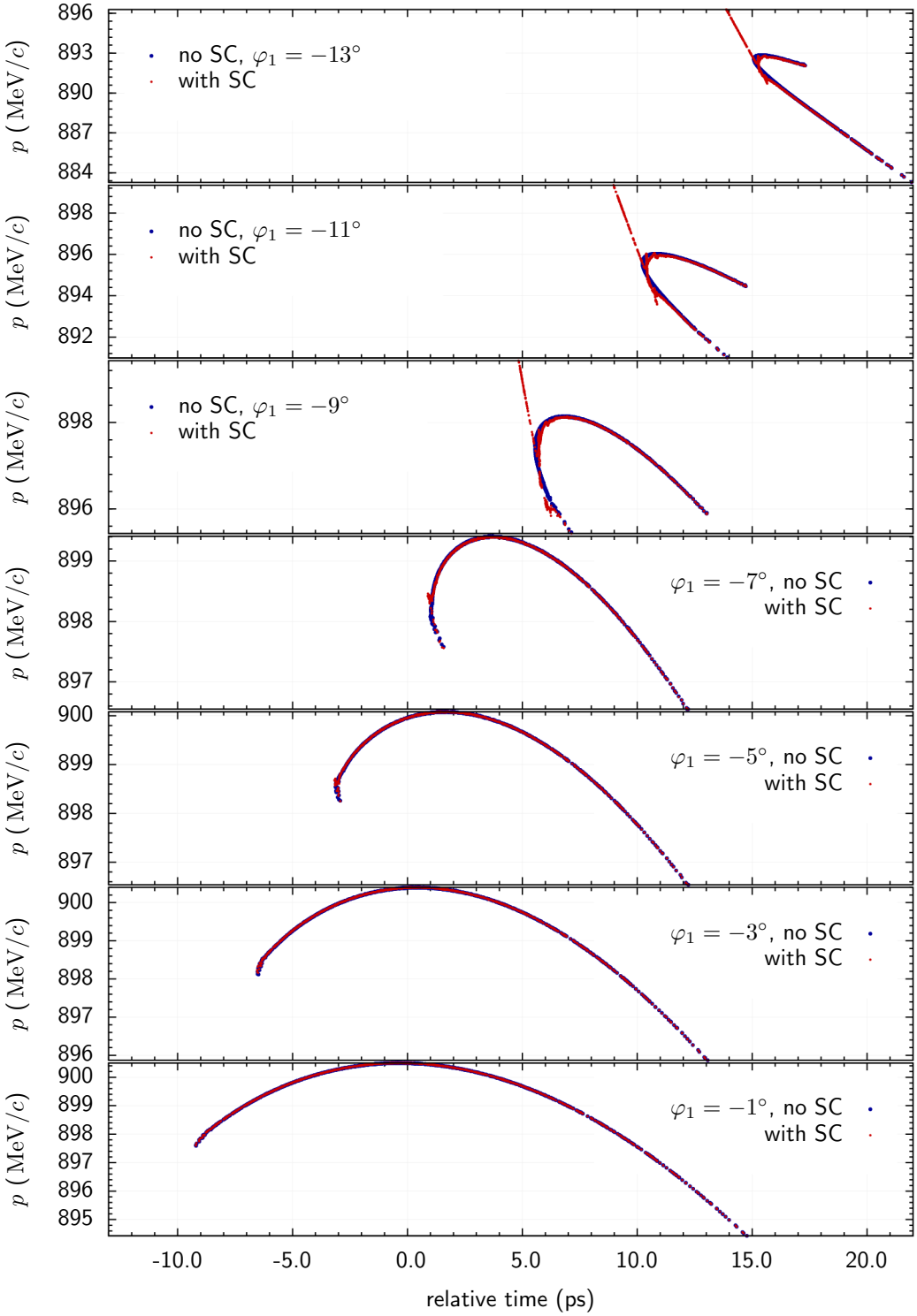

Figure 4.14: Effect of longitudinal space charge on the longitudinal phase space distribution and the bunch timing (SC: space charge).

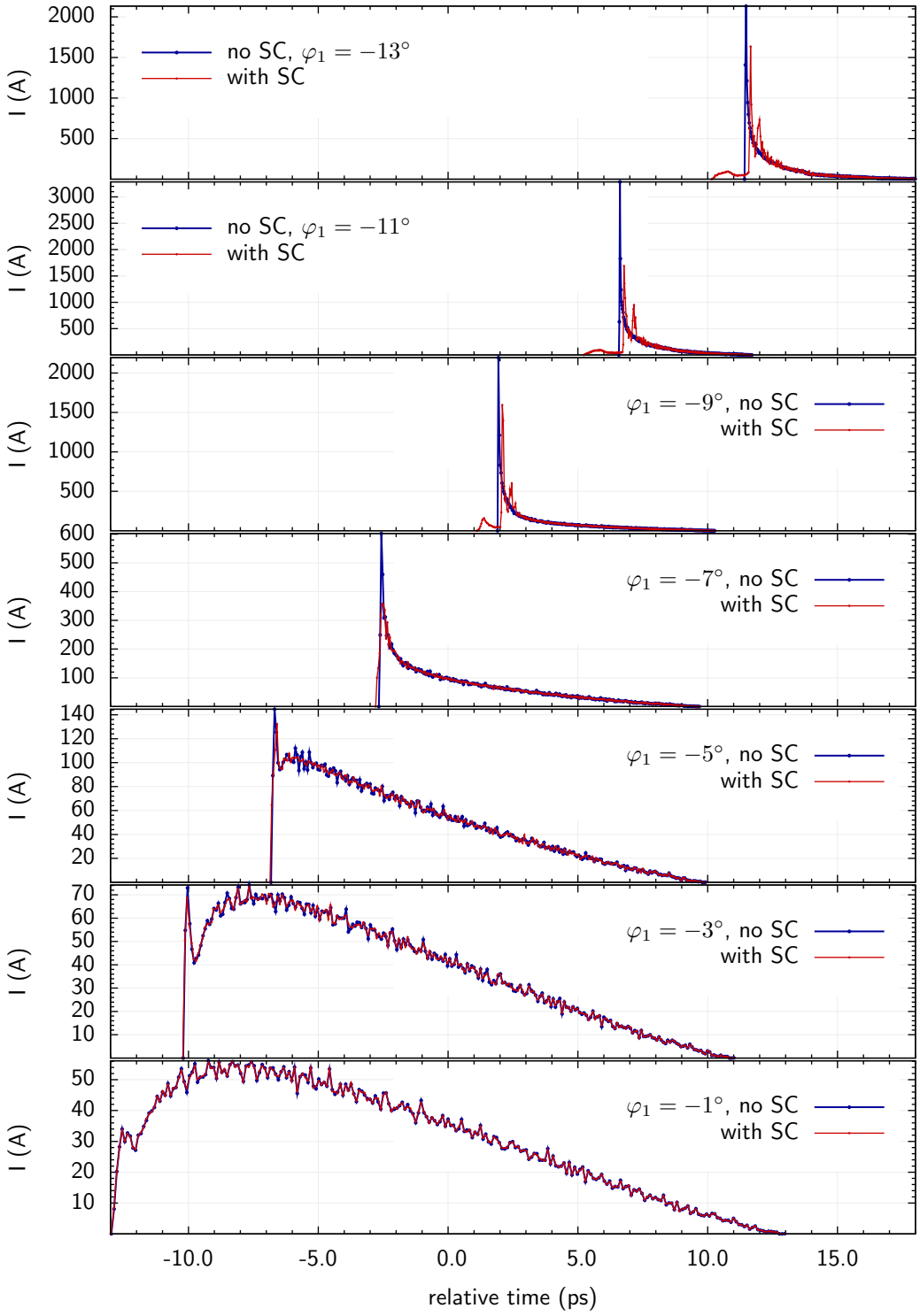

Figure 4.15: Effect of longitudinal space charge on the current profiles and the bunch timing (SC: space charge).

after ACC1 which is operated at a frequency of 3.9 GHz, the third harmonic of the 1.3 GHz RF of the other cavities (see Fig. 2.1). The purpose of this third-harmonic cavity is to linearize the compression process. A description of the principle can be found, e.g. in [Emm01].

With the third-harmonic cavity installed, the momentum of an electron entering the bunch compressor is given by

$$p(\zeta_i) = p_{\mathrm{gun}} + \frac{eA_1}{c}\cos(\varphi_1 - k_1\zeta_i) + \frac{eA_{3\mathrm{rd}}}{c}\cos(\varphi_{3\mathrm{rd}} - k_{3\mathrm{rd}}\zeta_i)\,, \tag{4.14}$$

where ζ_i is the longitudinal displacement to the reference particle upstream of the bunch compressor. A Taylor series expansion about the longitudinal position of the reference particle, yields

$$\begin{aligned} p(\zeta_i) =& p_{\mathrm{gun}} + \frac{eA_1}{c}\cos\varphi_1 + \frac{eA_{3\mathrm{rd}}}{c}\cos\varphi_{3\mathrm{rd}} \\ &+ \left(\frac{\partial p_{\mathrm{gun}}}{\partial\zeta_i} - \frac{eA_1}{c}k_1\sin\varphi_1 - \frac{eA_{3\mathrm{rd}}}{c}k_{3\mathrm{rd}}\sin\varphi_{3\mathrm{rd}}\right)\cdot\zeta_i \\ &+ \left(\frac{\partial^2 p_{\mathrm{gun}}}{\partial\zeta_i^2} - \frac{eA_1}{c}k_1^2\cos\varphi_1 - \frac{eA_{3\mathrm{rd}}}{c}k_{3\mathrm{rd}}^2\cos\varphi_{3\mathrm{rd}}\right)\cdot\zeta_i^2 + \cdots\,, \end{aligned} \tag{4.15}$$

and a momentum change with respect to the reference particle is given by

$$\begin{aligned} \frac{\Delta p}{p_0} = \delta =& \left(\frac{\partial p_{\mathrm{gun}}}{p_0\partial\zeta_i} - \frac{eA_1}{p_0 c}k_1\sin\varphi_1 - \frac{eA_{3\mathrm{rd}}}{p_0 c}k_{3\mathrm{rd}}\sin\varphi_{3\mathrm{rd}}\right)\cdot\zeta_i \\ &+ \left(\frac{\partial^2 p_{\mathrm{gun}}}{p0\partial\zeta_i^2} - \frac{eA_1}{p_0 c}k_1^2\cos\varphi_1 - \frac{eA_{3\mathrm{rd}}}{p_0 c}k_{3\mathrm{rd}}^2\cos\varphi_{3\mathrm{rd}}\right)\cdot\zeta_i^2 + \cdots \\ &= a\zeta_i + b\zeta_i^2 + \cdots\,. \end{aligned} \tag{4.16}$$

Here,

$$p_0 = p_{\mathrm{gun}} + \frac{eA_1}{c}\cos\varphi_1 + \frac{eA_{3\mathrm{rd}}}{c}\cos\varphi_{3\mathrm{rd}} \tag{4.17}$$

is the momentum of the reference particle. According to Eq. 4.8, the initial longitudinal displacement ζ_i of an arbitrary electron with respect to the reference particle is changed by the bunch compressor to

$$\zeta_f = \frac{\zeta_i}{C} = \zeta_i + R_{56}\cdot\delta + T_{566}\cdot\delta^2 + \cdots\,, \tag{4.18}$$

where C is the compression factor of the bunch compressor. When we insert Eq. 4.16, we get

$$\zeta_f = \frac{\zeta_i}{C} = \zeta_i + R_{56}\left(a\zeta_i + b\zeta_i^2\right) + T_{566}\left(a\zeta_i + b\zeta_i^2\right)^2 + \cdots\,. \tag{4.19}$$

By considering only terms up to second order, we get the following conditions for the coefficients a and b:

$$a = -\frac{1-C}{CR_{56}} \qquad \text{and} \qquad b = -\frac{(1-C)^2 T_{566}}{C^2 R_{56}^3}\,. \tag{4.20}$$

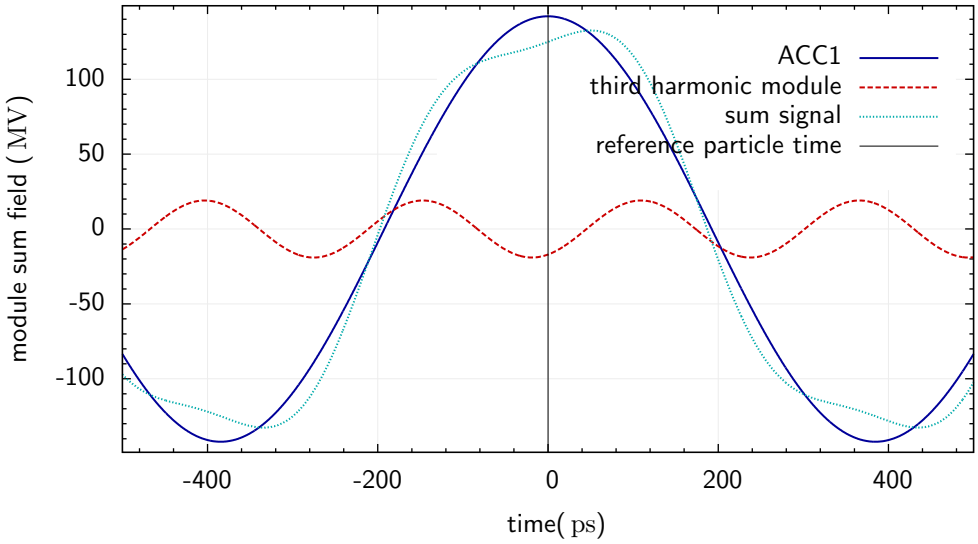

Figure 4.16: Resulting sum signal from ACC1 and the third harmonic cavity. The bunch is accelerated in the linearized part of it as indicated. Here, the resulting fields for an ACC1 phase setting of $\varphi_1 = 0°$ are shown.

For a very large compression factor C, the spread of the longitudinal positions is determined by the uncorrelated momentum spread from the gun. Furthermore, collective effects prevent a perfect compression of the bunch because similar to the previous example, substructures are generated.

For each phase and amplitude setting of ACC1 the conditions in Eq. 4.20 give a corresponding phase and amplitude setting for the third-harmonic cavity resulting in a linearized compression of the bunch. Each of these settings has the same slope and curvature of the resulting sum-field of ACC1 and the third harmonic at the time of the reference particle. The third derivative of the combined accelerating voltage, however, depends on the choice of the ACC1 phase. Figure 4.17 shows the phase space distributions after BC1 for four different settings of φ_1. A compression factor of $C = 20$ is chosen. Even with the linearization, the compression of the bunch tails is slightly different for the four ACC1 phases. Even though the central part of the distribution is identical in all four cases, the tails can cause a significant spike in the current profile.

Figure 4.16 shows an example of the resulting phase and amplitude relation between ACC1 and the third harmonic cavity together with the corresponding sum signal. In this example, an ACC1 phase setting of $\varphi_1 = 0°$ is used. The bunch is accelerated in the linearized part.

The influence of phase and amplitude changes of the two accelerating fields on the bunch arrival-time after the first bunch compressor has been studied using the same methods as before. Space charge forces have only been considered only upstream of ACC1. The compression factor is $C = 20$. Figure 4.18 shows the results of this

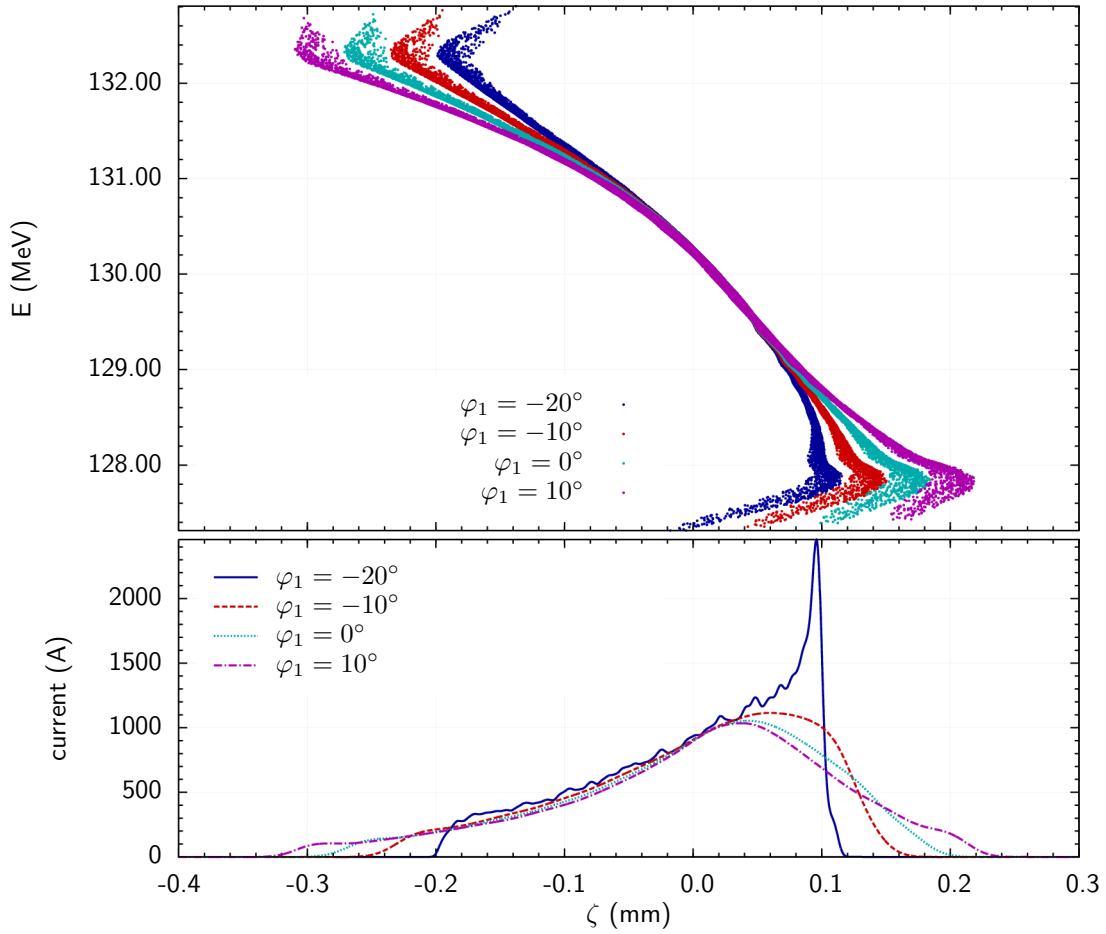

Figure 4.17: Phase space distributions and corresponding current profiles after BC1. The ACC1 accelerating field is linearized with a third-harmonic cavity. The results for different ACC1 phase settings are shown.

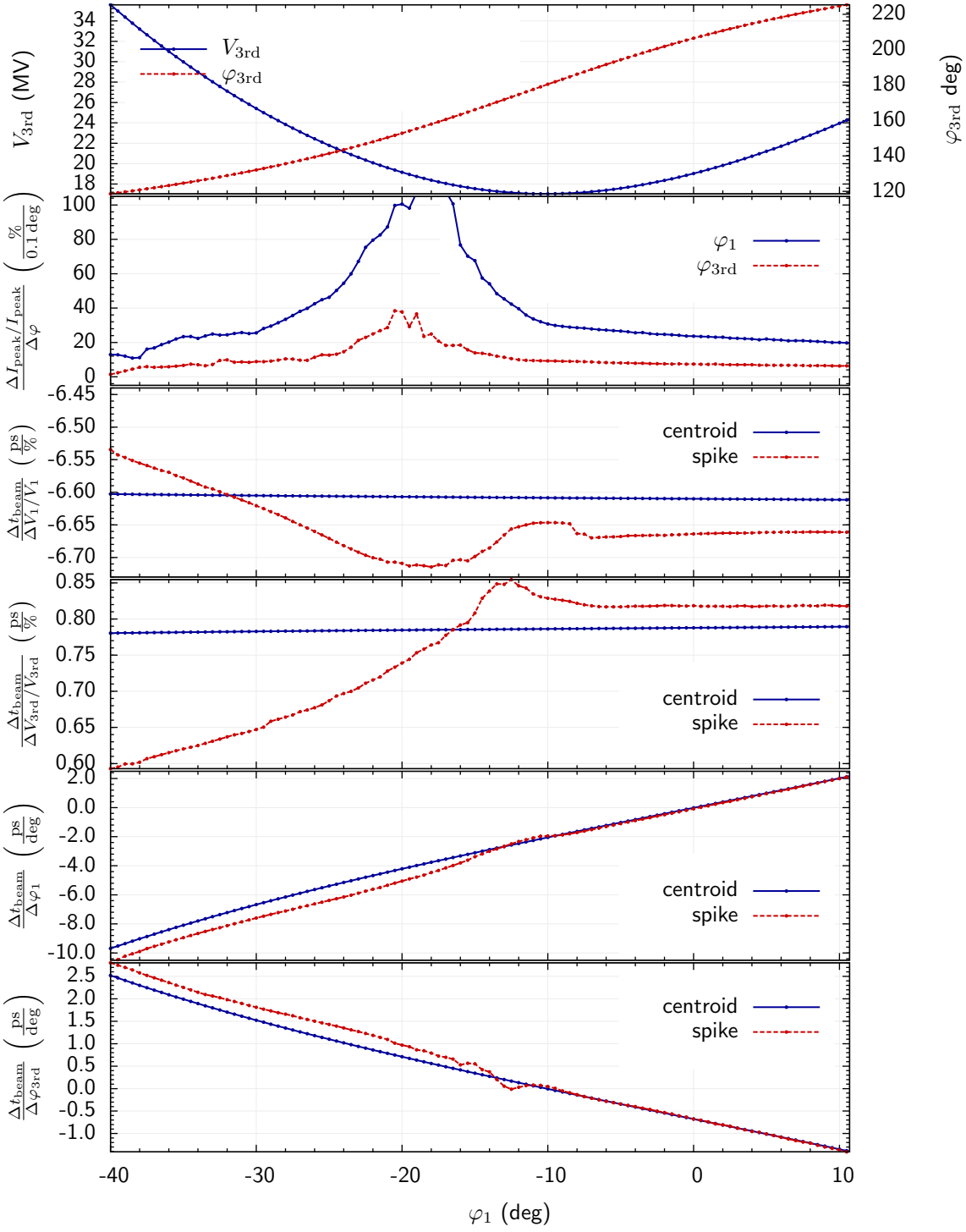

Figure 4.18: Sensitivity of the peak current and the bunch arrival-time after BC1 on changes of the phases and amplitudes of ACC1 and the third harmonic cavity (see text).

simulation. Different ACC1 phase settings have been analyzed, for each setting, the amplitude and phase of the third harmonic cavity have been readjusted. These settings are shown in Fig. 4.18 as well. For the linearization the third harmonic cavity decelerates the electron bunch and reduces their energy by about 16 MeV. In order to preserve the nominal energy of 130 MeV, the accelerating field in ACC1 was increased to result in an energy after ACC1 of about 146 MeV.

The first observation is that the peak current after the bunch compressor depends sensitively on the phases of ACC1 and of the third-harmonic cavity. Small deviations from the ideal phase decrease the peak current significantly. For both accelerating fields, this dependence is largest at ACC1 phases of about $\varphi_1 = -18°$. This maximum is caused by the tails of the phase space distribution contributing to the current profile (see Fig. 4.17).

The sensitivity of the bunch arrival-time on the ACC1 field amplitude A_1 is practically the same with and without the third-harmonic cavity in operation. Due to the smaller amplitude, the influence of the third-harmonic amplitude is significantly smaller than the one of ACC1.

It is interesting to note that with the working point for the ACC1 phase, the sensitivity of the bunch arrival-time to phase changes of ACC1 and the third-harmonic cavity can be significantly changed. When ACC1 is operated on-crest, the entire energy chirp needed for the bunch compression is generated with the third harmonic RF. Small phase changes of ACC1 have almost no influence on the bunch arrival-time for this setting. However, as expected, the electron beam timing then depends very sensitively on phase variations of the third harmonic RF. At an ACC1 phase setting of $\varphi_1 \approx -10°$, the situation is reversed and the electron beam timing is insensitive to small phase variations of the third harmonic RF. For even smaller ACC1 phase settings, the sensitivity of both phases increases. The optimum choice for the ACC1 phase depends on the phase stability achieved in ACC1 and the third-harmonic cavity.

5 Synchronization schemes

In this chapter, a brief description of a conventional RF based synchronization scheme and a short introduction to the optical synchronization scheme applied at FLASH is given. A detailed description of the single optical synchronization techniques and different subsystems developed within this thesis follows in the subsequent chapters.

5.1 Timing sensitive devices in the accelerator

As we have seen in chapter 4, the phases of the accelerating fields have to be tightly stabilized in order to achieve a stable electron beam arrival-time. Especially the phases of the cavities upstream of the bunch compressors are critical according to Eq. 4.12. For an aspired arrival-time stability of 10 fs, a timing stability of the 1.3 GHz cavity field of the same precision is required in the most sensitive cavities. This corresponds to a phase stability of around 0.005°.

A second category of timing sensitive devices are mode-locked lasers which are used inside an FEL facility at various locations. Among them are the photo-cathode laser and lasers for electro-optic beam diagnostics. Lasers used for pump-probe experiments with the FEL beam and the seed laser for the seeding option of FLASH are particularly sensitive to timing issues. Furthermore, there will be lasers measuring the arrival-time of the FEL pulses (see e.g. [MCW+08, GAB+08] for a first single-shot and high resolution scheme to measure arrival-times of XUV FEL pulses with respect to an infrared laser).

High-gain FELs operating in the XUV and X-ray range have lengths of several hundred meters up to a few kilometers. Many of the timing critical devices are located either in the injector (cavities, diagnostic lasers) or at the end of the accelerator (seed lasers, pump-probe lasers, diagnostic lasers). A stable distribution of a synchronization signal over large distances is, therefore, required.

5.2 Conventional RF based synchronization scheme

In a conventional linear accelerator, different sub-systems are synchronized by a common microwave master oscillator (MO) whose signal is distributed via coaxial cables. The timing of a remote sub-system is defined by detecting the phase relationship between an RF signal from the subsystem and the reference from the MO. For this purpose, a microwave mixer or a digital phase detector is used.

To measure the phase and amplitude of cavity fields, a pick-up antenna is used to provide the required RF signal. In the case of mode-locked lasers, the RF signal

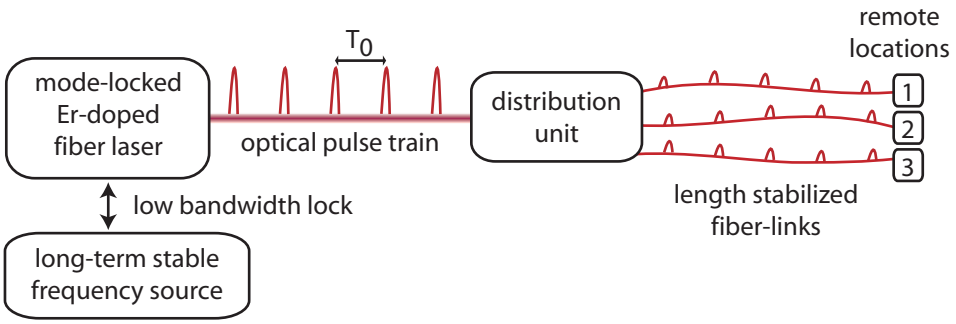

Figure 5.1: General concept of the optical synchronization system. A mode-locked laser is used as the timing reference and its laser pulse is distributed to the different remote locations via actively length stabilized fiber-links.

is generated by detecting the laser beam with a fast photo detector and a band-pass filter selecting a suitable higher harmonic of the pulse repetition frequency. The resolution of the timing detection based on a phase measurement improves with increasing frequency. To achieve sub-ps resolution, typically frequencies in the GHz range are used.

The RF synchronization system has two limitations. The first one is the reliability of the timing measurement. Mixers and phase detectors are highly temperature sensitive and even with a tight temperature stabilization a long-term stable operation is difficult to achieve. The second limitation is the transport of the reference signal from the MO to the sub-system. The thermal expansion and contraction of a several hundred meters long coaxial cable leads to time drifts of some picoseconds per degree C of temperature change, even if cables with very low temperature coefficients of $10^{-6}\,\mathrm{K}^{-1}$ are used.

A possible scheme for compensating the thermal drift is sending back part of the transmitted RF and perform a phase detection used to control a phase shifter which corrects for the drift. This scheme requires that each subsystem is supplied by its own RF cable whereas at FLASH the signals for the subsystems are coupled out from a common long cable installed along the entire length of the accelerator.

5.3 Optical synchronization scheme

A new synchronization concept for highly time-critical components in the accelerator was proposed at MIT in 2004 [KIK+04]. In this scheme, a mode-locked laser oscillator serves as the timing reference of the facility. The timing information is encoded in the highly accurate repetition rate of the *master laser oscillator* (MLO). The distribution to the single sub-systems is made via optical fibers. The general concept of the synchronization scheme is depicted in Fig. 5.1.

A suitable laser is an erbium-doped fiber laser operating at a central wavelength of 1550 nm, at a repetition frequency of around 200 MHz, and capable of producing

laser pulses with durations around 100 fs. In this wavelength range, many fiber-optic components are available, developed for the telecommunication industry. An important advantage of this wavelength is the possibility for a broadband transmission in dispersion compensated optical fibers.

One of the main advantages of this scheme is the fact that due to the short laser pulses, nonlinear optical methods can be applied to measure timing changes of the optical pulse train. An example is the timing detection between two lasers. If the two pulse trains overlap in an appropriate nonlinear crystal, a sum frequency signal is generated, the intensity of which depends sensitively on the temporal overlap of the pulses. With such a scheme, timing resolutions in the sub-10 fs and even sub-fs range are achievable.

In collaboration with Franz Kärtner's group at MIT, this cross-correlation scheme was developed within this thesis. It is applied to stabilize the optical length of the fiber-links used to distribute the reference signals. At the end of the fiber-link, part of the optical power is reflected and cross-correlated with the reference laser pulses. Length changes of the fiber are corrected with a piezo-electric fiber stretcher. A main advantage of this stabilization scheme with optical fibers and ultra-short light pulses is the superior resolution compared to RF schemes and the much lower costs of optical fibers.

At the remote locations, there are different possibilities of utilizing the laser pulses. Three different application schemes should be mentioned.

The first one is the synchronization of other mode-locked laser systems to the MLO. This is especially easy with a synchronization scheme in which the timing information is carried by the laser pulses, since again cross-correlating techniques of the two pulse trains in a nonlinear crystal can be applied. The feasibility of synchronizing two mode-locked lasers of different center frequency with such a scheme has been demonstrated and the two lasers could be long-term stably synchronized to each other with a precision of 0.3 fs [SKK$^+$03].

A second possibility of utilizing the laser pulses from the fiber-link is the extraction of a micro-wave signal needed for the cavities. This can be done with different schemes. An infinite pulse train of a mode-locked laser operating at a repetition frequency f_0 has Fourier components at $n \cdot f_0$, $n \in \mathbb{N}$. The simplest possibility to extract an RF signal of frequency nf_0 from the optical pulse train is to detect the pulse train with a photo detector of a bandwidth larger than nf_0 and to separate the frequency line nf_0 with a band-pass filter. With this scheme, RF signals can be extracted following the laser timing to better than 10 fs. The scheme is, however, temperature sensitive and the phase of the extracted RF signal depends on the optical power sent onto the photo-detector. In order to maintain the 10 fs stability over long durations, the temperature as well as the laser power have to be very stable. It may be preferable to use a Sagnac loop based interferometer for the extraction of a micro-wave signal [KLFK07, KCCK08] which is less sensitive to laser amplitude and temperature variations.

A third application is using the pulses from the reference laser for diagnostic purposes. As a part of this thesis, an electro-optic electron bunch arrival-time monitor

was developed [LHL+06, LHS07, LAF+08c]. A similar setup with minor modifications can be used to measure electron beam positions with micrometer resolution [LHL+06, HLS06]. Other possible applications are the seeding of Ti:Sapphire amplifiers with frequency-doubled pulses from the MLO (see e.g. [AZM+08]) as well as the amplitude and phase detection of a microwave signal in an electro-optic setup.

5.4 Required long-term frequency stability of the MLO

As we will see later, mode-locked lasers provide an excellent short-term timing-stability. Due to thermal and acoustic expansion and contraction of the laser resonator, however, the long-term stability is poor. Therefore, the laser frequency has to be stabilized. The most obvious reason for the required stabilization is the narrow bandwidth of a few hundred Hertz of the superconducting cavities. Without stabilization, the frequency of the laser may drift by a few thousand Hertz.

It may appear at first sight that slow drifts of the MLO repetition frequency are no problem, since they would correspond to slow time drifts of the whole accelerator, provided all timing signals are derived from the MLO. This simple point of view, however, is not correct.

The most stringent requirement on the stability of the MLO repetition frequency originates from different fiber-link lengths. Although it is in principle possible to choose the same length for all links, this would result in a maximum link length to all positions causing several disadvantages. Let us consider a fiber-link length L_0, which is adjusted such that the laser pulses traveling back through the link and incoming pulses from the MLO overlap in the cross-correlator. The fiber length is then given as

$$L_0 = L(f_0) = \frac{mc}{nf_0}\,, \tag{5.1}$$

where n is the refractive index of the fiber and m the number of laser pulses in the link. If the laser frequency f_0 changes by Δf, the relative fiber-link length change required to maintain the temporal overlap in the cross-correlator is then given by

$$\frac{\Delta L}{L_0} = \frac{L(f_0+\Delta f) - L(f_0)}{L(f_0)} = \left(\frac{f_0}{f_0+\Delta f} - 1\right) \tag{5.2}$$

$$\approx -\frac{\Delta f}{f_0} \qquad \text{for} \quad \Delta \mathrm{f} \ll \mathrm{f}_0\,. \tag{5.3}$$

The timing shift Δt of the synchronized component at the end of the fiber-link is given by

$$\Delta t = \frac{n\Delta L}{c}\,. \tag{5.4}$$

This is also the timing shift between two sub-systems from which one is synchronized directly from the laser, the other one by a fiber-link of length L_0. In Fig. 5.2, the effect is illustrated. It is evident that different link-lengths are only a problem due to the fact that in an accelerator, the relative timings between different devices at

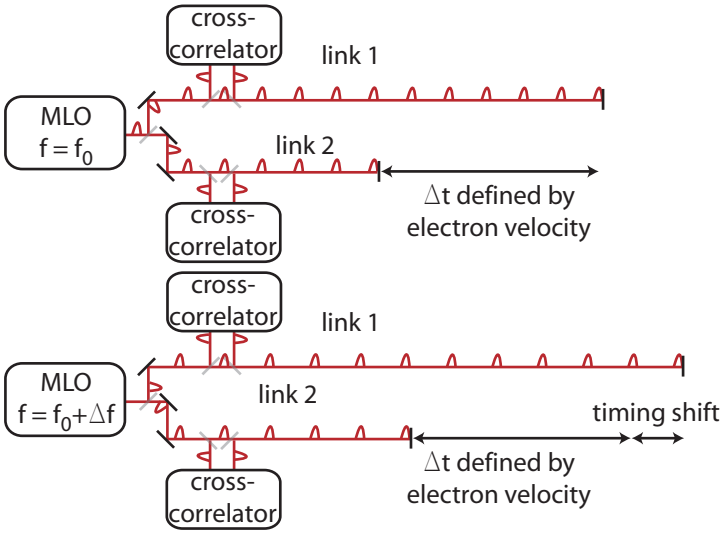

Figure 5.2: Illustration of the effect of MLO frequency changes on the fiber-link lengths.

the link-ends is defined by the duration, the electron beam needs to travel from one location to the other. The electrons travel almost at the speed of light and this duration is independent of the laser frequency. The situation is different, when no electron beam is involved. Let us assume we have two fiber-links of different lengths installed to the same location. Even if the laser frequency changes, the temporal offset of both pulse trains at the remote location remains constant.

In order to reduce the timing shift between the different fiber-links to a value smaller than ±5 fs, a laser frequency stability of $\frac{\Delta f}{f0} \approx \pm 2.5 \cdot 10^{-9}$ is required for a 400 m long fiber-link, which is the maximum length required at FLASH. At the European XFEL, the maximum link lengths will be around 4 km and for the same maximum timing shift, a laser frequency stability of $\frac{\Delta f}{f0} \approx \pm 2.5 \cdot 10^{-10}$ will be required.

At FLASH, the long-term frequency stability of the MLO is ensured by synchronizing the laser to the 1.3 GHz microwave master oscillator (MO) which is currently used for the coaxial timing distribution system. The 1.3 GHz oscillator is long-term stabilized by a synchronization loop to a temperature stabilized quartz oscillator operating at a frequency of 9.02775 MHz. According to specifications, the quartz oscillator provides a relative short-term frequency stability (< 10 s) of better than $2 \cdot 10^{-11}$, and, due to aging, a frequency shift of less than $1 \cdot 10^{-9}$ per day. Quartz oscillators are temperature sensitive. From the applied temperature regulation, one expects a frequency stability of $1 \cdot 10^{-8}$, corresponding to a time shift of 40 fs for a 400 m long link. Precise measurements on the MO frequency stability are, however, not available.

A sufficient frequency stability can be reached by replacing the quartz oscillator with an atomic clock, for example the rubidium standard used in the global

positioning system (GPS).

It should be noted that the frequency dependence discussed here is present in all kinds of synchronization schemes with different lengths of the distribution lines, also in interferometric schemes as described above. And even if the required long-term frequency stability is not available, this still allows for measurements on the femtosecond time scale. But in this case, the single signals distributed in the facility are not long-term stable with respect to each other and from time to time calibration measurements are required.

6 Master Laser Oscillator

A mode-locked, erbium-doped fiber laser, the *master laser oscillator* (MLO), is used as the timing reference in the optical synchronization system. In this chapter, a description of the laser, which was built and used within this thesis, is given and measurements of important properties are presented. A short introduction to the propagation of laser pulses in optical fibers is given in appendix D.

6.1 Requirements

Since a failure of the synchronization system may completely interrupt the machine operation, an important aspect is the reliability of the utilized sub-systems. Due to the fact that all timings are referenced to a single MLO, the reliability of the MLO is of special importance.

The timing information is encoded in the precise repetition rate of the laser. Fluctuations of the time separation between consecutive laser pulses are referred to as laser timing jitter and they are equivalent to fast repetition frequency changes of the laser. The different sub-systems, which are synchronized by the laser pulses, derive their timing either from the timing of single laser pulses, if the subsystem has a very high bandwidth, or from the average timing of a large number of consecutive laser pulses, which is the case for sub-systems with a low bandwidth. In the latter situation, timing fluctuations of single laser pulses are uncritical, since they average out. In the high-bandwidth sub-systems, however, no averaging takes place and single laser pulses define the timing. At FLASH, both types of subsystems exist and in order to synchronize subsystems of different bandwidths with respect to each other, the MLO timing needs to be stable from the laser Nyquist frequency $f_0/2$ to the bandwidth of the slowest sub-system. All timing jitter accumulated in this frequency range will result in a corresponding timing shift between the different sub-systems.

In order to enable accurate timing measurements using nonlinear optical methods like second harmonic generation and sum frequency generation, the laser pulses must be sufficiently short. Shorter pulse durations correspond to a broader optical spectrum and the required dispersion compensation in the fiber-links becomes quite demanding if the spectral width is too large. A compromise between the shortest pulse durations and a narrow optical spectrum has to be chosen and it was found during the course of this work that a transform limited pulse duration around 100 fs (FWHM) is a good choice.

The laser amplitude stability is of importance as many methods for the timing detection depend on the amplitude. The resolution of the timing detectors is, therefore,

deteriorated by amplitude noise.

Another important point is the laser pulse energy and the average optical power. A too low output power has the disadvantage that more optical amplifiers have to be applied, thereby increasing the complexity of the system and deteriorating its performance.

6.2 Setup

Due to their superior stability, compact size, and ease of use, fiber lasers are an interesting alternative to solid-state lasers for the generation of femtosecond pulses at near infrared wavelengths. They became more and more important over the recent years. Within a previous PhD thesis [Win08], a stretched pulse fiber laser [OHF93, TIHN93] operating at a repetition rate of 54 MHz was developed as a candidate for the MLO of the optical synchronization system. Although this laser type features an excellent noise performance and reliability, it turned out not to be the ideal choice for an MLO because of its low repetition rate.

The repetition rate of 54 MHz corresponds to a pulse spacing of around 3.7 m in fiber and 5.5 m in air. In order to establish a temporal overlap between the laser pulses and a second signal, for example a second laser pulse train, long fiber or free-space delays would be needed. Both alternatives are unfavorable. While a 5.5 m free space delay requires a spacious and fragile optical system, a 3.7 m fiber delay leads to unacceptable dispersive pulse broadening.

The situation can be improved by utilizing a soliton fiber laser [MS84, Mol85] operating at a significantly increased repetition rate of around 200 MHz. Such a laser with a repetition rate of 194 MHz, 167 fs long laser pulses, and an output power around 40 mW was demonstrated in [CSIK07].

The four times higher repetition rate simplifies establishing the temporal overlap with other signals. Furthermore, it allows to transmit a four times higher optical average power at the same level of nonlinear pulse distortion, which scales only with the pulse peak intensity and, therefore, with the pulse energy. The increased repetition rate improves the signal to noise ratio of arrival-time detectors, which average over a large number of pulses, by a factor of four.

Another advantage of the soliton laser compared to the stretched pulse laser is the significantly narrower optical spectrum making the dispersion compensation easier.

For these reasons, a soliton fiber laser running at 216.7 MHz was finally chosen for the FLASH master laser oscillator. The setup is depicted in Fig. 6.1. In comparison to [CSIK07], the laser resonator was realized in a sigma-configuration[1] which allows for the installation of a piezo mounted mirror for a large bandwidth repetition rate control. The erbium-doped fiber is pumped by two 974 nm pump-diodes with nominal output powers of 580 mW each. Different polarization states are used to combine the signals yielding a maximum available pump power of slightly above 1 W.

[1] In the MIT realization the two collimators are facing each other.

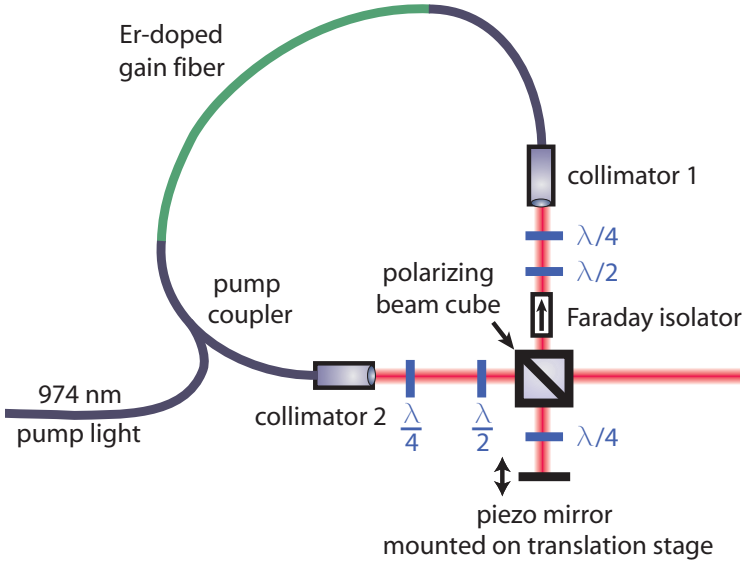

Figure 6.1: Schematic setup of the 216.7 MHz soliton fiber laser, the master laser oscillator (MLO) of the optical synchronization system.

section	fiber type	fiber length (cm)	$D(1550\,\text{nm})$ $\left(\frac{\text{ps}}{\text{nm km}}\right)$
collimator 1	SMF28	6.0	~ 17
gain fiber	Liekki ER80-8/125	50.0	~ 8
pump coupler	Lucent980	16.2	~ -2.4
collimator 2	SMF28	6.0	~ 17
free space		23.3	0

Table 6.1: Fiber lengths of the 216.7 MHz soliton laser.

The repetition rate of this laser was chosen to be 216.7 MHz, which is the sixth sub-harmonic of the 1.3 GHz RF. The net dispersion inside the laser resonator was decreased compared to [CSIK07]. The lengths and dispersion parameters of the fibers are shown in table 6.1.

For some measurements, a 200 MHz prototype was used. This laser cannot be locked to the machine reference oscillator.

6.3 Operation principle

As discussed in appendix D, there are mainly two ways for an optical pulse to experience an optical phase shift leading to a pulse shape change. The first one is due to dispersion and, depending on the sign of the dispersion parameter D (see Eq. D.6), can be positive or negative. The dispersive phase shift is given in Eq. D.11. A second

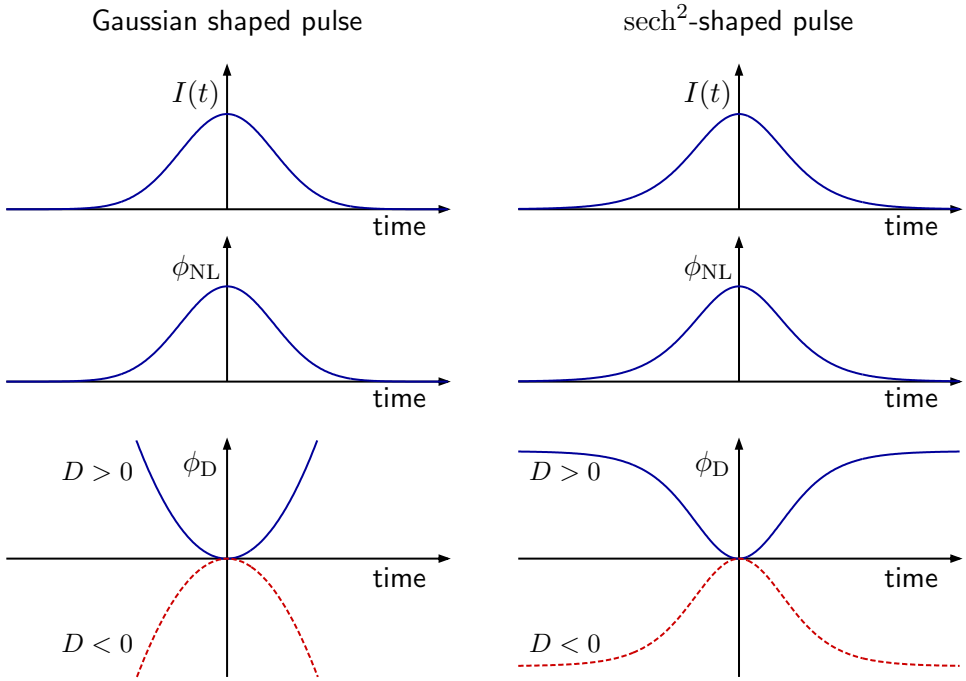

Figure 6.2: Nonlinear and dispersive phase shifts for a Gaussian- and sech^2-shaped laser pulse in an optical fiber. For a sech^2-shaped laser intensity profile and the proper pulse width and energy, the dispersive and the nonlinear phase shift exactly cancel each other, if the fiber dispersion is anomalous ($D > 0$).

source of phase shifts is non-linear effects inside the fiber. The dominant non-linear effect is self-phase modulation (SPM) and the sign for this phase change is always positive (see Eq. D.16).

In Fig. 6.2, the two phase shifts are depicted for a Gaussian shaped and for a sech^2-shaped laser intensity profile. In case of the sech^2-shaped laser intensity profile, the two phase shifts exactly cancel each other in presence of anomalous dispersion and for the correct pulse width and energy. In this case, a laser pulse propagates through the optical fiber without changing its shape and the resulting pulse is called a *soliton*. For an ideal soliton with an intensity profile

$$P(t) = P_0 \mathrm{sech}^2\left(\frac{t}{\sigma_{T_0}}\right) = P_0\left(\frac{1}{e^{\frac{t}{\sigma_{T_0}}} + e^{\frac{-t}{\sigma_{T_0}}}}\right)^2, \tag{6.1}$$

the relation between pulse width σ_{T_0} and peak power P_0 is given by

$$P_0 = \frac{D}{\gamma \sigma_{T_0}}. \tag{6.2}$$

In the MLO, solitons are generated. Due to the strong amplification in the gain

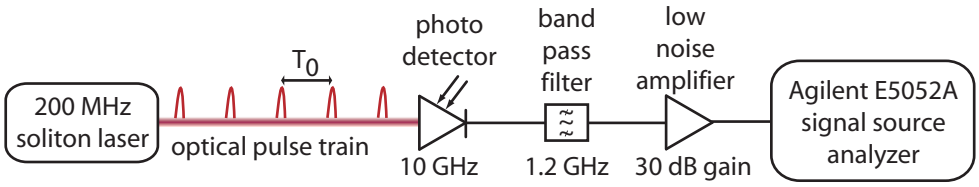

Figure 6.3: Schematic setup to measure the timing stability of a 200 MHz repetition rate laser.

fiber and the significant intensity change after the output coupler, the widths of the solitons in the MLO are, however, not exactly constant along the entire laser.

The MLO is a mode-locked laser and in order to establish the mode-locking, an intensity dependent loss mechanism is required. This is done by nonlinear polarization evolution: A polarizing beam cube is used as an output coupler and with two wave-plates, elliptically polarized light is generated and coupled into the fiber. Inside the fiber, the two polarization states experience a different nonlinear phase shift, according to their pulse energies[2]. When the pulses exit the fiber, the different phase shifts of both polarization states lead to a polarization change. The nonlinear phase shift is intensity dependent and it is largest at the peak intensity of the pulse. Different amplitudes of the polarization states lead to a stronger polarization change at the peak intensity part of the pulse than in the tails. With two additional wave-plates, the polarization of the pulse can be adjusted in a way that the losses for the peak intensity part of the pulse are minimized, i.e. such that most of the peak intensity part of the pulse remains inside the resonator. The pulse tails, however, have a different polarization and more intensity is coupled out.

6.4 Measurement of the timing stability

To measure the timing stability of the MLO, the setup depicted in Fig. 6.3 was used. The optical pulse train is detected with a fast photo detector. With a bandpass filter, the sixth harmonic of the laser repetition rate $f_0 = 200\,\mathrm{MHz}$ is filtered out. The harmonic is amplified with a 30 dB gain low noise RF amplifier. With a signal source analyzer, the single side-band phase noise $\mathcal{L}_\phi(f_m)$ which is defined as

$$\mathcal{L}_\phi(f_m) = \frac{\Delta\phi^2_{\mathrm{rms}}}{\Delta f} \tag{6.3}$$

is measured at different offset frequencies $f_m = f_c - f$. Here, $\Delta\phi_{\mathrm{rms}}$ is the rms phase variation of the carrier frequency f_c occurring at the offset frequency f_m, and Δf is the measurement bandwidth.

[2] In addition to self-phase modulation, a second nonlinear effect has to be considered, namely a phase shift caused by the interaction of the two orthogonal polarization states. This interaction is referred to as *cross-phase modulation*.

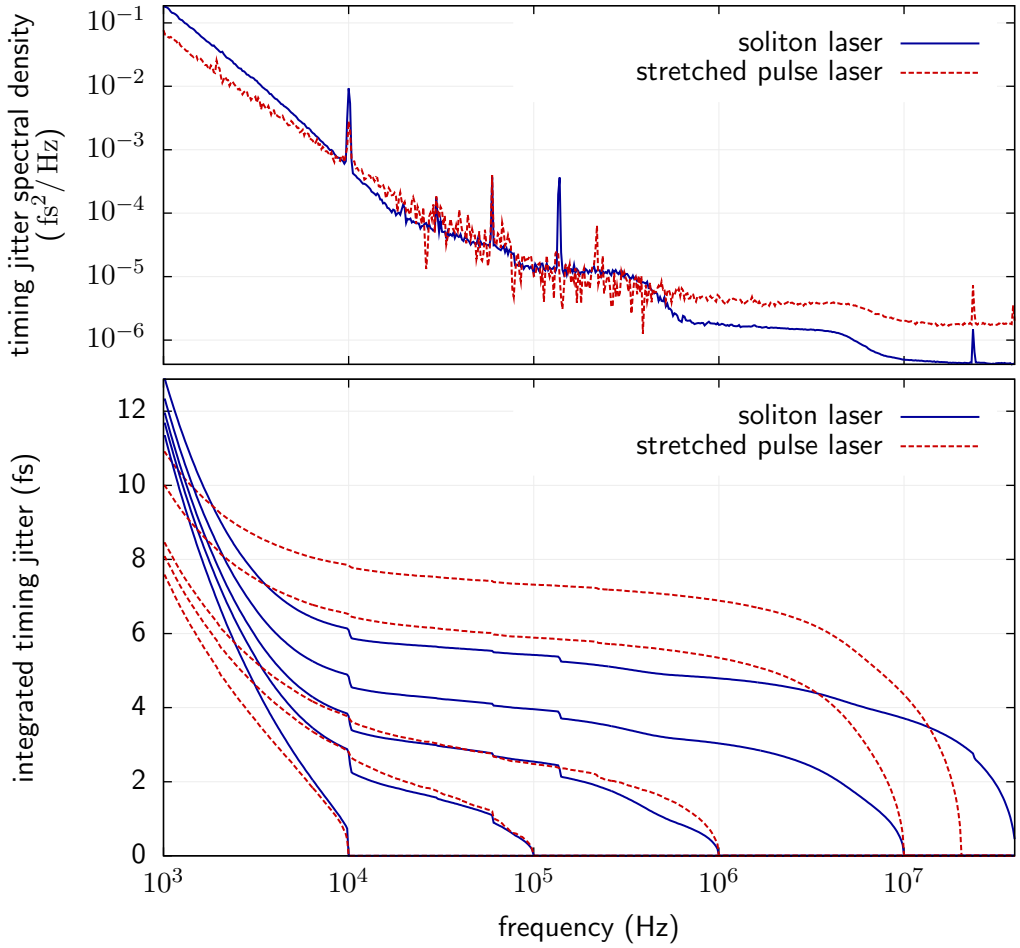

Figure 6.4: Timing stability of a 200 MHz soliton and a 40.8 MHz stretched-pulse fiber laser. Top: Timing jitter spectral density, bottom: integrated timing jitter starting the integration at different frequencies. The measurement of the stretched-pulse laser is from [Win08].

The timing jitter spectral density $\mathcal{S}_t(f_m)$ is then given by

$$\mathcal{S}_t(f_m) = \frac{2}{(2\pi f_c)^2}\mathcal{L}_\phi(f_m)\,, \tag{6.4}$$

and the integrated timing jitter Δt_{rms} occurring in the frequency interval $[f_1, f_2]$ can be expressed by

$$\Delta t_{\mathrm{rms}}[f_1, f_2] = \sqrt{\int_{f1}^{f_2} \mathcal{S}_t(f_m)\mathrm{d}f_m}\,. \tag{6.5}$$

Figure 6.4 shows the resulting timing stability of a 200 MHz soliton laser. In comparison, the timing stability measured for a 40.8 MHz stretched pulse laser, first planned to be used as the MLO, is shown. The maximum frequency at which the timing stability can be measured is 40 MHz, limited by the signal source analyzer. Both lasers show an excellent timing stability. The integrated timing jitter of the 200 MHz laser in the frequency range from [10 kHz, 40 MHz] is 6 fs. In the frequency range from [10 kHz, 10 MHz] it is 4.7 fs which compares well with the measurement done in [KCCK07], where in this frequency range a timing jitter of 5.19 fs was measured using an optical timing detection scheme. The measurements in [KCCK07] indicate also that the RF based measurement scheme is resolution limited at large frequencies. With the optical detection scheme in [KCCK07], a timing jitter of 0.72 fs was measured in the frequency range [1 MHz, 10 MHz], compared to 3 fs with the RF based scheme.

The reason for the better timing stability of the 200 MHz laser compared to the 40.8 MHz stretched pulse laser at high offset frequencies is probably only related to the better signal to noise ratio in this measurement: As the repetition rate is around five times higher, the power in the spectral lines is also increased by a factor of five.

The laser noise increases significantly at low frequencies. This is caused by changes of the resonator length due to vibrations and thermal expansion as well as by instabilities of the optical pump power. In order to provide the required long-term frequency stability, the laser is phase-locked to a microwave source. The best choice for the locking bandwidth is the frequency, at which the timing stability of the microwave source gets worse than that of the laser. In case of the 200 MHz laser, a good choice is a locking bandwidth around 10 kHz. Much higher locking bandwidths are hard to achieve due to mechanical resonances of the piezo-mirror.

6.5 Locking of the MLO to an RF source

In order to lock the laser to the master oscillator of the machine, the setup depicted in Fig. 6.5 was applied. Similar to the timing stability measurement, a harmonic of the laser repetition rate is filtered out from a photo-detector signal. A phase detection between this signal and the 1.3 GHz reference signal from the RF master oscillator is performed in a microwave mixer. The error signal is detected with an ADC[3]. A PID[4]

[3] analog to digital converter
[4] proportional-integral-derivative controller

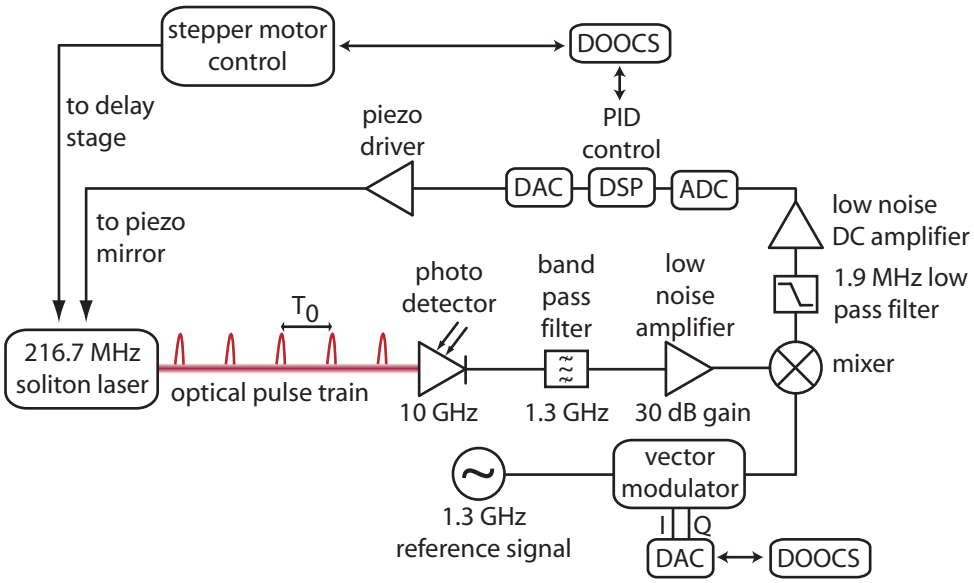

Figure 6.5: Schematic setup to lock the MLO to the 1.3 GHz master oscillator of FLASH.

controller, implemented on a DSP, calculates the control voltage which is produced by a DAC and sent through a high voltage amplifier to the piezo controlling the mirror position in laser. The parameters of this control loop can be adjusted using the machine control system DOOCS. Another DOOCS server is responsible for the control of the motorized delay stage onto which the piezo mirror is mounted. If the piezo reaches its correction limits, the delay stage is moved to keep the piezo within its range. In this way, the laser can be kept in the RF lock over very long periods of time. During this thesis, many months of continuous laser frequency stabilization were achieved.

The phase of the 1.3 GHz reference signal can be adjusted using a vector modulator. This offers the possibility of changing the laser timing with respect to the machine reference which allows for an easy establishment of the temporal overlap between the laser pulses and a machine signal.

The timing stability between the external RF source and the laser is mainly determined by the accuracy of the phase detection process. In this setup, the in-loop measurement of the error signal gave a stability between 40 fs and 50 fs. Due to the use of a conventional microwave mixer for the phase detection, the system is not long-term stable, as the mixer is temperature sensitive. It is planned to replace the phase detection scheme by a Sagnac-loop interferometer [KLFK07, KCCK08] with which it will be possible to achieve a long-term stable lock between the laser and the RF source with sub-10 fs stability.

When all timings are referenced to the MLO, the long-term stability of the RF lock is not important as long as the frequency stability of the microwave signal is

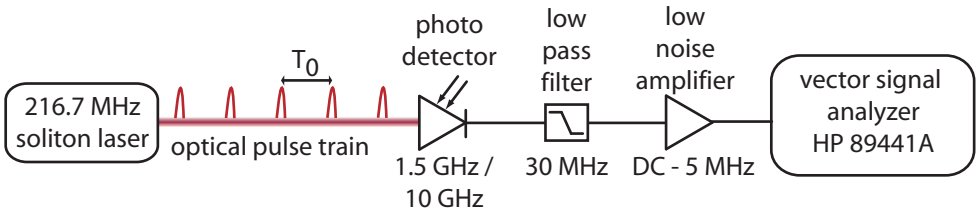

Figure 6.6: Schematic setup to measure the laser amplitude noise.

sufficiently good, as discussed in the previous chapter.

6.6 Measurement of the relative intensity noise

The relative intensity noise of the MLO is measured by detecting the laser intensity with a photo detector and by separating the baseband of the photo detector signal with a low pass filter (see Fig. 6.6). This signal is amplified and measured with a vector signal analyzer.

Figure 6.7 shows the measured relative intensity noise of the MLO. The laser shows an excellent performance and the integrated noise in the frequency range from 10 Hz to 1 MHz is 0.016 %. This is about a factor of two better than the noise measured for the 40.8 MHz stretched pulse laser. The sharp spikes in the noise spectrum in Fig. 6.7 are due to the experimental set-up and not produced by the laser itself.

6.7 Measurement of the optical spectrum under different operation conditions

The optical spectrum and the laser output power of the MLO can be adjusted by tuning the laser wave-plates and by changing the pump-power. Figure 6.8 shows the optical spectrum for three different pump-power settings and wave-plate adjustments resulting in a maximum output power. The output power for the three settings is 154 mW, 71 mW, and 57 mW. The corresponding pump-power settings can be found in table 6.2. This table also contains the spectral width of an sech^2-shaped curve which was fitted to the central part of the optical spectrum. It is interesting to note that the spectral width is very similar for all three settings. This is an indication that the intra-resonator power is quite similar in all settings and that the out-coupling ratio is much larger when the laser is operated at an output power of 154 mW as opposed to 57 mW.

The optical spectrum of an ideal sech^2-shaped temporal intensity profile would also be a sech^2-shaped intensity distribution. In Fig. 6.8 the sech^2-fits to the central part of the optical spectrum are shown and the agreement is very good for the central part. In the tails, however, the measured optical spectrum, shows pronounced spectral sidebands. These sideband are due to the periodically changed pulse energy

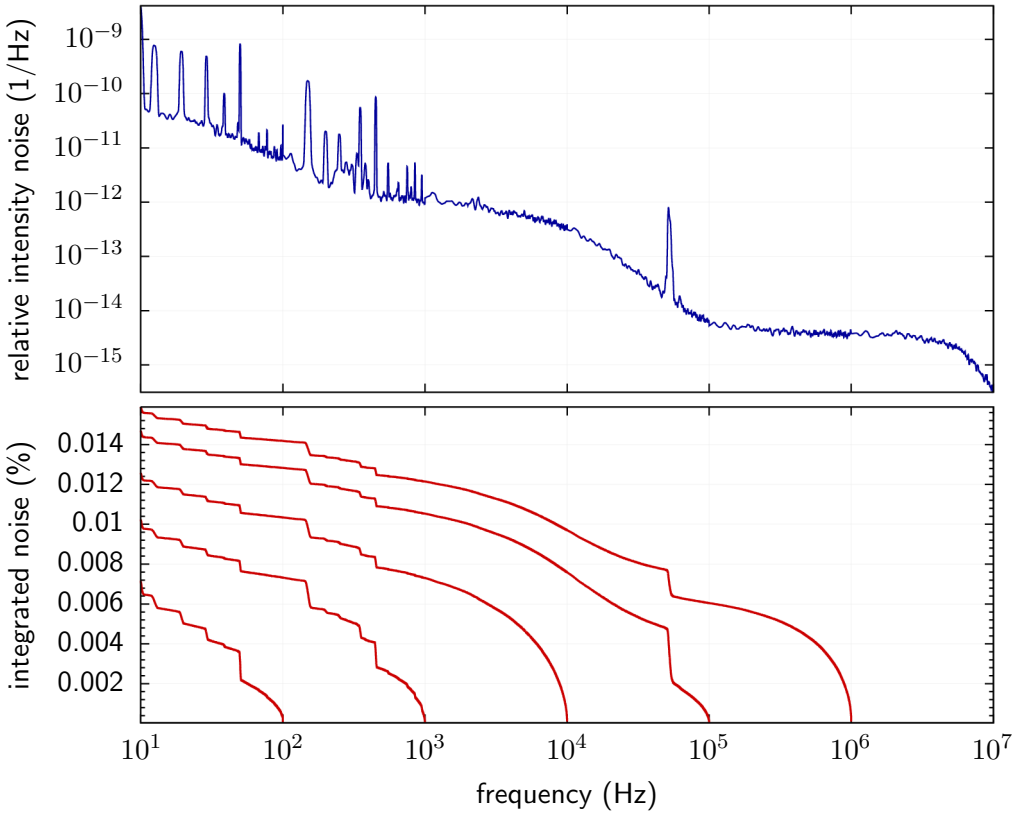

Figure 6.7: Relative intensity noise of the 216.7 MHz soliton fiber laser. Top: spectral relative intensity noise density. Bottom: integrated relative intensity noise starting the integration at different offset frequencies. The integrated noise in the frequency range from 10 Hz to 1 MHz is 0.016 %.

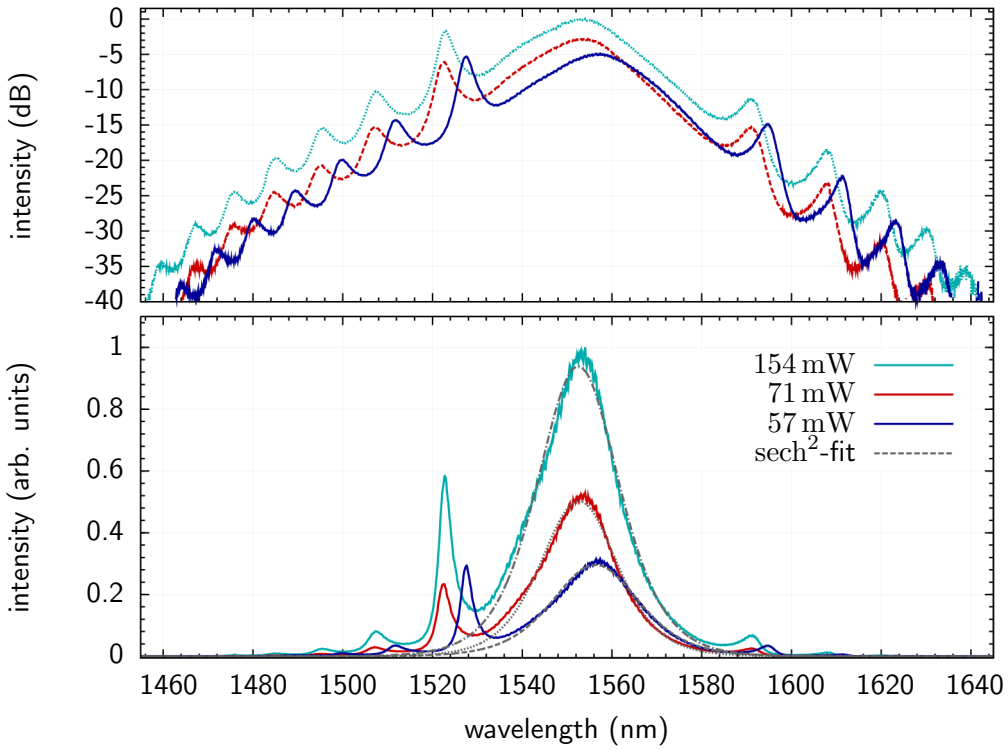

Figure 6.8: Optical spectra of the 216.7 MHz soliton laser for different pump power settings. The wave-plates are optimized for a maximum output power of 154 mW, 71 mW, and 57 mW, respectively.

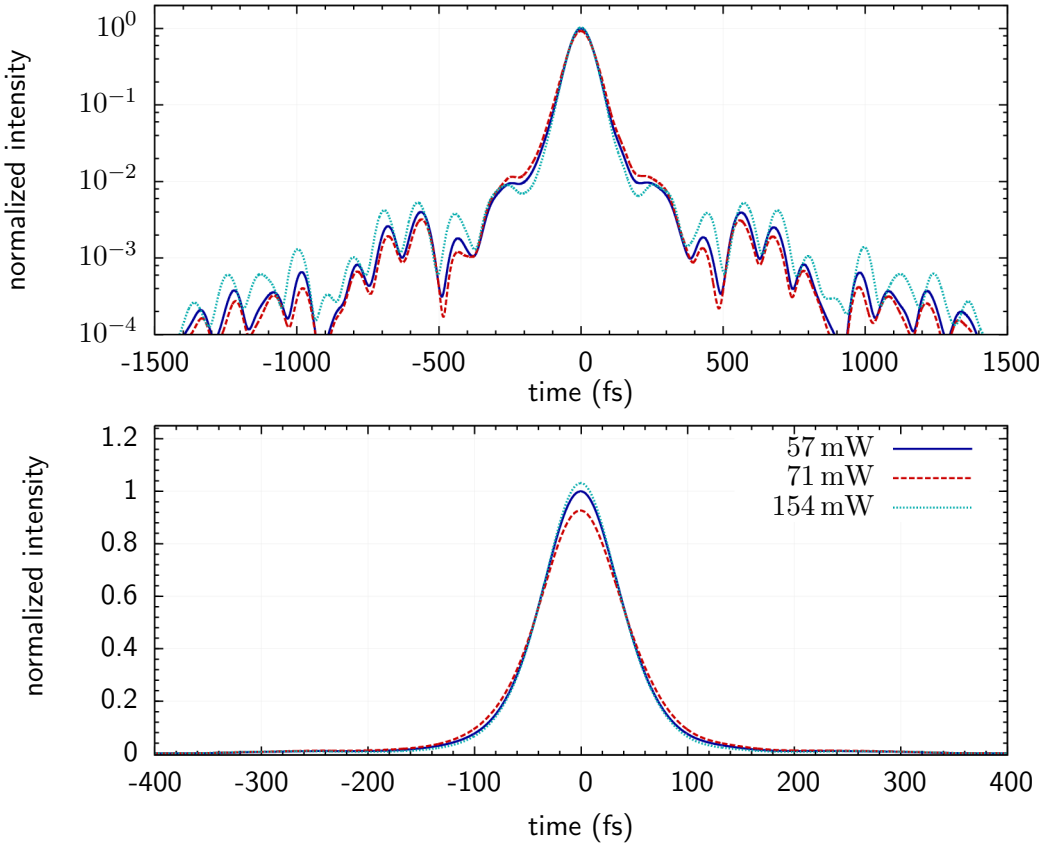

Figure 6.9: Pulse shapes of the 216.7 MHz fiber laser as calculated from the optical spectra. The laser output power is 154 mW, 71 mW, and 57 mW, respectively. All pulse shapes are normalized to the individual pulse energies.

caused by the output coupler and the amplification in the gain fiber and they are characteristic for the soliton-like pulse formation [Kel92].

Using the measured optical spectra, the expected temporal pulse shapes were calculated by Fourier transformation under the assumption that transform limited pulses exit the laser. These temporal profiles are depicted in Fig. 6.9. The corresponding pulse durations are listed in table 6.3. FWHM pulse durations around 90 fs are expected from the optical spectrum for the three different output power settings.

Figure 6.10 shows the optical spectrum for a constant pump-power but for different wave-plate settings. The output power varies between 101 mW and 141 mW. Table 6.2 again summarizes the operation conditions and the pulse properties. It is clearly visible that the spectral shape changes significantly for the different settings. Furthermore, the resonant sidebands at the short-wavelength side of the optical spectrum get more pronounced when the output-power is decreased. The central wavelength shifts to larger wavelengths when the laser output power is decreased. The observed optical spectra are not yet entirely understood. Sources for the asymmetry

output power (mW)	pulse energy (pJ)	estimated pump power (mW)	FWHM spectrum ($sech^2$-fit) (nm)
59	272	435	22.9
76	351	520	20.1
154	711	960	21.5
101	466	890	26.5
111	512	890	27.4
121	558	890	27.1
131	605	890	25.3
141	651	890	23.1

Table 6.2: Properties of the 216.7 MHz fiber laser beam. Top: different pump power settings and wave-plates optimized for maximum output power. Bottom: constant pump power but different wave-plate settings. The last column shows the FWHM of the $sech^2$-fit to the optical spectrum (see Figs. 6.8 and 6.10).

FWHM autocorrelation from spectrum (fs)	FWHM autocorrelation measured (fs)	FWHM pulse duration from spectrum (fs)	FWHM pulse duration $sech^2$-fit (fs)	FWHM pulse duration Gauss-fit (fs)
136	137	85	85	96
156	151	94	96	108
146	136	88	87	98
94	88	61	58	64
94	93	65	60	67
105	108	68	63	71
115	113	72	71	80
125	127	78	80	90

Table 6.3: Autocorrelation and pulse widths for the above settings of the 216.7 MHz fiber laser. In addition to the measured autocorrelation widths also the ones determined from the pulse shapes derived from the optical spectrum are shown (see Figs. 6.9 and 6.11). The last two columns show the pulse widths of $sech^2$ and Gaussian-shaped laser intensity profiles resulting from fits to the measured autocorrelation.

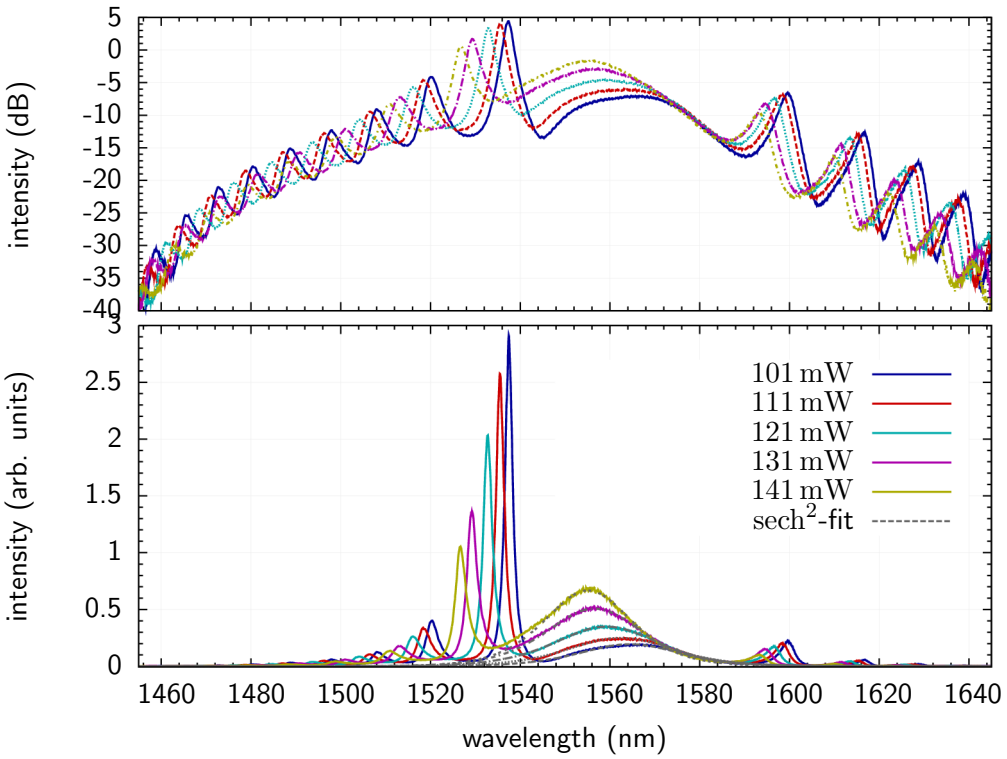

Figure 6.10: Optical spectra of the 216.7 MHz soliton fiber laser for a constant pump power of around 890 mW and different wave-plate settings. The laser output power ranges between 101 mW to 141 mW.

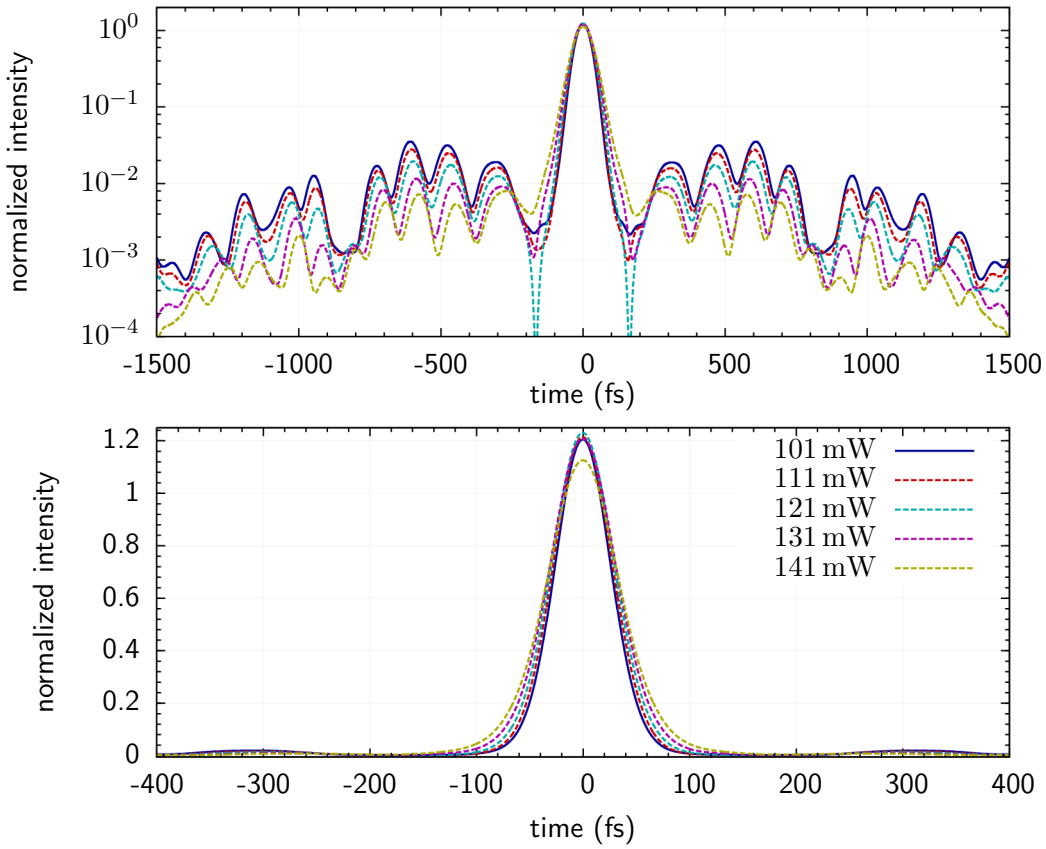

Figure 6.11: Pulse shapes of the 216.7 MHz fiber laser as calculated from the optical spectra. A constant pump power but different wave-plate settings are used, resulting in a output power of 101 mW to 141 mW. All pulse shapes are normalized to the individual pulse energies.

of the spectral sidebands are the wavelength dependent gain in the erbium-fiber as well as third order fiber dispersion. A possible source for the shift of the central wavelength is an intensity dependent gain profile of the erbium fiber caused by gain saturation.

The temporal pulse shapes calculated from the optical spectra are shown in 6.11, the corresponding pulse durations are presented in table 6.3. The expected pulses get as short as 60 fs FWHM as the laser output power decreases and the spectral width increases.

6.8 Measurement of the pulse duration under different operation conditions

To verify the expected pulse durations, interferometric autocorrelation measurements were performed. Figure 6.12 shows the measured autocorrelation trace for a laser

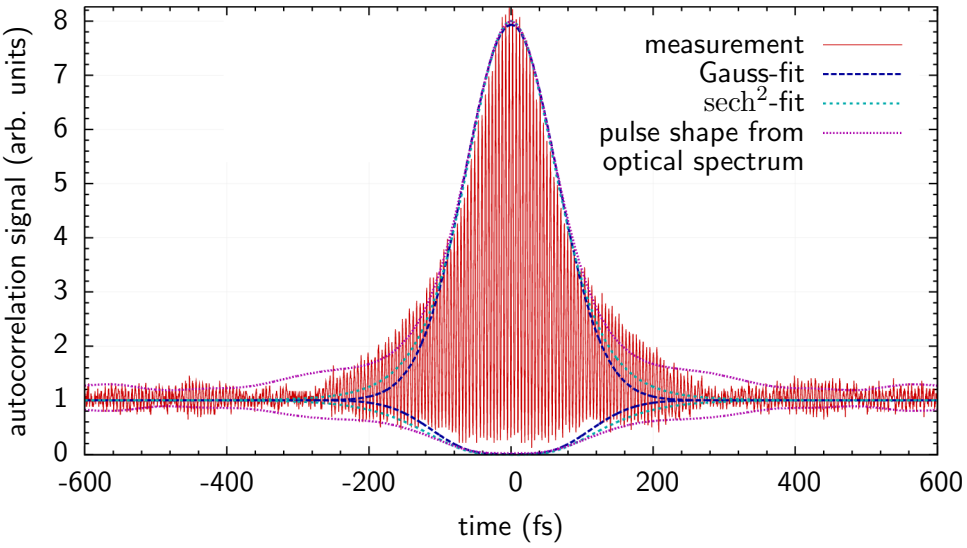

Figure 6.12: Interferometric autocorrelation of the 216.7 MHz soliton fiber laser operated at an output power of 154 mW. In addition, the envelopes resulting from fits assuming Gaussian and sech^2-shaped intensity profiles are shown as well as the envelope resulting from the pulse shape determined from the optical spectrum.

output-power of 154 mW. In addition, the fit-results are shown when assuming a Gaussian-shaped and a sech^2-shaped intensity profile. Furthermore, the expected autocorrelation trace for a temporal profile as calculated from the optical spectrum is shown. The last one shows the best agreement with the measurement.

From the fact that interference fringes are visible also in the tails of the autocorrelation trace, it can be deduced that the pulses coming from the laser are nearly transform-limited.

Figure 6.13 shows the autocorrelation traces when the laser is operated at different pump-power settings. For each pump power setting, the wave-plates are adjusted for maximum output power. In Fig. 6.14 the autocorrelation traces for the situation of a constant pump-power and different wave-plate settings is shown. In table 6.3 the FWHM durations of the measured autocorrelation traces as well as of the Gaussian- and sech^2-shaped fits is shown. In addition, the table shows the autocorrelation widths which are expected from the temporal profiles calculated from the optical spectra. The results show that in nearly all operation modes a pulse duration below 100 fs FWHM is reached. The shortest laser pulses that are generated are around 60 fs FWHM.

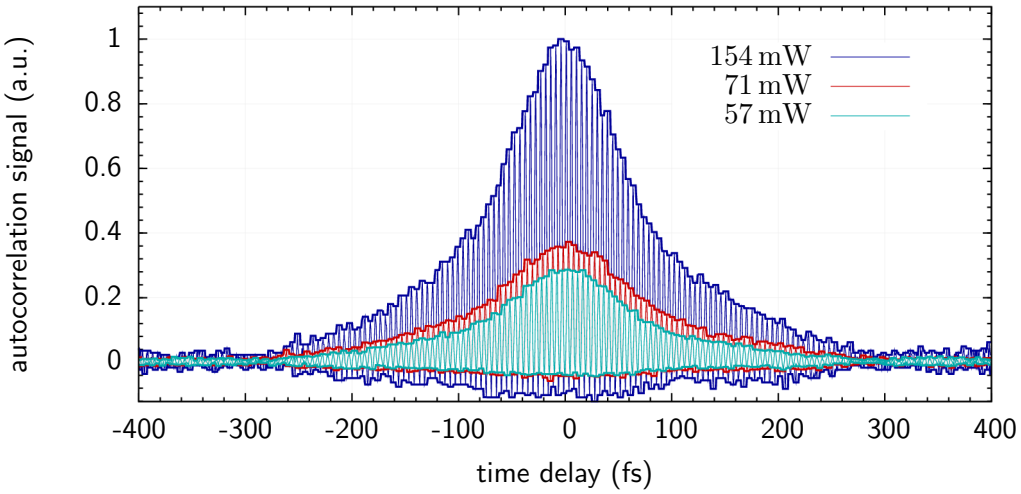

Figure 6.13: Interferometric autocorrelation of the 216.7 MHz laser operated at an output power of 154 mW, 71 mW, and 57 mW, respectively.

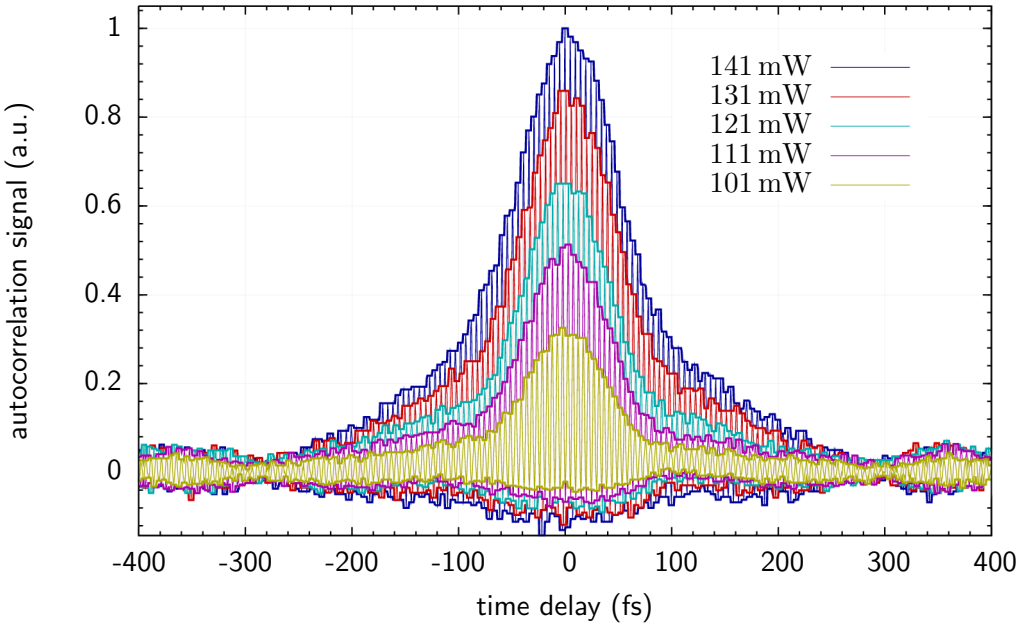

Figure 6.14: Interferometric autocorrelation of the 216.7 MHz laser operated at a constant pump power but at different wave-plate settings with an output power between 101 mW and 141 mW.

7 Fiber-link stabilization

An actively stabilized distribution scheme based on optical fibers and a balanced optical cross-correlator was developed in order to distribute the timing information provided by the MLO within the accelerator without deteriorating its accuracy. The development of the cross-correlator and first test of the fiber-link stabilization were done in collaboration with Franz Kärtner's group at MIT.

7.1 Setup

The principle of the fiber-link stabilization has already been described before and the schematic setup is depicted in Fig. 7.1. The laser pulses are transmitted via optical fibers to the remote device to be synchronized. At the link end, part of the laser power is used for the synchronization and another part is reflected and travels back through the same fiber to the location of the MLO. In an optical cross-correlator, the relative timing between the reflected laser pulse train and the pulse train coming directly from the MLO is measured. By this method, all changes of the link transit time happening on a time scale longer than the link round trip time can be detected. For a 400 m long fiber-link the round-trip time is around 4 μs. Timing changes of the link are mainly induced by thermal expansion or extraction of the fiber, temperature induced changes of the refractive index and by vibrations and mechanical stress[1]. Vibrations act on the fastest time scale, but even these times are typically longer than a millisecond. Even at link-lengths of 4 km, as they will be needed for the European XFEL, the round trip time is only 40 μs and not a limitation for the measurement of the link timing.

The optical cross-correlator is sensitive to the polarization of the incident light. A standard single-mode fiber is used in the fiber-link, in which the polarization of the light changes by temperature variations or by mechanical stress. In order to make sure that the polarization of the laser pulses returning from the link remains constant in spite of polarization changes in the fiber, a Faraday rotating mirror instead of a normal mirror is used at the end of the fiber-link. In this way, the polarization of the reflected light is rotated by 90° and the reflected light pulses see the opposite polarization change of the incoming pulses. When the reflected pulses arrive at the optical cross-correlator, their polarization is turned by 90° compared to the polarization with which they were coupled into the fiberlink. Only rapid changes

[1] It was found that even changes of the air humidity have an effect on the link round-trip time. A possible explanation is that the properties of the fiber cladding depend on the air humidity, which causes mechanical stress on the fiber.

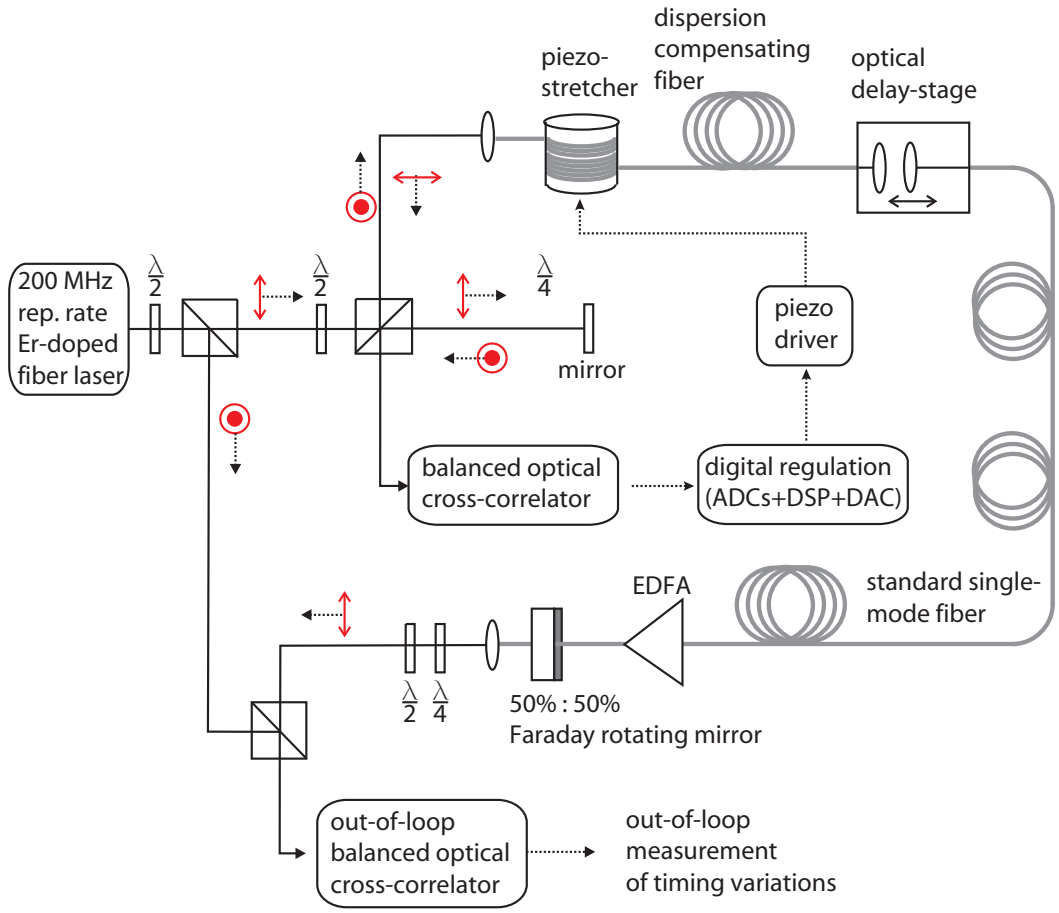

Figure 7.1: Schematic setup of the fiber-link stabilization. The fiber-link ends after the Faraday rotating mirror and, in this case, the timing-stability of the laser pulses from the fiber-link is measured by performing a second cross-correlation with the pulses from the laser.

of the fiber birefringence occurring on a time scale of less than the round-trip time lead to polarization variations of the returning laser pulses. The birefringence is changed by the same sources as the fiber length (see above) and so, changes of the birefringence happen on a time scale which is long compared to the link round-trip time.

A piezo-electric fiber-stretcher and an optical delay stage are used to compensate for timing changes detected by the cross-correlator. The regulation scheme is the same as used for the MLO.

The analog signal from the cross-correlator is digitized with an ADC and sent to a PID controller implemented in a digital signal processor. The PID signal is converted into an analog signal in a DAC, amplified, and sent to the piezo-electric fiber stretcher. The fiber stretcher has a mechanical resonance around 18 kHz and in order to be able to use a high gain of the control-loop, a regulation bandwidth from 500 Hz to 1 kHz is used. Since the timing changes of the fiber-link are very slow, this regulation bandwidth is sufficiently fast.

When the maximum range of the fiber stretcher has been reached, the optical delay stage is moved, under the control of a DOOCS server, until the fiber stretcher is again within its regulation range. By moving the delay stage, the server is also capable of establishing the temporal overlap between the pulse trains from the laser and from the fiber-link. This is needed when the system is initially started or when the MLO has lost its RF lock for a longer period in which the link timing changed by more than the laser pulse duration ($\sim 100\,\mathrm{fs}$).

An erbium-doped fiber amplifier (EDFA) is installed before the Faraday rotating mirror to compensate for laser power losses along the fiber-link. This amplifier leads to an increased output power from the semi-transparent Faraday rotating mirror and it amplifies the back-traveling laser pulses a second time, compensating for the power loss from the mirror. The pulse energy in the link is kept below 100 pJ in order to reduce nonlinear effects.

In the setup depicted in Fig. 7.1, the laser pulses from the fiber-link are guided into a second cross-correlator and their timing is compared with the timing of the pulses directly from the laser. This allows for the verification of the stabilization accuracy of the fiber-link.

7.1.1 Laser pulse broadening in the fiber-link

Since short laser pulses are needed at the remote-location and at the fiber-link cross-correlator, a dispersion compensating fiber is installed inside the fiber-link. This fiber has a dispersion factor of $D \approx -120 \frac{\mathrm{ps}}{\mathrm{nm\,km}}$, compared to $D \approx 17 \frac{\mathrm{ps}}{\mathrm{nm\,km}}$ for standard single mode fiber. About a seventh of the length of the standard single-mode fiber is required to compensate for the dispersion of the standard fiber. The dispersive length (see appendix D) of a Gaussian laser pulse with a FWHM pulse duration of 100 fs is about 7.9 cm in standard single-mode fiber and slightly larger than 1 cm in the dispersion compensating fiber. In order to prevent significant pulse broadening by the fiber-link, the length of the dispersion compensating fiber has

to be correct within $\sim 1\,\mathrm{cm}$, independent of the link length. This is achieved by measuring the autocorrelation of the pulses returning from the link while the fiber lengths are adjusted.

Even if the ratio between the lengths of the standard fiber and the dispersion compensating fiber is ideally chosen, the pulse will still broaden by the fiber-link. One of the reasons is the fact that about 10% of the third-order dispersion β_3 from the standard fiber is not corrected for by the dispersion compensating fiber. This can only be overcome by an additional third-order correction or an additional fiber type used in the dispersion correction.

A second reason for a pulse broadening by the fiber-link is polarization mode dispersion (PMD). The group velocities of orthogonal polarization components are identical only for a perfectly symmetric optical fiber. In a real fiber, however, the core is not perfectly round and the material purity is not perfect which together with local imperfections and mechanical stress creates variations of the refractive index. This results in different group velocities for different polarization states. The *fast-axis* of a fiber is defined as the polarization orientation leading to the fastest propagation velocity. Perpendicular to this axis is the *slow-axis* of the fiber. A long fiber can be considered to be composed of many sections with different orientations of the fast and slow axis. At every section interface, the power of a pulse from either the fast or the slow axis of the previous section couples into both axes of the new section. The distribution of the pulse energy between both axes is determined by the angle between the fast axis of the previous and the new section. The consequence is that a single laser pulse coupled into the fiber splits up into many laser pulses, all traveling at a slightly different group velocity. The superposition of all these single laser pulses results in a pulse which is broadened compared to the initial pulse.

The manufacturers of optical fibers in many cases specify the rms widths of the pulse broadening due to PMD, which is typically around $80\,\mathrm{fs}/\,\mathrm{km}^{1/2}$, for the standard single-mode fiber as well as for the dispersion compensating fiber. This corresponds to about 50 fs of pulse broadening due to PMD after a 400 m long fiber-link. The model the fiber manufacturers assume is an infinite number of sections with different slow- and fast axis orientations, resulting in a symmetric pulse broadening. According to [Aud08], in practice, optical fibers are unpredictable and can be composed from two up to a large number of sections. A small number of sections can have the consequence that PMD broadens the pulse asymmetrically.

In practice, the remaining higher order dispersion and PMD induced pulse broadening lead to a lower limit of the achievable pulse duration. For a 400 m long fiber-link and an initial laser pulse duration of 100 fs FWHM this is about 200 fs to 250 fs for a single passage through the link and about 300 fs to 400 fs after a complete link round-trip.

It should be noted that the presented fiber stabilization scheme also works with polarizations maintaining fibers, by which the effect of PMD can be eliminated.

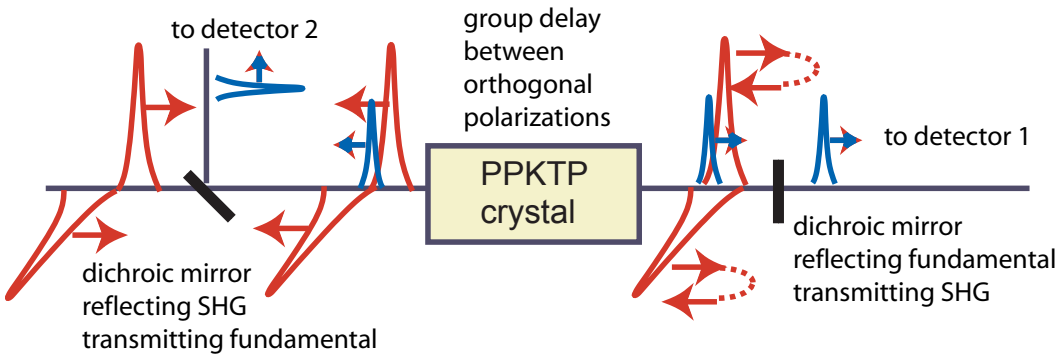

Figure 7.2: Operation principle of the balanced optical cross-correlator.

7.2 Balanced optical cross-correlator

The precision with which the optical length of the fiber-link can be stabilized is limited by the resolution of the detector measuring the relative timing between the pulses from the MLO and the returning pulses from the fiber-link. A conventional scheme is to detect the laser pulse train by a photo detector and to use RF based schemes for the timing detection. In order to overcome resolution and long-term stability issues of microwave phase detection schemes, a timing detection scheme based on balanced optical cross-correlation in a nonlinear crystal was developed [KCZ+07].

Inside a nonlinear crystal, the two pulse trains generate a sum-frequency signal, which in case of identical optical fundamental frequencies of the two pulse trains is the second harmonic of the fundamental frequency. For two pulse trains with central wavelengths of 1550 nm, the wavelength of the second harmonic wave is 775 nm. The power level of this second harmonic signal is proportional to $|E_{\mathrm{sum}}|^2$, where $E_{\mathrm{sum}} = E_1 + E_2$ is the sum of the electrical fields from the two optical pulse trains, which for short optical pulses depends strongly on the temporal overlap of the two pulse trains.

The easiest way to realize an optical cross-correlator is to directly use the power level of the second harmonic signal as a measure of the relative timing between the two pulse trains. A disadvantage is, however, that this signal not only depends on the temporal overlap of the two pulse trains but also on their light intensity. Power level variations of either of them will be misinterpreted as a change of the relative timing.

In order to overcome this intensity dependence, a balanced optical cross-correlator based on a single type-II PPKTP[2] crystal was developed. The schematic layout is depicted in Fig. 7.2. For the second harmonic generation (SHG) in a type-II crystal, two light waves with perpendicular polarizations are required. This is a big advantage compared to type-I crystals, where only one polarization is required for the SHG, since in the latter case, a background signal of both pulse trains is generated even

[2] PPKTP: periodically poled Potassium Titanium Oxide Phosphate ($KTiOPO_4$)

if the pulses do not have temporal overlap. In contrast, the type-II crystal allows a background free detection of the temporal overlap.

The two light waves with perpendicular polarization, called the *ordinary* and the *extraordinary* wave, experience a different refractive index in the anisotropic PPKTP crystal and thus travel at different group velocities. Depending on their temporal offset, this causes the two pulses to shift over each other while they travel through the crystal. Only at the locations in the crystal, where both pulses have temporal overlap, a second harmonic signal is generated, the intensity of which depends on the temporal overlap. The second harmonic is coupled out and sent to the first detector, while the fundamental waves are reflected by a dichroic mirror. Inside the crystal, the two light pulses generate a second sum-frequency signal and they further shift with respect to each other. The second harmonic signal is again coupled out by a dichroic mirror and measured with a second detector. In the recent crystals, which were however not used for the measurements within this thesis, the dichroic mirror reflecting the fundamental is realized by a coating on the crystal surface.

When the two light pulses enter the crystal with a temporal offset as depicted in Fig. 7.2, the temporal shift between them is such that at the end of the crystal they completely overlap. After the reflected pulses passed the crystal a second time, their temporal offset is identical to the initial one but their order is changed. The integrated overlap of the two pulses is identical for both ways through the crystal, giving the same second harmonic intensity at both detectors. With a different temporal offset between the pulses entering the crystal, the integrated overlap of both ways through the crystal differs from each other, resulting in different second harmonic intensities at both detectors. By using the difference signal of both detectors for the timing measurement and by measuring near the situation, where both detectors give identical signal strengths, amplitude changes of the incident light pulses are strongly suppressed. Figure. 7.3 shows the measured signals of the two detectors when the relative timing between the two optical pulse trains is changed. Photo-multiplier tubes have been chosen as the detectors in this measurement and the duration of the laser pulses was about 100 fs FWHM for both pulse trains. The difference signal of both detectors is an S-shaped curve and for a symmetric signal from both detectors, the zero-crossing is not affected by laser amplitude changes. The slope of the S-shaped curve, however, will be modified. In the measurement, the two detector signals have a slightly different shape, resulting in an asymmetric difference signal. This leads to a reduced suppression of laser amplitude noise. The reason for this different response is not yet understood.

For a sustained energy transfer from the fundamental light waves to the second harmonic signal, the phase matching between these signals is very important. When the propagation velocities of the fundamental and the second harmonic wave differ from each other, the phase between both signals is shifted along the crystal and when the shift reaches 180°, light energy is transferred back from the second harmonic to the fundamental wave. To achieve sustained energy transfer to the second harmonic wave, a crystal with periodic poling is used, resulting in *quasi-phase-matching*. At every position a phase shift of 180° between the fundamental and the second har-

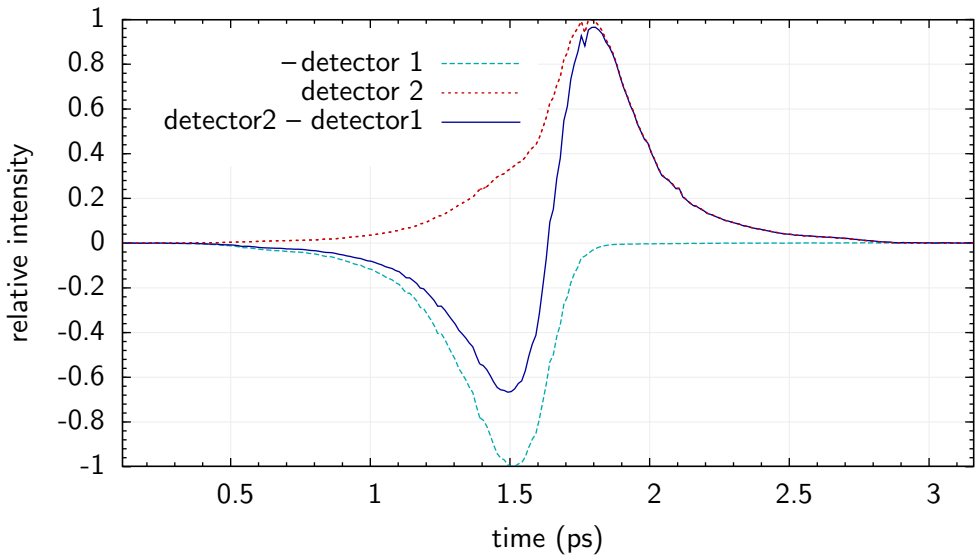

Figure 7.3: Measured signal strength of the two cross-correlator detectors for different temporal offsets of the two laser pulses at the crystal entrance. The zero-crossing of the difference signal is used for measurements of timing variations between both optical pulse trains.

monic wave is reached, the crystal orientation is rotated by 180°. The poling period required for this is determined by the difference between the indices of reflection of the fundamental and the second harmonic wave. For KTP[3], the required poling period is 46.2 μm.

The conversion efficiency of the crystal was measured to be about $4 \cdot 10^{-3}$ for 200 fs long laser pulses (FWHM) with a pulse energy of 77 pJ [KCZ+07].

7.3 Measurement results of the fiber-link stability

The long-term stability of the optical fiber length stabilization cannot be measured with the internal cross-correlator which is part of the feedback loop. Instead, an independent external cross-correlator (see Fig. 7.1) is used, which will be referred to as the out-of-loop cross-correlator. Figure 7.4 shows a measurement of the spectral timing jitter density of a stabilized 300 m long fiber-link. The fiber was wound onto a spool and placed inside a laboratory. The integrated timing jitter in the frequency range from 10 Hz to 100 kHz is 9.2 fs. One can clearly see that this measurement is limited by the detector noise floor. The increased noise with a maximum at about 800 Hz and the long tail towards higher frequencies comes from a not well adjusted feedback loop. Only at frequencies lower than a few hundred Hertz, noise contributions from vibrations, which are not entirely suppressed by the feedback loop, are visible.

[3] Potassium Titanium Oxide Phosphate ($KTiOPO_4$)

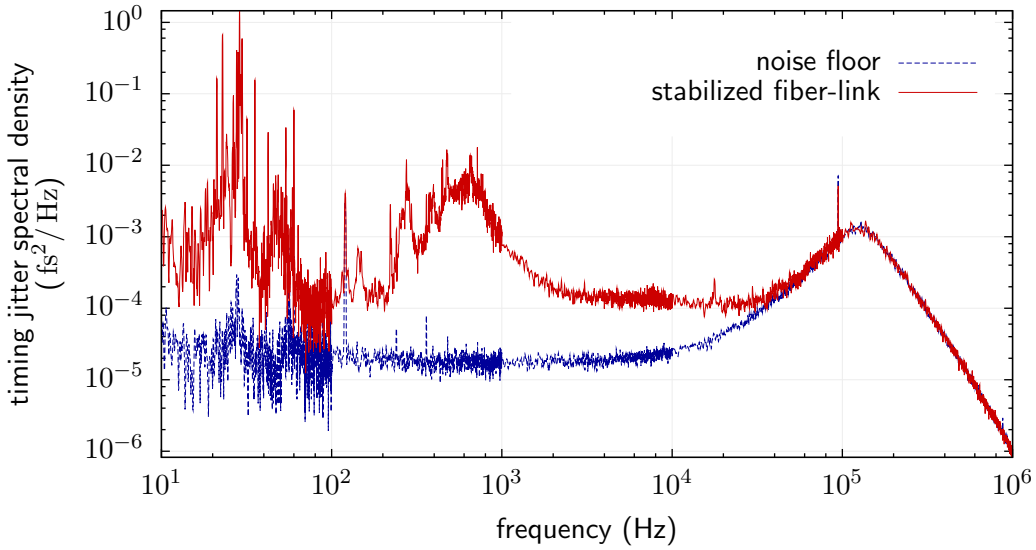

Figure 7.4: Measured spectral timing jitter density of a 300 m long stabilized fiber-link.

In order to investigate the influence of a noisy accelerator environment on the stability of the fiber-link, a 400 m long link was installed around the circumference of an accelerator hall. A 200 MHz soliton laser was used as the reference laser. By means of an optical delay stage and a fiber stretcher, the fiber-link was stabilized over a period of twelve hours. As in the previous measurement, the timing stability of the link was measured with an out-of-loop cross-correlator, in which the timing of laser pulses from the link-end and from the laser was compared [LCM+07].

The laser was not locked to an RF source in order to long-term stabilize the laser frequency. A laser frequency change has the consequence that the actuators have to change the link-length to keep the temporal overlap between the pulses from the laser and those returning from the link constant. When this correction is made, the temporal overlap in the out-of-loop cross-correlator is still the same.

Figure. 7.5 shows the results of this long-term measurement. In order to correct for relatively fast changes of the laser frequency, both actuators, fiber stretcher and optical delay line, were continuously changing the fiber-link length (top and center plot). The bottom plot shows the timing change after the fiber-link, which is measured with the second, out-of-loop, balanced cross-correlator. The measurement bandwidth is 200 kHz. The overall rms timing jitter is 7.5 fs but it is obvious that there is a systematic slow timing drift present. This drift is visualized by the red curve, which represents a floating average over 100 s. The rms timing jitter about this smooth curve amounts to 4.4 fs rms.

The slow timing drift of about 25 fs over the entire duration is most likely a measurement artifact. The required polarization for the out-of-loop cross-correlator was manually adjusted with wave-plates after the fiber-link. During the measurement period, however, the polarization in the fiber-link changed and after 12 h, the optical

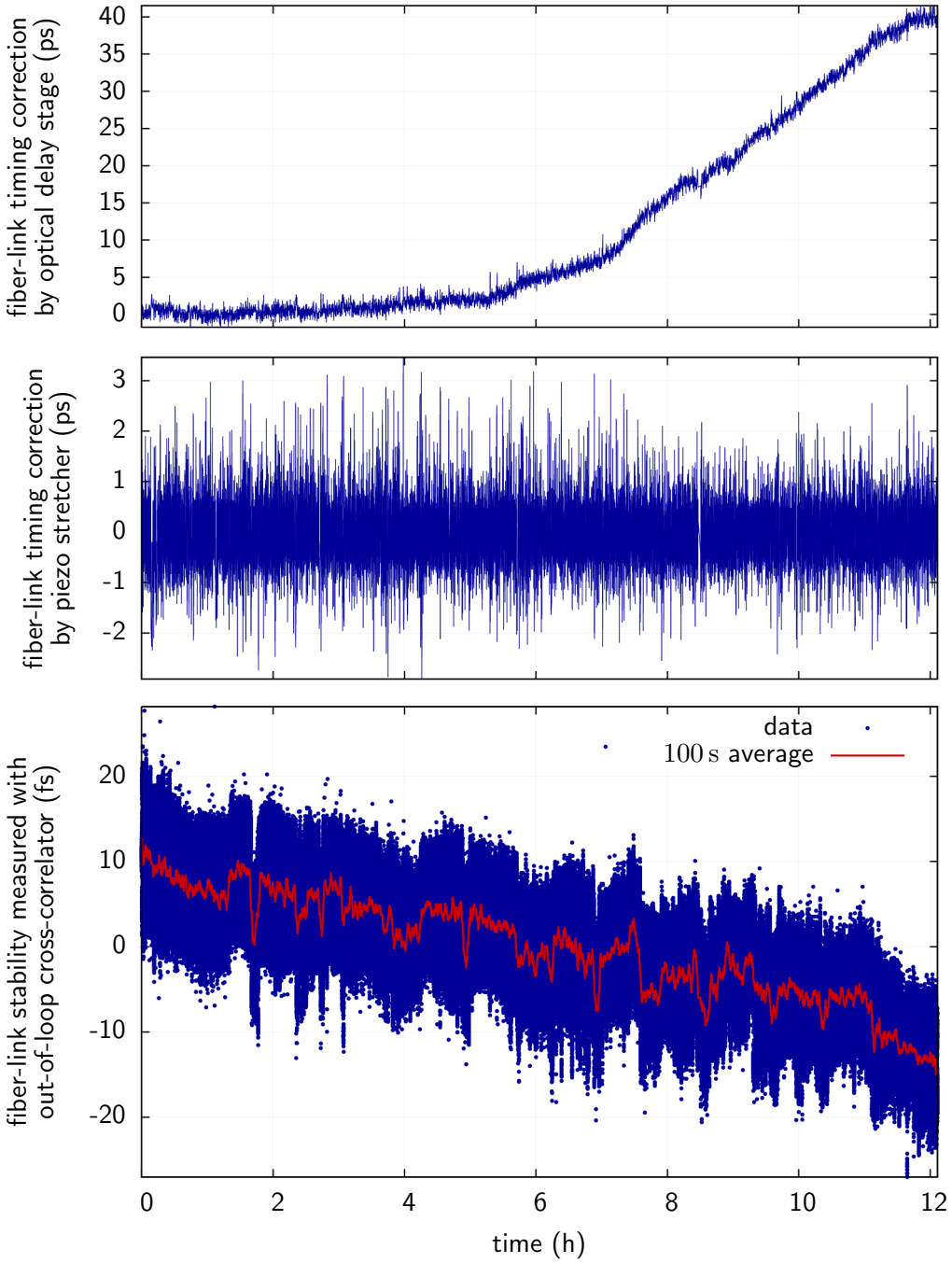

Figure 7.5: Measured short- and long-term stability of a 400 m long stabilized fiber-link. The fiber is installed around the circumference of an accelerator hall. Top: length correction by the optical delay stage. Center: length correction by the piezo fiber-stretcher. Bottom: Timing change after the fiber-link measured with the out-of-loop cross-correlator.

power entering the cross-correlator was reduced by 20%. The out-of-loop cross-correlator was not perfectly balanced and the observed timing drift could very well be a remaining amplitude dependence of the cross-correlator.

It is interesting to note that a timing correction of about 40 ps is required. The reason can either be a larger change of the laser frequency, or, more likely, thermal expansion of the fiber.

The temperature coefficient of an optical fiber has two contributions: The thermal expansion coefficient

$$\alpha_{\text{t-e}} = \frac{1}{L}\frac{\partial L}{\partial T}\,, \tag{7.1}$$

and the thermo-optic coefficient

$$\alpha_{\text{t-o}} = \frac{1}{n}\frac{\partial n}{\partial T}\,. \tag{7.2}$$

Both coefficients have contributions from the optical fiber itself and from the cladding material surrounding the fiber (see e.g. [LTMU89]). The timing change after the fiber-link with temperature is then given by

$$\frac{\mathrm{d}t}{\mathrm{d}T} \approx \frac{nL}{c}\left(\alpha_{\text{t-e}} + \alpha_{\text{t-o}}\right)\,. \tag{7.3}$$

In the last equation we neglect the fact that the group velocity inside a fiber is slightly different from the phase velocity. The thermal expansion coefficient of a standard silica-fiber of $\alpha_{\text{t-e}} < 10^{-6}$ [LTMU89] is small compared to the contribution from the thermo-optic coefficient, which is about $\alpha_{\text{t-o}} \approx 8\cdot 10^{-6}$ [LTMU89]. A timing change of 40 ps corresponds to a fiber-temperature change of about 2.5°C with the numbers given above. Such a temperature change is indeed realistic, as the fiber was installed along the windows of the accelerator hall and the measurement took place from midnight to noontime.

7.4 Fiber-links installed at FLASH

Two of the described fiber-links with lengths of around 230 m and 300 m have been installed at FLASH. One of them was operated for over 6 months. The experimental setup is very similar to the one depicted in Fig. 7.1. A modification is two additional motorized wave-plates which are installed in front of the collimator at the link entrance. They are used to adjust the polarization at the end of the fiber-link. This is required for bunch arrival-time monitors installed at the end of the fiber-links. The fiber-links are driven with the pulses from the 216.7 MHz MLO. The laser frequency is locked to the master oscillator of the machine.

Figure 7.6 shows the overall timing correction of the piezo-stretcher and the optical delay line which is required to stabilize the fiber-links. The first thing we notice is that the fast timing corrections we observed in Fig. 7.5 are not existing anymore.

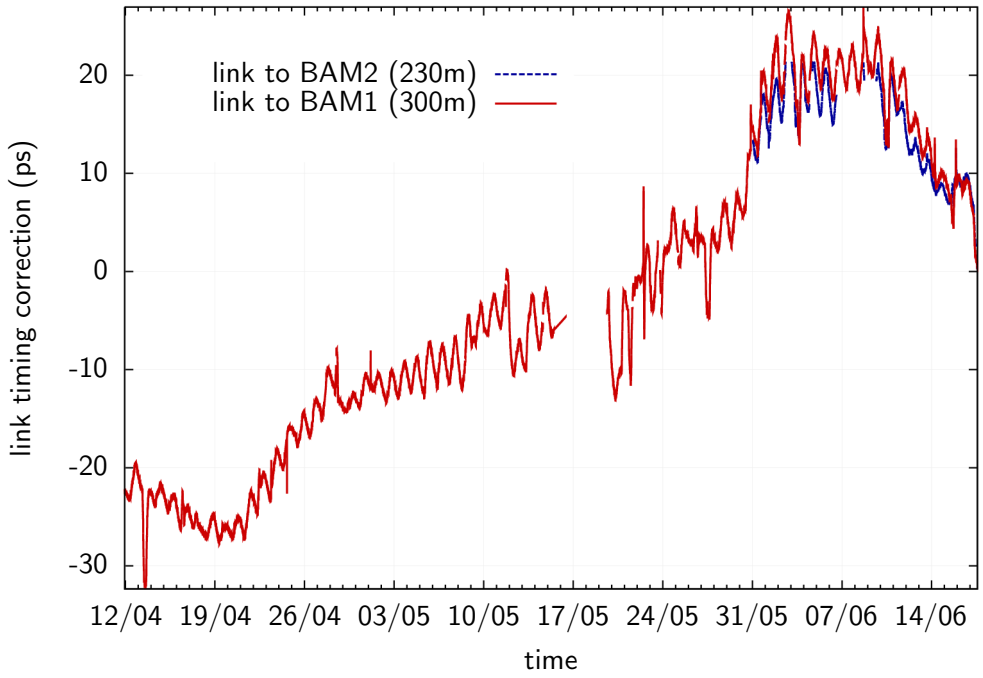

Figure 7.6: Required timing correction of two fiber-links installed at FLASH over a period of two months.

The reason is the stabilized laser frequency. Also the error signal of the feedback-loop was much smaller and the in-loop measurements gave a timing stability of the fiber-links of only 0.2 fs at a measurement bandwidth of 3 kHz.

Over about two months, more than 50 ps of timing correction was required. This is caused by a temperature increase of the tunnel between April and June. The temperature induced oscillations of the correction signal from day to night are also clearly visible.

An interesting observation was made after the installation of a new 1.3 GHz master oscillator. The correction signal of the fiber-links showed an oscillation with a period of about three minutes and the required timing correction is larger for the 300 m fiber-link than for the 230 m link (see Fig. 7.7). A possible explanation is a frequency oscillation of the master oscillator. A relative frequency change of about $\pm 4 \cdot 10^{-8}$ peak-peak would be required to explain the measured timing change of the fiber-links. Such a large frequency change exceeds the specified stability range of the oscillator of $1 \cdot 10^{-8}$. Since the MLO had to be disassembled, no further investigations on this topic were possible, but it is evident that the observed oscillation was not a problem of the optical synchronization system but is was also visible on the FEL pulse energy, when it was low (see Fig. 7.8). Further investigations on this topic are planned.

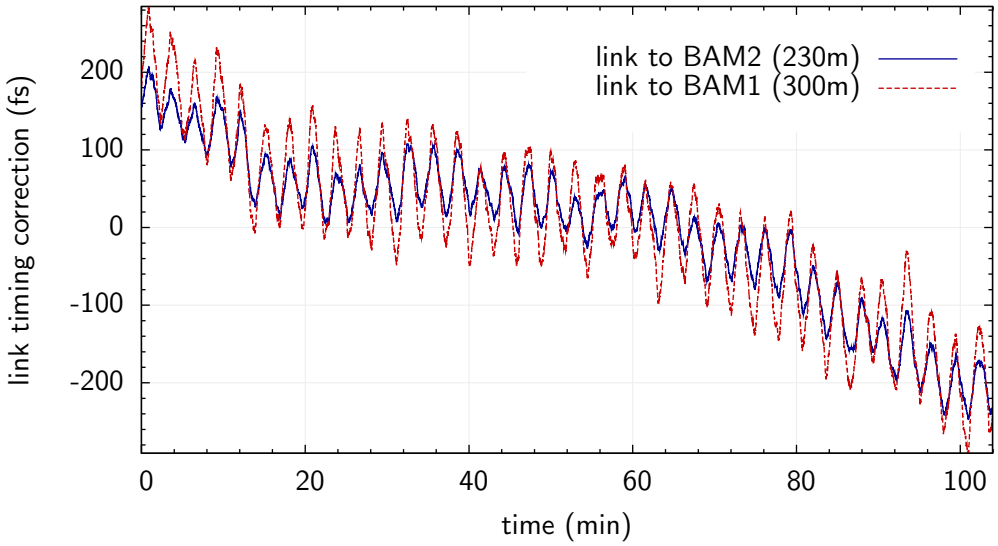

Figure 7.7: Short-term oscillation of the required link-timing correction of two fiber-links installed at FLASH. The oscillations appeared after a new 1.3 GHz master oscillator was installed.

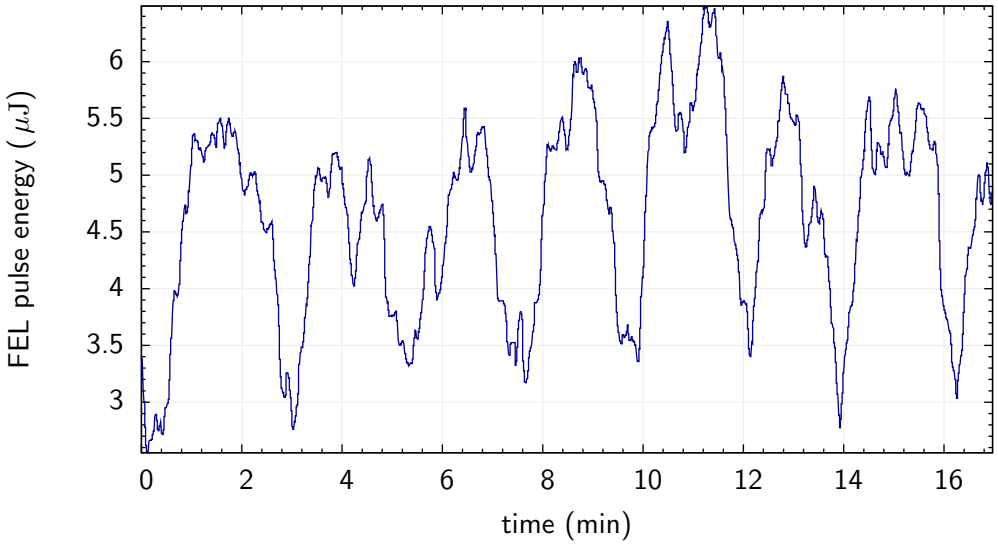

Figure 7.8: Short-term oscillation of the FEL pulse energy. The oscillations appeared after a new 1.3 GHz master oscillator was installed and when the FEL pulse energy was low.

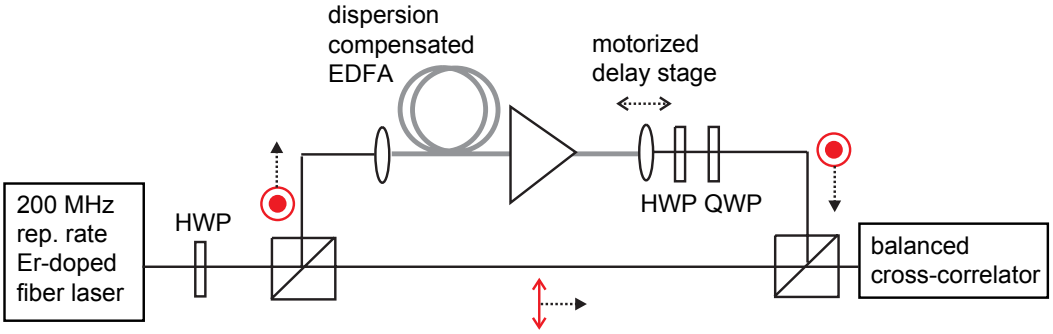

Figure 7.9: Experimental setup to characterize the influence of an EDFA on the timing stability of an optical pulse train.

7.5 Influence of erbium-doped fiber amplifiers on the timing stability of optical pulse trains

A key component of the optical synchronization system is the erbium-doped fiber amplifier (EDFA). These amplifiers are needed at many locations of the system and a complete chain from the laser to the component to be synchronized will contain three or more EDFAs. The first one will be installed after the distribution unit of the laser to provide sufficient laser intensity for the cross-correlator. A second EDFA is installed inside the fiber-link to compensate for losses in the fiber-link. A third one is installed after the link in order to provide sufficient laser power for the end-station. A careful characterization of the influence of the EDFAs on the performance of the synchronization system is important.

The balanced optical cross-correlator was utilized to measure the timing jitter added by an EDFA with sub-femtosecond resolution (see Fig. 7.9) [LAF+08a]. The 100 fs long laser pulses of a 200 MHz soliton laser are amplified by a counter-pumped EDFA. Since the cross-correlator requires short laser pulses, the EDFA was dispersion compensated. The timing jitter contribution of the EDFA was measured for various optical input-powers and different powers of the 974 nm pump light. Since the response of the cross-correlator depends on the intensity and pulse length of the incoming laser pulses, a new calibration of the detector was performed for every set of parameters.

Figure 7.10 shows the integrated timing jitter added by the EDFA in the frequency range from 500 Hz to 4.5 MHz. For a weakly pumped EDFA and optical input powers below 1 mW, the added timing jitter reaches up to 40 fs. Under optimized working conditions, the added timing jitter is around 0.5 fs (rms).

The gain fiber is not entirely saturated for weak pump powers and hence, absorption of the pulse train occurs. At large amplifications, the output pulse energies reach up to 0.5 nJ (100 mW output power). The laser pulses are distorted at these pulse energies due to nonlinearities inside the optical fiber (see Figs. 7.11 and 7.12) and intensity noise of the optical pulse train is converted into changes of the pulse

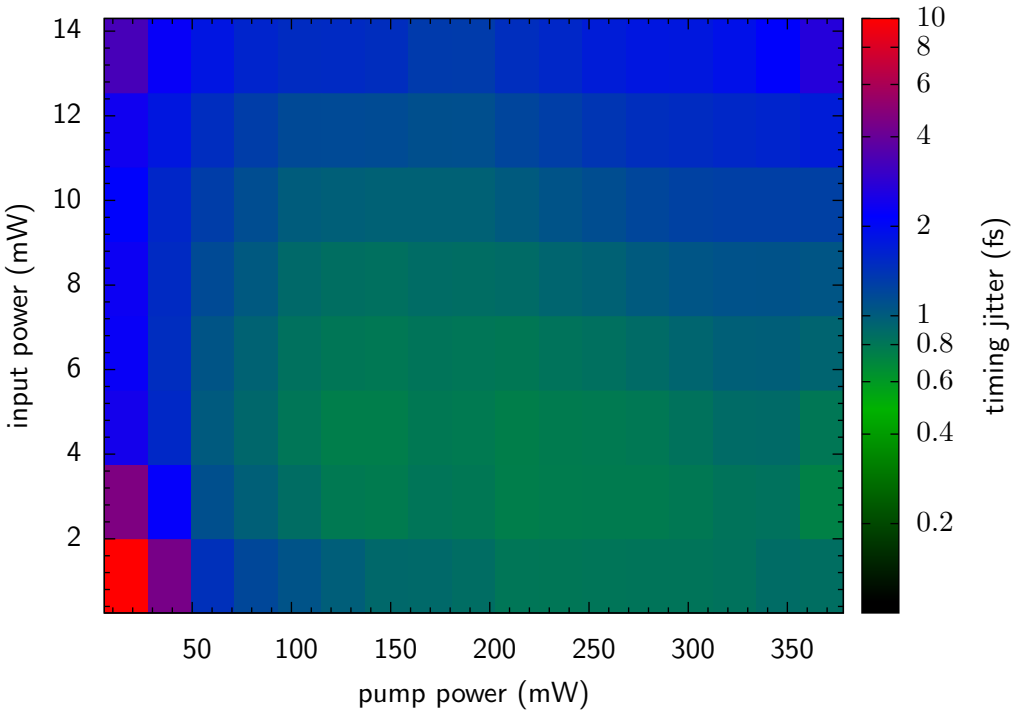

Figure 7.10: Timing jitter added to the optical pulse train by the EDFA measured in the frequency range from 500 Hz to 4.5 MHz.

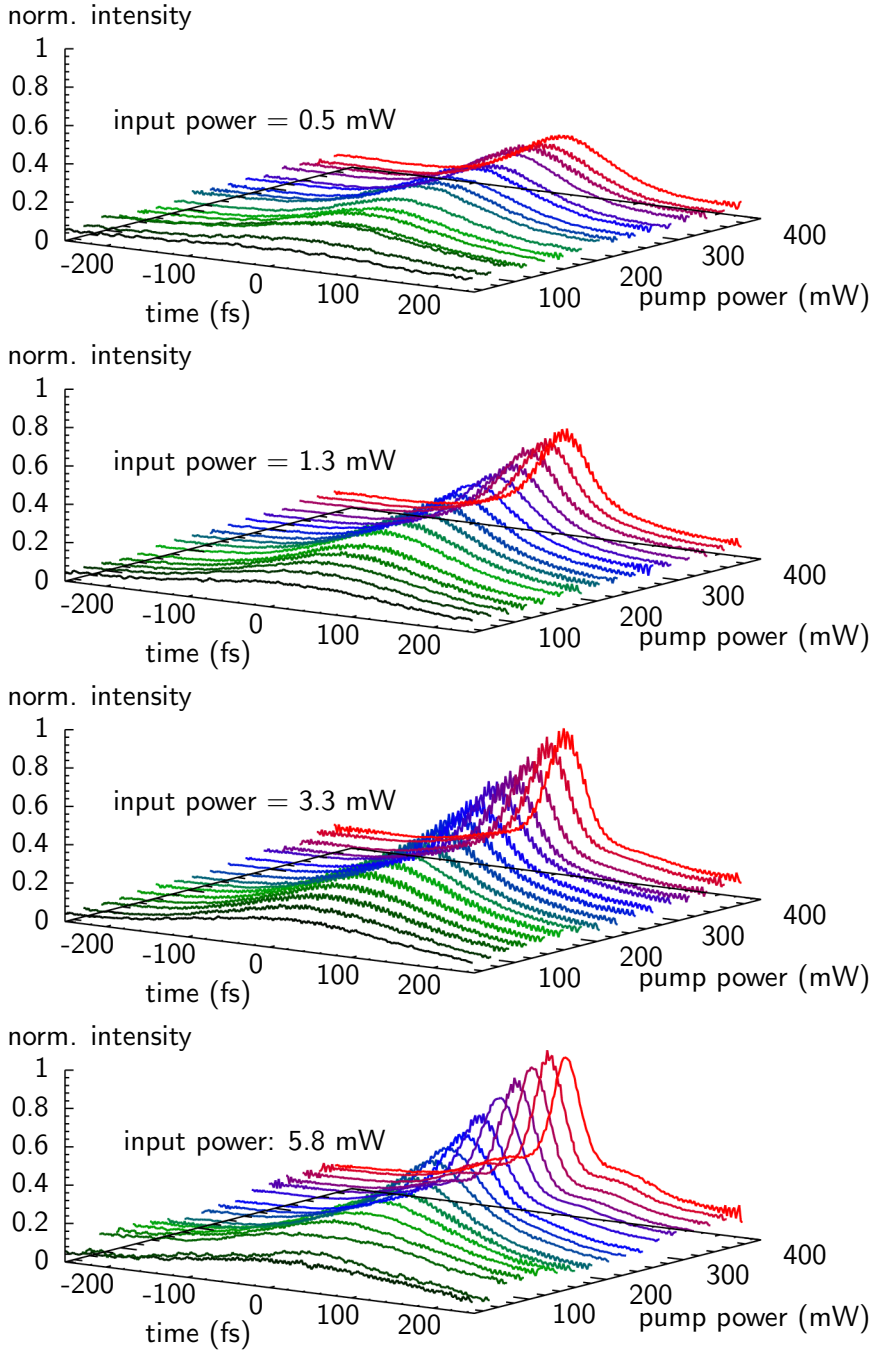

Figure 7.11: Autocorrelation traces of the amplified laser pulses for different optical input powers and different pump powers of the EDFA.

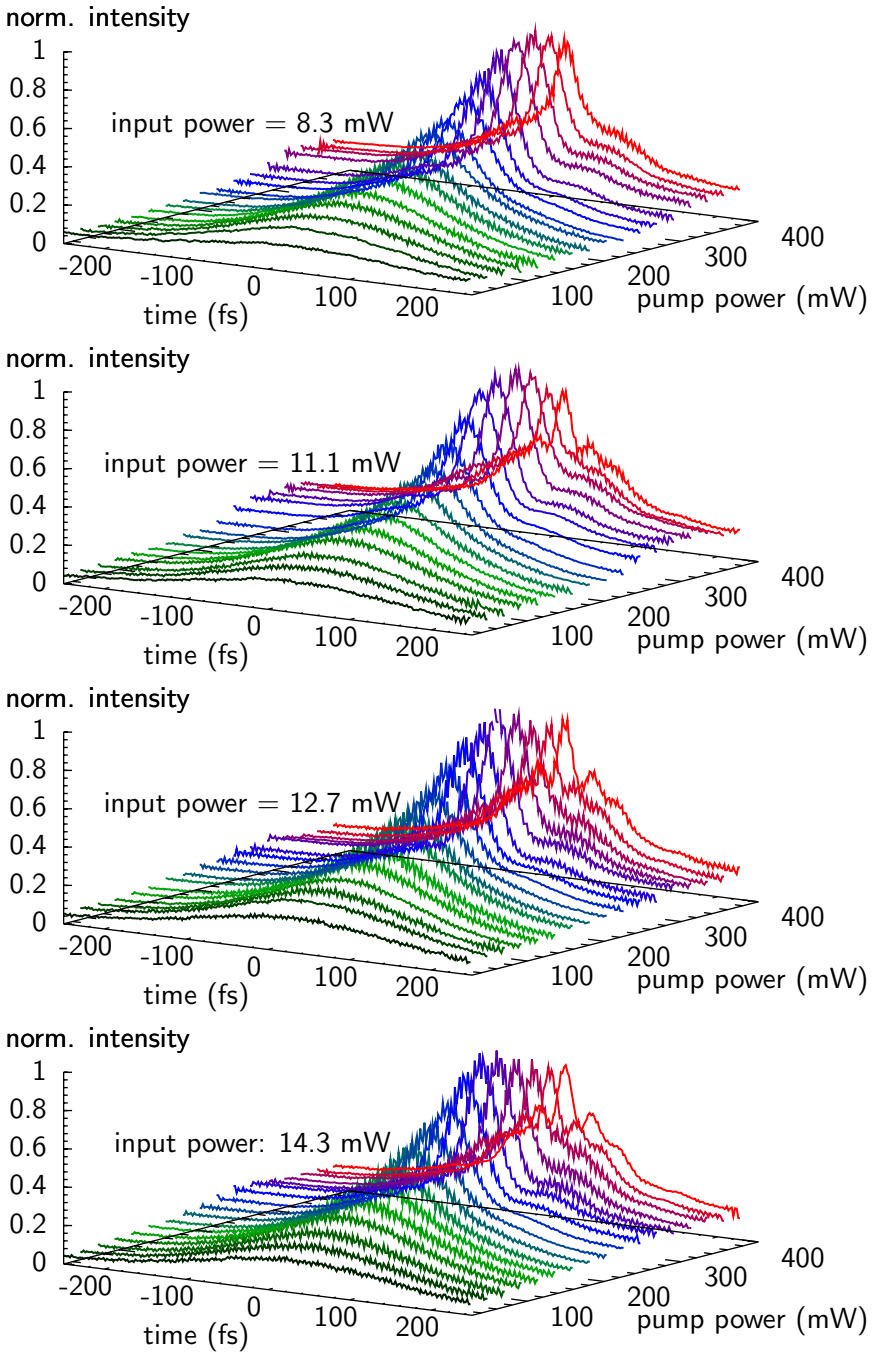

Figure 7.12: Autocorrelation traces of the amplified laser pulses for different optical input powers and different pump powers of the EDFA (continued).

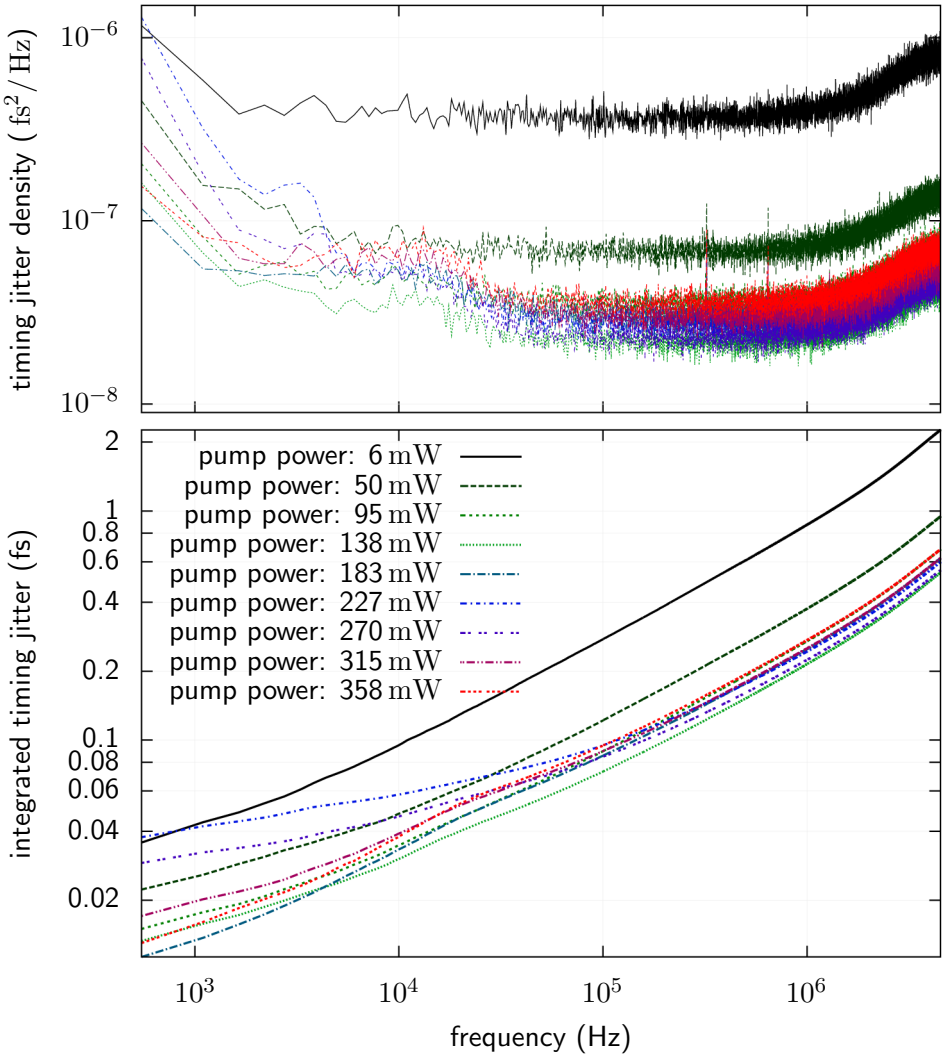

Figure 7.13: Top: timing jitter spectral density of the amplified laser pulses for different EDFA pump power settings and an optical input power of 3.3 mW. Bottom: integrated timing jitter added by the EDFA starting the integration at 500 Hz.

shape.

Figure 7.13 shows the spectral density distribution of the timing jitter added by the EDFA (top). An amplifier used after the photo-multiplier tubes of the balanced optical cross-correlator is responsible for the increasing timing jitter contribution above about 1 MHz. The bottom plot shows the integrated noise starting the integration at 500 Hz and in the frequency range below 1 MHz only 0.2 fs of timing jitter is added for optimized conditions.

7.6 Drift-free RF based timing detector

The fiber-link stabilization scheme presented above provides a very good stability. However, it is not easily possible to further distribute the timing information, which was transported to a remote location via a fiber-link, to additional devices nearby, without significantly deteriorating the timing stability. The reason is the above-mentioned change of the refractive index of the fiber with temperature.

When we consider a 20 m long standard single-mode fiber by which the timing signal is transmitted to another device, 1°C of temperature change would already shift the timing by around 800 fs (see Eq. 7.3), assuming the temperature coefficients mentioned above. This has the consequence that either, every device needs its own stabilized fiber-link, which is rather expensive, or, the length change of the short distribution fiber to the second device has to be precisely measured and, if needed, corrected for with an actuator. This requires an accurate timing detection, and in order to provide a cheap and simple alternative to the above described sub-femtosecond resolution optical cross-correlator, a long-term stable, high resolution RF based detection scheme was developed within this thesis. In a first prototype, realized within a diploma thesis [Zem08], the resolution and long-term stability of this detection scheme was measured to be better than 20 fs.

Conventional RF based timing detection schemes for measuring temporal changes between two optical pulse trains use two photo-detectors, one for each pulse train, to generate an electrical signal from the light pulses. From each photo-detector signal a high harmonic of the laser repetition rate is selected with a band-pass filter. These signals are amplified and a phase detection between both signals is performed, typically in a microwave mixer. This concept has a couple of limitations deteriorating its long-term stability. The first one is the dependence of the phase of the selected harmonic on the laser amplitude and the temperature of the photo-detector. Since two different photo-detectors are used, this can cause a relative time shift between both signals. Another limitation comes from a temperature dependence of the band-pass filters. A temperature change leads to a phase change of their output signal, which due to two different filters again leads to a relative timing shift between both signals. Finally, the mixer output signals depends on the mixer temperature and temperature changes are misinterpreted as changes of the relative timing between both pulse trains.

To overcome these long-term stability limitations, the scheme depicted in Fig. 7.14

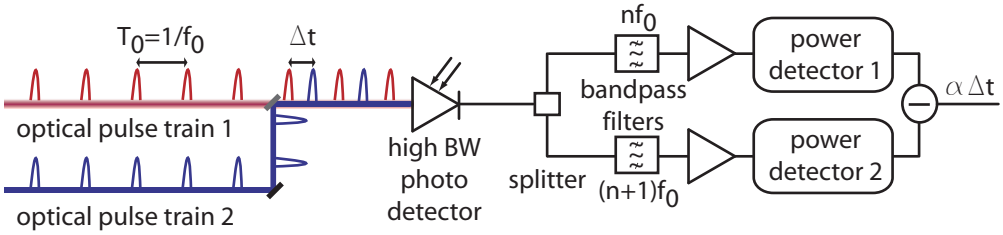

Figure 7.14: Schematic setup of the RF based timing detector. Two optical pulse trains are guided onto the same photo detector and the power levels at two different harmonics of the laser repetition rate are measured. Due to interference of the RF signals, the power levels in the harmonics change with variations of the temporal offset Δt between both pulse trains. From the difference signal of both power levels, variations of Δt can be deduced without being deteriorated by laser amplitude changes.

was developed. The two laser pulse trains are combined and guided onto the same photo-detector. When the laser pulses have a temporal offset Δt, the RF spectrum from the photo-detector is modulated. The reason is that the contributions from both pulse trains to the n-th harmonic of the laser repetition frequency f_0 have a relative phase shift of $\phi(nf_0) = 2\pi n f_0 \Delta t$, so they interfere with each other.

Figure 7.15 shows an example of this interference for two different values of Δt. The power levels of the spectral lines changes due to variations of Δt and when we consider the last two frequency lines in the bottom plot of Fig. 7.15 ($f = 22f_0$ and $f = 23f_0$), the power levels of these lines react in opposite directions when Δt is changed. Changes of the laser amplitudes, however, have the same effect on both spectral lines. By measuring the difference of two spectral lines of equal power levels, we can measure timing changes without being dependent on laser amplitude changes.

Figure 7.16 shows the difference signal between the power levels of the spectral lines with $f = 22f_0$ and $f = 23f_0$ as a function of the temporal offset Δt. The signal has the highest slope at the zero crossings and for a temporal offset near $\Delta t = 1/2 \cdot T_0$. This temporal offset is the ideal choice for the timing measurement.

Since the detection scheme uses only a single photo-detector to measure both pulse trains, temperature changes of the detector do not affect the measurement anymore, as the effect is identical for both pulse trains. Also a temperature induced phase shift from the band-pass filters does not influence the measurement, since only the power levels of the spectral lines are detected. By taking the difference signal between two adjacent frequency lines, also the dependence on the laser amplitude can be suppressed.

Figure 7.17 shows a measurement from [Zem08], where the long-term stability of the detector was investigated. For this, the pulse train of the laser was split and the two pulse trains were guided onto the photo-detector with a temporal offset near $\Delta T \approx T_0/2$. In order to get a high resolution, the measurement scheme was realized at the 44-th and 45-th harmonic of a 216.7 MHz laser. An rms stability of 19 fs over

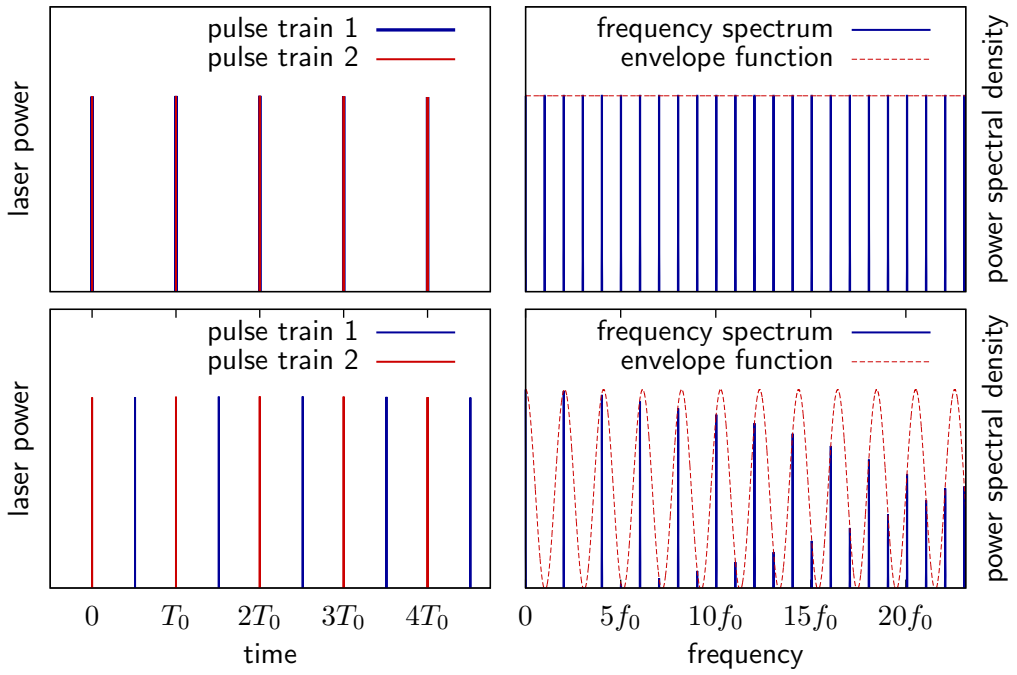

Figure 7.15: Superposition of two optical pulse trains (left) and corresponding power spectral density of the photo-detector signal (right). Top: the pulses from both pulse trains have temporal overlap. Bottom: The temporal offset between both pulse trains is $\Delta t \approx 0.49 \cdot T_0$.

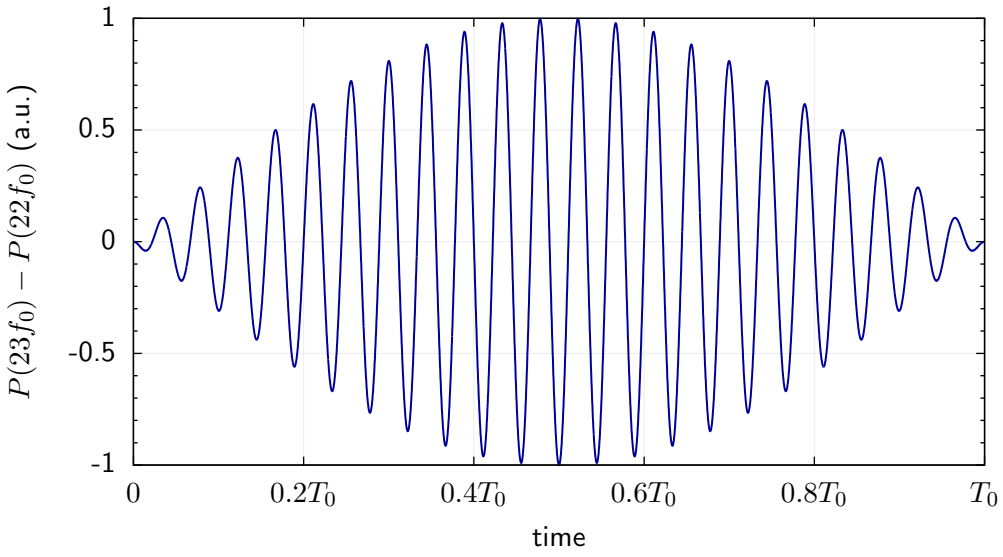

Figure 7.16: Difference signal between the power levels of the 22$^{\text{nd}}$ and 23$^{\text{rd}}$ harmonics of the laser repetition rate as a function of the temporal offset Δt.

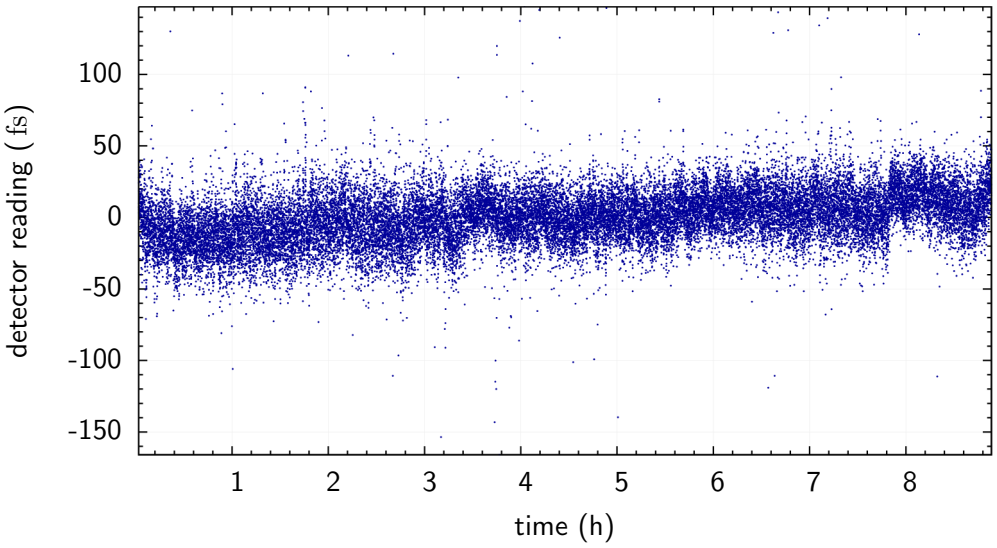

Figure 7.17: Long-term stability of the RF based timing detector, measured by splitting the laser output and by delaying the two signals by $\Delta T \approx T_0/2$ before sending both signals onto the same photo-detector. Over about 9 hours, the rms stability of the detector is 19 fs. The measurement is from [Zem08].

about 9 hours was achieved.

As expected, the resolution of this scheme is significantly lower than the one from the optical cross-correlator. However, the scheme is cheaper and much easier to realize, since the detector is not polarization dependent and not very sensitive to the laser pulse duration unless the pulses become long enough so that the selected frequency components start to decrease significantly.

It is planned to use this scheme for the synchronization of devices at FLASH which do not require the ultimate performance of the cross-correlator based stabilization scheme.

8 Bunch arrival-time monitor

In order to take full advantage of the short electron bunches and the resulting short photon pulse durations on the order of 10 fs and below, arrival-time measurements of the electron bunches with the same 10 fs precision are required. The precise knowledge of the bunch arrival-times can be utilized to improve the resolution of pump-probe experiments by sorting the events according to their measured arrival-times. Furthermore such a precise arrival-time detection allows identifying sources of the jitter and finally stabilizing the arrival-time of the electron bunches by using the measurements as an input for an arrival-time feedback.

Previous arrival-time monitors like the electro-optic methods described in chapter 3 have so far only been demonstrated to provide resolutions of about 60 fs rms [Cav05]. This resolution is dominated by the accuracy of the RF based laser synchronization. The electro-optic methods described in chapter 3 use Ti:Sapphire lasers which are expensive and require continuous maintenance thus making the systems unsuitable as online monitors. Furthermore, the measurement frequency is limited to a few Hertz due to the data acquisition with a gated camera and hence only the arrival-time of a single bunch out of the bunch-train can be measured. Many experiments, however, require the knowledge of all arrival-times along the bunch train.

In the course of this thesis, a bunch arrival-time monitor (BAM) has been developed which uses the laser pulses of the optical synchronization system. Thereby, additional sources of jitter are avoided. Furthermore, the arrival-time information can be distributed with high stability to different locations in the accelerator.

A first prototype of the arrival-time monitor used a ring-type beam pick-up whose signal was sent through a 30 m long cable to an electro-optic detection scheme. The final system uses a button-type beam pick-up, and the electro-optic detection takes place directly at the pick-up. By this, the resolution of the final system is almost an order of magnitude better than in the prototype.

8.1 Principle of the arrival-time monitor

A schematic of a first BAM prototype is shown in Fig. 8.1. The pulse train of a 40.625 MHz stretched pulse laser is split and guided into two electro-optical amplitude modulators (EOMs). The EOMs have a bandwidth of around 20 GHz and they consist of a Mach-Zehnder interferometer. Inside the EOM, the laser signal is split and travels through two waveguides which contain a lithium niobate crystal ($LiNbO_3$). In the presence of an electrical field, $LiNbO_3$ becomes birefringent. An RF signal is applied to the two waveguides with opposite polarity and the resulting

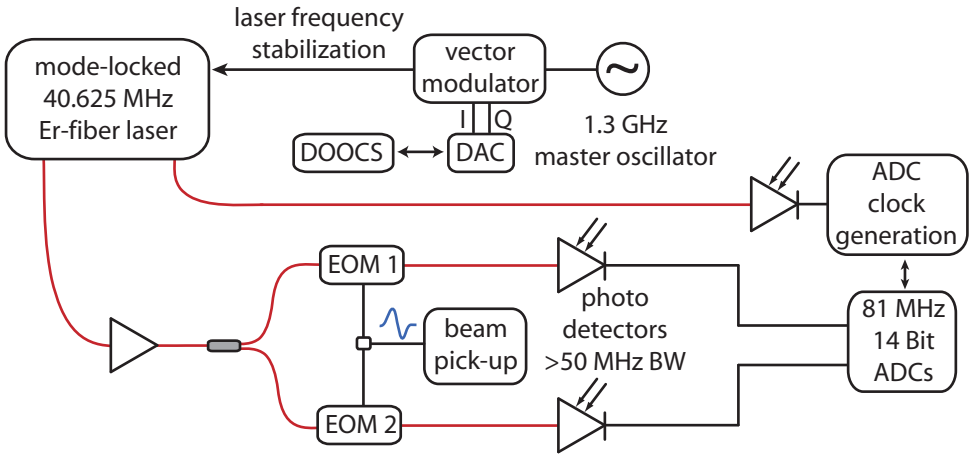

Figure 8.1: Schematic setup to measure the arrival-time of the beam pick-up signal.

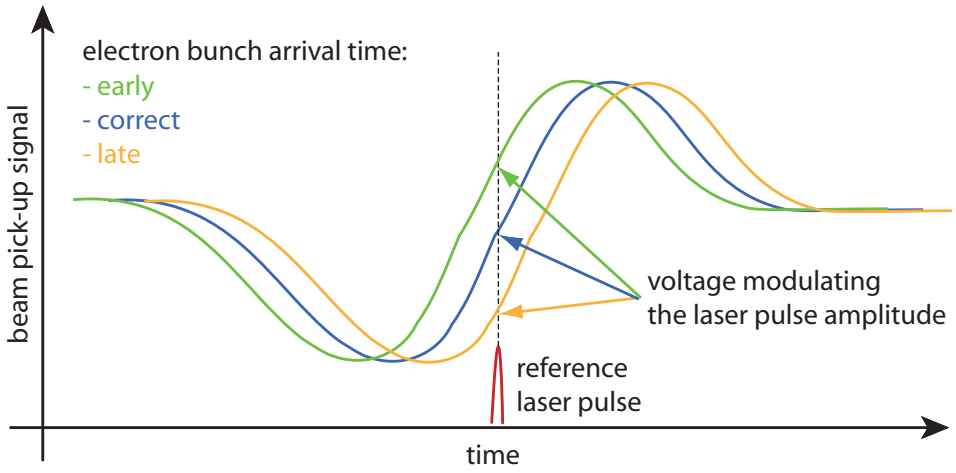

Figure 8.2: Operation principle of the bunch arrival-time monitor.

birefringence causes a phase shift between the laser pulses in both waveguides. By recombining the two laser pulses, this phase shift is translated into an amplitude modulation of the output laser pulse train.

The modulation voltage is derived from the signal of a beam pick-up with a bandwidth of several GHz. An electron bunch passing the pick-up induces a voltage signal, the shape of which is determined by the time derivative of the electron bunch charge density folded with the beam pick-up response. The zero-crossing of this voltage signal is a measure of the bunch centroid arrival-time.

The laser is locked to the 1.3 GHz reference signal of the machine and a vector modulator allows shifting the timing between the laser and the machine reference. This allows scanning the laser pulse over the signal from the beam pick-up.

The timing of the laser pulse train is adjusted such that one laser pulse coincides with the zero-crossing of the beam pick-up signal (see Fig. 8.2). This laser pulse defines the reference time, and timing changes of the electron bunches with respect to this reference lead to a different modulation voltage seen by the pulse. By this, the arrival-time of the electron bunch is encoded onto the laser pulse amplitude. The laser pulse energy is detected with a photo-detector and digitized with a fast ADC. The ADC is clocked at twice the repetition rate of the laser in order to provide the possibility to sample the signal and the baseline. Since the signal from the photo detector has a width of only ~ 3 ns, the detection of the laser amplitude is sensitive to a jitter of the ADC clock. To minimize this jitter, the ADC clock is generated directly from the laser by feeding the second harmonic of the laser repetition rate into a limiting amplifier. The resulting ADC clock has a timing jitter of less than 1 ps rms. With this setup, the pulse energy of the modulated laser pulse can be determined with an accuracy of about 0.2–0.4%.

8.2 Arrival-time measurements with a ring-type beam pick-up

In the first series of measurements, a ring-type beam pick-up was used. A schematic of the pick-up is shown in Fig. 8.3. It consists of a thin metal ring with an inner diameter of 34 mm. The beam induced transient signal is coupled out using two feed-throughs mounted in opposite directions in the horizontal plane. After 30 m of cable, the signal has a peak-to-peak voltage of more than 30 V and a bandwidth of more than 5GHz. At the zero-crossing position, the slope is 0.25 V/ ps.

The maximum modulation voltage of the EOMs is ± 5 V. In order to prevent damage of the EOMs, a limiter with a bandwidth of 26 GHz is installed. Figure 8.4 shows the pick-up signal after 30 m of cable and behind the limiter, measured with an oscilloscope with 8 GHz analog bandwidth. Using the vector modulator, the sampling laser pulse was shifted over the beam pick-up signal. The bottom plot of Fig. 8.4 shows the laser pulse energy at different sampling positions along the beam pick-up signal. The shape of the beam pick-up signal is mapped inversely onto the pulse energy. At large negative beam pick-up voltages the pulse energy is increased to a

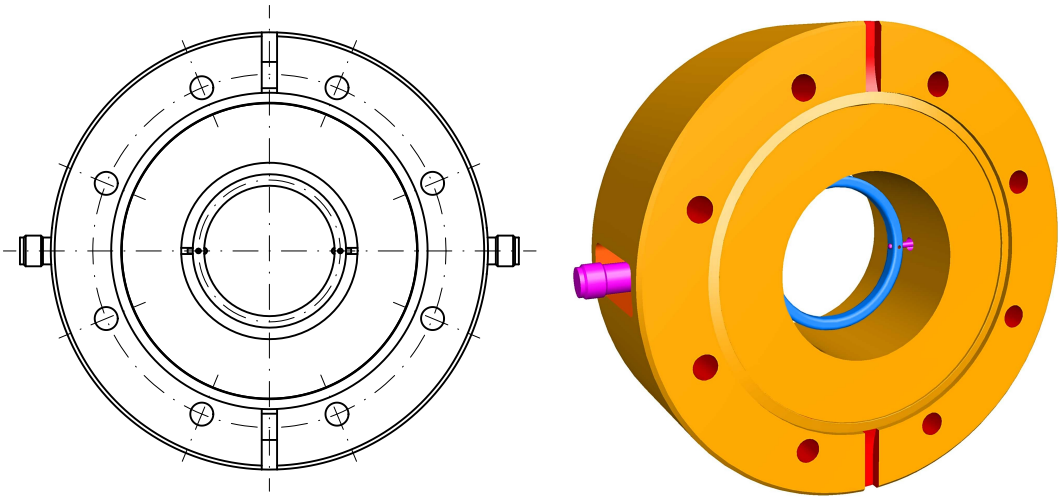

Figure 8.3: Technical drawing and 3D model of the ring-type beam pick-up used for the bunch arrival-time measurements.

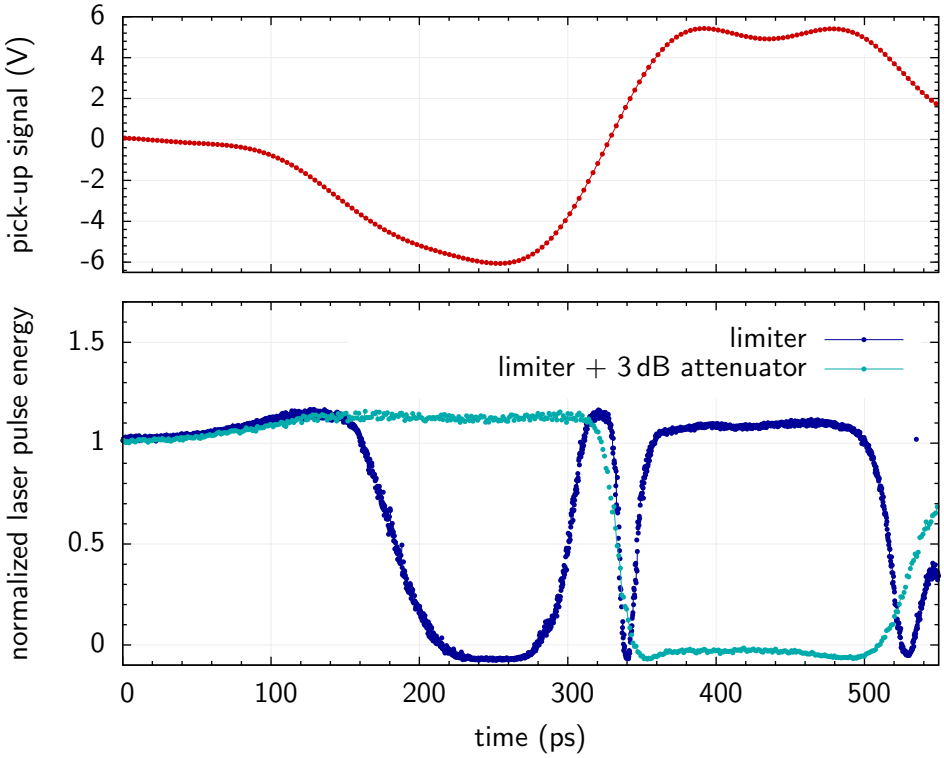

Figure 8.4: Signal of the ring-type beam pick-up limited to ±5 V and measured with an oscilloscope with 8 GHz analog bandwidth (top). The bottom plot shows the measured laser pulse energy at different sample positions along the beam pick-up signal, with and without attenuation by 3dB.

level where the photo detector saturates. Without attenuation of the beam pick-up signal, the phase shift in the two waveguides of the EOM becomes larger than 180°, yielding over-rotation.

The arrival-time measurement is performed at the zero crossing of the beam pick-up signal, corresponding to a time of about 330 ps in Fig. 8.4. Here, the transient signal has the steepest slope and a variation of the bunch charge changes the slope but the zero-crossing position remains constant. In order to ensure that the laser pulses always sample the pick-up signal near the zero-crossing, time changes of the electron beam are compensated for by a slow feedback acting on the vector modulator (VM). The arrival-time of the electron beam is then composed of the VM setting and the arrival-time change predicted from the laser pulse energy.

In order to reduce the sensitivity to external perturbations and to laser pulse energy variations, the analysis steps depicted in Fig. 8.5 are applied. From the ADC raw data (top), first the laser pulse energy is calculated (center). In the figure, an oscillation of the pulse energy is visible long time after the last electron bunch arrived. This modulation comes from ground currents generated by the klystrons driving the accelerating cavities. Since these disturbances may also occur during the electron bunch trains, the energy of each laser pulse is normalized to the energy of the previous laser pulse (see bottom plot). This correction acts as a high pass filter and all external disturbances and variations of the pulse energy, occurring on a longer time scale than the duration between two laser pulses, are strongly suppressed.

8.2.1 Determination of the resolution of the BAM prototype

The resolution of the arrival-time detection is determined by the accuracy with which the laser pulse energy can be measured and by the BAM calibration factor, which is the conversion factor between pulse energy and arrival-time. The calibration factor is determined by sampling the slope of the beam pick-up signal around the zero-crossing. Typical values in this first prototype setup are around $S = 80\,\mathrm{fs}/\left(0.01\frac{\Delta E}{E}\right)$, when the unattenuated beam pick-up signal is used. The accuracy of the laser amplitude detection of $\sigma_E = 0.2$–0.4% is degraded by a factor of $\sqrt{2}$ due to the normalization. This results in a resolution σ_t of the detector of

$$\sigma_t = \sqrt{2}\sigma_E \cdot S \approx 23\,\mathrm{fs}\,\mathrm{to}\,45\,\mathrm{fs}\,. \tag{8.1}$$

In order to validate the resolution expected from the BAM calibration factor and the noise on the pulse energy measurement, the beam pick-up signal was split and connected to the two EOMs (see Fig. 8.1). The splitting reduces the amplitude of the bipolar pick-up pulse and, therefore, reduces the resolution. The resolutions of the two arrival-time detectors expected from the calibration factors and the laser pulse energy noise are 99 fs and 88 fs, respectively. Figure 8.6 shows the arrival-times measured by both detectors for a long sequence of electron bunches. Both detectors show a slow, almost periodic oscillation of the arrival-time. The difference of the two signals has an rms width of 126 fs which is in good agreement with the expected $132\,\mathrm{fs} = \sqrt{99^2 + 88^2}\,\mathrm{fs}$.

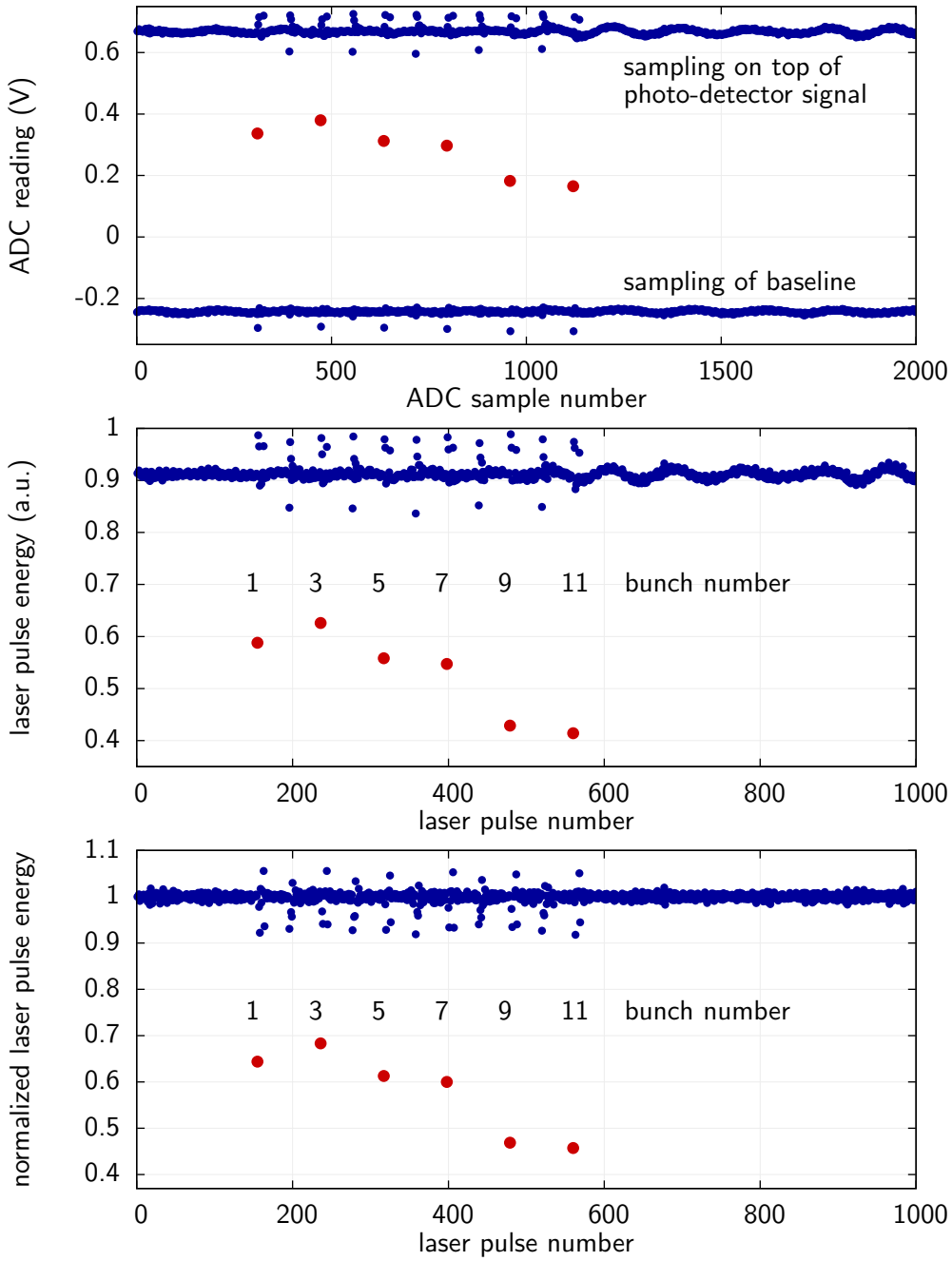

Figure 8.5: Analysis steps to determine the energy of the modulated laser pulses. From the ADC reading (top), the laser pulse energies (center) are calculated which are then normalized to the pulse energy of the previous laser pulses (bottom). The modulated laser pulses near the zero-crossing of the beam pick-up signal are shown in red. With the 40.625 MHz laser, only every second bunch in the bunch train can be measured.

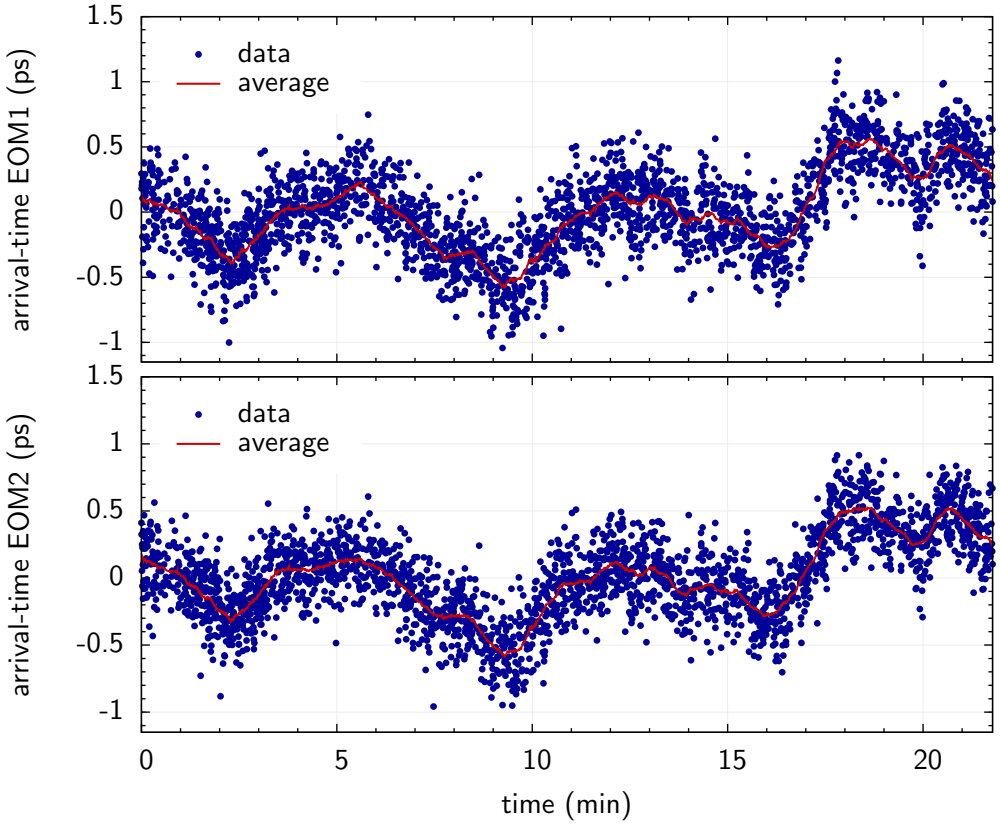

Figure 8.6: Arrival-time determination of the zero-crossing of the pick-up signal: The pick-up signal was split and connected to two EOM arrival-time detectors.

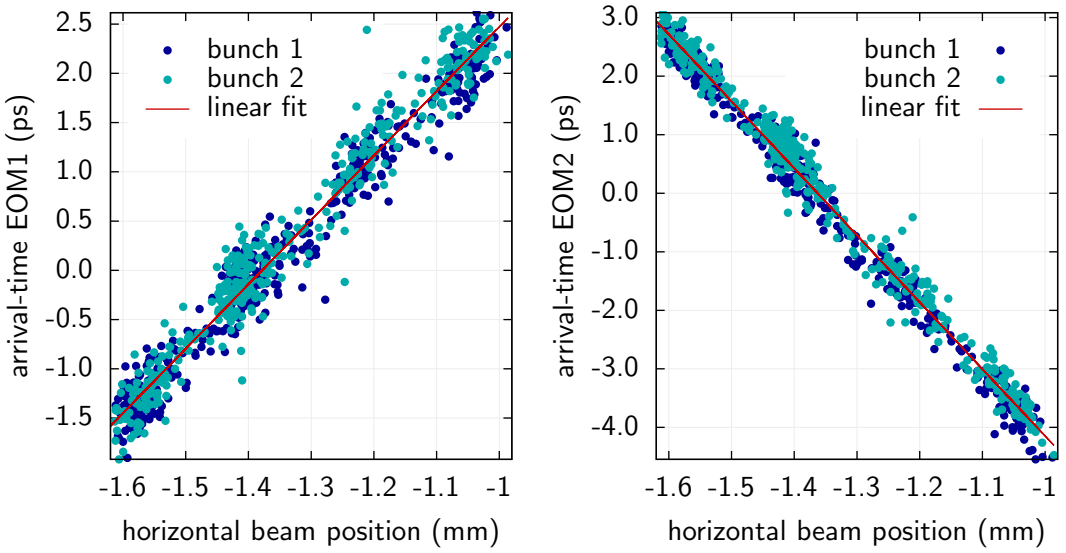

Figure 8.7: Dependence of the arrival-times of the zero-crossings from the two signals of the ring-type beam pick-up on the horizontal beam position.

8.2.2 Orbit dependence of the beam pick-up signal

In an attempt to improve the resolution of the detectors, the two outputs on opposite sides of the beam pick-up were connected to the two independent EOMs. In this configuration, the expected resolutions amount to 33 fs for both EOM detectors. The difference signal between the two detectors, however, was found to have an rms width of more than 1.5 ps. The explanation is that the zero-crossing of the beam pick-up signal depends on the transverse position of the electron beam. This dependence was experimentally investigated (see Fig. 8.7) by changing the horizontal and vertical beam orbit with corrector coils by ± 0.3 mm, yielding an orbit dependence of the two detector signals of

$$\begin{aligned} a_{x,1} &= (6.94 \pm 0.05)\frac{\text{fs}}{\mu\text{m}} \quad a_{x,2} = (-10.7 \pm 0.02)\frac{\text{fs}}{\mu\text{m}} \\ a_{y,1} &= (0.16 \pm 0.07)\frac{\text{fs}}{\mu\text{m}} \quad a_{y,2} = (-0.29 \pm 0.02)\frac{\text{fs}}{\mu\text{m}}\,. \end{aligned} \tag{8.2}$$

With these values, the arrival-time t can be calculated from the times t_1 and t_2 measured at the two EOM detectors and the independently measured beam positions x and y according to

$$t = t_1 + a_{1,x}x + a_{1,y}y \tag{8.3}$$

$$t = t_2 + a_{2,x}x + a_{2,y}y. \tag{8.4}$$

After applying these corrections, the rms width of the difference signal between the two phase detectors is reduced to 300 fs which is dominated by the limited resolution of the beam position monitors (BPMs) of around 20 μm.

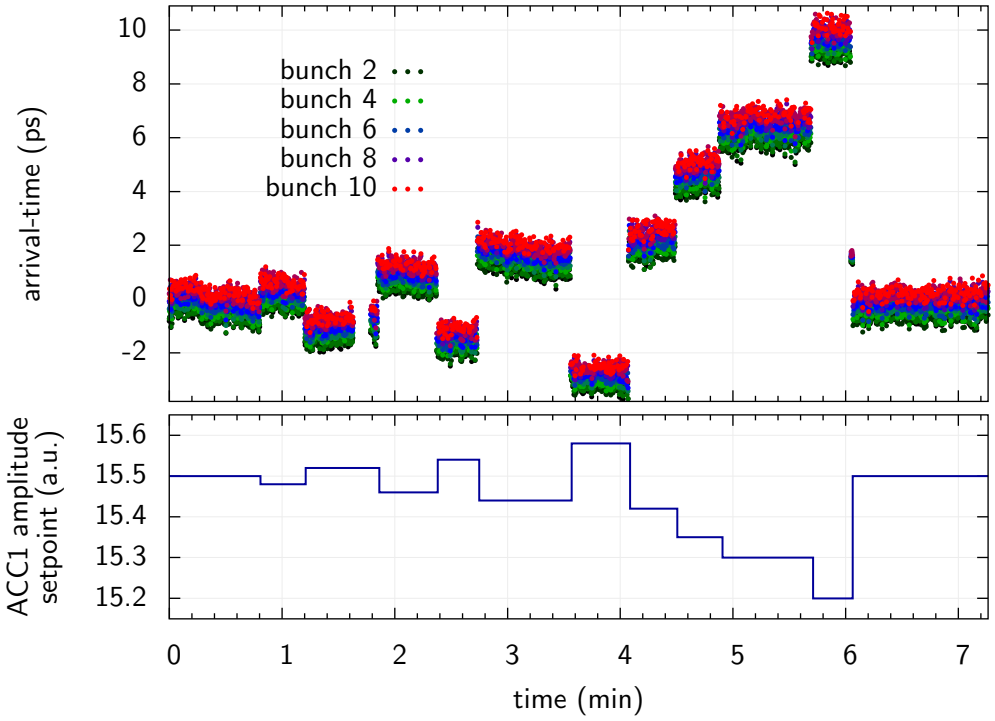

Figure 8.8: Electron bunch arrival-time for different settings of the ACC1 field amplitude. The different colors denote different bunches in the train (black: bunch 1, red: bunch 10).

Both outputs of the beam pick-up necessarily see the same beam arrival-time. This offers the possibility of determining the horizontal beam position very accurately:

$$x = \frac{t_2 - t_1 + (a_{2,y} - a_{1,y})y}{a_{1,x} - a_{2,x}}. \tag{8.5}$$

Using the errors given above and assuming a vertical orbit change of less than $\pm 100\,\mu$m, this results in a resolution for the horizontal beam position of $3\,\mu$m over a 1 mm range.

This can be considered as a proof-of-principle for the planned beam position monitors in the bunch compressor chicanes. They will use the same arrival-time measurement technique but a different beam pick-up to achieve sub $5\,\mu$m resolution over a 10 cm aperture [HLS06].

8.2.3 Arrival-time measurements of the electron bunches

The precise beam position information (see Eq. 8.5) can be used to calculate the arrival-times with much higher precision than by using the BPM read-outs. Error propagation yields an rms timing error of 27 fs.

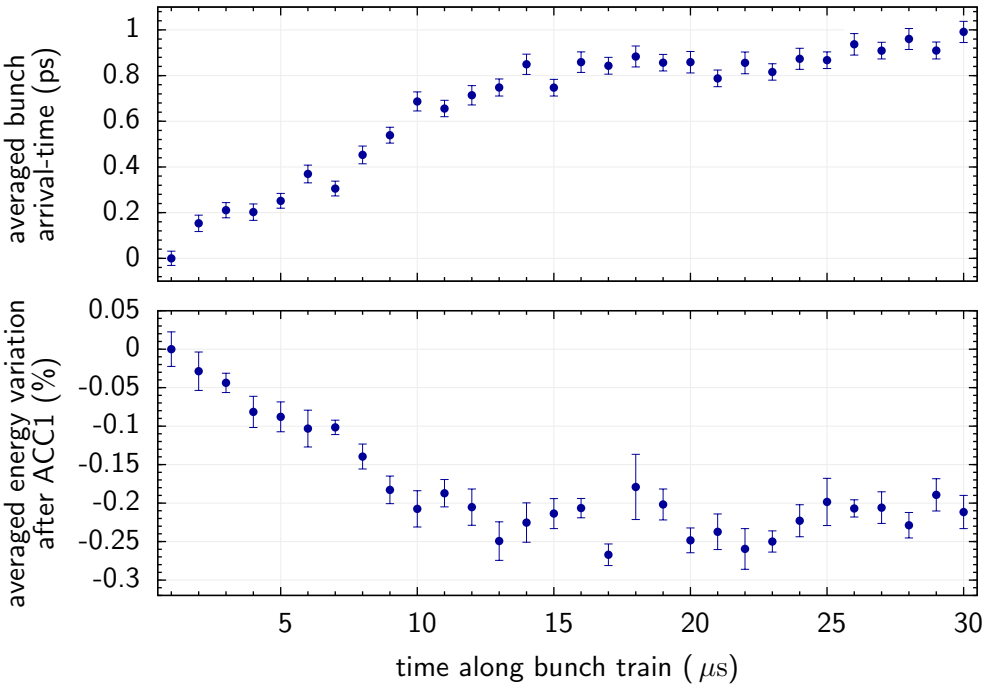

Figure 8.9: Comparison of the averaged arrival-time at the end of the accelerator and the energy variation along the bunch train downstream of ACC1.

Figure 8.8 shows an example of a position-corrected arrival-time measurement. Arrival-time changes have been produced by varying the accelerating voltage in ACC1. The different colors denote different bunches along the bunch train. The measurement is in good agreement with the expected arrival-time changes. In addition, the measurement shows that there is a systematic arrival-time difference of about 1 ps between the first and the last bunch inside a bunch train. This is caused by not fully compensated beam loading in the cavities. The first bunches remove energy from the accelerating field and if this energy loss is not fully replenished, the next bunches experience a lower field amplitude and gain less energy. In the bunch compressors, the lower energy is translated into a later arrival-time.

The rms arrival-time jitter of the bunch trains is about 200 fs. The relative rms jitter of the timing between two adjacent bunches inside the same train is between 40 to 60 fs.

Figure 8.9 shows a comparison between the average arrival-time measured by a BAM system at the end of the machine and the average energy deviation derived from the signal of a synchrotron radiation monitor [Ger07] in the first bunch compressor. A large energy slope in the first part of the bunch train is visible which is again due to uncompensated beam loading in the cavities. This energy change along the bunch is transformed inside the bunch compressor chicanes into arrival-time differences. The observed energy change of 0.2% along the train corresponds to an arrival-time change

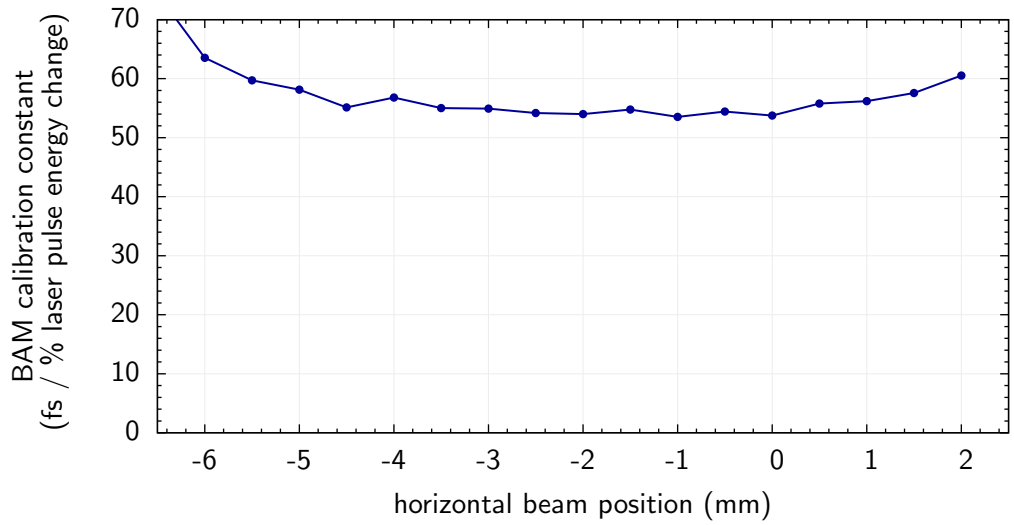

Figure 8.10: Change of the BAM calibration constant with the horizontal beam position. The ring-type beam pick-up is used with combined outputs.

of 1.2 ps, assuming an $R_{56} = -180$ mm for BC1. This is in reasonable agreement with the BAM measurement of 1 ps.

8.2.4 Reduction of the orbit dependence of the beam pick-up

Although it is possible to simultaneously measure the horizontal beam position and the bunch arrival-time as described above, the large orbit dependence of the beam pick-up signal requires the use of two arrival-time detectors, one for each port of the beam pick-up. Furthermore, precise calibration factors for the position dependence are required over a large range of beam positions, in order to provide reliable measurements.

The large horizontal orbit dependence can be significantly reduced by combining the two opposite pick-up signals in a broadband resistive network. The position dependence of the combined signal is reduced to

$$a_x = (-0.190 \pm 0.022)\frac{\text{fs}}{\mu\text{m}} \quad a_y = (-0.060 \pm 0.032)\frac{\text{fs}}{\mu\text{m}}\,. \tag{8.6}$$

In the horizontal plane, the orbit dependence is reduced by a factor of 30 to 50 compared to the situation without a combiner.

When the combined signal is used, the BAM calibration constant shows very little orbit dependence (see Fig. 8.10).

In the measurements presented in this section, the pick-up signal was guided to the EOM by a 30 m long cable. This cable attenuates the high frequency components of the signal and leads to a signal broadening which is increased further by dispersion. Furthermore, the cable length changes with temperature introducing unknown drifts in the arrival-time.

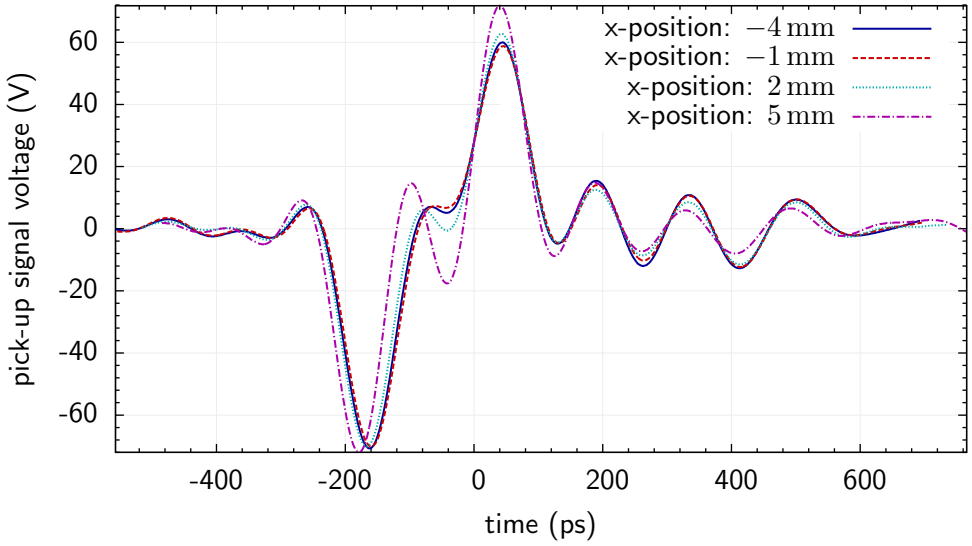

Figure 8.11: Signal shape of the ring-type beam pick-up for different horizontal beam positions. The two outputs of the pick-up are combined and the measurement was performed with an oscilloscope with 8 GHz analog bandwidth installed next to the pick-up.

An improved resolution and long-term stability can be achieved by placing the EOMs close to the pick-up.

Figure 8.11 shows a measurement of the beam pick-up signal without the 30 m of cable. The two outputs of the pick-up are combined and the measurement was performed with an oscilloscope with 8 GHz analog bandwidth installed next to the pick-up. The signal shape is depicted for four different horizontal beam positions. As one can see, the signal has a bump right next to the zero-crossing which is used for the arrival-time measurement. After the long cable, this bump was smeared out. The strength of this bump changes significantly with beam position.

The reason for this bump and also for the strong orbit dependence of the zero-crossing of the pick-up signal is a notch in the frequency spectrum at around 5 GHz. This corresponds to a quarter circumference of the ring-electrode in the pick-up. A beat between the fundamental and third harmonics of the ring causes the strong orbit dependence [HLS07].

8.3 The BAM system for FLASH

In order to avoid the negative effects of a long cable, the EOMs have been installed inside the tunnel, next to the pick-up. The BAMs are supplied by laser pulses from the master laser oscillator via length stabilized fiber-links. The schematic layout of the system is depicted in Fig. 8.12. Optical delay stages are installed for each EOM, in order to be able to adjust the timing of the laser pulses with respect to the

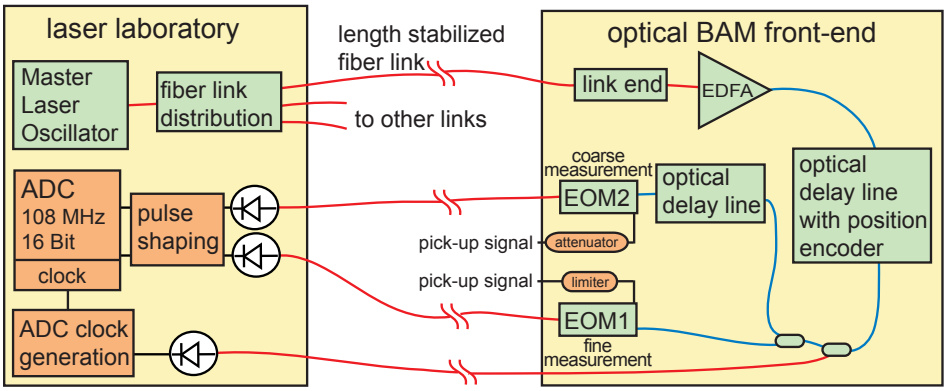

Figure 8.12: Schematic layout of the bunch arrival-time monitors for FLASH.

zero-crossing of the pick-up signal. A slow feedback acting on the first delay stage keeps the laser pulse always near the zero-crossing position. The bunch arrival-time is computed from the known optical delay and the laser pulse energy. An absolute position encoder measures the optical delay and provides sub-micrometer resolution. The absolute length of 120 mm is precise to within 3 μm.

One EOM is supplied by an unattenuated beam pick-up signal which has been limited to ± 5 V. This signal has a very steep slope at the zero-crossing and yields a highly precise arrival-time detection. The dynamic range of this measurements, however, is only around 3–4 ps. The second EOM is supplied by an attenuated pick-up signal yielding a dynamic range of about ± 35 ps but inferior resolution. In the case of large electron bunch timing changes, the delay stage is adjusted according to this coarse measurement to bring the first EOM back into its optimum range. By this combination, the BAM system can cope with large timing jumps of the electron beam and still maintains excellent resolution. The dynamic range for slow changes of the electron beam is only limited by the length of the optical delay stage.

The signals of the EOMs as well as a laser signal, which was split off after the first delay stage, are sent outside the tunnel. There, the laser signal is used to generate the clock pulses of the ADC. This scheme has the advantage that a change of the optical delay does not affect the ADC sampling position, since all three signals experience the same timing change.

Since the repetition rate of the MLO is 216.7 MHz and no ADC at twice the repetition rate was available, a different detection scheme than in the BAM prototype was applied. An ADC sampling rate of 108.35 MHz was chosen allowing to measure only every second laser pulse. In order to measure again the baseline as well as the laser pulse, part of the photo-detector signal is sent to a second ADC whose gate pulse is 1 ns earlier.

Due to a better internal distribution of the ADC clock, the timing stability of the ADCs is improved compared to the prototype. This yields a better resolution for the laser amplitude. The normalized laser amplitude can be determined with a precision

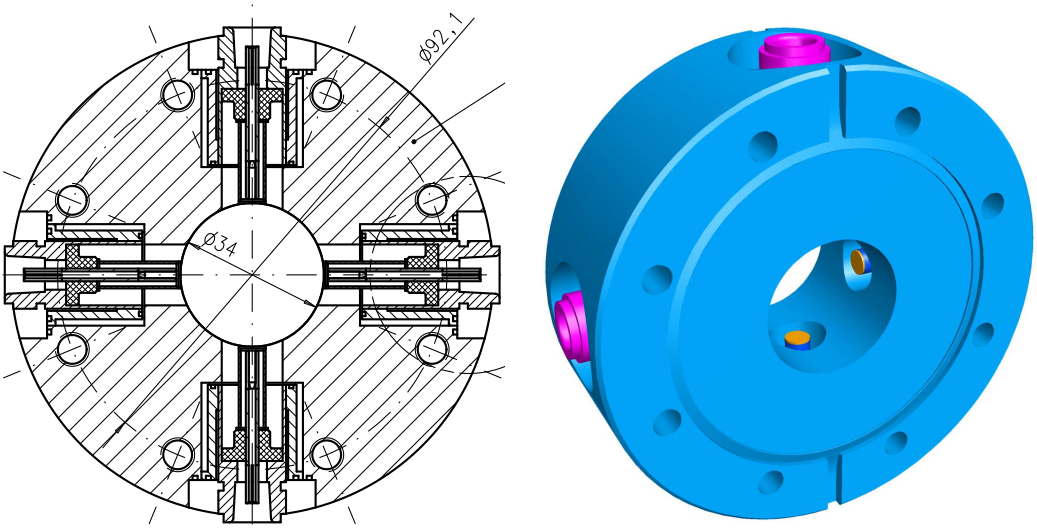

Figure 8.13: Technical drawing and 3D model of the button-type beam pick-up used for the bunch arrival-time measurements.

of 0.1% to 0.3%.

The first two BAMs at FLASH are located at two different locations between BC2 and the collimator in front of the undulators.

8.3.1 Button-type beam pick-up

In order to avoid the strong orbit dependence of the ring-type beam pick-up, a button-type pick-up was developed by Kirsten Hacker [HLS07]. A large slope at the zero-crossing of the voltage signal to ensure a high resolution and a low maximum voltage to prevent amplitude dependencies caused by the limiter were design criteria.

Figure 8.13 shows a schematic of the resulting design. In order to reduce the orbit dependence, again the outputs on opposite sides are combined. One of the combined signals is strongly attenuated and used for the coarse arrival-time measurement, while the other one is limited to peak voltages of $\pm 5\,\mathrm{V}$ and used for the high precision measurement.

The combined signal measured with an oscilloscope of 8 GHz analog bandwidth is shown in Fig. 8.14 for different horizontal beam positions. The signal duration is half as long as the signal from the ring-type pick-up. As expected from a button-type pick-up, the amplitude changes with beam position. The pre-ringing is an artifact of the oscilloscope because the bandwidth of the signal is much higher than 8 GHz.

Figure 8.15 shows the laser pulse energy from the coarse and the fine EOM as a function of the time delay between laser pulse and pick-up signal. Using the attenuated pick-up signal, a high bandwidth measurement of the pick-up signal's shape is possible. The bandwidth of the EOMs is about 20 GHz. The pre-ringing observed in the oscilloscope measurement is vanished. As seen before, the limited

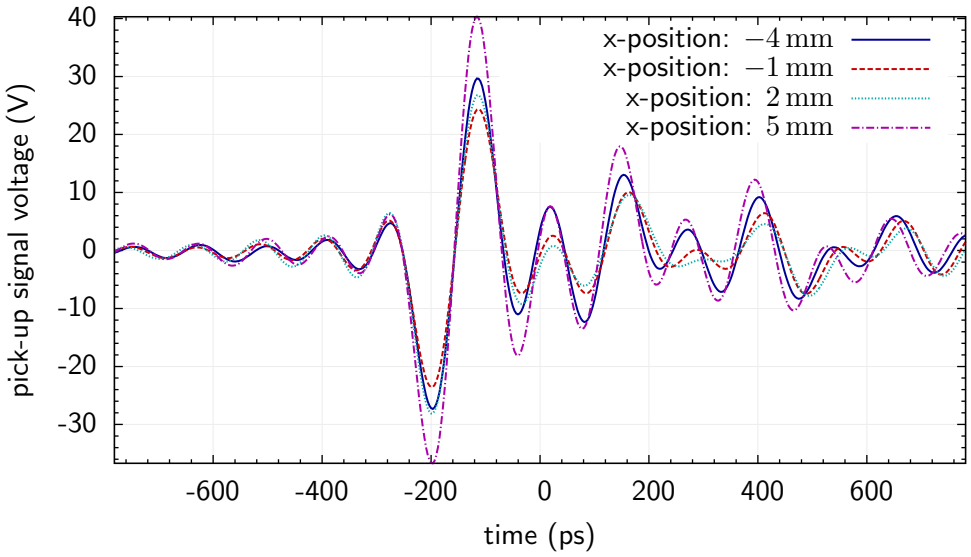

Figure 8.14: Signal shape of the button-type beam pick-up for different horizontal beam positions. The two outputs of the pick-up are combined and the measurement was performed with an 8 GHz bandwidth oscilloscope installed next to the pick-up.

signals cause at some time delays a phase shift larger than 180° in both arms of the Mach-Zehnder interferometer. The bottom plot of Fig. 8.15 shows the steep signal change at the zero-crossing position of the pick-up signal.

8.3.2 Orbit dependence of the pick-up signal

Figure 8.16 shows the arrival-time of the zero-crossing of the button-type beam pick-up signal as a function of the beam orbit. The combined horizontal ports of the pick-up were used as the input of the EOM. There is no dependence of the arrival-time on the vertical beam position visible. The arrival-time of the zero-crossing shifts, however, for changes of the horizontal orbit. The curve is expected to be symmetric around $x = 0$ but the symmetry point is shifted to $x \approx 3\,\mathrm{mm}$. A possible explanation is a misaligned pick-up.

Figure 8.17 shows the dependence of the BAM calibration constant on the beam orbit. No orbit dependence is visible in both directions.

8.3.3 Charge dependence of the pick-up signal

The dependence of the arrival-time of the pick-up signal zero-crossing on the bunch charge is depicted in Fig. 8.18. The beam was accelerated on-crest in the entire machine and, therefore, longitudinally uncompressed. Charge changes lead to a different dynamics in the electron gun and cause arrival-time changes. In order to investigate the charge dependence of the beam pick-up, the arrival-time was measured simulta-

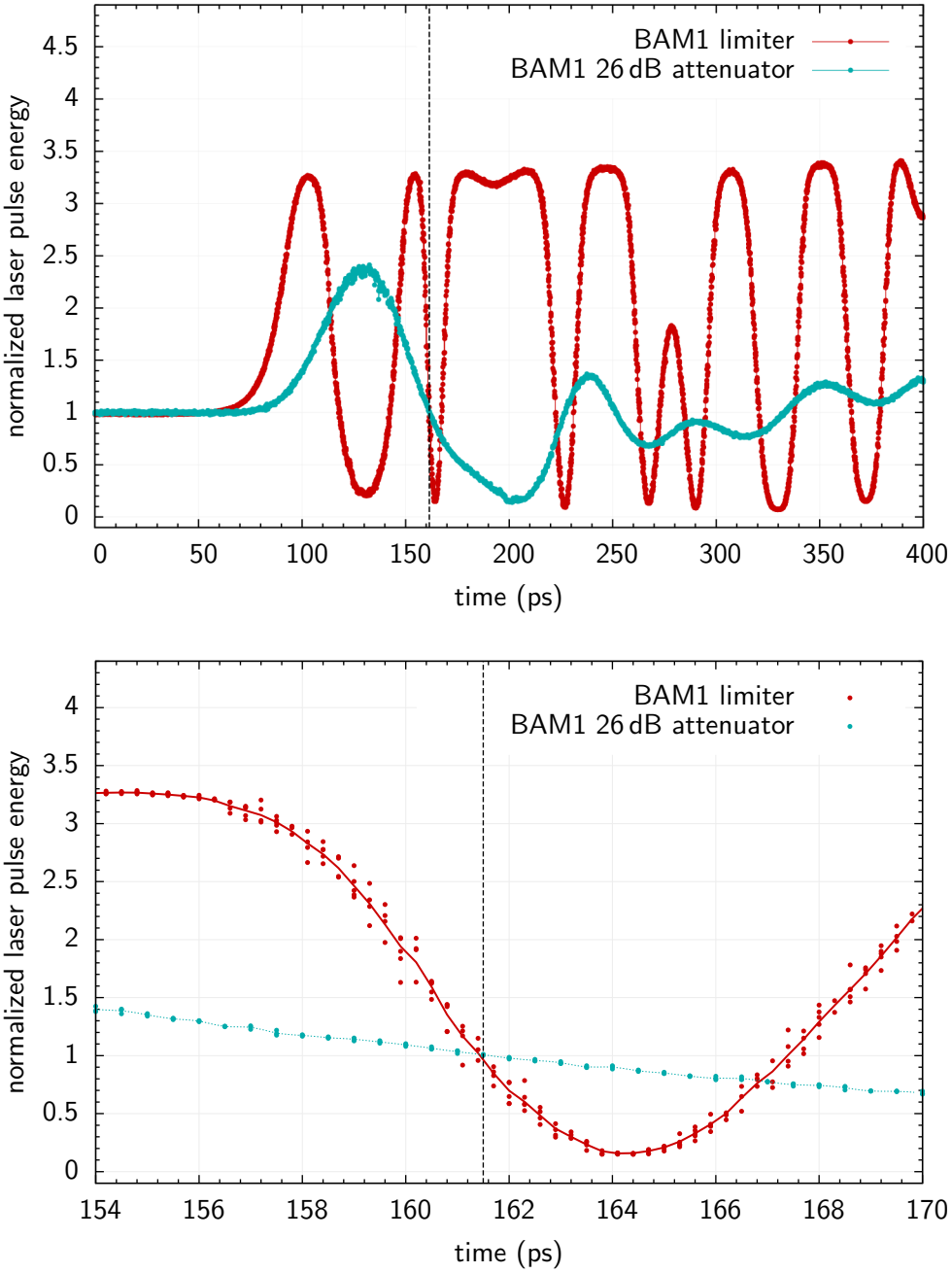

Figure 8.15: Scan of laser pulses over the signal of the button-type beam pick-up. The working point for the bunch arrival-time detection is indicated with a dashed line. Top: scan over a large part of the pick-up signal. Bottom: time scan near the working point.

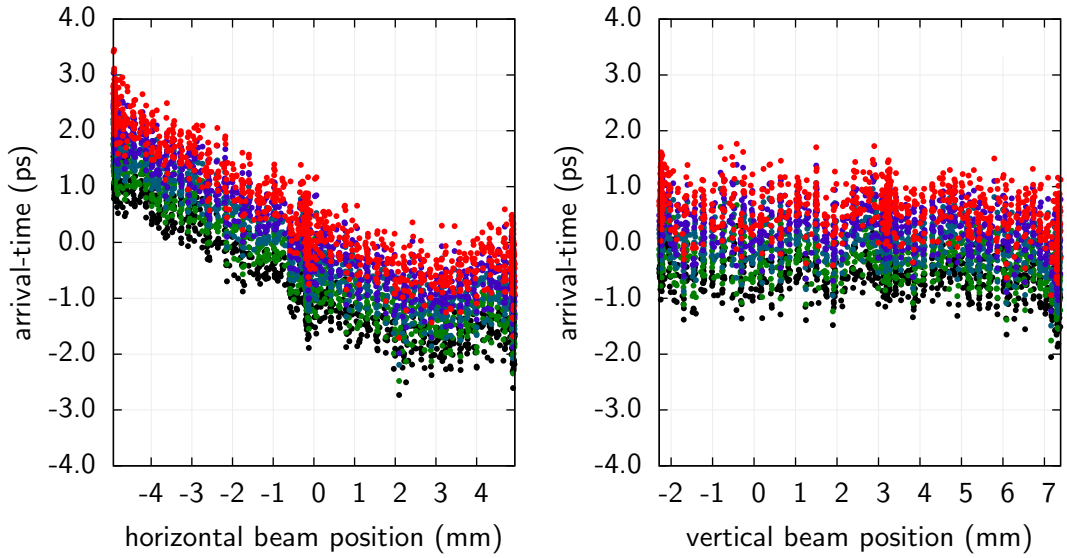

Figure 8.16: Arrival-time of the zero-crossing of the button-type beam pick-up signal as a function of the beam orbit. The two horizontal outputs were combined and used as the input signal of the BAM.

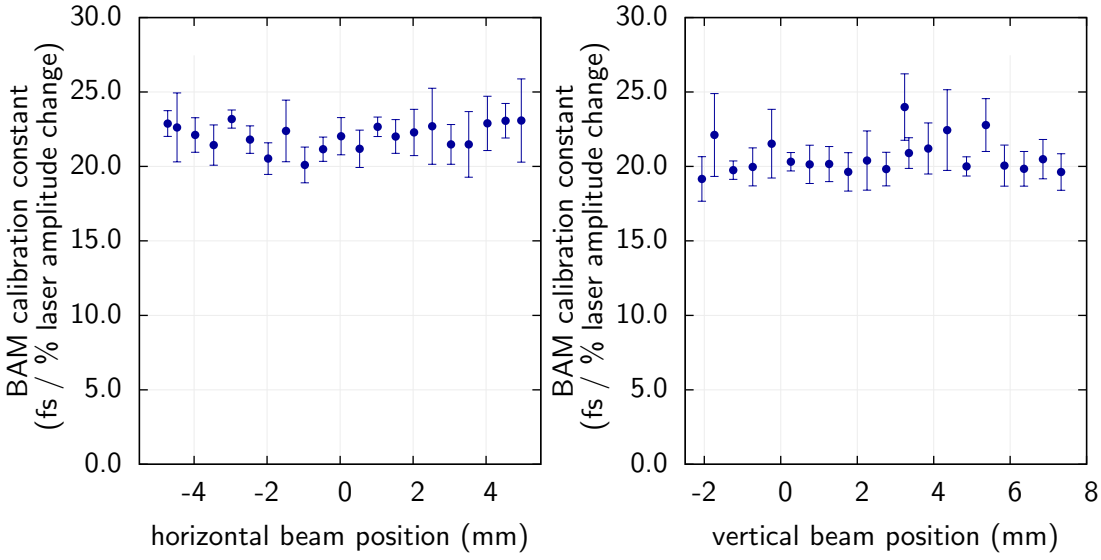

Figure 8.17: Dependence of the BAM calibration constant on the beam orbit.

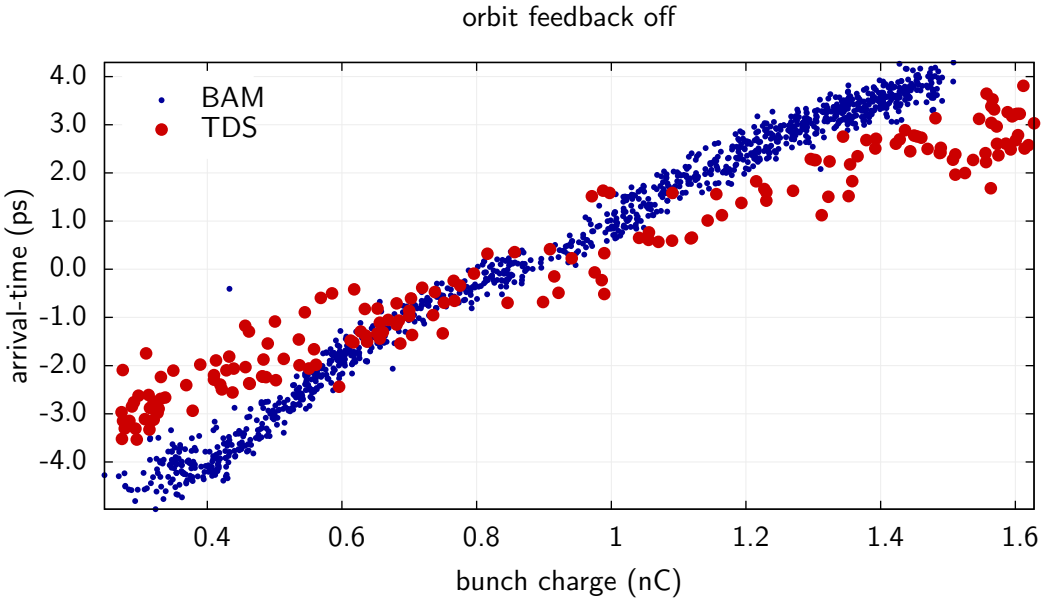

Figure 8.18: Dependence of the arrival-time of the pick-up signal's zero-crossing on the bunch charge. An arrival-time measurement done with the transverse deflecting structure (TDS) is shown for comparison.

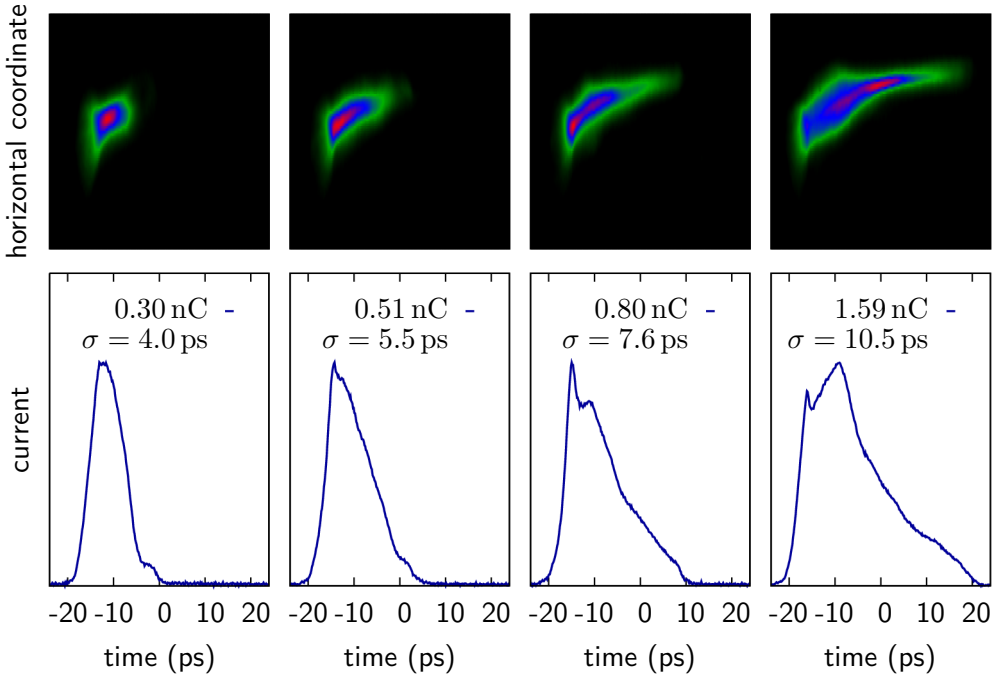

Figure 8.19: Variation of the longitudinal charge distribution for different bunch charges. The measurement was done with the transverse deflecting structure.

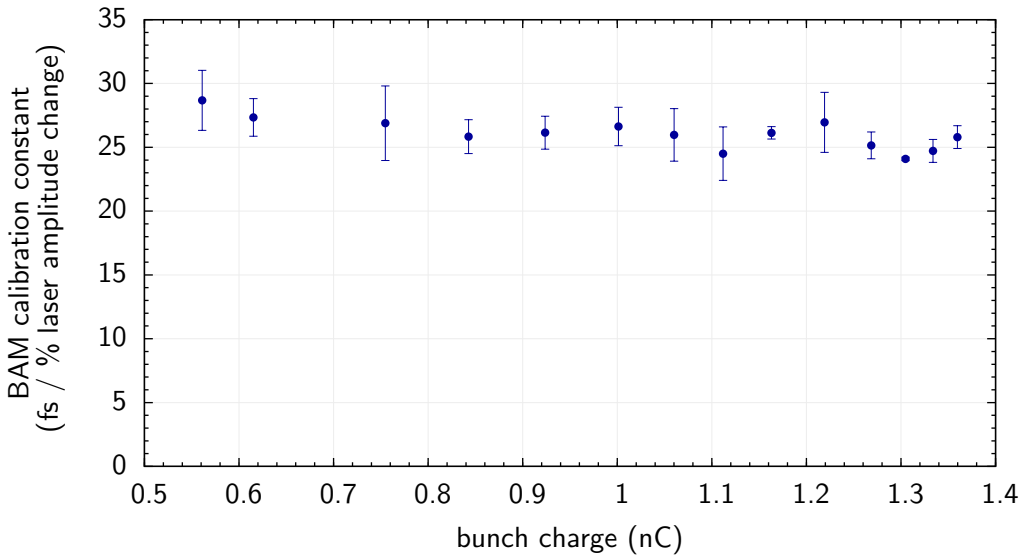

Figure 8.20: Dependence of the BAM calibration constant on the bunch charge.

neously with the transverse deflecting structure (TDS). The results are also shown in Fig. 8.18.

The TDS shows a slightly smaller dependence of the bunch arrival-time on the charge. The explanation of the larger dependence of the BAM can be understood from the measurements of the longitudinal charge distribution shown in Figure 8.19. Four different bunch charges are shown and it is clearly visible that a change of the bunch charge changes the longitudinal bunch profile significantly. The rms bunch length increases almost by a factor of three within the charge range shown in Fig. 8.18.

The assumption that the BAM measures the beam centroid is only true, when the electron bunch duration is short compared to the transient signal of the beam pick-up. When the electron bunches get sufficiently long, the shape of the pick-up signal depends also on the charge profile and the zero-crossing position may shift. The observed difference between the TDS and the BAM indicates that the pick-up is sufficiently fast to be affected by the bunch profile changes.

Under normal FEL operation conditions, this dependence of the pick-up signal on the bunch charge is significantly reduced, since the bunches are longitudinally compressed.

Figure 8.20 shows the dependence of the BAM calibration constant on the bunch charge. Also this measurement was performed for an on-crest operation of the accelerator. Without longitudinal shape changes of the electron beam one would expect that the BAM calibration constant decreases anti-proportionally with charge. However, it remains almost constant over the entire charge range. This is also an indication that the pick-up signal shape changes for different longitudinal charge distributions of the electron bunches.

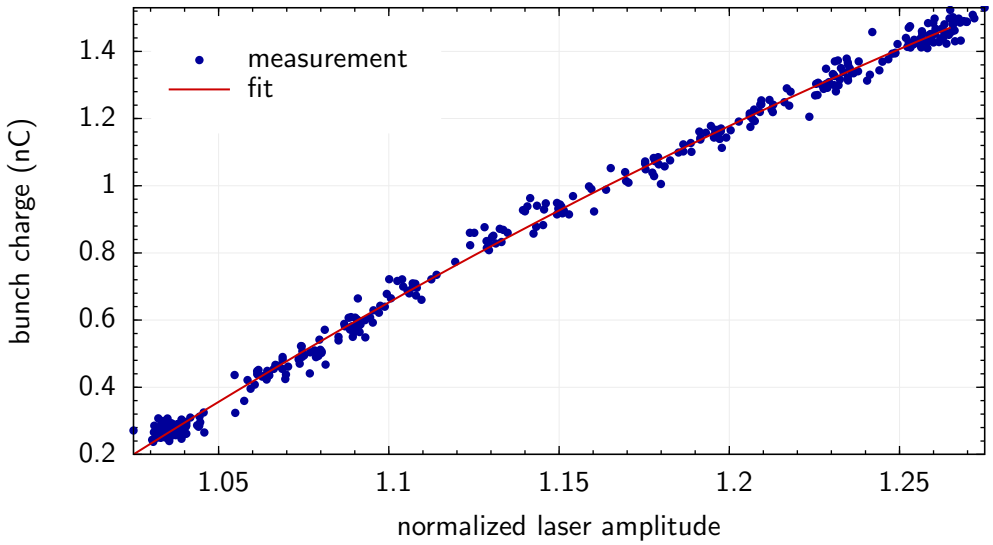

Figure 8.21: Correlation between the normalized amplitude of two laser pulses which sample the ringing of the beam pick-up signal and the bunch charge measured with a toroid. From the laser amplitudes, the bunch charge can be determined with a precision of 32 pC.

8.3.4 Fast charge measurement with a BAM

The pick-up signal is ringing for a duration of several hundred nanoseconds after the bunch arrived. As a consequence, not only the energy of the laser pulse near the zero-crossing is changed, but also the energy of the following pulses. Some of the laser pulses sample a maximum of the ringing signal and hence, their energy depends on the bunch charge. This effect can be used to determine the bunch charge. Figure 8.21 shows the energy ratio of laser pulses arriving 7 and 13 pulses later than the pulse at the zero-crossing. From this ratio, the bunch charge can be determined with a precision of 32 pC after the laser amplitude was calibrated against a toroid. The advantage of using the BAM for the charge determination instead of a toroid is the fact that a fast feedback based on the BAM can use the charge measurement for corrections. Since the charge is calculated on the same ADC board as the arrival-time, this avoids long transmission times.

Unfortunately, the calibration constants depend sensitively on the beam orbit and the bunch length at the pick-up position. But maybe, this dependence can be reduced by using different or more laser pulses for the charge determination.

8.4 Bunch arrival-time measurements at FLASH

We have seen already earlier that the arrival-time may change significantly along the bunch train, for example due to beam loading in the cavities. Figure 8.22 shows the bunch arrival-time for ten consecutive trains. In this situation, a beam loading

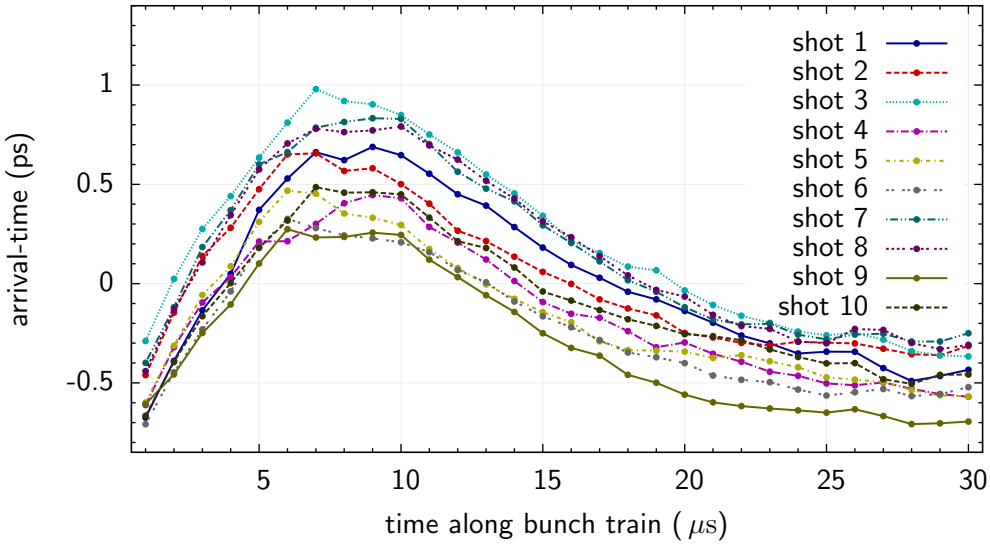

Figure 8.22: Bunch arrival-time distribution along the bunch train for ten consecutive trains.

compensation was used which replenishes energy in the cavity. Even with this beam loading compensation, a significant systematic timing change along the bunch train is observed. This shows that the beam loading compensation is not yet optimized. Measurements with a BAM provide an ideal tool to study beam loading effects.

The bunch arrival-times fluctuate from one train to the next. The systematic shape of the arrival-time distribution, however, remains largely invariant.

This invariance of the arrival-time pattern can be used to estimate the resolution of the bunch arrival-time monitor by correlating the arrival-times of two adjacent bunches.

Figure 8.23 shows the correlation between two adjacent bunches in the bunch train for normal FEL operation (left) and for an accelerator setting in which BC1 is bypassed (right). The correlation widths are 24.7 fs (left) and 22 fs (right), respectively, corresponding to BAM resolutions of 17.5 fs and 15.6 fs. This is much worse than expected from the BAM calibration constant and the pulse energy noise of the laser, which would give a BAM resolution of about $4 - 5$ fs.

A possible explanation is fast noise acting on a time scale shorter than the bunch spacing of 1 μs. When BC1 is bypassed, arrival-time jitter due to fast amplitude or phase fluctuations in ACC1 does not exist. Since the measured correlation widths are very similar in both cases, this indicates that the source of the fast noise is probably the electron gun or the photo cathode laser. The gun cavity is a very likely source, since it is normal conducting and has a much shorter time constant than superconducting cavities.

Figure 8.24 shows the dependence of the relative jitter between adjacent bunches along the pulse train (left). The electron beam was accelerated on-crest. There is a steep increase at the beginning of the bunch train which is not yet understood.

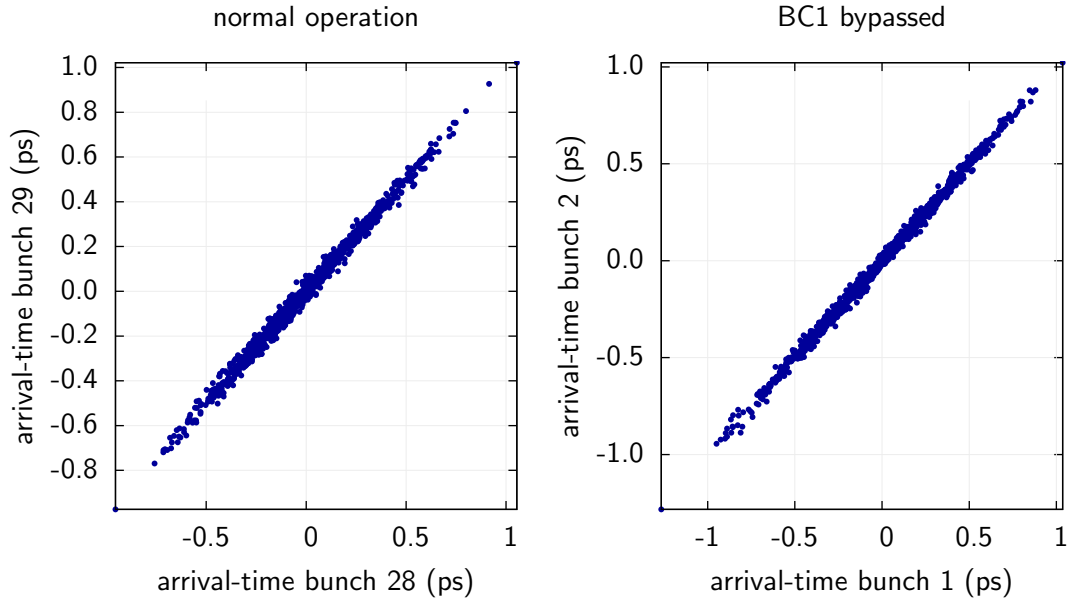

Figure 8.23: Correlation between the arrival-times of two adjacent bunches in the bunch train. The BAM resolutions estimated from the correlation widths of 1000 consecutive shots are 17.5 fs (left) and 15.6 fs (right).

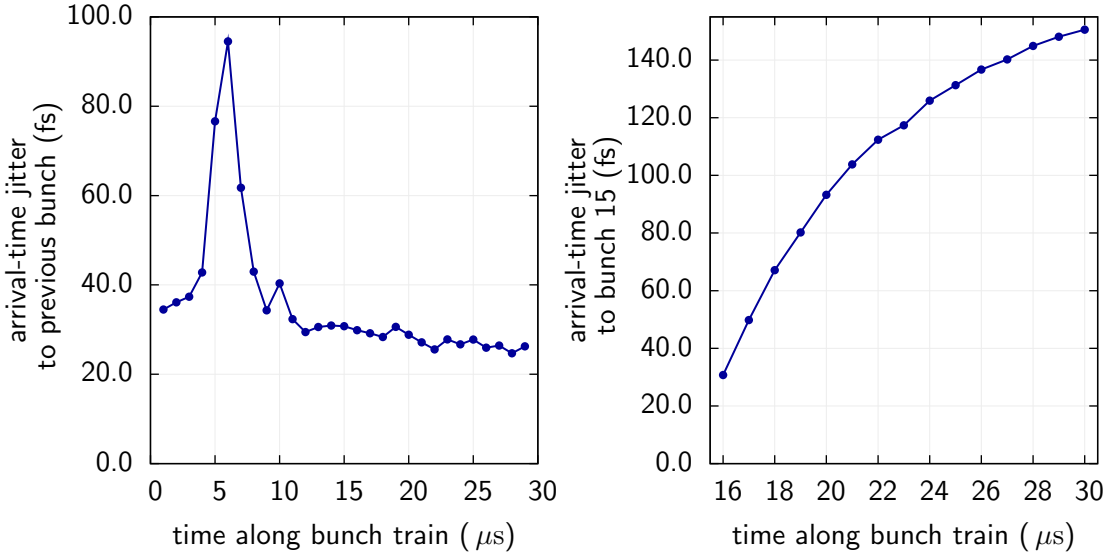

Figure 8.24: Left: Dependence of the uncorrelated arrival-time jitter between two adjacent bunches along the bunch train. Right: Correlation width between bunch 15 and the following bunches.

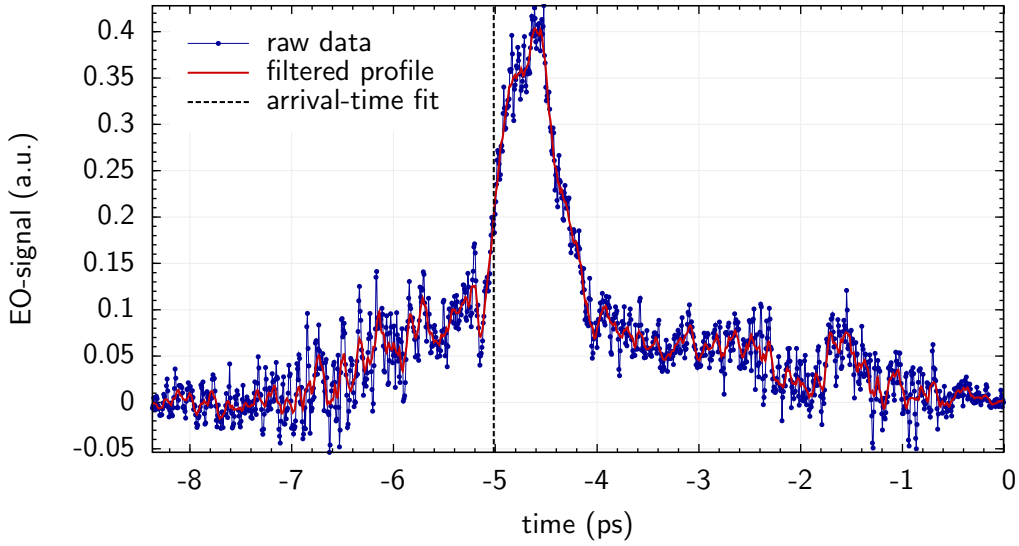

Figure 8.25: Determination of the bunch arrival-time from the electro-optic spectral decoding signal.

After about twelve bunches, the jitter remains constant. The right hand side plot shows the relative jitter between bunch 15 and the following bunches. The jitter increases rapidly. If the arrival-time information of the BAM is used for a feedback system, this uncorrelated jitter cannot be corrected for and it is, therefore, important to decrease it. The fast noise in the electron gun can be reduced by reducing the feedback gain of the cavity regulation. In the meantime, the timing stability of the photo-cathode laser has been significantly improved, after a damaged cable for an RF reference signal was repaired. This was not the case in this measurement, but we will see the improvement in chapter 10.

8.4.1 Comparison of arrival-time measurements with a BAM and with electro-optic spectral decoding

In order to validate the arrival-time determination with the BAM, a comparison with the electro-optic spectral decoding (EOSD) setup at FLASH was made. Figure 8.25 shows the bunch profile measured with EOSD. To determine an arrival-time from this profile, it is low-pass filtered and a linear regression is made for the leading edge of the resulting profile. The arrival-time is defined by the half-maximum position of the leading edge of the filtered signal.

Figure 8.26 shows the bunch arrival-time measured by a BAM and by the EOSD setup. Arrival-time changes are induced by changing the ACC1 amplitude. There is a good correlation between both measurements.

The Ti:Sapphire laser of the EOSD setup was synchronized to the 1.3 GHz reference of the machine by a conventional RF phase detection scheme as it is also used for the MLO. The accuracy with which both lasers were synchronized to the 1.3 GHz

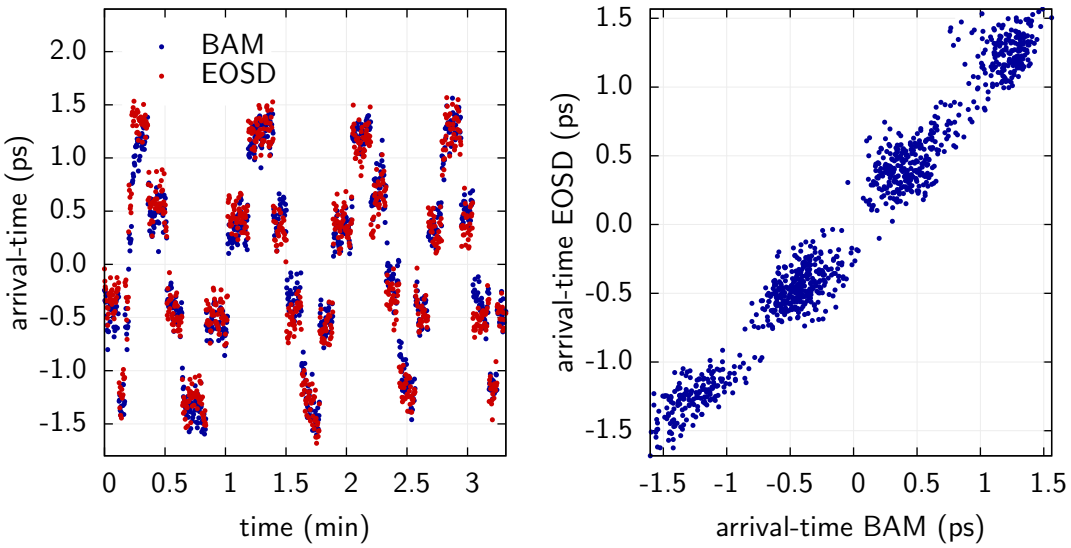

Figure 8.26: Bunch arrival-time measured by a BAM and an electro-optic spectral decoding setup. The bunch arrival-time was changed by varying the amplitude of ACC1.

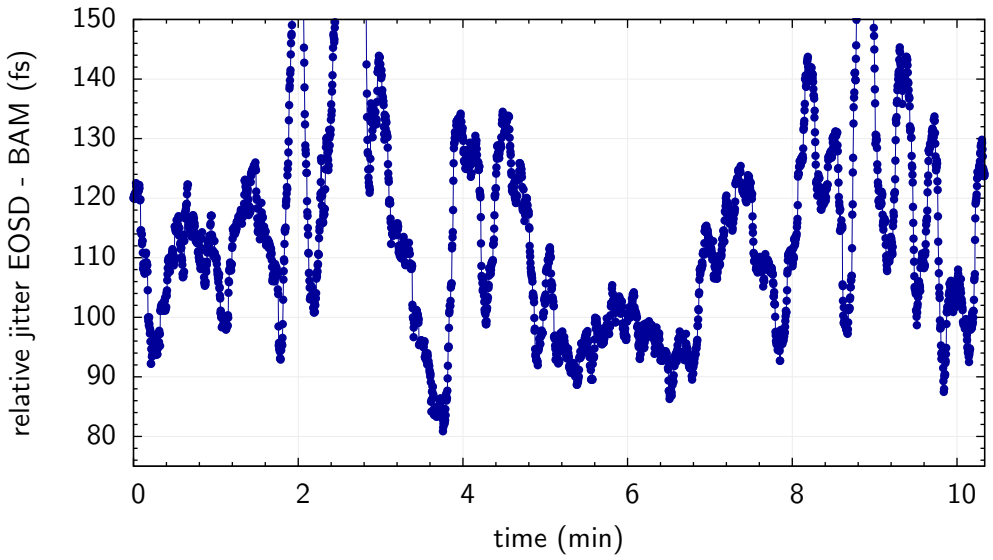

Figure 8.27: Relative jitter between the arrival-times measured by a BAM and by an electro-optic spectral decoding setup. Each point corresponds to the jitter of 100 shots.

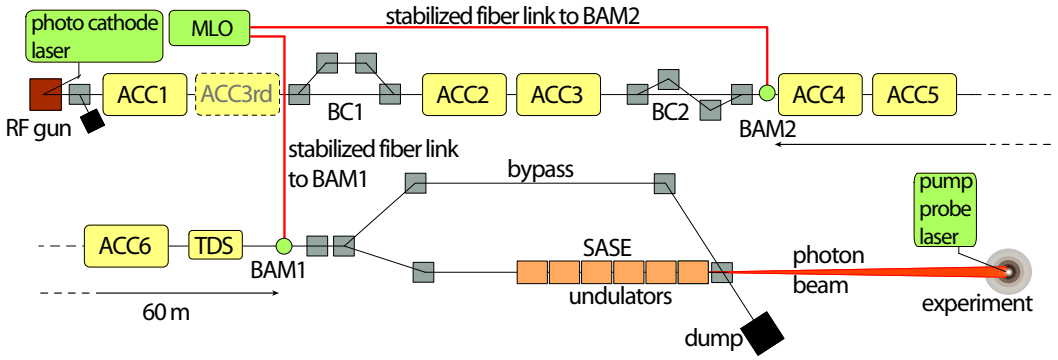

Figure 8.28: Locations of the two bunch arrival-time monitors used for the resolution measurement.

reference was about 50 fs for short time scales of several seconds. Over longer periods, the timing of the lasers drifts, due to the already discussed limitations of the RF phase detection.

Figure 8.27 shows the relative jitter between both arrival-time monitors. Each point corresponds to 100 shots or 20 s. The regulation parameters of both lasers were tuned during the measurement. The minimum relative jitter is 80 fs. This is very close to the expected 70 fs of jitter resulting from both laser synchronizations.

8.5 Measurement of the BAM resolution and the stability of the optical synchronization system.

In order to measure the resolution of the BAMs without perturbation by fast timing changes of the accelerator, two arrival-time monitors were installed 60 m apart in a straight section of the accelerator (see 8.28). Each BAM was supplied with laser pulses from the MLO by its own stabilized fiber-link. Since there is no longitudinal dispersion in the straight section, both BAMs should measure the same relative changes of the electron bunch arrival-times [LAF$^+$08c].

Figure 8.29 shows the correlation of the arrival-times of 1500 bunches measured synchronously with both BAMs. The uncorrelated jitter amounts to 8.4 fs, which corresponds to a resolution of better than 6 fs for a single BAM. This resolution contains the instability of a fiber-link and the integrated laser timing jitter in the frequency range from about 3 MHz to 108 MHz. The lower limit of 3 MHz arises from the length difference of the two fiber-links.

The figures 8.30 to 8.33 show the arrival-time variations detected by both BAMs and the difference signal of the arrival-times. Different measurement periods of 9 minutes (Fig. 8.30), 1.5 hours (Fig. 8.31), 4.5 hours (Fig. 8.32) and 7 hours (Fig. 8.33) are shown. Table 8.1 summarizes these measurements.

Slow, almost periodic arrival-time drifts are seen by both monitors. They cancel in the difference signal. From time to time, erratic excursions are visible with both

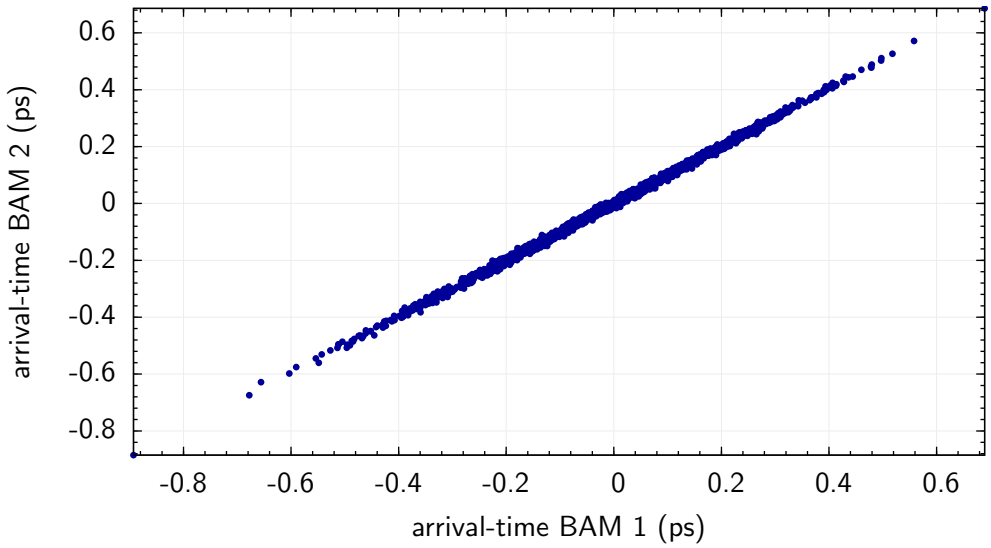

Figure 8.29: Correlation of the arrival-times measured with two BAMs which are separated by 60 m. The correlation width of the 1500 shots is 8.4 fs, corresponding to a resolution of better than 6 fs for a single BAM.

measurement duration	rms arrival-time difference BAM1 - BAM2 (fs)	corresponding rms resolution of single BAM (fs)
9 min	8.4	< 6
1.5 h	13.1	< 9.3
4.5 h	19.4	< 13.7
7 h	28.0	< 20

Table 8.1: Summary of correlation measurements between two BAMs.

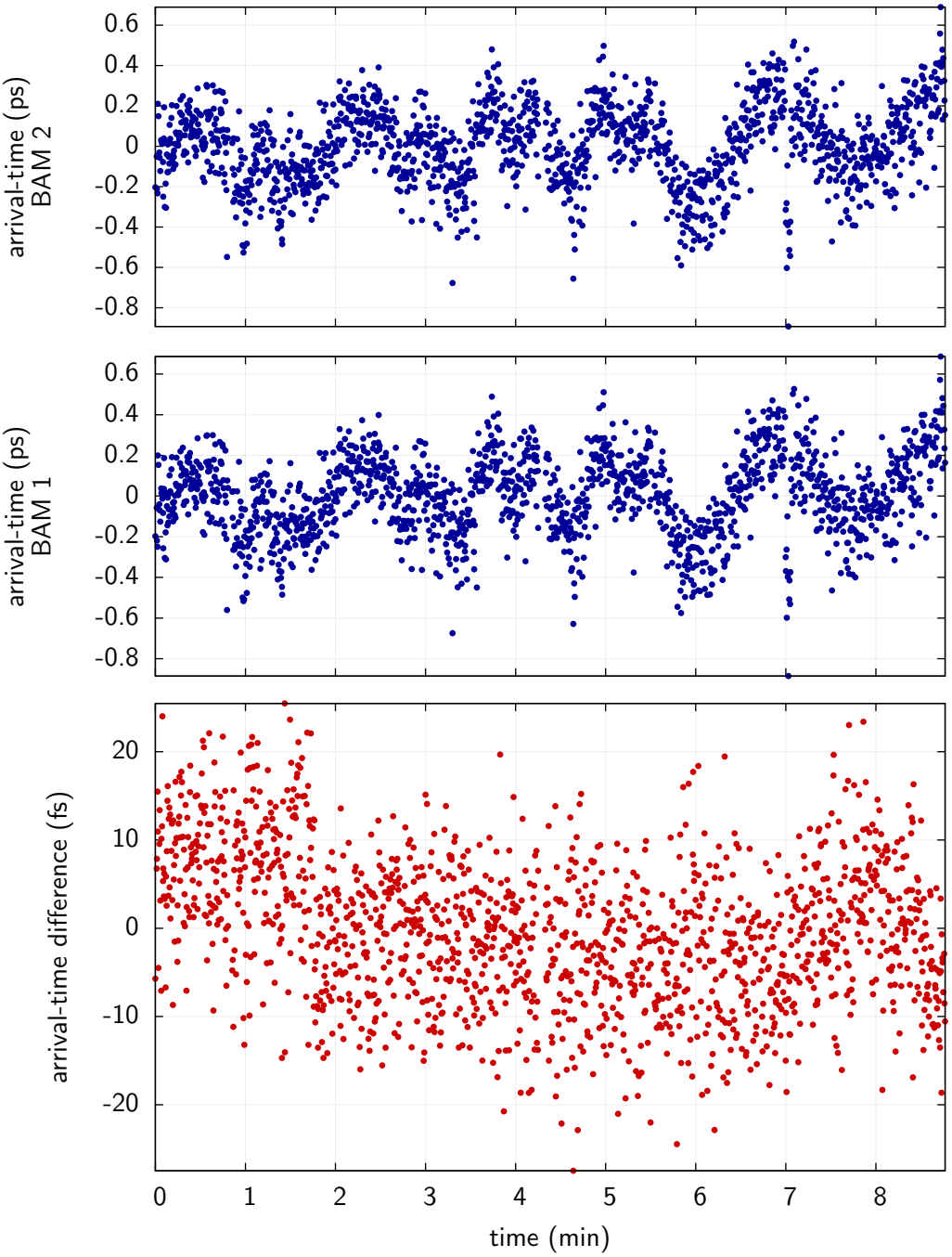

Figure 8.30: Arrival-time measured by two BAMs over a duration of about 9 minutes together with the difference signal of both measurements. The jitter of this difference signal amounts to 8.4 fs, corresponding to a BAM resolution of better than 6 fs.

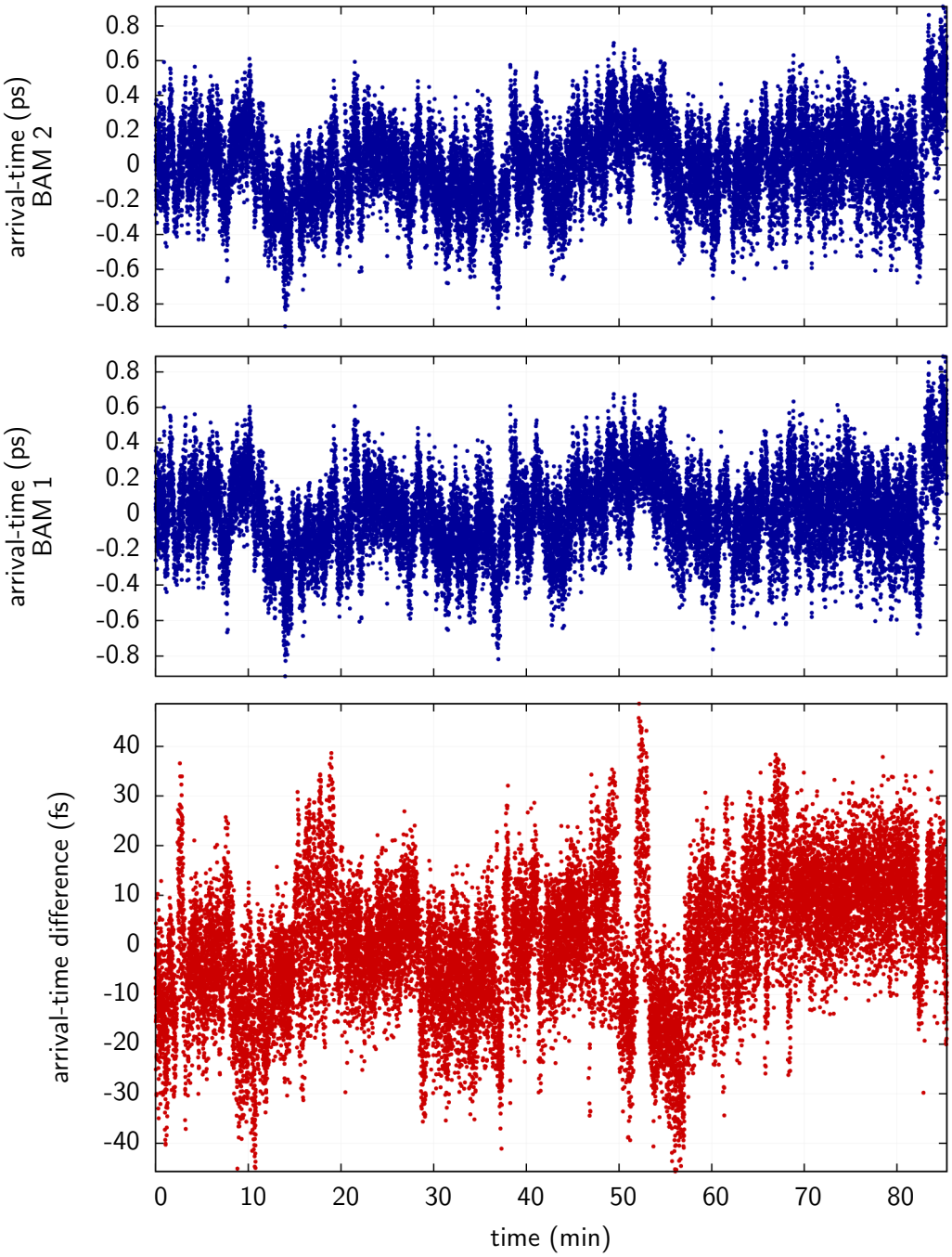

Figure 8.31: Arrival-time measured by two BAMs over a duration of about 1.5 hours together with the difference signal of both measurements. The jitter of this difference signal amounts to 13.1 fs, corresponding to a BAM resolution of 9.3 fs.

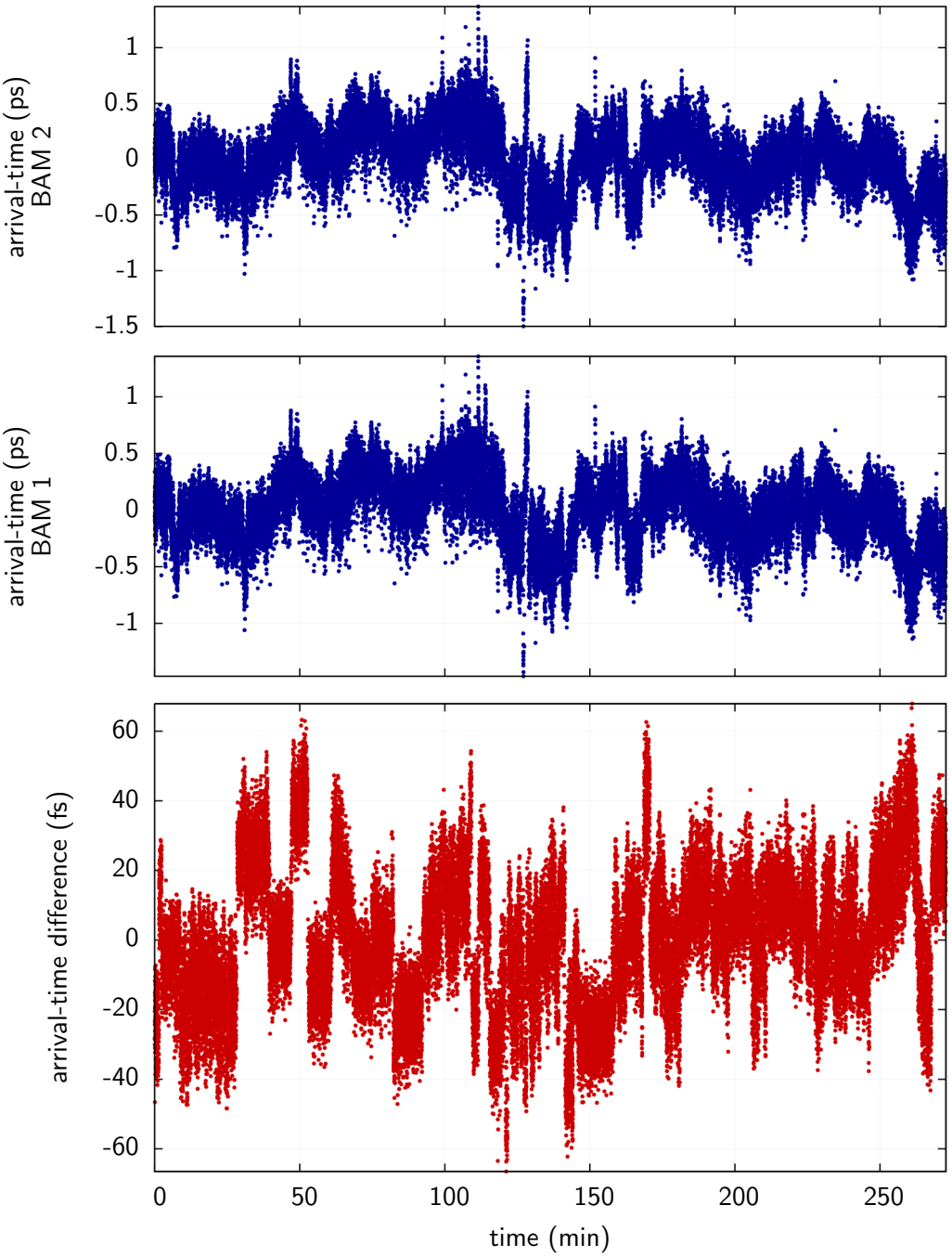

Figure 8.32: Arrival-time measured by two BAMs over a duration of about 4.5 hours together with the difference signal of both measurements. The jitter of this difference signal amounts to 19.4 fs, corresponding to a BAM resolution of 13.7 fs.

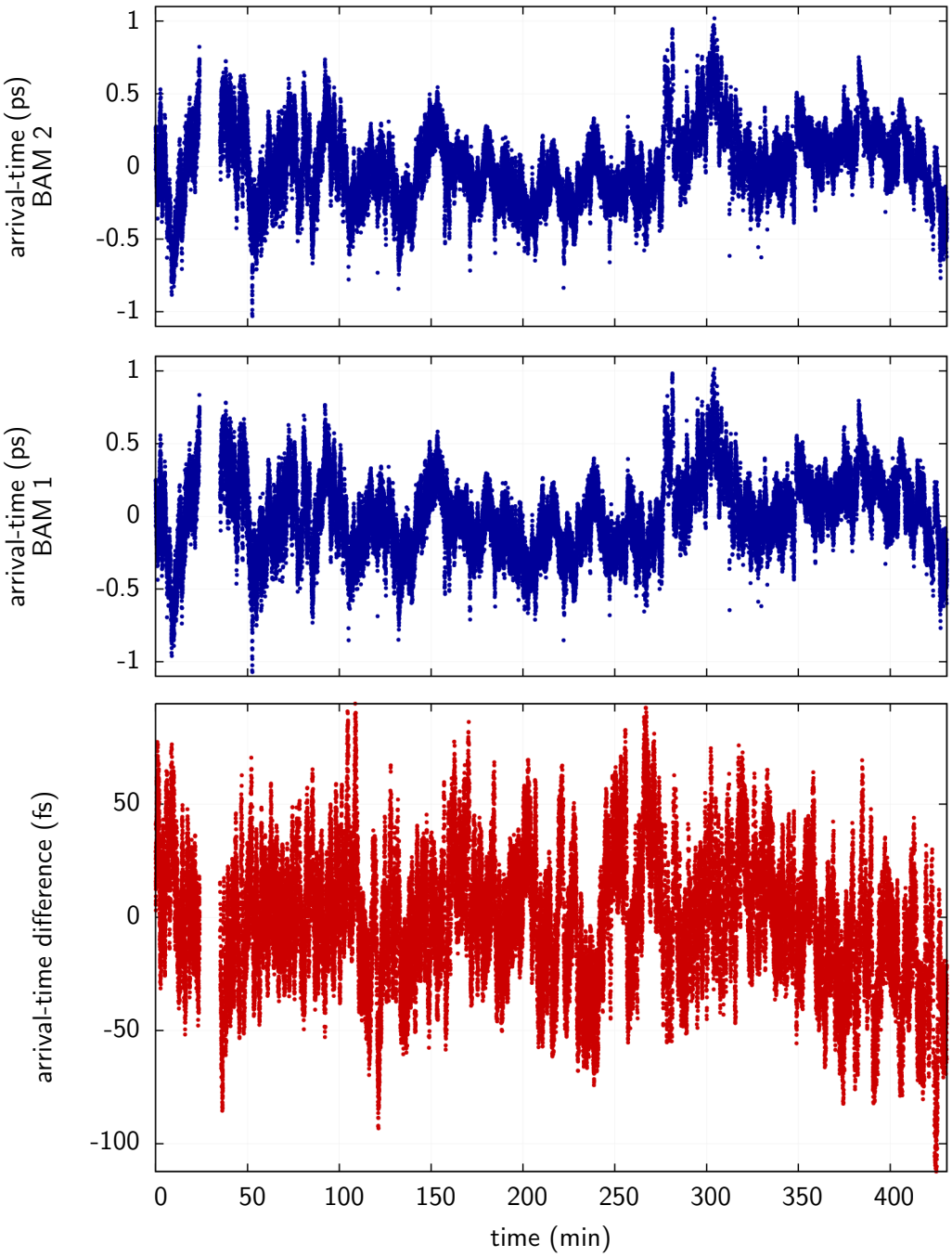

Figure 8.33: Arrival-time measured by two BAMs over more than 7 hours together with the difference signal of both measurements. The jitter of this difference signal amounts to 28 fs, corresponding to a BAM resolution of better than 20 fs.

monitors. The most likely explanation is accelerator tuning during FEL operation by the operators. Also the difference signal shows the erratic excursions, and a possible explanation is a change of the longitudinal bunch profile, on which both BAM pick-up signals react slightly different.

Essential prerequisites for this excellent time resolution were a fast button-type beam pick-up, the combination of opposite pick-up signals, the installation of the EOMs directly at the pick-up, and a precise laser pulse energy measurement of better than 0.2%. For the distribution of the arrival-time information, the optical synchronization system is mandatory.

9 Injector timing characterization and correction

As we have seen in chapter 4, timing changes of the electron beam occurring upstream of the first magnetic chicane are suppressed to some extent in the bunch compressors. In case of the non-linear compression scheme without the linearizing third harmonic cavity, as it is currently used, the compression factor for the electrons in the resulting current spike is very high and under normal operating conditions only a few percent of the injector timing change remain after the compression. Timing changes of the electron bunch centroid, however, are only suppressed by a factor of four to five for normal ACC1 phases of $\varphi_{\mathrm{ACC1}} = -7^\circ$ to -8°. When the phase space is linearized, the current spike will be gone and the entire bunch will be compressed symmetrically. To reduce bunch distortions by collective effects, the compression factor will be smaller than the one in the current spike in the present situation.

Stable bunch timing from the injector is mandatory in all kinds of schemes in which the electron beam is manipulated with an external laser beam. Examples are a seed laser at the undulator and a laser heater [HBE+04, AZDK08], which will be used in future FELs to increase the beam energy spread in order to avoid microbunching instabilities. In many cases, the timing of the bunch centroid is essential.

We have seen in chapter 4 that the longitudinal phase space distribution from the injector depends strongly on the timing between the photo-cathode laser and the gun. Since changes of the longitudinal properties in the injector affect the longitudinal beam properties after final compression and, therefore, the lasing performance of the FEL, a detailed understanding of the timing of the photo-cathode laser and the gun is mandatory.

9.1 Measurement of the relative timing between gun and photo-cathode laser

To study the relative timing between photo-cathode laser and gun, the effect is used that the charge of the emitted electron bunches depends on the gun phase. Figure 9.1 shows the measured, emitted charge for different settings of the gun phase. In addition, the result of an ASTRA simulation is shown. As before, a gun phase of $\varphi_{\mathrm{gun}} = 0^\circ$ corresponds to the setting where the energy gain for the electrons is the highest. At very small phases ($\varphi_{\mathrm{gun}} < -46^\circ$), all electrons are accelerated in the backward direction and no charge is emitted. Increasing the gun phase beyond -46° allows part of the electrons to leave the cavity. In the phase range from -44°

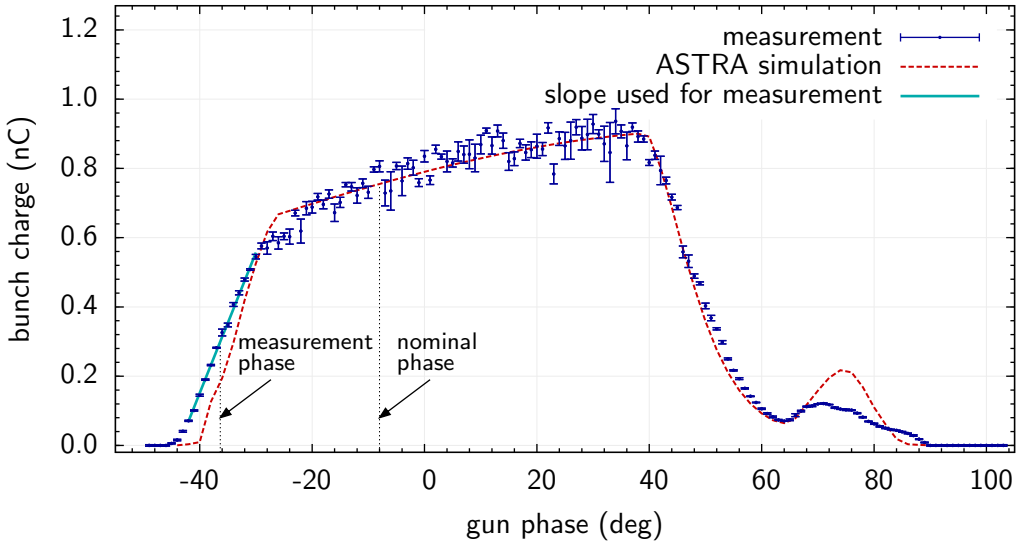

Figure 9.1: Charge emitted by the electron source for different phases of the RF gun.

to −30°, less and less of the generated electrons are lost and around −30°, almost all electrons find their way out of the gun. If the gun phase is further increased, the bunch charge continues to rise. The reason is the Schottky effect, a reduction of the electron work function of the CsTe-cathode in presence of an electrical field. This increases the quantum efficiency of the cathode. At around 40°, the first electrons are lost again. The 'bump' around 70° corresponds to the situation where a part of the electrons is accelerated such that inside the full cell of the gun (see Fig. 2.3), the electrons change their direction of motion and are emitted an RF period later.

The strong dependence of the emitted charge on the gun phase between −44° and −30° can be used to determine timing fluctuations between the photo-cathode laser and the gun [SHK+06], since the emitted charge changes by about 28 pC per picosecond change of the relative timing. Both, the nominal gun operation phase as well as the phase used for the timing measurement are indicated in Fig. 9.1.

The resolution of this measurement is mainly limited by two parameters. The first one is the resolution of the toroid, which is used to measure the emitted charge. This is around 3.7 pC (rms) in the current configuration, corresponding to a timing sensitivity of about 130 fs. The second contribution is the amplitude stability of the photo cathode laser, which is typically around 2% (rms). During the measurements, the emitted charge was around 400 pC and 2% laser amplitude jitter correspond to 8 pC of charge jitter or a timing resolution of around 280 fs. The two contributions limit the single shot resolution to around 310 fs. Both limitations could be overcome, either by improving the toroid system or by measuring in addition to the bunch charge the laser amplitude with a photo-detector.

The following measurements aimed to study systematic timing effects in the injector and to analyze possible limitations of a timing correction. For these measure-

ments, the limited single shot resolution was not a problem, since averaged values can be used. 100 consecutive shots were averaged in each measurement resulting in an accuracy of the mean values of around 30 fs.

9.2 Photo-cathode laser response measurement

The FLASH accelerator is capable of producing long pulse trains of up to 800 pulses distributed over a duration of up to 800 μs. This long pulse train allows for fast feedback systems acting within the macro-pulse to stabilize the electron beam. This is a tremendous advantage compared to normal-conducting accelerators, as the noise floor of most subsystems is significantly lower at higher frequencies above a few kHz, compared to the low frequency range. A denser bunch spacing decreases the frequency band contributing to the noise floor in a beam based feedback used to stabilize a measured property of the electron beam.

A planned feedback system will use an arrival-time measurement of the photo-cathode laser beam to stabilize the laser timing across the macro-pulse. A possible limitation of such a feedback is the response time with which the laser reacts to timing corrections. The photo-cathode laser is actively mode-locked, and its timing is defined by two acousto-optic modulators (AOMs), operated at 13.5 MHz and 108 MHz, and one electro-optic modulator (EOM), driven by a 1.3 GHz RF signal. The AOMs define the coarse timing, while the EOM due to its higher operation frequency is responsible for the fine timing.

To study the response of the photo cathode laser to timing changes, a vector modulator was installed in the 1.3 GHz reference line of the laser, allowing for timing shifts of the RF signal driving the EOM. The vector modulator was controlled by two fast DACs providing changes of the RF timing at a rate of 1 MHz. To measure the timing response of the laser, electron macro-pulses consisting of 30 bunches with a spacing of 2 μs were generated. The averaged charges of the single bunches were measured at the 'measurement phase' indicated in Fig. 9.1 for a constant laser timing. The same measurement was performed for the situation, where after 10 μs a timing step of 2.14 ps was added to the 1.3 GHz signal driving the EOM. Again, the average charge was measured across the macro-pulse and from the difference of both measurements and the knowledge of the charge slope of $28\,\frac{\mathrm{pC}}{\mathrm{ps}}$, the timing response of the laser can be evaluated.

Figure 9.2 shows the results of this measurement. As one can see, the laser needs around 6 μs to follow the timing step. Furthermore, it oscillates around the new set-point with a period of around 70 kHz. After 50 μs, the oscillation amplitude is damped to around half of its original value. It should be noted that the oscillation can also be caused by an amplitude change of the laser instead of a timing change, since the measurement principle cannot distinguish between both effects. In order to evaluate this, a parallel detection of the laser pulse amplitude should be performed.

With around 6 μs, the laser response is sufficiently fast to perform timing corrections within the electron macro-pulse. As we will see later, the oscillation is not

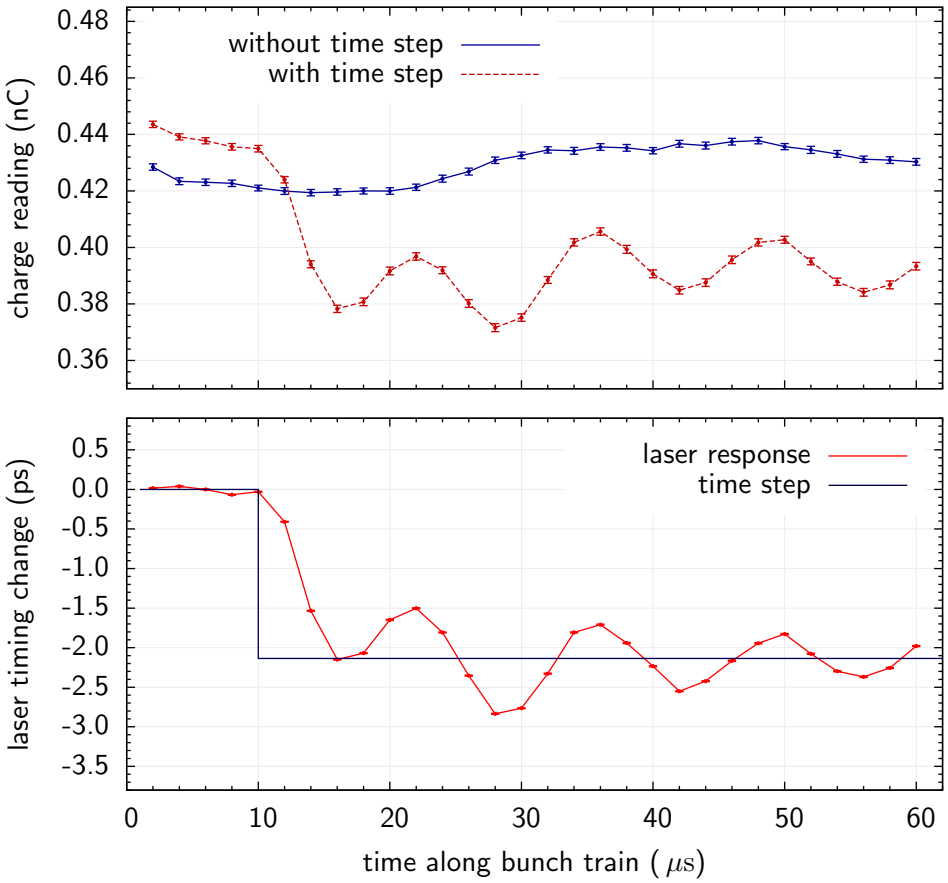

Figure 9.2: Response measurement of the photo cathode laser to a time step.

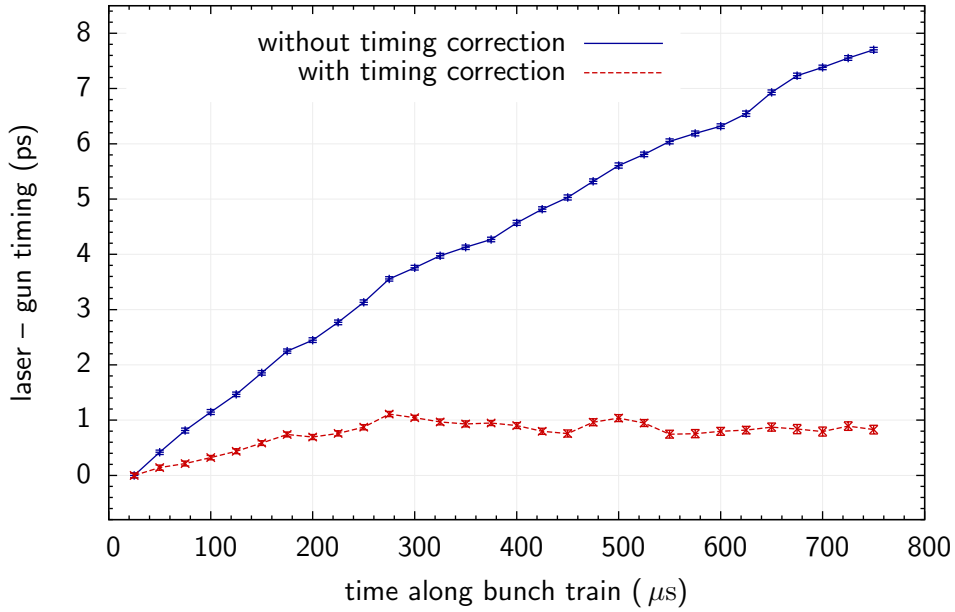

Figure 9.3: Correction of the timing between photo cathode laser and gun RF by adding a timing slope of about 6.4 ps over the 800 μs of the bunch train to the laser timing.

a limitation, since under normal conditions, such a large timing step will never be applied.

9.3 Correction of the photo-cathode laser timing across the electron macro-pulse

To evaluate systematic timing changes across the macro-pulse, a bunch train consisting of 30 pulses separated by 25 μs was generated. As before, the timing change is evaluated from the charge reading and the calibration factor. Figure 9.3 shows that the relative timing between laser and gun changes by about 8 ps over the 800 μs long bunch train. A probable reason for this behavior is a temperature change of the EOM during the macro-pulse [Sch07].

To evaluate whether a correction of this systematic timing change is possible with the timing of the photo-cathode laser, a linear timing slope of 6.4 ps was added along the 800 μs long bunch train. As one can see in Fig. 9.3, the relative timing between laser and gun can be flattened rather well as a result. Since the timing correction is much smoother than during the step-response measurement, no disturbing oscillations are visible. There is still a timing change of around 1 ps present over the first 250 μs, even after the correction. To compensate for this transient effect, a more complicated timing correction pattern has to be chosen across the macro-pulse.

Only systematic timing changes across the macro-pulse can be corrected with

such an approach. To improve the timing stability, in addition to a feed forward correction, a feedback system based on a precise timing measurement has to be applied.

10 Longitudinal feedback system

In order to improve the electron bunch arrival-time and compression stability, fast feedback systems have been developed. They are based on a BAM and on the measurement of diffraction radiation energy using a pyro-electric detector.

10.1 Bunch arrival-time feedback

The accelerating field amplitude of ACC1 has the largest influence on the bunch arrival-time. In order to improve the arrival-time stability along the bunch trains, the arrival-time information of previous bunches provided by a BAM is used to calculate an amplitude correction for the accelerating field in ACC1 (see Fig. 10.1). This is done with a PID controller implemented on the FPGA[1] of the ADC sampling the laser pulses of the BAM. The resulting amplitude correction is sent via a RocketIO transceiver to the ACC1 controller, where the correction is applied [LAF$^+$08d, LAF$^+$08b].

Figures 10.2 and 10.3 show the arrival-time stability along the bunch-train without and with feedback. Without the feedback, the arrival-time jitter is between 250 fs and 350 fs. The systematic variation along the bunch train is caused by beam loading, which was not compensated during this measurement.

The feedback loop needs the BAM information from a previous bunch. In the present configuration, there is a total delay of about 6 μs in the feedback loop which explains that the first six bunches are not stabilized. The delay has two contributions.

[1] field programmable gate array

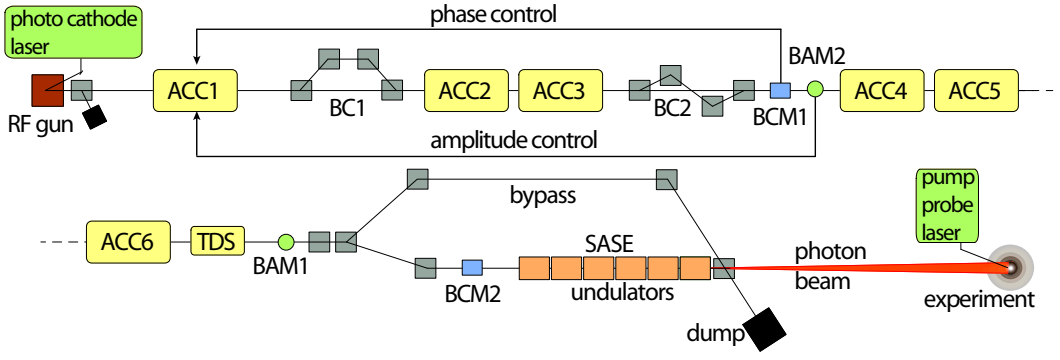

Figure 10.1: Schematic principle of the bunch arrival-time and compression feedback.

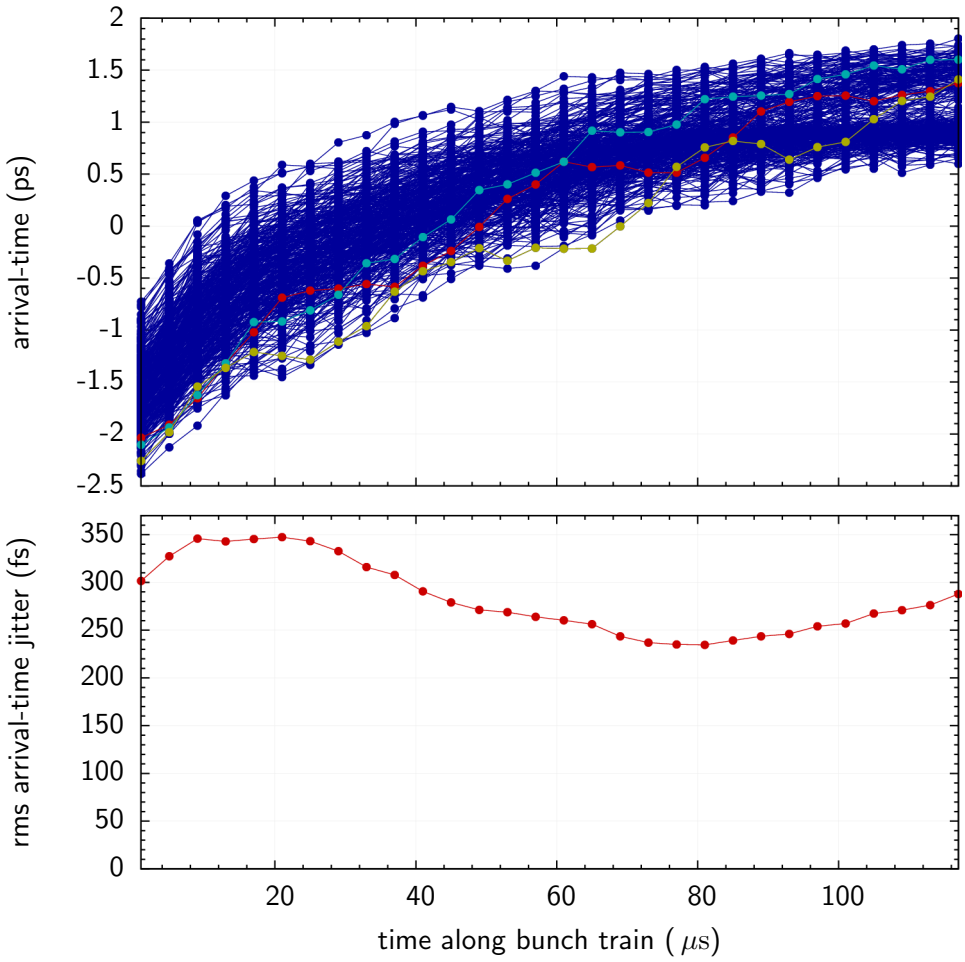

Figure 10.2: Bunch arrival-time stability of the electron beam without the arrival-time feedback. Top: arrival-times of 400 bunch trains, the indicated curves show three consecutive bunch trains. Bottom: rms arrival-time jitter over 400 bunch trains.

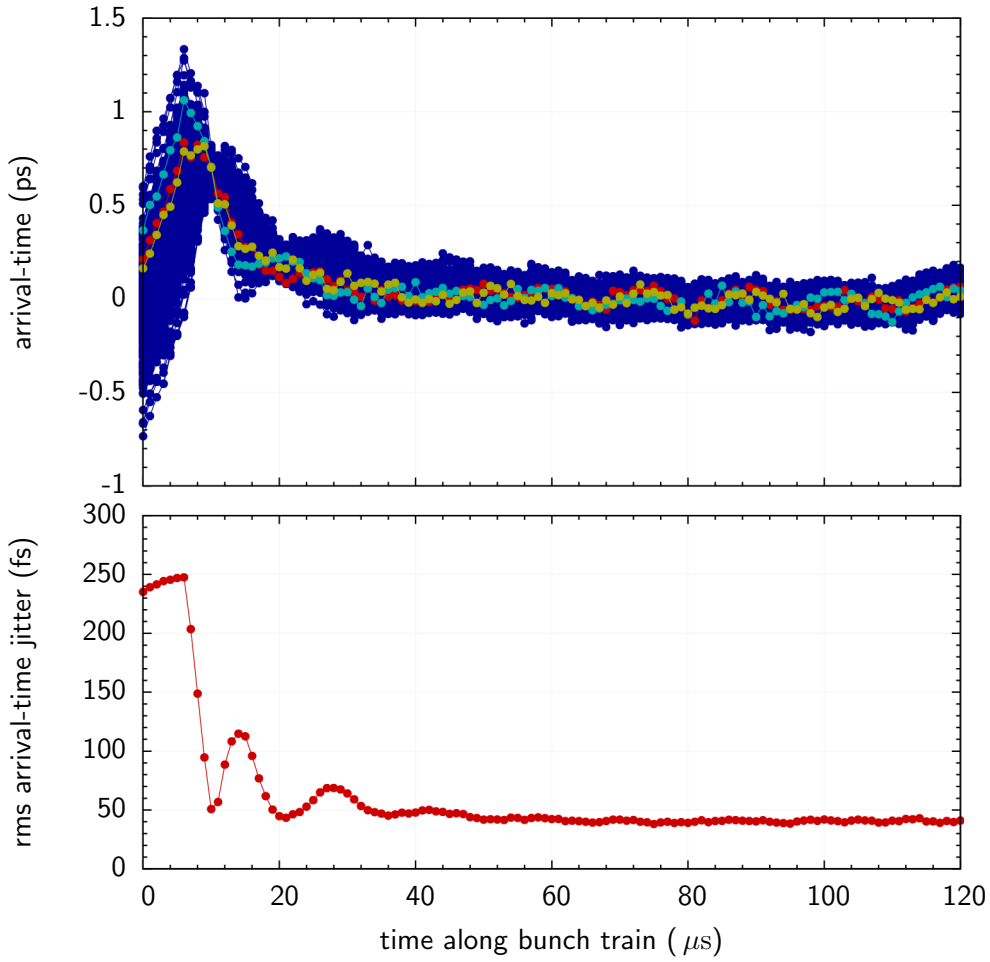

Figure 10.3: Bunch arrival-time stability of the electron beam with the arrival-time feedback active. Top: arrival-times of 400 bunch trains, the indicated curves show three consecutive bunch trains. Bottom: rms arrival-time jitter over 400 bunch trains.

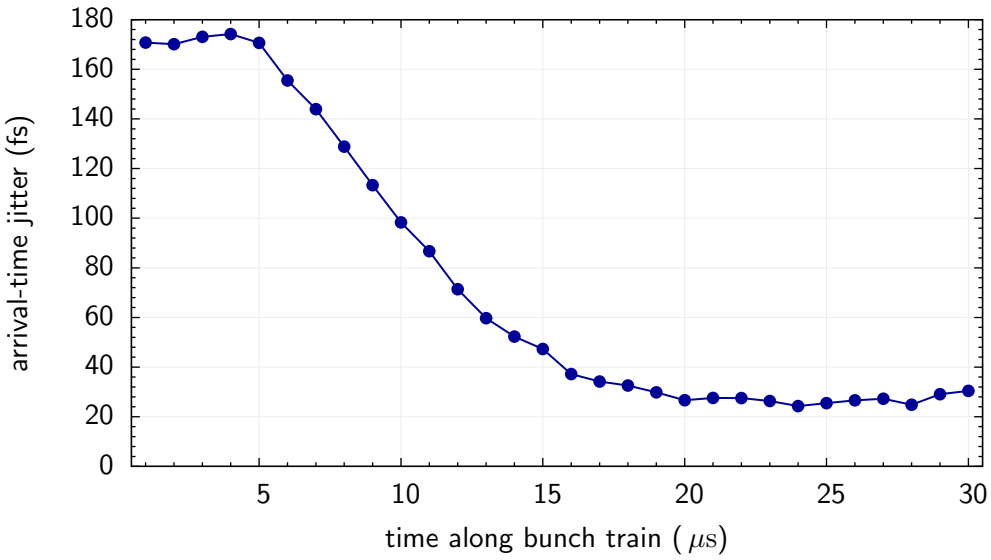

Figure 10.4: Best bunch arrival stability achieved with the feedback.

One is the time-of-flight from the electron bunch to the BAM as well as the laser pulse travel-time from the BAM to the ADC. This causes a delay of about 2 μs. The other contribution is the time needed for the feedback calculations and for the transmission to the ACC1 controller, corresponding to about 4 μs.

Since the beam loading was not stabilized by a feed-forward, the later bunches arrive later than expected. After the feedback starts acting, it takes about 20 μs until the arrival-time set-point is reached. This duration is determined by the long time constant of the superconducting cavities. Note that the time needed for the stabilization could be reduced by using a normal conducting cavity to apply the corrections. After stabilization, the arrival-time jitter along the bunch train is reduced to about 40 fs, compared to 240 fs of jitter in the unstabilized case. In this measurement, the arrival-time from BAM1 (see Fig. 10.1) was used.

The achieved stability is worse than the resolution of the BAMs. The reason is fast bunch-to-bunch noise (see Fig. 8.24) which may be caused by amplitude and phase fluctuations of the RF gun field as well as by arrival-time fluctuations of the photo cathode laser. All noise generated within the feedback latency time cannot be compensated for. From Fig. 8.24, one expects that the regulation stability is limited to around 100 fs for a latency of 6 μs. The reason for the achieved stability of 40 fs is that ACC1 was operated about 5° off-crest, so that arrival-time fluctuations of the electron source are partially compressed in the magnetic chicanes.

Figure 10.4 shows the arrival-time stability achieved after a damaged RF cable of the photo-cathode laser had been repaired. This improved the timing stability of the machine to 180 fs without the feedback. With an active arrival-time feedback, a stability of 25 fs was achieved. In this measurement BAM2 was used and the control-algorithm was improved, yielding a shorter latency time.

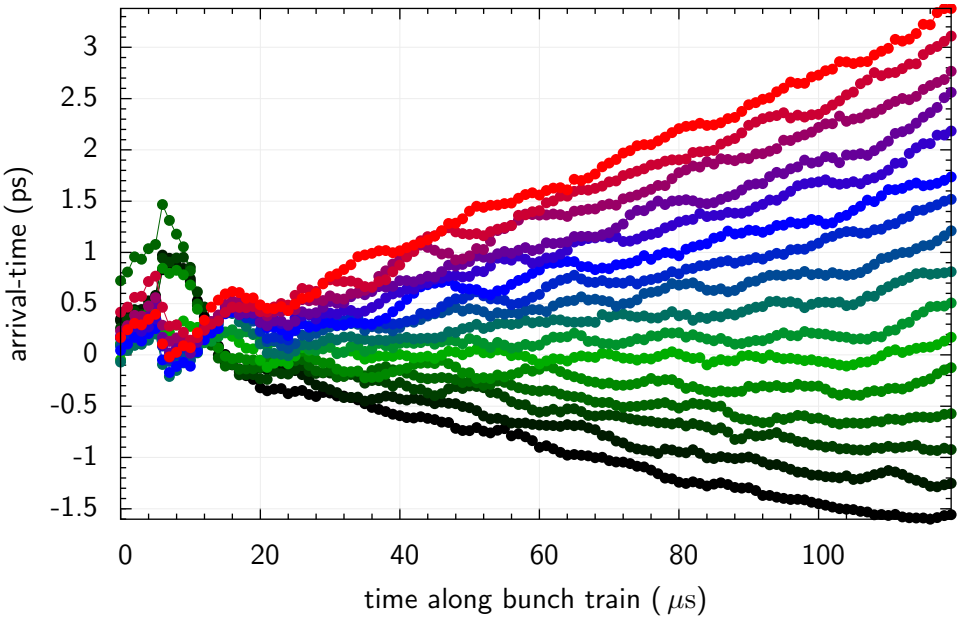

Figure 10.5: Generation of well defined arrival-time patterns along the electron bunch train using the bunch arrival-time feedback.

As we have seen in chapter 4, the bunch arrival-time changes by about 6 ps when the accelerating voltage of ACC1 is changed by 1%. By using this sensitivity factor, we can estimate the voltage stability achieved with the arrival-time feedback. The measured arrival-time stability of 25 fs corresponds to an amplitude stability of the accelerating field of $4.2 \cdot 10^{-5}$.

The digital feedback offers the possibility to define different arrival-time set-points along the bunch train. This allows, for example, to generate well defined arrival-time patterns along the bunch train (see Fig. 10.5) which can be very useful in pump-probe experiments. By this, a complete time scan can be carried out within a single bunch train.

10.2 Beam compression feedback

The same feedback scheme was applied to stabilize the bunch compression process. The bunch compression monitor (BCM) after BC2 is used as a detector. It consists of a diffraction radiator and a pyro-electric detector measuring the radiation pulse energy. Changes of the compression monitor signal are corrected for with the phase of ACC1.

The improvement on the compression stability is measured with an independent BCM located upstream the undulator (see Fig. 10.1). Figure 10.6 shows the effect of the feedback on the stability of the BCM signal. A calibration was performed, in order to deduce the ACC1 beam phase stability from the BCM signal. Without the

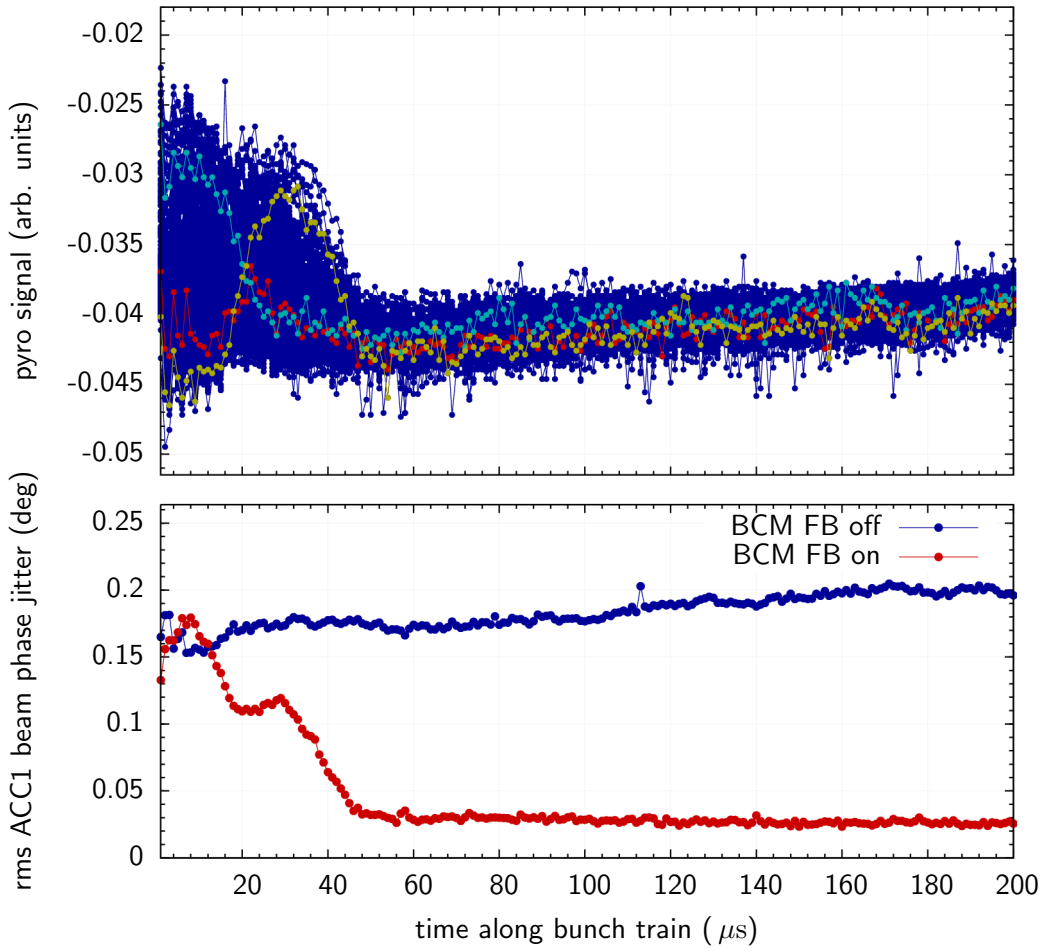

Figure 10.6: Effect of the bunch compression feedback. Top: signal of a bunch compression monitor at the end of the machine. The three indicated curves show three consecutive bunch trains. Bottom: Stability of the beam phase in ACC1 without (blue) and with (red) the bunch compression feedback.

compression feedback, the beam phase stability is about 0.2°. This is mainly limited by bunch arrival-time fluctuations from the electron source. With active feedback, an impressive ACC1 beam phase stability of 0.025° is achieved for the stabilized part of the bunch train.

During this measurement, the signal of the BCM in the feedback loop was regulated to a constant set-point. The signal of the BCM at the end of the machine, however, shows a small slope as a function of the bunch number. This could be caused by the arrival-time slope from the electron source (see chapter 9), which was not compensated during these measurements.

The bunch arrival-time feedback as well as the bunch compression feedback have been active in the measurement shown in Fig. 10.6. In this configuration, it takes longer to achieve a stabilized bunch train. The two feedbacks are not independent, since phase variations in ACC1 also change the beam energy and, therefore, the bunch arrival-time. An improved control algorithm is presently being implemented. By adding an amplitude correction to the accelerating field, when a phase change is applied, the feedbacks will be decoupled and a faster stabilization of the bunch train will be reached.

The unstabilized first part of the bunch train can in principle be prevented from producing FEL radiation by disturbing the beam orbit of these bunches with a fast kicker. This would allow removing the fluctuating FEL pulses.

The arrival-time feedback based on the BAM stabilizes the arrival-time of the beam centroid. In order to stabilize the leading spike as well, which produces the FEL radiation, the bunch shape must be kept stable. This is achieved by the compression feedback. The arrival-time relation between centroid and spike is influenced by the phase of ACC1. The simulations presented in chapter 4 show that an ACC1 beam phase stability of 0.025° corresponds in the worst case to an arrival-time fluctuation of 25 fs between the centroid and the spike.

10.3 Effect of the feedback systems on the FEL radiation stability

The arrival-time and bunch compression feedbacks lead to a significantly improved stability of the FEL pulse energies. Figure 10.7 shows the FEL radiation pulse energy along the bunch train for three different settings: without both feedbacks (top), with active bunch compression feedback (center) and with additional arrival-time stabilization (bottom).

Without any beam based feedback, a strong variation of the FEL radiation pulse energy along the bunch train is observed, caused by energy and peak current variations along the bunch train. With both feedbacks active, the pulse energy distribution is almost flat except for a minor decrease towards later bunches, which could be caused by the arrival-time slope generated in the electron source. Figure 10.8 demonstrates that the feedback loops lead to an impressive growth of the average FEL pulse energy.

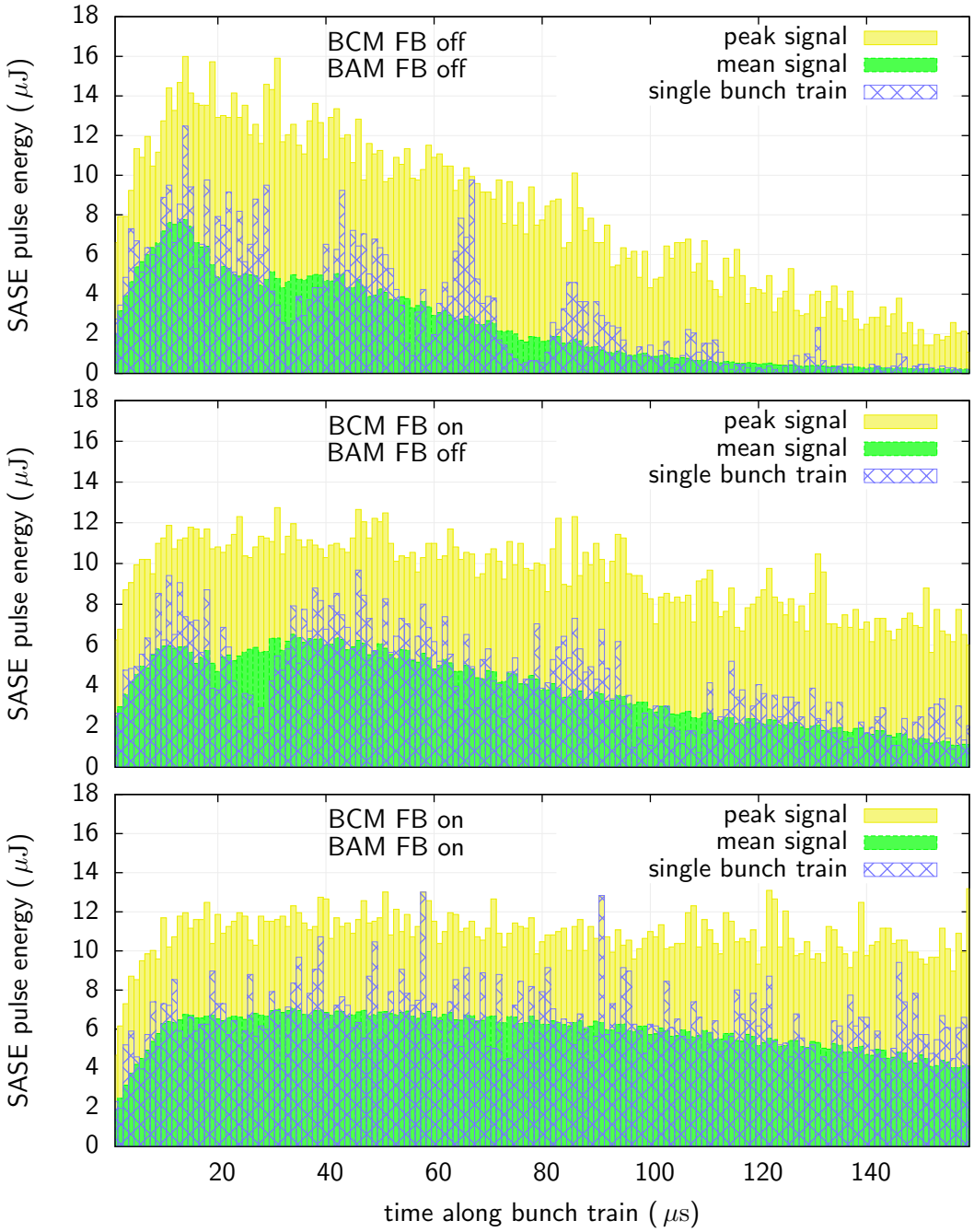

Figure 10.7: Distribution of the FEL radiation pulse energy along the bunch train with and without active bunch compression and arrival-time feedbacks. The peak and mean values are calculated over 600 bunch trains. Top: no feedbacks, center: with bunch compression feedback, bottom: with bunch-compression and arrival-time feedback.

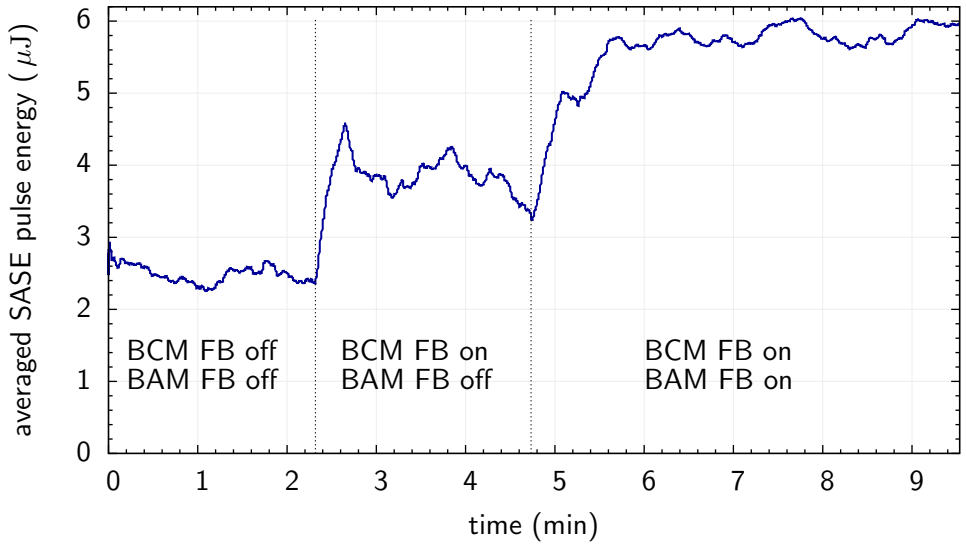

Figure 10.8: Average FEL radiation pulse energy with and without active compression and arrival-time feedbacks.

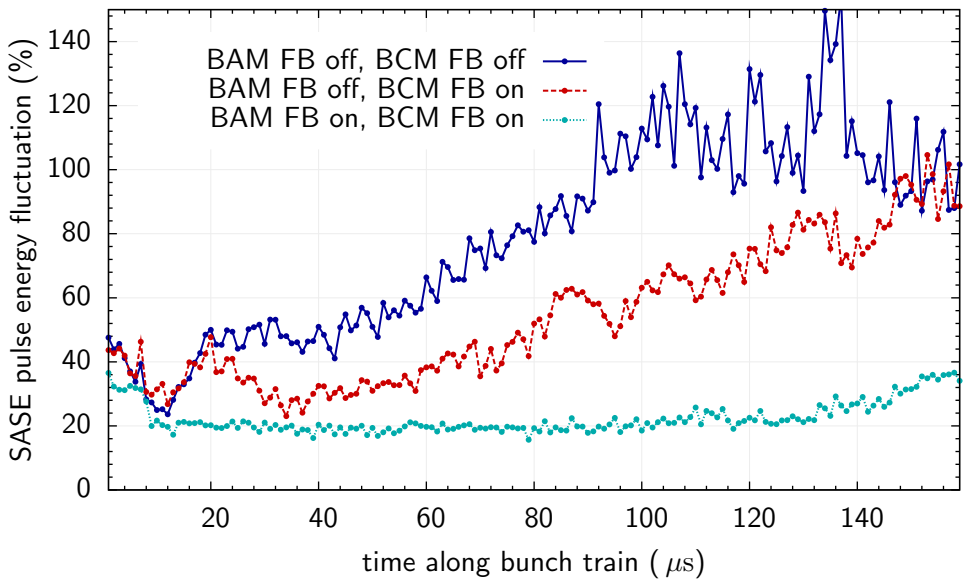

Figure 10.9: Effect of the bunch compression and arrival-time feedback on the stability of the FEL pulse energy along the bunch train. Each setting shows the fluctuations over 600 consecutive bunch trains (about 2 minutes).

The feedbacks do not only remove FEL pulse energy variations along the pulse train but they also reduce pulse energy fluctuations significantly. Figure 10.9 shows the shot-to-shot fluctuations along the bunch train for the three different settings. In this figure, the rms fluctuation of each position in the bunch-train is divided by the average pulse energy generated by this electron bunch. With the feedbacks, the fluctuations can be reduced to about 20%.

11 Conclusions and outlook

High-gain free-electron lasers are capable of generating sub-10 fs long light pulses. In order to take full advantage of these extremely short light pulses, synchronization with a so far unprecedented timing accuracy is required.

Within this thesis, an optical synchronization system providing sub-10 fs stability has been developed and was implemented at the ultra-violet and soft X-ray free-electron laser FLASH at DESY, Hamburg. The system is applied to measure the electron bunch arrival-time with an unprecedented resolution of better than 6 fs. Based on these precise arrival-time measurements, a feedback system has been implemented, stabilizing the electron bunch-arrival time to within 25 fs rms. The improved stability of the electron beam reduces fluctuations of the FEL pulse energies significantly. In future, the system will allow to perform pump-probe experiments between the FEL and external laser pulses with an accuracy of better than 10 fs.

The timing-reference of the optical synchronization system is an erbium-doped, mode-locked fiber-laser operating at a repetition rate of 216.7 MHz that has been developed in the framework of this thesis. It produces 60 to 90 fs long laser pulses and the timing information is encoded in the precise repetition frequency.

The laser pulses are distributed to the remote-locations using dispersion compensated optical fiber-links. At the remote locations, part of the laser power is reflected and travels back through the same fiber. Changes of the optical transit time are detected with femtosecond resolution using optical cross-correlation techniques. A feedback based on this measurement acts on a piezo-electric fiber-stretcher and an optical delay stage in order to stabilize the optical length of the fiber-link.

An electro-optic bunch arrival time monitor (BAM) has been developed with the intention to measure the electron bunch arrival-time using the laser pulses from a fiber-link. The signal of a beam pick-up with a bandwidth of more than 10 GHz is guided into an electro-optic modulator. Here, the laser pulse amplitude is modulated by the bipolar voltage signal from the beam pick-up. Working close to the zero-crossing of the pick-up signal, very precise arrival-time information can be extracted.

To evaluate the stability of the optical synchronization system and the resolution of the arrival-time monitors, two BAMs have been installed in a straight section of the accelerator, separated by 60 m. Each BAM was supplied by pulses from the reference laser via its own stabilized fiber-link. From the difference of the arrival-times measured by both BAMs, a BAM resolution of better than 6 fs has been deduced. This number includes the stability of the optical synchronization system.

A feedback system using the precise arrival-time information of a BAM has been developed. It acts on the bunch-arrival time by varying the acceleration field of the superconducting cavities preceding the first magnetic bunch compressor chicane

BC1. With this feedback, an impressive bunch arrival-time stability of 25 fsf could be achieved.

The feedback stabilizes the arrival time of the bunch centroid. At FLASH, the FEL radiation is produced by a leading current spike of a longitudinally compressed electron bunch. In order to stabilize also the arrival-time of this current spike, a second feedback has been developed which stabilizes the bunch compression process. It is based on measurements of the radiation energy from a diffraction radiator. Variations of the bunch-compression are corrected for by phase changes of the accelerating cavities upstream of the bunch compressor BC1. With this compression feedback, a so far unprecedented beam phase stability of 0.025° was achieved for the accelerating 1.3 GHz field.

The combination of arrival-time and bunch compression feedback improves the stability of the FEL radiation significantly. Furthermore, the feedbacks remove systematic FEL pulse energy variations along the bunch train. This is a mandatory requirement for the long bunch-train operation of superconducting FELs like FLASH or the future European XFEL.

In order to take full advantage of the optical synchronization system and the enhanced stability of the FEL, the next step will be to synchronize also the optical lasers, which are used for pump-probe experiments in combination with the FEL pulses, by cross-correlating them with the optical pulse train from a stabilized fiber-link. This will allow for timing resolutions of better than 10 fs in these kinds of experiments.

A further improvement of the electron bunch arrival-time and compression stability can be expected if it turns out possible to reduce the rapid timing fluctuations that are presently observed in the electron gun.

A Abbreviations

abbreviation	definition
ACC	accelerating module
ADC	analog to digital converter
AOM	acousto-optic modulator
ASTRA	a space charge tracking code [Flo08]
BAM	bunch arrival-time monitor
BBO	Beta Barium Borate (β-BaB_2O_4
BC	bunch compressor
BCM	bunch compression monitor
BPM	beam position monitor
CSR	coherent synchrotron radiation
CTR	coherent transition radiation
DAC	digital to analog converter
DOOCS	distributed object oriented control system
DSP	digital signal processor
EDFA	erbium-doped fiber amplifier
EOM	electro-optic modulator
EOSD	electro-optic spectral decoding
FEL	free-electron laser
FFT	fast Fourier transform
FLASH	free-electron laser in Hamburg
FPGA	field programmable gate array
FWHM	full width at half maximum
GVD	group velocity dispersion
HHG	high harmonic generation
KTP	Potassium Titanium Oxide Phosphate ($KTiOPO_4$)
LBO	Lithium Triborate (LiB_3O_5)
LCLS	Linac Coherent Light Source
MLO	master laser oscillator
MO	master oscillator
OTR	optical transition radiation

Table A.1: Abbreviations used inside the text.

abbreviation	definition
PID	proportional-integral-derivative
PITZ	photo injector test facility at DESY Zeuthen
PMD	polarization mode dispersion
PPKTP	periodically poled KTP
RF	radio frequency
rms	root mean square
SASE	self-amplified spontaneous emission
SC	space charge
SHG	second harmonic generation
SPM	self-phase modulation
TDS	transverse deflecting structure
VM	vector modulator

Table A.2: Abbreviations used inside the text (continued).

B Transfer matrix formalism

In this appendix, we introduce the transfer matrix formalism, which allows the description of the movement of particles along the beam line in a simple way. A more detailed discussion can be found in [Wie03a], [RS93], or [Bro82].

The motion of a particle in the accelerator can be characterized in canonical phase space by a six-dimensional canonical vector $\hat{\boldsymbol{X}} = (\boldsymbol{x}, \boldsymbol{p})$ with the spatial coordinates $\boldsymbol{x} = (x, y, s)$ and the momentum vector $\boldsymbol{p} = (p_x, p_y, p_s)$. Here x and y denote the transverse displacement from the design orbit and s is the coordinate along the reference orbit. Instead of the canonical phase space, it is common in accelerator physics to use the geometrical coordinates $\boldsymbol{X}$. In this geometrical phase space, also called *trace space*, the coordinates describing the particle motion are

$$\boldsymbol{X}(s) = \begin{pmatrix} x \\ x\prime \\ y \\ y\prime \\ \zeta \\ \delta \end{pmatrix}, \tag{B.1}$$

where x and y denote the horizontal and vertical displacement from the reference orbit, and ζ is the longitudinal displacement from the reference particle. The coordinates $x' = \mathrm{d}x/\mathrm{d}s$ and $y' = \mathrm{d}y/\mathrm{d}s$ describe the horizontal and the vertical slopes with respect to the reference trajectory, $\delta = \Delta p/p$ is the relative deviation from the reference momentum. If the momentum of the particles is constant also these coordinates are canonically conjugated.

A sketch of the coordinate system is shown in Fig. B.1. This coordinate system is orthogonal, right-handed (x,y,s), and it follows the reference particle along the design orbit.

In order to guide a beam of charged particles through a beam line and to change the particle energy we make use of the Lorentz force

$$\boldsymbol{F} = q(\boldsymbol{E} + \boldsymbol{v} \times \boldsymbol{B}), \tag{B.2}$$

where q is the charge of the particle, $\boldsymbol{v}$ its velocity, and $\boldsymbol{E}$ and $\boldsymbol{B}$ are the electric and magnetic field vectors. Electric fields are generally used to accelerate the particles, while magnetic fields deflect and focus the beam. In the following, we will concentrate on the effect of magnetic fields on the particle motion.

Since the equation of motion for a charged particle under the influence of an arbitrary distribution of electromagnetic fields cannot be solved explicitly, some sim-

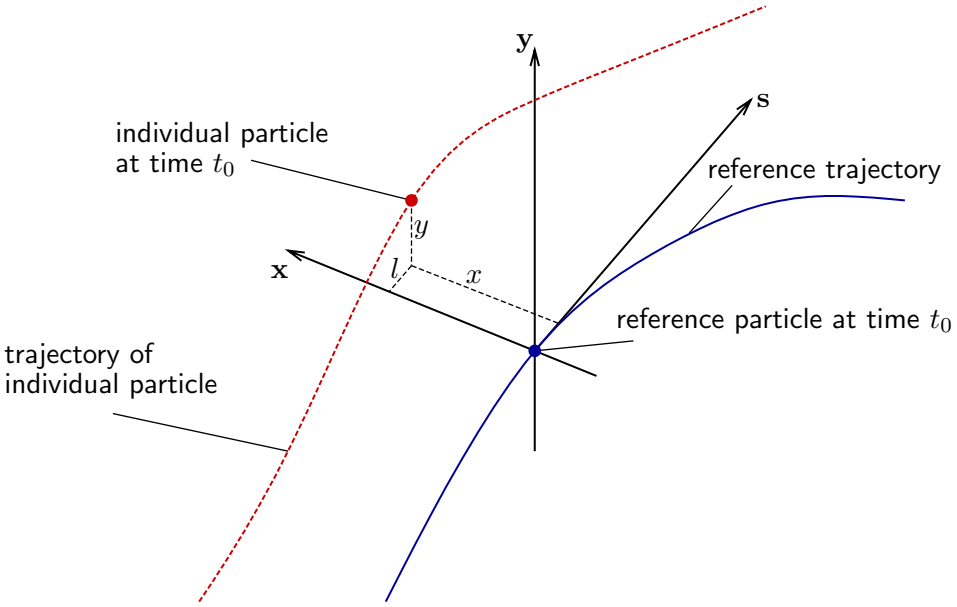

Figure B.1: Accelerator coordinate system.

plifications and restrictions have to be used in order to derive mathematical tools to describe the motion of particles in the accelerator.

If the beam line consists only of drift spaces, dipole, and quadrupole magnets, the magnetic fields depend linearly on the deviation of the particle from the reference path. Then, the equations of horizontal and vertical motion can be written as

$$u''(s) + K_u(s)u(s) = \frac{1}{\rho_u(s)} \cdot \delta, \tag{B.3}$$

where $u(s)$ stands for $x(s)$, $y(s)$, respectively. The parameter $\rho_u(s)$ denotes the bending radius of the reference trajectory at the position s and $K_u(s)$ is defined as

$$\begin{array}{rcl} K_x(s) & = & -k(s) + \frac{1}{\rho_x^2(s)} \\ K_y(s) & = & k(s) + \frac{1}{\rho_y^2(s)} \end{array} \qquad \text{with} \qquad k(s) = \frac{qg(s)}{p}\,. \tag{B.4}$$

Here $g(s)$ is the gradient of the magnetic field in the quadrupole. For the magnets, the so called *hard-edge model* is used: we assume that the magnetic field starts and ends abruptly at the beginning and end of the magnet and that the field gradient is constant inside the magnet.

Inside a quadrupole and for $K_u > 0$, the left hand side of Eq. (B.3) simplifies to the form of a harmonic oscillator. The principal solutions of this homogeneous

equation are

$$\left.\begin{array}{rcl} C_u(s) &=& \cos\left(\sqrt{K_u}s\right) \\ S_u(s) &=& \frac{1}{\sqrt{K_u}}\sin\left(\sqrt{K_u}s\right) \end{array}\right\} \quad \text{for} \quad K_u > 0$$

$$\left.\begin{array}{rcl} C_u(s) &=& \cosh\left(\sqrt{K_u}s\right) \\ S_u(s) &=& \frac{1}{\sqrt{K_u}}\sinh\left(\sqrt{K_u}s\right) \end{array}\right\} \quad \text{for} \quad K_u < 0\,. \tag{B.5}$$

Together with a particular solution u_i of the inhomogeneous equation we can formulate the general solution of Eq. (B.3) as

$$\begin{array}{rcll} u(s) &=& u_0 C_u(s) + u_0' S_u(s) + \delta \cdot \eta_u(s) & \\ u'(s) &=& u_0 C_u'(s) + u_0' S_u'(s) + \delta \cdot \eta_u'(s) & \text{with} \quad \eta_u(s) = \dfrac{u_i}{\delta}\,. \end{array} \tag{B.6}$$

The terms $\delta\cdot\eta_u(s)$ and $\delta\cdot\eta_u'(s)$ describe the momentum dependent part of the motion and the function $\eta_u(s)$ is called the *dispersion function*. The constants u_0 and u_0' are the initial parameters of the particle trajectory. It can be shown that the dispersion trajectory $\eta_u(s)$ can be expressed in terms of $C_u(s)$ and $S_u(s)$ by [RS93]

$$\eta_u(s) = \eta_{u0} C_u(s) + \eta_{u0}' S_u(s) + S_u(s)\int_{s_0}^{s} \frac{1}{\rho_u(\tau)} C_u(\tau)\,\mathrm{d}\tau - C_u(s)\int_{s_0}^{s} \frac{1}{\rho_u(\tau)} S_u(\tau)\,\mathrm{d}\tau\,, \tag{B.7}$$

where η_{u0} and η_{u0}' denote the initial conditions of the dispersion function. Equation (B.7) states that outside of bending magnets the dispersion function propagates like any other particle trajectory and therefore, outside of bending magnets we cannot distinguish the motion caused by dispersion from the 'normal' particle motion.

The longitudinal displacement ζ of an arbitrary particle with respect to the reference particle transforms according to [Bro82]

$$\begin{aligned} \zeta \;=\; & x_0 \underbrace{\int_{s_0}^{s} \frac{C_x(\tau)}{\rho_x(\tau)}\,\mathrm{d}\tau}_{R_{51}} + x_0' \underbrace{\int_{s_0}^{s} \frac{S_x(\tau)}{\rho_x(\tau)}\,\mathrm{d}\tau}_{R_{52}} + y_0 \underbrace{\int_{s_0}^{s} \frac{C_y(\tau)}{\rho_y(\tau)}\,\mathrm{d}\tau}_{R_{53}} \\ & + y_0' \underbrace{\int_{s_0}^{s} \frac{S_y(\tau)}{\rho_y(\tau)}\,\mathrm{d}\tau}_{R_{54}} + \delta R_{56} + \zeta_0, \end{aligned} \tag{B.8}$$

where ζ_0 denotes the initial longitudinal deviation from the reference particle. The matrix element R_{56} is defined as the change of the orbit length ΔS divided by the relative momentum deviation of the particle:

$$R_{56} = \frac{\Delta S}{\delta} = \int_{s_0}^{s} \frac{\eta_x(\tau)}{\rho_x(\tau)}\,\mathrm{d}\tau + \int_{s_0}^{s} \frac{\eta_y(\tau)}{\rho_y(\tau)}\,\mathrm{d}\tau. \tag{B.9}$$

Equations (B.6) and (B.8) can be combined to a matrix equation

$$\begin{pmatrix} x \\ x' \\ y \\ y' \\ \zeta \\ \delta \end{pmatrix} = \underbrace{\begin{pmatrix} R_{11} & R_{12} & R_{13} & R_{14} & R_{15} & R_{16} \\ R_{21} & R_{22} & R_{23} & R_{24} & R_{25} & R_{26} \\ R_{31} & R_{32} & R_{33} & R_{34} & R_{35} & R_{36} \\ R_{41} & R_{42} & R_{43} & R_{44} & R_{45} & R_{46} \\ R_{51} & R_{52} & R_{53} & R_{54} & R_{55} & R_{56} \\ R_{61} & R_{62} & R_{63} & R_{64} & R_{65} & R_{66} \end{pmatrix}}_{\boldsymbol{R}} \begin{pmatrix} x_0 \\ x'_0 \\ y_0 \\ y'_0 \\ \zeta_0 \\ \delta_0 \end{pmatrix}, \tag{B.10}$$

where the transfer matrix $\boldsymbol{R}$ is

$$\boldsymbol{R} = \begin{pmatrix} C_x & S_x & 0 & 0 & 0 & R_{16} \\ C'_x & S'_x & 0 & 0 & 0 & R_{26} \\ 0 & 0 & C_y & S_y & 0 & R_{36} \\ 0 & 0 & C'_y & S'_y & 0 & R_{46} \\ R_{51} & R_{52} & R_{53} & R_{54} & R_{55} & R_{56} \\ 0 & 0 & 0 & 0 & 0 & 1 \end{pmatrix}. \tag{B.11}$$

The matrix elements R_{16} and R_{36} characterize the dispersion η_u, and the elements R_{26} and R_{46} represent the angular dispersion η'_u generated by the magnet described by the transfer matrix $\boldsymbol{R}$ in the x-, y-plane, respectively:

$$\begin{aligned} R_{16} &= S_x(s) \int_{s_0}^{s} \frac{1}{\rho_x(\tau)} C_x(\tau)\,\mathrm{d}\tau - C_x(s) \int_{s_0}^{s} \frac{1}{\rho_x(\tau)} S_x(\tau)\,\mathrm{d}\tau \\ R_{26} &= S'_x(s) \int_{s_0}^{s} \frac{1}{\rho_x(\tau)} C_x(\tau)\,\mathrm{d}\tau - C'_x(s) \int_{s_0}^{s} \frac{1}{\rho_x(\tau)} S_x(\tau)\,\mathrm{d}\tau \\ R_{36} &= S_y(s) \int_{s_0}^{s} \frac{1}{\rho_y(\tau)} C_y(\tau)\,\mathrm{d}\tau - C_y(s) \int_{s_0}^{s} \frac{1}{\rho_y(\tau)} S_y(\tau)\,\mathrm{d}\tau \\ R_{46} &= S'_y(s) \int_{s_0}^{s} \frac{1}{\rho_y(\tau)} C_y(\tau)\,\mathrm{d}\tau - C'_y(s) \int_{s_0}^{s} \frac{1}{\rho_y(\tau)} S_y(\tau)\,\mathrm{d}\tau\,. \end{aligned} \tag{B.12}$$

Using Eq. (B.10) we can calculate the transformation of the vector $\boldsymbol{X}$ through the entire beam line by simple multiplications of the transfer matrices $\boldsymbol{R}_j$ $(j = 1, \ldots, n)$ corresponding to the different elements in the beam line

$$\boldsymbol{X}_f = \boldsymbol{R}_n \cdot \boldsymbol{R}_{n-1} \cdot \ldots \cdot \boldsymbol{R}_1 \cdot \boldsymbol{X}_i, \tag{B.13}$$

where the subscripts i and f denote the initial and final position, respectively.

The transfer matrices of the most common beam line elements can be found in Appendix C.

C Transfer matrices of important beam line elements

The derivation of the most common beam line elements can be found in [RS93] and [Bro82]. Here we present only the results. It is always assumed that the elements are mounted in a way that they do not produce any coupling between the (x, x')- and (y, y')-plane.

Drift Space is the simplest element in a beam line. In the matrix formalism it can be described by the transfer matrix

$$\boldsymbol{R}_{\mathrm{Drift}}(l) = \begin{pmatrix} 1 & l & 0 & 0 & 0 & 0 \\ 0 & 1 & 0 & 0 & 0 & 0 \\ 0 & 0 & 1 & l & 0 & 0 \\ 0 & 0 & 0 & 1 & 0 & 0 \\ 0 & 0 & 0 & 0 & 1 & 0 \\ 0 & 0 & 0 & 0 & 0 & 1 \end{pmatrix}, \tag{C.1}$$

where l denotes the length of the drift space along the beam line. Since $1/\rho = 0$, where ρ denotes the bending radius of the reference trajectory, no dispersion is created in a drift space (see Eq. (B.12)).

Quadrupole Magnet with a uniform magnetic field gradient g can be described with help of a parameter $k = eg/p$, where p is the reference momentum of the particles. For $k > 0$ the transfer matrix is

$$\boldsymbol{R}_{\mathrm{Quad}}(k, l) = \begin{pmatrix} \cosh\phi & \frac{1}{\sqrt{|k|}}\sinh\phi & 0 & 0 & 0 & 0 \\ \sqrt{|k|}\sinh\phi & \cosh\phi & 0 & 0 & 0 & 0 \\ 0 & 0 & \cos\phi & \frac{1}{\sqrt{|k|}}\sin\phi & 0 & 0 \\ 0 & 0 & -\sqrt{|k|}\sin\phi & \cos\phi & 0 & 0 \\ 0 & 0 & 0 & 0 & 1 & 0 \\ 0 & 0 & 0 & 0 & 0 & 1 \end{pmatrix}. \tag{C.2}$$

For $k < 0$ the on-diagonal 2×2-matrices for x and y have to be interchanged:

$$\boldsymbol{R}_{\mathrm{Quad}}(k,l) = \begin{pmatrix} \cos\phi & \frac{1}{\sqrt{|k|}}\sin\phi & 0 & 0 & 0 & 0 \\ -\sqrt{|k|}\sin\phi & \cos\phi & 0 & 0 & 0 & 0 \\ 0 & 0 & \cosh\phi & \frac{1}{\sqrt{|k|}}\sinh\phi & 0 & 0 \\ 0 & 0 & \sqrt{|k|}\sinh\phi & \cosh\phi & 0 & 0 \\ 0 & 0 & 0 & 0 & 1 & 0 \\ 0 & 0 & 0 & 0 & 0 & 1 \end{pmatrix} \tag{C.3}$$

In both equations $\phi = l\sqrt{|k|}$, where l is the magnetic length of the quadrupole. For $k > 0$ the quadrupole is focusing in the vertical plane and defocusing in the horizontal plane. For $k < 0$ the situation is vice versa. Since $1/\rho = 0$, no dispersion is created in a quadrupole magnet.

Sector Dipole Magnet is a dipole magnet whose end faces are perpendicular to the central beam trajectory. The transfer matrix of a horizontally deflecting sector dipole magnet with a uniform magnetic field is

$$\boldsymbol{R}_{\mathrm{SDM}}(\rho_x,\alpha) = \begin{pmatrix} \cos\alpha & \rho_x\sin\alpha & 0 & 0 & 0 & \rho_x(1-\cos\alpha) \\ -\frac{1}{\rho_x}\sin\alpha & \cos\alpha & 0 & 0 & 0 & \sin\alpha \\ 0 & 0 & 1 & \rho_x\alpha & 0 & 0 \\ 0 & 0 & 0 & 1 & 0 & 0 \\ -\sin\alpha & -\rho_x\,(1-\cos\alpha) & 0 & 0 & 1 & -\rho_x\,(\alpha-\sin\alpha) \\ 0 & 0 & 0 & 0 & 0 & 1 \end{pmatrix}. \tag{C.4}$$

Here, α is the deflection angle and ρ_x denotes the bending radius of the beam trajectory. Since $1/\rho_x \neq 0$, horizontal dispersion is generated.

Rectangular Dipole Magnet is a dipole magnet with parallel magnet faces, i.e. its end faces are not perpendicular to the central beam trajectory. If the magnet is installed symmetrically with respect to the central beam trajectory, it can be described introducing an additional edge focusing matrix

$$\boldsymbol{F}(\rho_x,\alpha) = \begin{pmatrix} 1 & 0 & 0 & 0 & 0 & 0 \\ \frac{\tan\alpha/2}{\rho_x} & 1 & 0 & 0 & 0 & 0 \\ 0 & 0 & 1 & 0 & 0 & 0 \\ 0 & 0 & -\frac{\tan\alpha/2}{\rho_x} & 1 & 0 & 0 \\ 0 & 0 & 0 & 0 & 1 & 0 \\ 0 & 0 & 0 & 0 & 0 & 1 \end{pmatrix}. \tag{C.5}$$

The transfer matrix for the rectangular dipole magnet can then be expressed as a matrix product of $\boldsymbol{F}(\rho_x,\alpha)$ and $\boldsymbol{R}_{\mathrm{SDM}}(\rho_x,\alpha)$:

$$\boldsymbol{R}_{\mathrm{RDM}}(\rho_x,\alpha) = \boldsymbol{F}(\rho_x,\alpha)\cdot\boldsymbol{R}_{\mathrm{SDM}}(\rho_x,\alpha)\cdot\boldsymbol{F}(\rho_x,\alpha)\,. \tag{C.6}$$

Since $1/\rho_x \neq 0$, horizontal dispersion is generated.

D Propagation of light pulses in optical fibers

A short introduction to the propagation of ultra-short light pulses through optical fibers is given. It is based on [Agr01], where much more details can be found.

D.1 Fiber losses

Optical fibers provide an excellent tool for distributing optical light at minimum losses. The light power $P(L)$ after transmission through an optical fiber of length L can be expressed by

$$P(L) = P_0 e^{-\alpha L}\,, \tag{D.1}$$

where P_0 is the initial light power and α the attenuation constant. For standard single mode fibers at a wavelength around 1550 nm, the attenuation constant can be as small as 0.2 dB/ km.

D.2 Dispersion

The refractive index inside of materials depends on the optical wavelength and when an optical pulse propagates through an optical fiber of length L, the different frequency components receive a phase shift of

$$\phi(\omega) = n_0(\omega) k L\,, \tag{D.2}$$

where $n_0(\omega)$ is the frequency dependent refractive index and

$$k = \frac{2\pi}{\lambda} \tag{D.3}$$

the angular wave number.

The product $n_0(\omega)k$ is called the mode-propagation constant $\beta(\omega)$ and by expanding it into a Taylor series about the central frequency of the laser pulse ω_0

$$\beta(\omega) = n_0(\omega)\frac{\omega}{c} = \beta_0 + \beta_1(\omega-\omega_0) + \frac{1}{2}\beta_2(\omega-\omega_0)^2 + \frac{1}{6}\beta_3(\omega-\omega_0)^3 + \cdots\,, \tag{D.4}$$

where

$$\beta_k = \left(\frac{\mathrm{d}^k\beta}{\mathrm{d}\omega^k}\right)_{\omega=\omega_0} \qquad \text{with} \quad \mathrm{k} \in \mathbb{N}_0\,, \tag{D.5}$$

the fact that the refractive index differs for different optical wavelengths can be expressed in the coefficients β_i. The propagation of the optical pulse with the group velocity $v_g = n_0(\omega_0)/c$ is described by the parameter β_1, the parameter β_2 describes the group velocity dispersion (GVD), and the terms β_k with $k > 2$ are describing the higher order dispersion, which have to be considered, if the spectral width $\Delta\omega$ is not small compared to the central frequency ω_0.

For pulse broadening due to dispersion, the most important parameter is β_2 and in fiber optics, typically the so called dispersion parameter D is used, which is connected to β_2 by

$$D = -\frac{2\pi c}{\lambda^2}\beta_2 \,. \tag{D.6}$$

D.3 Dispersive pulse broadening

To evaluate the broadening of an optical pulse due to dispersion let us parametrize the electrical field distribution $\boldsymbol{E}(\boldsymbol{r}, t)$ of the optical pulse by

$$\boldsymbol{E}(\boldsymbol{r}, t) = \frac{1}{2}\hat{x}\left[F(x, y)A(z, t)e^{i(\beta_0 z - \omega_0 t)} + \text{c.c.}\right] , \tag{D.7}$$

where x and y are the transverse coordinates and z the longitudinal coordinate inside the optical fiber, $F(x, y)$ the modal distribution inside the fiber, and $A(z, t)$ the slowly varying pulse envelope.

With the Fourier-transformation, the transition between time-domain and frequency-domain can be made, which for the pulse envelope $A(z, t)$ is given by

$$\tilde{A}(z, \omega - \omega_0) = \int_{-\infty}^{\infty} A(z, t)e^{i(\omega-\omega_0)t}\mathrm{d}t \tag{D.8}$$

$$A(z, t) = \frac{1}{2\pi}\int_{-\infty}^{\infty} \tilde{A}(z, \omega - \omega_0)e^{-i(\omega-\omega_0)t}\mathrm{d}(\omega - \omega_0) \,. \tag{D.9}$$

The effect of dispersion can be considered in frequency domain by a phase shift and after a fiber of length L the pulse envelope is given by

$$\tilde{A}(z + L, \omega - \omega_0) = \tilde{A}(z, \omega - \omega_0)e^{iL(\beta_0+\beta_1(\omega-\omega_0)+\frac{1}{2}\beta_2(\omega-\omega_0)^2+\frac{1}{6}\beta_3(\omega-\omega_0)^3+\cdots)} \,. \tag{D.10}$$

Only the β_k with $k > 2$ lead to a pulse broadening.

After the dispersive phase shift has been applied in the frequency domain, the pulse can be transformed back into time domain according to Eq. D.9, and the phase shift $\phi_D(z, t)$ due to dispersion can be determined from the separation of the complex envelope function $A(z + L, t)$ according to

$$A(z + L, t) = |A(z + L, t)|\, e^{i\phi_D(z,t)} \,. \tag{D.11}$$

For a transform limited Gaussian-shaped pulse envelope

$$A(z, t) = A_0 e^{-\frac{t^2}{2\sigma^2 T_0}} \tag{D.12}$$

the above phase shift due to a non-vanishing β_2 leads to a pulse broadening which can be expressed in terms of the dispersive length

$$L_D = \frac{\sigma_{T_0}^2}{|\beta_2|} \,. \tag{D.13}$$

After the fiber of length L, the pulse length is increased to

$$\sigma_T(L) = \sigma_{T_0} \left[1 + \left(\frac{L}{L_D} \right)^2 \right]^{\frac{1}{2}} \,. \tag{D.14}$$

For a Gaussian pulse with a duration of 100 fs FWHM, the dispersive length is about 7.9 cm in a standard single mode fiber.

D.4 Self-phase modulation

Due to the small core-size and long interaction length in an optical fiber, the laser pulses can experience significant nonlinearities even at low laser pulse energies. The most important nonlinear effect is the dependence of the refractive index of the fiber on the optical intensity. In first order, the refractive index $n(\omega, |E|^2)$ can be expressed by

$$n(\omega, |E|^2) = n_0(\omega) + n_2 \, |E|^2 \,, \tag{D.15}$$

where $n_0(\omega)$ is the refractive index for very small light intensities as it was introduced above, $|E|^2$ is the optical intensity, and n_2 is a coefficient characterizing the strength of the nonlinearity, which depends on the material and geometric dimensions of the optical fiber.

An optical pulse propagating through a fiber of length L experiences a phase change due to nonlinearities which is given by

$$\phi_{\mathrm{NL}} = n_2 \, |E|^2 \, kL \,. \tag{D.16}$$

Since this phase change is induced by the pulse itself, ϕ_{NL} is referred to as *self-phase modulation* (SPM).

Instead of n_2 quite often the parameter

$$\gamma = \frac{n_2 k}{A_{\mathrm{eff}}} \tag{D.17}$$

is used, where A_{eff} is the effective core area, defined as

$$A_{\mathrm{eff}} = \frac{\left(\iint_{-\infty}^{\infty} |F(x,y)|^2 \, \mathrm{d}x\mathrm{d}y \right)^2}{\iint_{-\infty}^{\infty} |F(x,y)|^4 \, \mathrm{d}x\mathrm{d}y} \,. \tag{D.18}$$

With γ, the phase change by SPM can be expressed by

$$\phi_{\mathrm{NL}}(t) = \gamma P(t) L \,, \tag{D.19}$$

where $P(t)$ it the time dependent laser power.

Similar to the dispersive length a nonlinear length can be defined, providing the length scale over which nonlinear effects become important for the pulse evolution:

$$L_{\mathrm{NL}} = \frac{1}{\gamma P_0}\,. \tag{D.20}$$

Here, P_0 is the peak power of the laser pulse. In standard single mode fibers with $\gamma \approx 1\,\mathrm{W}^{-1}\,\mathrm{km}^{-1}$, the nonlinear length is around 1.1 m for a Gaussian-shaped laser pulse with a duration of 100 fs FWHM and a pulse energy of 100 pJ. If $L_D \ll L_{\mathrm{NL}}$, the dispersive pulse broadening occurs much faster than the formation of nonlinear distortions, so that the effect of nonlinearities is negligible.

D.5 Nonlinear Schroedinger Equation and split step technique

The propagation of the envelope function A in optical fibers is described by the nonlinear Schrödinger (NLS) equation which includes all the effects discussed above. Its derivation can be found in many textbooks, also in [Agr01], and it is given by

$$\begin{aligned}\frac{\partial A}{\partial z} + \frac{\alpha}{2}A + \frac{i\beta_2}{2}\frac{\partial^2 A}{\partial T^2} - \frac{\beta_3}{6}\frac{\partial^3 A}{\partial T^3} \\ = i\gamma\left(|A|^2 A + \frac{i}{\omega_0}\frac{\partial}{\partial T}\left(|A|^2 A\right) - T_R A\frac{\partial |A|^2}{\partial T}\right)\,.\end{aligned} \tag{D.21}$$

A frame of reference moving with the group velocity $v_g = 1/\beta_1$ is used in this equation and T is defined by

$$T = t - \beta_1 z\,. \tag{D.22}$$

The left hand side of the Eq. D.21 describes the dispersive effects and the attenuation of the laser pulses inside the fiber, while the right hand side includes the nonlinear effects. In addition to the self phase modulation discussed in the previous section, two more nonlinear effects are included in Eq. D.21: The term proportional to ω^{-1} describes the effect of *self-steepening*, which occurs for very short and broadband optical pulses and causes a reduced velocity with which the peak of the pulse propagates. This leads to an increasing slope of the trailing part of the pulse. The last term, which is proportional to T_R, describes the Raman effect: If the optical spectrum becomes very broad, the shorter-wavelength tail can transfer power to the longer-wavelength tail. The parameter T_R is around 3 fs at a wavelength of 1550 nm.

It is not possible to solve Eq. D.21 analytically. The equation can, however, be solved numerically with the so called split-step Fourier method. In this method, the dispersive and the nonlinear interactions are treated separately while the pulse is propagated from z to $z + \Delta z$. In a first step, the effect of nonlinearities on the initial pulse envelope function $A(z, T)$ is applied. The resulting envelope function is Fourier transformed in the frequency domain and the dispersive effects are applied according

to D.10. The resulting envelope function $A(z, \omega - \omega_0)$ is transformed back into the time domain using the inverse Fourier transformation and the next propagation steps from $z + \Delta z$ to $z + 2\Delta z$ and so on are calculated in the same way. By using a fast Fourier transform (FFT) algorithm, this scheme is relatively fast.

E Images and drawings of selected experimental set-ups

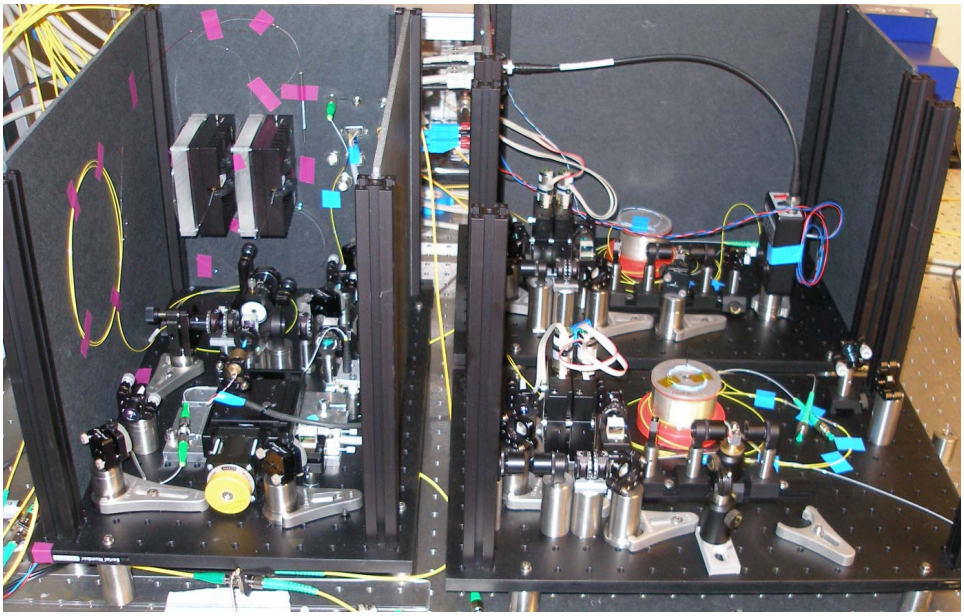

Figure E.1: Prototypes of the master laser oscillator (left) and two fiber-link stabilization units (right) used at FLASH.

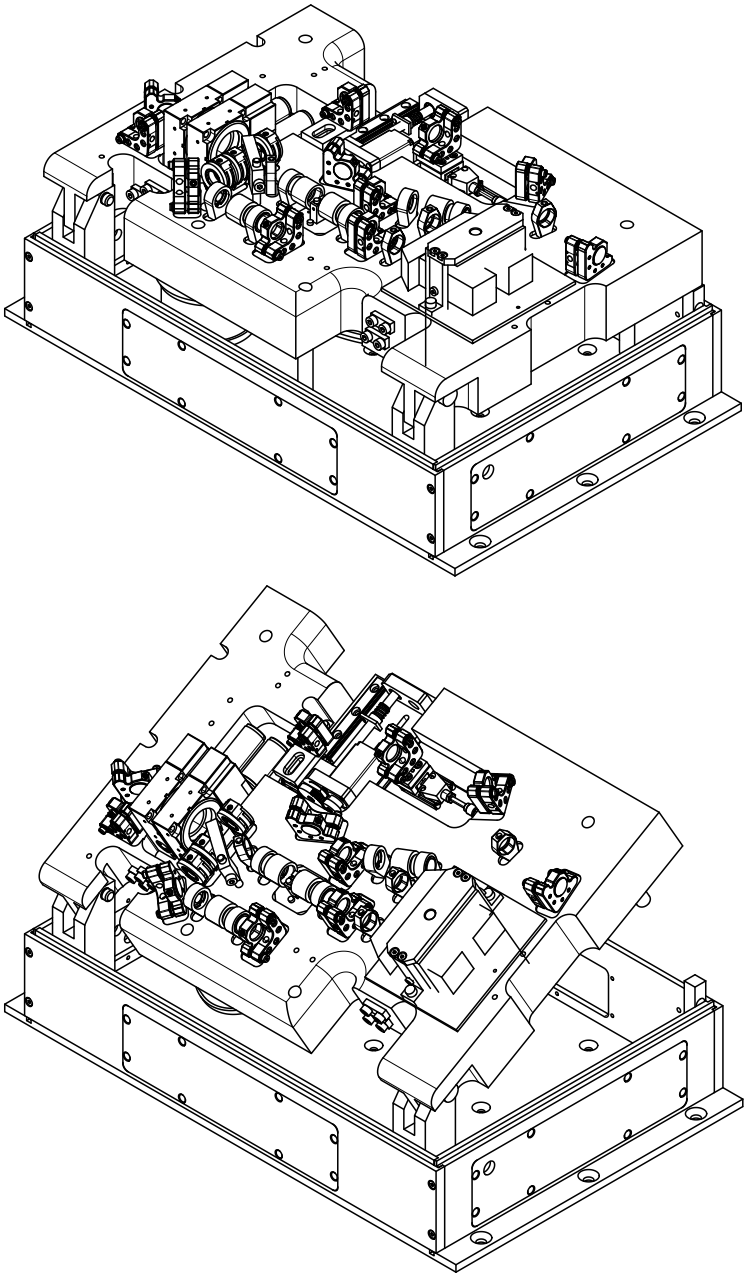

Figure E.2: Engineered version of the fiber-link stabilization front-end. The fiber spool with dispersion compensating fiber is installed underneath the optical set-up of the balanced cross-correlator. The bottom layer contains the electronics for a power level monitoring as well as an RF based back-up circuit to monitor fiber-link length changes.

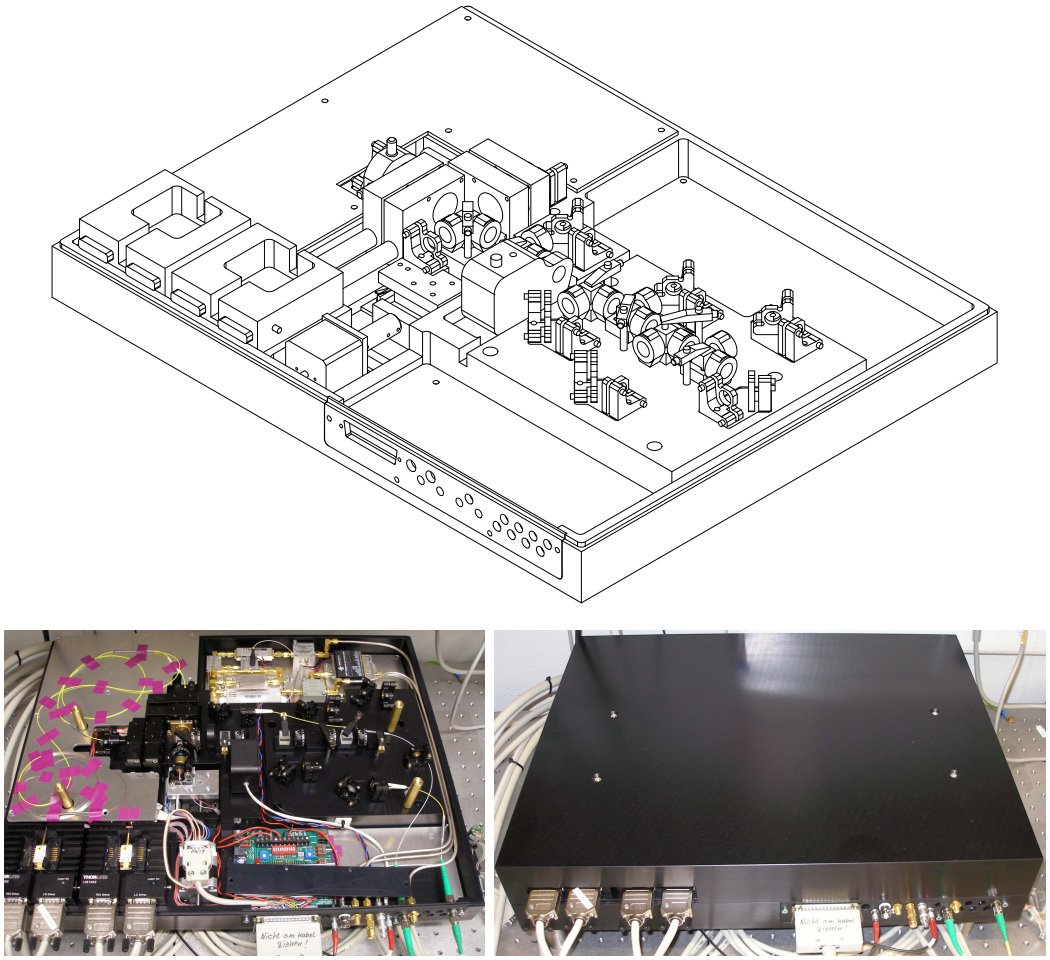

Figure E.3: Engineered version of the master laser oscillator (MLO). The setup includes the laser as well as a light distribution unit with six output ports. The fiber part of the laser oscillator is temperature stabilized and four wave-plates inside the oscillator are motorized. An RF based circuit to synchronize the laser to an RF source is also included.

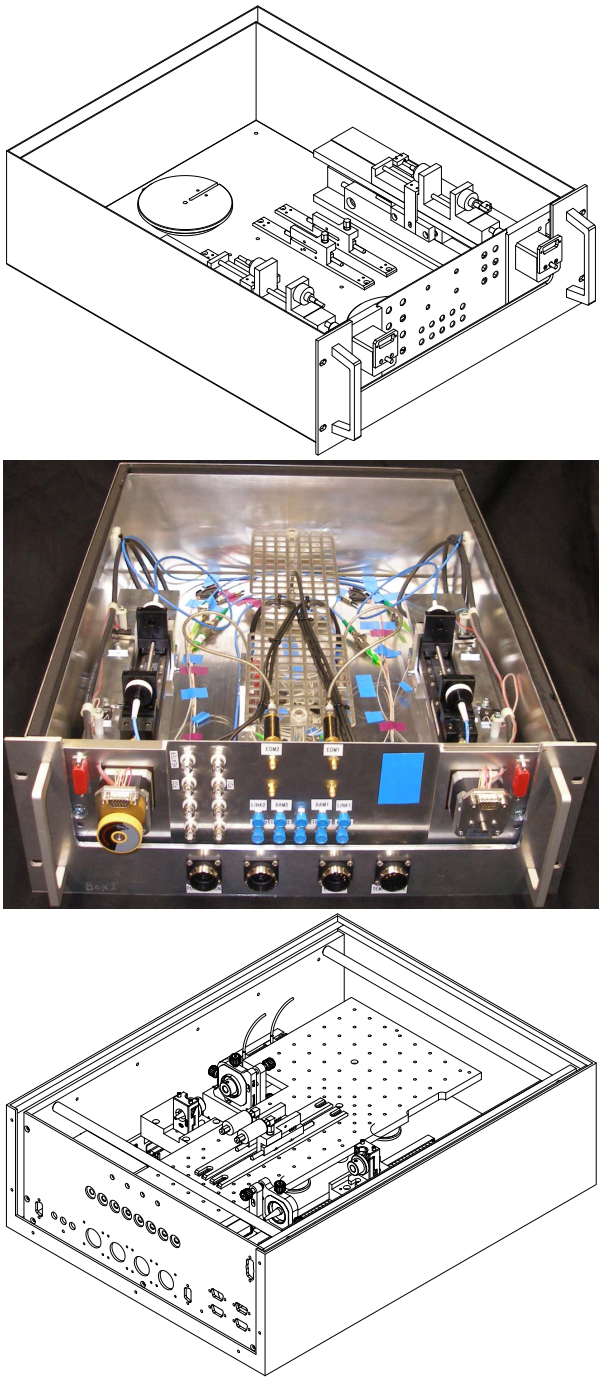

Figure E.4: Technical drawing and image of the optical front-end used for the bunch arrival-time measurements (top and middle). Both BAMs used during this thesis are based on this design. The bottom drawing shows an improved design. Among other things, optical delay stages with a significantly improved reliability are used.

Figure E.5: BAM readout and regulation electronics. The aluminum chassis contains two photo detectors the signals of which are split and connected to two 16 bit, 108.3 MHz ADCs each. Adequate delays ensure that the two ADCs sample peak and baseline of the laser pulses coming from an optical BAM front-end. Alternatively, one of the four ADCs can be used to sample the signal of a bunch compression monitor. The FPGA installed on the VME board calculates the fast correction signals for the bunch arrival-time and bunch compression feedbacks. These corrections are sent via an optical RocketIO link (green cables) to the digital controller board of the first accelerating module ACC1.

Bibliography

[A+00] B. Aune et al., *Superconducting TESLA cavities*, Phys. Rev. ST AB **3** (2000).

[A+02a] J. Arthur et al., *Linac coherent light source (LCLS) conceptual design report*, Tech. Report SLAC-R-593, SLAC, 2002.

[A+02b] V. Ayvazyan et al., *Generation of GW radiation pulses from a VUV free electron laser operating in the femtosecond regime*, Phys. Rev. Lett. **88** (2002).

[A+02c] V. Ayvazyan et al., *A new powerful source for coherent VUV radiation: Demonstration of experimental growth and saturation at the TTF free electron laser*, Eur. Phys. J. D **20** (2002), 149–156.

[A+06] V. Ayvazyan et al., *First operation of a free-electron laser generating GW power radiation at 32 nm wavelength*, Eur. Phys. J. D **37** (2006), 297 – 303.

[AAA+00] J. Andruszkow et al., *First observation of self-amplified spontaneous emission in a free-electron laser at 109 nm wavelength*, Phys. Rev. Lett. **85** (2000), no. 18, 3825–3829 (english).

[AAA+07] W. Ackermann et al., *Operation of a free-electron laser from the extreme ultraviolet to the water window*, Nature Photonics **1** (2007), 336 – 342.

[ABC+07] M. Altarelli et al., *The European X-Ray Free-Electron Laser - Technical design report*, Tech. Report DESY 2006-097, DESY, 2007.

[ABH+06] K. Abrahamyan et al., *Experimental characterization and numerical simulations of the electron source at PITZ*, Nucl. Instr. and Meth. A **558** (2006), 249 – 252.

[Agr01] G. P. Agrawal, *Nonlinear fiber optics*, ACADEMIC PRESS, 2001.

[Aud08] F. Audet, *PMD vs. mode coupling*, application note 186, EXFO, 2008.

[AZDK08] G. Angelova, V. Ziemann, M. Dohlus and Y. Kot, *The XFEL laser heater*, Proceedings of the EPAC 2008 Conference, Genoa, Italy, 2008.

[Azi09] A. Azima, private communication, January 2009.

[AZM+08] G. Angelova et al., *Observation of two-dimensional longitudinal-transverse correlations in an electron beam by laser-electron interactions*, Phys. Rev. ST AB **11** (2008).

[B+01] R. Brinkmann et al., *TESLA: The superconducting electron positron linear collider with an integrated X-ray laser laboratory. Technical design report. Part 2: The accelerator*, Tech. report, DESY-01-011, 2001.

[B+07] C. Bocchetta et al., *FERMI@Elettra - Conceptual Design Report*, Tech. report, Sincrotrone Trieste, 2007.

[BCF+02] R. Baraniuk et al., *Rice Wavelet Toolbox*, Dec 2002, www.dsp.rice.edu/software/rwt.shtml.

[Beh08] C. Behrens, *Detection and spectral measurements of coherent synchrotron radiation at FLASH*, Master's thesis, University of Hamburg, 2008.

[Beu07] B. Beutner, *Measurement and analysis of coherent synchrotron radiation effects at FLASH*, Ph.D. thesis, University of Hamburg, 2007.

[BJM+04] G. Berden et al., *Electro-optic technique with improved time resolution for real-time, nondestructive, single-shot measurements of femtosecond electron bunch profiles*, Phys. Rev. Lett. **93** (2004), no. 11.

[Bro82] K. L. Brown, *A first- and second-order matrix theory for the design of beam transport systems and charged particle spectrometers*, SLAC Report 75 (1982).

[BSP+94] R. Bonifacio, L. D. Salvo, P. Pierini, N. Piovella and C. Pellegrini, *Spectrum, temporal structure, and fluctuations in a high-gain free-electron laser starting from noise*, Phys. Rev. Lett. **73** (1994), 70 – 73.

[Cav05] A. L. Cavalieri, *Clocking femtosecond x rays*, Phys. Rev. Lett. **94** (2005).

[CSIK07] J. Chen, J. W. Sickler, E. P. Ippen and F. X. Kärtner, *High repetition rate, low jitter, low intensity noise, fundamentally mode-locked 167 fs soliton Er-fiber laser*, Opt. Lett. **32** (2007), no. 11, 1566 – 1568.

[CSS05] S. Casalbuoni, B. Schmidt and P. Schmueser, *Far-infrared transition and diffraction radiation part I: Production, diffraction effects and optical propagation*, Tech. Report TESLA Report 2005-15, DESY, 2005.

[DH08] H. Delsim-Hashemi, *Infrared single shot diagnostics for the longitudinal profile of the electron bunches at FLASH*, Ph.D. thesis, University of Hamburg, 2008.

[Emm01] P. Emma, *X-band RF harmonic compensation for linear bunch compression in the LCLS*, Tech. Report SLAC-TN-05-004, SLAC, November 2001.

[FFG+01] M. Ferrario, K. Flöttmann, B. Grigoryan, T. Limberg and P. Piot, *Conceptual design of the XFEL photoinjector*, Tech. Report TESLA FEL 2001-03, DESY, 2001.

[FLL+88] M. Ferray et al., *Multiple-harmonic conversion of 1064 nm radiation in rare gases*, J. Phys. B: Atom. Molec. Phys. **21** (1988), L31–L35.

[Flo08] K. Floettmann, *ASTRA - A space charge tracking algorithm*, DESY, 2008.

[G+05] L. Giannessi et al., 1st *Technical Design Report for the seeding @ SPARC experiment*, Tech. report, INFN-LNF, 2005.

[G+07] O. Grimm et al., *Magnetic measurements with the FLASH infrared undulator*, TESLA FEL 2007-08, University of Hamburg, 2007.

[GAB+08] C. Gahl et al., *A femtosecond x-ray/optical cross-correlator*, Nature Photonics **2** (2008), 165 – 169.

[Ger07] C. Gerth, *Synchrotron radiation monitor for energy spectrum measurements in the bunch compressor at FLASH*, Proceedings of the DIPAC 2007 conference, Venice, Italy, 2007.

[GF45] V. Ginzburg and I. Frank, Journ. Phys. USSR 9 **353** (1945).

[HBE+04] Z. Huang et al., *Suppression of microbunching instability in the linac coherent light source*, Phys. Rev. ST AB **7** (2004).

[HFS08] K. Honkavaara, B. Faatz and S. Schreiber, *Status of FLASH*, Proceedings of the FEL 2008 Conference, Gyeongju, Korea, 2008.

[HLS06] K. Hacker, F. Loehl and H. Schlarb, *Large horizontal aperture BPM for use in dispersice sections of magnetic chicanes*, Proceedings of the EPAC 2006 conference, Edinburgh, Scotland, 2006.

[HLS07] K. Hacker, F. Loehl and H. Schlarb, *Large horizontal aperture BPM and precision bunch arrival pickup*, Proceedings of the DIPAC 2007 conference, Venice, Italy, 2007.

[Jac98] J. D. Jackson, *Classical electrodynamics*, 3rd ed., John Wiley & Sons, Inc., 1998 (english).

[KAB+08] S. Khan et al., *sFLASH: An experiment for seeding VUV radiation at FLASH*, Proceedings of the FEL 2008 Conference, Gyeongju, Korea, 2008.

[KCCK07] J. Kim, J. Chen, J. Cox and F. X. Kärtner, *Attosecond-resolution timing jitter characterization of free-running mode-locked lasers*, Opt. Lett. **32** (2007), no. 24, 3519 – 3521.

[KCCK08] J. Kim, J. A. Cox, J. Chen and F. X. Kärtner, *Drift-free femtosecond timing synchronization of remote optical and microwave sources*, Nature Photonics **2** (2008).

[KCZ+07] J. Kim et al., *Long-term femtosecond timing link stabilization using a single-crystal balanced cross correlator*, Opt. Lett. **32** (2007), no. 9, 1044 – 1046.

[Kel92] S. M. Kelly, *Characteristic sideband instability of periodically amplified average soliton*, Electron. Lett. **28** (1992), no. 8.

[KIK+04] J. Kim et al., *Large-scale timing distribution and RF-synchronization for FEL-facilities*, Proceedings of the FEL 2004 Conference, Trieste, Italy, 2004.

[KLFK07] J. Kim, F. Ludwig, M. Felber and F. X. Kärtner, *Long-term stable microwave signal extraction from mode-locked lasers*, Opt. Lett. **15** (2007), 8951 – 8959.

[LAF+08a] F. Löhl et al., *Influence of erbium-doped fiber amplifiers on the timing stability of optical pulse trains*, Conference on Lasers and Electro Optics 2008, San Jose, USA, 2008.

[LAF+08b] F. Loehl et al., *Observation of 40 fs synchronization of electron bunches for FELs*, Proceedings of the FEL 2008 conference, Gyeongju, Korea, 2008.

[LAF+08c] F. Loehl et al., *Experimental determination of the timing stability of the optical synchronization system at FLASH*, Proceedings of the EPAC 2008 conference, Genoa, Italy, 2008.

[LAF+08d] F. Loehl et al., *Measurement and stabilization of the bunch arrival time at FLASH*, Proceedings of the EPAC 2008 conference, Genoa, Italy, 2008.

[LCM+07] F. Loehl et al., *Sub-10 femtosecond stabilization of a fiber link using a balanced optical cross correlator*, Proceedings of the PAC 2007 conference, Albuquerque, New Mexico, USA, 2007.

[LHG+08] G. Lambert et al., *Injection of harmonics generated in gas in a free-electron laser providing intense and coherent extreme-ultraviolet light*, Nature Physics **4** (2008), 296 – 300.

[LHL+06] F. Loehl et al., *A sub-100 fs electron bunch arrival-time monitor system for FLASH*, Proceedings of the EPAC 2006 conferemce, Edinburgh, Scotland, 2006.

[LHS07] F. Loehl, K. Hacker and H. Schlarb, *A sub-50 femtosecond bunch arrival time monitor system for FLASH*, Proceedings of the 8th European Workshop on Beam Diagnostics and Instrumentation for Particle Accelerators, Venice, Italy, 2007.

[LS97] R. Lai and A. J. Sievers, *On using the coherent far IR radiation produced by a charged-particle bunch to determine its shape: I Analysis*, Nucl. Instr. and Meth. **A 397** (1997), 221–231 (english).

[LSC+06] F. Löhl et al., *Measurements of the transverse emittance at the FLASH injector at DESY*, Phys. Rev. ST AB **9** (2006).

[LTMU89] C. E. Lee, H. F. Taylor, A. M. Markus and E. Udd, *Optical-fiber fabry-perot embedded sensor*, Opt. Lett. **14** (1989), 1225 – 1227.

[MCW+08] T. Maltezopoulos et al., *Single-shot timing measurement of extreme-ultraviolet free-electron laser pulses*, New J. Phys. **10** (2008).

[Mol85] L. F. Mollenauer, *Solitons in optical fibres and the soliton laser*, Phil Trans. R. Soc. Lond. A **315** (1985), 437–450.

[MS84] L. F. Mollenauer and R. H. Stolen, *The soliton laser*, Opt. Lett. **9** (1984), no. 1.

[OHF93] M. H. Ober, M. Hofer and M. E. Fermann, *42-fs pulse generation from a mode-locked fiber laser started with a moving mirror*, Opt. Lett. **18** (1993), 367 – 369.

[Röh08] M. Röhrs, *Investigation of the phase space distribution of electron bunches at the FLASH-linac using a transverse deflecting structure*, Ph.D. thesis, University of Hamburg, 2008.

[RS93] J. Roßbach and P. Schmüser, *Basic course on accelerator optics, Lectures given at the CERN Accelerator School*, DESY internal report M-93-02 (1993).

[SCC+00] R. W. Schoenlein et al., *Generation of femtosecond pulses of synchrotron radiation*, Science **287** (2000), no. 5461, 2237 – 2240.

[Sch05a] B. Schmidt, *Pyrodetektoren für schnelle signale - high speed, low noise*, Tech. report, DESY, 2005.

[Sch05b] S. Schreiber, *The injector of the VUV-FEL at DESY*, Proceedings of the FEL 2005 Conference, Stanford, USA, 2005.

[Sch07] S. Schreiber, private communication, June 2007.

[Sch08] P. Schmueser, private communication, November 2008.

[SDR08] P. Schmüser, M. Dohlus and J. Rossbach, *Ultraviolet and soft x-ray free-electron lasers*, vol. 229, Springer, 2008.

[Shi06] T. Shintake, *X-ray FEL Project Design Concept*, Tech. report, RIKEN Spring-8, 2006.

[SHK+06] H. Schlarb, N. Heidbrook, H. Kapitza, F. Ludwig and N. Nagad, *Precision rf gun phase monitor system for FLASH*, Proceedings of the EPAC 2006 conference, Edinburgh, Scotland, 2006.

[SKK+03] T. R. Schibli et al., *Attosecond active synchronization of passively mode-locked lasers by balanced cross correlation*, Opt. Lett. **28** (2003), 947 – 949.

[SSJ+05] J. Seres et al., *Source of coherent kiloelectronvolt x-rays*, Nature **433** (2005).

[SSY99] E. L. Saldin, E. A. Schneidmiller and M. Yurkov, *The physics of Free Electron Lasers*, Springer-Verlag, Berlin, 1999.

[Ste07] B. Steffen, *Electro-optic methods for longitudinal bunch diagnostics at FLASH*, Ph.D. thesis, University of Hamburg, 2007.

[The02] The TTF FEL Team, *SASE FEL at the TESLA Test Facility, Phase 2*, TESLA-FEL-2002-01, DESY (2002).

[TIHN93] K. Tamura, E. P. Ippen, H. A. Haus and L. E. Nelson, *77-fs pulse generation from a stretched-pulse mode-locked all-fiber ring laser*, Opt. Lett. **18** (1993), 1080 – 1082.

[V+07] C. Vaccarezza et al., *Status of the SPARX FEL project*, Proceedings of the FEL 2007 Conference, Novosibirsk, Russia, 2007.

[Wes08] S. Wesch, *Spektroskopie kohärenter Übergangsstrahlung zur strukturanalyse von elektronenpaketen am FLASH-beschleuniger*, Master's thesis, University of Hamburg, 2008.

[Wie03a] H. Wiedemann, *Particle Accelerator Physics I, Basic principles and linear beam dynamics*, 2nd ed., Springer, Berlin, Heidelberg, New York, 2003.

[Wie03b] H. Wiedemann, *Particle Accelerator Physics II, Nonlinear and higher-order beam dynamics*, 2nd ed., Springer, Berlin, Heidelberg, New York, 2003.

[Win08] A. Winter, *Fiber laser master oscillators for optical synchronization systems*, Ph.D. thesis, University of Hamburg, 2008.

[WMG+02] I. Wilke et al., *Single-shot electron-beam bunch length measurements*, Phys. Rev. Lett. **88** (2002), no. 12.

[Zem08] J. Zemella, *Driftfreier Detektor zur Messung des Zeitversatzes zweier verschiedener Laserpulszüge*, Master's thesis, University of Hamburg, 2008.

[ZZ96] A. A. Zholents and M. S. Zolotorev, *Femtosecond x-ray pulses of synchrotron radiation*, Phys. Rev. Lett. **76** (1996), no. 912, 912 – 915.

Acknowledgements

This work would not have been possible without the great support I was given during the course of this thesis.

First of all, I would like to thank my advisors Prof. Dr. Jörg Roßbach and PD Dr. Bernhard Schmidt for introducing the field of accelerator physics to me and giving me the opportunity and the help to prepare my thesis at DESY.

For his assistance and careful reading of my thesis, I would like to thank Prof. Dr. Peter Schmüser.

I am grateful to Prof. Dr. F. Ömer Ilday from the Bilken University for interesting discussions on fiber-lasers and fiber-optics.

Special thanks go to Dr. Holger Schlarb for the many fruitful discussions about synchronization requirements in an FEL and about possible approaches to fulfill the requirements. Furthermore, I would like to thank the members of the synchronization team at FLASH: Dr. Frank Ludwig, Matthias Felber, and Karl-Heinz Matthiesen, who helped me solving many electronics problems, Dr. Vladimir Arsov, with whom I spent a lot of time comparing our arrival-time monitors, Jost Müller for the many nights we spent in the lab characterizing EDFAs, Dr. Axel Winter, Kirsten Hacker, Sebastian Schulz, and Johann Zemella. My fellow PhD students Marie Kristin Bock, Laurens Wißmann, and Patrick Geßler I wish all the best for their future work.

I am grateful to Jaroslaw Szewinski and Wojciech Jalmuzna for the software support of the longitudinal feedback system. I like to thank Jörg Thomas and Gerhard Grygiel for their help with stepper motor controls, Olaf Hensler and Dr. Kay Rehlich for the introduction and help with DOOCS servers, Thomas Bruns for the support of the VME crates I used, Lyudvig Petrosyan for his help with ADCs and timing boards, Gevorg Petrosyan for his help with the DSP programming, and Vladimir Rybnikov for helping me with the FLASH data acquisition system.

Without the tremendous support of our technicians Albert Schleiermacher, Bernd Beyer, Matthias Hoffmann, and Jens Hansen, the realization of the many set-ups would not have been possible and I am grateful for all their help.

For the interesting discussions on beam pick-up designs I like to thank Dr. Manfred Wendt. I am indebted to Dr. Nicoleta Baboi, Helmut Remde, and Silke Vilcins-Czvitkovits for their help during the installation of the beam pick-ups. Furthermore,

I would like to thank Burghard Sparr for his support during the installation of optical fibers and many tons of lead in the accelerator tunnel.

Special thanks go to Dr. Siegfried Schreiber, Dr. Katja Honkavaara, and Dr. Bart Faatz for providing me with many opportunities of measuring at FLASH and for giving me the support for various installations at FLASH. I also like to thank the entire FLASH shift crew for the chance of learning from them and for the support they gave to me during my measurements.

My colleagues at MIT, Prof. Dr. Franz X. Kärtner, Dr. Jungwon Kim, and Jian Chen I like to thank for my interesting and productive visits in Cambridge.

I would like to thank Lars Fröhlich, Dr. Bolko Beutner, Eduard Prat, Stephan Wesch, Christopher Behrens, Dr. Michael Röhrs, Dr. Christopher Gerth, and Dr. Axel Knabbe whom I kept from work with endless but productive discussions on various physical and non-physical topics.

I am grateful to PD Dr. Bernhard Schmidt, Dr. Katja Honkavaara, Dr. Holger Schlarb, Prof. Dr. Ivan Bazarov, Kirsten Hacker, and Dr. Vladimit Arsov for proofreading parts of this thesis.

Many thanks go to Ms. Nikodem for her great support with many administrative issues. I will never forget how she managed to send my posters which I forgot in Hamburg to a conference in Italy within a single day.

For the mechanical construction of the fiber-link mechanics, I would like to thank Katharina Jähnke.

Finally, I like to thank my friends and my family for their tremendous support.